Quantum Computing and Quantum Bits in Mesoscopic Systems

Edited by
Anthony Leggett, Berardo Ruggiero
and **Paolo Silvestrini**

QUANTUM COMPUTING AND QUANTUM BITS IN MESOSCOPIC SYSTEMS

QUANTUM COMPUTING AND QUANTUM BITS IN MESOSCOPIC SYSTEMS

Edited by

A. J. Leggett
University of Illinois at Urbana-Champaign
Urbana, Illinois

B. Ruggiero
Istituto di Cibernetica del CNR
Pozzuoli, Naples, Italy

and

P. Silvestrini
Seconda Universitá di Napoli
Aversa, Naples, Italy

Produced under the auspices of Regione Campania

Springer Science+Business Media, LLC

Library of Congress Cataloging-in-Publication Data

Quantum computing and quantum bits in mesoscopic systems/edited by Anthony Leggett, Berardo Ruggiero and Paolo Silvestrini.
p. cm.
Includes bibliographical references and index.
ISBN 978-1-4613-4791-0 ISBN 978-1-4419-9092-1 (eBook)
DOI 10.1007/978-1-4419-9092-1
1. Coherence (Nuclear physics). 2. Quantum theory. 3. Quantum computers. 4. Mesoscopic phenomena (Physics). I. Leggett, Anthony. II. Ruggiero, Berardo. III. International Workshop on Macroscopic Quantum Coherence and Computing (2002: Naples, Italy) IV. Silvestrini, Paolo.

QC794.6.C58Q36 2004
539.7'5—dc22

2003060038

ISBN 978-1-4613-4791-0

©2004 Springer Science+Business Media New York
Originally published by Kluwer Academic / Plenum Publishers, New York in 2004
Softcover reprint of the hardcover 1st edition 2004

http://www.wkap.com

10 9 8 7 6 5 4 3 2 1

A C.I.P. record for this book is available from the Library of Congress

All rights reserved

No part of this book may be reproduced, stored in a retrieval system, or transmitted in any form or by any means, electronic, mechanical, photocopying, microfilming, recording, or otherwise, without written permission from the Publisher, with the exception of any material supplied specifically for the purpose of being entered and executed on a computer system, for exclusive use by the purchaser of the work

Permissions for books published in Europe: *permissions@wkap.nl*
Permissions for books published in the United States of America: *permissions@wkap.com*

PREFACE

This volume is an outgrowth of the third international workshop on Macroscopic Quantum Coherence and Computing (MQC^2) held in Napoli, Italy, in June 2002. The volume, far from being exhaustive, represents an interesting update of the subject and, hopefully will stimulate further work.

Quantum information science is a new field of science and technology which requires the collaboration of researchers coming from different fields of physics, mathematics and engineering. In fact, the workshop has been characterized by the broad interdisciplinary background of its participants, and it has been designed to stimulate thinking on both fundamental and applied research: for the former aspect we have addressed some fundamental aspects of quantum physics, enhancing the connection between the quantum behaviour of macroscopic systems and information theory. For the applied aspect we have tried to stimulate discussions relevant to practical implementation of quantum computing and information processing devices. On the experimental side the volume reports a recent and earlier observations of quantum behavior in several physical systems, including nuclear and electron spin using MR techniques, quantum-optical systems, coherently coupled Bose–Einstein condensates, quantum dots, superconducting quantum interference devices, Cooper pair boxes, and electron pumps in the context of the Josephson effect. In these systems we have discussed all the required steps, from fabrication, through characterization to the final basic implementation for quantum computing. On the theoretical side, the complementary expertise of the speakers provided models of the various mesostructures, and of their response to external control signals, addressing the thorny problem of minimizing decoherence. Moreover we have improved our understanding of the formal theory of quantum information encoding and manipulation. We hope that this interdisciplinary character of the workshop has been able to encourage exchange and collaborations between different communities working on mesoscopic and quantum computation fields.

This initiative is organized within the activities of MQC2 Association on "Macroscopic Quantum Coherence and Computing" in collaboration with Città della Scienza and the Istituto Italiano per gli Studi Filosofici, under the auspices of the Italian Society of Physics (SIF). We are indebted to V. Corato, C. Granata, L. Longobardi, and S. Rombetto for scientific assistance.

A. J. Leggett
B. Ruggiero
P. Silvestrini

CONTENTS

1. WHEN IS A QUANTUM-MECHANICAL SYSTEM "ISOLATED"? 1
A. J. Leggett

2. MANIPULATION AND READOUT OF A JOSEPHSON QUBIT 13
D. Vion, A. Aassime, A. Cottet, P. Joyez, H. Pothier, M. H. Devoret,
C. Urbina and D. Esteve

3. AHARONOV–CASHER EFFECT SUPPRESSION OF MACROSCOPIC FLUX TUNNELING 23
Jonathan R. Friedman and D. V. Averin

4. SQUID SYSTEMS IN VIEW OF MACROSCOPIC QUANTUM COHERENCE AND ADIABATIC QUANTUM GATES 31
V. Corato, C. Granata, L. Longobardi, S. Rombetto, M. Russo, B. Ruggiero,
L. Stodolsky, J. Wosiek, and P. Silvestrini

5. TEST OF AN rf-SQUID SYSTEM WITH STROBOSCOPIC ONE-SHOT READOUT UNDER MICROWAVE IRRADIATION 41
P. Carelli, M. G. Castellano, F. Chiarello, C. Cosmelli, R. Leoni,
F. Sciamanna, C. Scilletta, and G. Torrioli

6. SQUID RINGS AS DEVICES FOR CONTROLLING QUANTUM ENTANGLEMENT AND INFORMATION 47
M. J. Everitt, P. B. Stiffell, T. D. Clark, R. J. Prance, H. Prance,
A. Vourdas, and J. F. Ralph

7. MANIPULATING QUANTUM TRANSITIONS IN A PERSISTENT CURRENT QUBIT 59
T. D. Clark, J. F. Ralph, M. J. Everitt, P. B. Stiffell, R. J. Prance, and H. Prance

8. VORTICES IN JOSEPHSON ARRAYS INTERACTING WITH NONCLASSICAL MICROWAVES IN A DISSIPATIVE ENVIRONMENT 69
A. Konstadopoulou, J. M. Hollingworth, A. Vourdas, M. Everitt,
T. D. Clark, and J. F. Ralph

9. REALIZATION OF THE UNIVERSAL QUANTUM CLONING AND OF THE NOT GATE BY OPTICAL PARAMETRIC AMPLIFICATION 77
F. Sciarrino, C. Sias, and F. De Martini

10. NEW QUANTUM NANOSTRUCTURES: BORON-BASED METALLIC NANOTUBES AND GEOMETRIC PHASES IN CARBON NANOCONES 87
V. H. Crespi, P. Zhang, and P. E. Lammert

11. TRANSPORT INVESTIGATIONS OF CHEMICAL NANOSTRUCTURES 95
W. Liang, M. Bockrath, and H. Park

12. LONG-RANGE COHERENCE IN BOSE–EINSTEIN CONDENSATES 101
F. S. Cataliotti

13. A SIMPLE QUANTUM EQUATION FOR DECOHERENCE THROUGH INTERACTION WITH THE ENVIRONMENT 111
E. Recami and R. H. A. Farias

14. SEARCHING FOR A SEMICLASSICAL SHOR'S ALGORITHM 123
P. Giorda, A. Iorio, S. Sen, and G. Vitiello

15. LOW T_c JOSEPHSON JUNCTION RESPONSE TO AN ULTRAFAST LASER PULSE 133
P. Lucignano, A. Tagliacozzo, and F. W. J. Hekking

16. INFLUENCE OF THE MEASUREMENT PROCESS ON THE STEP WIDTH IN THE COULOMB STAIRCASE 139
R. Schäfer, B. Limbach, P. vom Stein, and C. Wallisser

17. JOSEPHSON JUNCTION TRIANGULAR PRISM QUBITS COUPLED TO A RESONANT LC BUS: QUBITS AND GATES FOR A HOLONOMIC QUANTUM COMPUTER 149
S. P. Yukon

18. INCOHERENT AND COHERENT TUNNELING OF MACROSCOPIC PHASE IN FLUX QUBITS 161
S. Saito, H. Tanaka, H. Nakano, M. Ueda, and H. Takayanagi

19. DECOHERENCE IN FLUX QUBITS DUE TO 1/f NOISE IN JOSEPHSON JUNCTIONS 171
D. J. Van Harlingen, B. L. T. Plourde, T. L. Robertson, P. A. Reichardt, and J. Clarke

20. ZEEMAN SPLITTING IN QUANTUM DOTS 185
S. Lindemann, T. Ihn, T. Heinzel, K. Ensslin, K. Maranowski, and A. C. Gossard

21. GATE ERRORS IN SOLID-STATE QUANTUM COMPUTER ARCHITECTURES 193
X. Hu, and S. Das Sarma

22. QUANTUM COMPUTING WITH ELECTRON SPINS IN QUANTUM DOTS 201
L. M. K. Vandersypen, R. Hanson, and L. H. Willems van Beveren, J.M. Elzerman, J. S. Greidanus, S. De Franceschi, and L. P. Kouwenhoven

23. RELATION BETWEEN DEPHASING AND RENORMALIZATION PHENOMENA IN QUANTUM TWO-LEVEL SYSTEMS 211
A. Shnirman and G. Schön

24. SUPERCONDUCTING QUANTUM COMPUTING WITHOUT SWITCHES 219
M. J. Feldman and X. Zhou

25. SCALABLE ARCHITECTURE FOR ADIABATIC QUANTUM COMPUTING OF NP-HARD PROBLEMS 229
W. M. Kaminsky, and S. Lloyd

26. SEMICLASSICAL ANALYSIS OF *1/f* NOISE IN JOSEPHSON QUBITS 237
E. Paladino, L. Faoro, A. D'Arrigo, and G. Falci

27. SOLID-STATE ANALOG OF AN OPTICAL INTERFEROMETER 247
K. Yu. Arutyunov, T. T. Hongisto, and J. P. Pekola

28. SINGLE ELECTRON TRANSISTORS WITH Al/AlO_x/Nb AND Nb/AlO_x/Nb JUNCTIONS 255
R. Dolata, H. Scherer, A. B. Zorin, and J. Niemeyer

29. TIME-LOCAL MASTER EQUATIONS: INFLUENCE FUNCTIONAL AND CUMULANT EXPANSION 263
H.-P. Breuer, A. Ma, and F. Petruccione

INDEX 273

QUANTUM COMPUTING AND QUANTUM BITS IN MESOSCOPIC SYSTEMS

WHEN IS A QUANTUM-MECHANICAL SYSTEM "ISOLATED"?

A. J. Leggett[a]
Department of Physics, University of Illinois, 1110 W. Green Street, Urbana, IL 61801-3080

Abstract: In this talk I address the question: Under what conditions can we legitimately describe a quantum-mechanical system by a Schrödinger equation in its own right, and how are these conditions related to the degree of "entanglement" with its environment? As examples of systems that are often claimed to be strongly entangled with their environments but nevertheless seem to be well described by one-particle-like Schrödinger equations, I consider (a) Cooper pairs tunnelling between two different "boxes" and (b) quantum-optical systems confined to a cavity. In both cases I argue that the most "obvious" arguments grossly overestimate the true degree of entanglement.

Keywords: Entanglement, Decoherence, Adiabatic approximation

I want to devote this talk to a question that is ubiquitous in physics yet surprisingly rarely discussed, namely: Why can we ever apply the textbook quantum mechanics of isolated systems to the real world? After all, in real life there is no such thing as an isolated physical system, and moreover, even in cases where the system in question looks at first sight rather well "isolated" such as the photons discussed in cavity QED, one not infrequently hears the view expressed that it must in fact be strongly "entangled" with its environment. So how come we can still apply textbook quantum mechanics to such systems, with apparent success and the necessity of only small corrections? And what, exactly, is the relationship between the concepts of "isolation" and (lack of) "entanglement"? While some aspects of this problem are by now rather well known (and thus will be only briefly discussed below), others, while they may well be widespread "folk-knowledge", have not to my knowledge been explicitly discussed in the literature.

Let us start with a very simple consideration, which by now is indeed rather well appreciated. Imagine that we are dealing with an atom of a particular kind which possesses two approximate energy eigenstates of interest, $|s\rangle$ and $|p\rangle$. We wish to produce in this atom a finite value of the electric polarization $\mathbf{P}$, which for convenience we

[a]E-mail: aleggett@uiuc.edu

Edited by Leggett *et al.*, Kluwer Academic/Plenum Publishers, 2004

will view from the frame rotating with frequency $\omega_{ps} \equiv (E_p - E_s)/\hbar$. Suppose that (for example) the operator $\hat{\Pi}_z$ of the z-component of polarization has matrix elements

$$\langle s|\Pi_z|s\rangle = \langle p|\Pi_z|p\rangle = 0, \quad \langle s|\Pi_z|p\rangle = \langle p|\Pi_z|s\rangle = p_0 \neq 0. \tag{1}$$

Then it is clear that to produce a finite polarization we must create on the atom a *linear superposition* of the form

$$\psi_{\text{at}} = \alpha|s\rangle + \beta|p\rangle$$

and the (rotating-frame) expectation value of Π_z will then be

$$\langle\psi_{\text{at}}|\Pi_z|\psi_{\text{at}}\rangle = 2p_0 \text{Re}\, \alpha^*\beta \tag{2}$$

Now, how are we going to create such a superposition? The obvious way is to apply an electric field close to the resonance frequency ω_{ps}. But in quantum mechanics the radiation field must be described in terms of photons, and the states $|n\rangle_\gamma$ corresponding to different numbers of photons n are mutually orthogonal: $\langle n|n'\rangle_\gamma = \delta_{nn'}$. Suppose then we start with the atom in state $|s\rangle$ and the radiation field in the one-photon state $|1\rangle_\gamma$. As a result of the atom–photon interaction, the state of the atom–photon system that evolves is of the *entangled* form

$$\psi_{\text{at,rad}} = \alpha|s\rangle|1\rangle_\gamma + \beta|p\rangle|0\rangle_\gamma \tag{3}$$

since when the atom makes the $s \to p$ transition the photon is automatically absorbed. But since the atomic polarization operator $\hat{\Pi}_z$ is a unit operator with respect to the radiation field, its expectation value in the state (2) is given by

$$\begin{aligned}\langle\psi_{\text{at,rad}}|\hat{\Pi}_z|\psi_{\text{at,rad}}\rangle = {} & |\alpha|^2_\gamma\langle 1|1\rangle_\gamma\langle s|\hat{\Pi}_z|s\rangle + |\beta|^2_\gamma\langle 0|0\rangle_\gamma\langle p|\hat{\Pi}_z|p\rangle \\ & + 2\text{Re}\, \alpha^*\beta_\gamma\langle 1|0\rangle_\gamma\langle p|\hat{\Pi}_z|s\rangle\end{aligned} \tag{4}$$

But in view of (1) and the condition ${}_\gamma\langle 1|0\rangle_\gamma = 0$, this is automatically zero! So we can never produce a finite atomic polarization by starting with a state of the radiation field corresponding to a single photon. It is clear that the same conclusion holds when this initial state is any "Fock state" $|n\rangle_\gamma$.

Of course the solution is well known: What we must do is to prepare the radiation field not in a Fock state $|n\rangle_\gamma$, but in a *coherent state*, or more generally in a superposition of states of the form

$$\Psi_{\text{rad}} = \sum_n c_n|n\rangle_\gamma \tag{5}$$

Then, following through the argument as above, and supposing that the effect of the atom–photon interaction is to implement the evolution

$$|s\rangle|n\rangle_\gamma \to \alpha_n|s\rangle|n\rangle_\gamma + \beta_n|p\rangle|n-1\rangle_\gamma \tag{6}$$

(where in fact $\beta_n \sim$ const. $\sqrt{n}$ for sufficiently short times), we see that the expectation value of the polarization in the final state is

$$\langle \hat{\Pi}_z \rangle = 2p_0 \sum_n (\alpha_n^* \beta_n C_n^* C_{n-1}) \tag{7}$$

which is in general nonzero as long as one or more of the quantities $C_n^* C_{n-1}$ is nonzero. In particular, if the C_n have the values appropriate in a coherent state, then it turns out that

$$\langle \hat{\Pi}_z \rangle = \alpha p_0 E_z \tag{8}$$

where E_z is the c-number quantity given (in the rotating frame) by

$$E_z = \langle \Psi_{\text{rad}} | \hat{E}_z | \Psi_{\text{rad}} \rangle \tag{9}$$

$\hat{E}_z$ being the quantum-mechanical operator of the electric field. More generally, when the radiation field starts in a large-amplitude coherent state with the expectation value of photon number equal to N, we find that (to order N^{-1}) the interaction Hamiltonian has the property

$$\hat{H}_{\text{int}} |\Psi_{\text{at}}\rangle |\Psi_{\text{rad}}\rangle = |\Psi'_{\text{at}}\rangle |\Psi_{\text{rad}}\rangle \tag{10}$$

Thus the atom–photon system remains forever disentangled, and the quantity Ψ_{rad} falls out of any expectation value referring only to the atom. As a result, under these conditions the standard textbook approach, in which the atom is treated as an isolated quantum-mechanical system subject to a classical electric radiation field, is completely justified.

It is clear that this is a special case of a more general situation: whenever the "environment" of the system starts off in an (exact or approximate) coherent state and this state is an eigenstate of the environment operator which enters the system–environment interaction, then it should be valid to treat this operator as a classical quantity and treat the system as an isolated quantum-mechanical system subject to a Schrödinger equation containing this classical variable. Of course, it is not at all obvious a priori that a typical "environment", even if it is macroscopic in scale, will automatically or naturally be found in a coherent state; for some interesting considerations relevant to this question, see Ref. [1].

In any case, there are many everyday cases where this kind of resolution is not available. Perhaps the most obvious (though the resolution in this case is rather straightforward, see below) is that of a charged particle interacting with the zero-point radiation field (rather than with some external field imposed by the experimenter, as above). In this case, if we imagine adiabatically turning off the interaction, the state of the radiation field so attained (which crudely speaking corresponds to the "initial" state in the above argument) is the groundstate $|0\rangle_\gamma$, so when we turn the interaction back up to its real-life value the state of the particle–photon system we generate is certainly entangled. Yet application of standard quantum mechanics to the electron (etc.) as a simple quantum-mechanical system seems to give, in many cases, essentially perfect agreement with experiment (for example, in a Davisson–Germer type diffraction experiment).

The resolution of this prima facie paradox lies, of course, in the classic work of the 1940s and 1950s on renormalization in quantum electrodynamics. Most of the effect

of the particle–radiation interaction, and, in particular, the effect of interaction with radiation modes of frequency much higher than the characteristic frequency of particle motion, can be buried in a renormalization of the parameters of the particle such as mass, charge, magnetic moment, and so on. Only a small residual part is left corresponding to interaction with frequencies of the order of, or not much larger than, the frequency of particle motion; effects of this residual interaction include "real" transition processes such as bremsstrahlung and a small effective dependence of the particle parameters on its exact state, for example, the Lamb shift; so long as one is not interested in these effects, textbook "single-particle" quantum mechanics works just fine. A specific result of these considerations is that once mass renormalization is taken into account (i.e., the "experimental" mass is used in the equations), the interference effects characteristic of quantum mechanics take place with 100% efficiency; for example, the fringe visibility in an (ideal) neutron interferometer is 100%, despite the fact that (via its magnetic moment) the state of the ("bare") neutron is strongly entangled with that of the zero-point radiation field. In effect, the neutron drags its cloud of virtual photons along with it, so that by the time the two beams in the interferometer reconverge at the final (detection) point, the state of the radiation field is the same for both beams and hence factors out of the expression for any expectation value referring to the neutron.

It does not seem to be universally appreciated (in particular in much of the quantum measurement literature) that this is actually a special case of a much more generic and everyday state of affairs. The mere fact that a particular system is entangled, even strongly, with its environment does not mean that it cannot display interference effects! To discuss this question in generic terms, it is useful to specialize to the case of a two-state system and attempt a rough-and-ready definition of the "degree of entanglement" of the system with its environment. I will do this as follows. To avoid irrelevant complications, assume that the "universe" (≡ system + environment) is in a pure state and define the reduced density matrix $\hat{\rho}$ of the system as the trace over the environment variables of the corresponding universe density matrix. It is then natural to try to define the "degree of entanglement" $\mathcal{E}$ as some invariant (i.e. basis-independent) function of $\hat{\rho}$, and a possible (though not unique) choice is

$$D = 2(1 - \mathrm{Tr}\,\hat{\rho}^2) \tag{11}$$

If we choose a basis $|1\rangle$, $|2\rangle$ for our system such that $\rho_{11} = \rho_{22}$, we can write

$$\Psi_{\mathrm{un}} = \frac{1}{\sqrt{2}}(|1\rangle|\chi_1(\xi)\rangle + |2\rangle|\chi_2(\xi)\rangle) \tag{12}$$

where $\chi_{1,2}(\xi)$ are states of the environment, and our definition (11) then reduces to

$$\mathcal{E} = 1 - |\langle\chi_1(\xi)|\chi_2(\xi)\rangle|^2 \tag{13}$$

so that the degree of entanglement is zero if the environment states χ_1, χ_2 defined in this basis are identical and unity if they are mutally orthogonal. Actually, it may be in some sense more "physical" to discuss the considerations below in terms of the "degree of purity"

$$\eta \equiv 1 - \mathcal{E} = 2\mathrm{Tr}\,\hat{\rho}^2 - 1 = |\langle\xi_1|\xi_2\rangle|^2 \tag{14}$$

I will now show by an explicit example that even when $\mathcal{E}$ is very close to one the system may still show highly coherent dynamics (cf. Refs. [2,3]). Consider the case where the Hamiltonian of the two-state system in question is of the canonical "spin-boson" form; that is, with the usual convention that the states $|1\rangle$, $|2\rangle$ are eigenstates of the Pauli operator $\hat{\sigma}_z$

$$\hat{H}_{\mathrm{SB}} = \frac{1}{2}\Delta_0\hat{\sigma}_x - \frac{1}{2}\hat{\sigma}_z\sum_i C_i x_i + \hat{H}_{\mathrm{sho}} \tag{15}$$

where $\hat{H}_{\mathrm{sho}}$ describes a bath of simple harmonic oscillators i with coordinate variables x_i and frequencies ω_i. If the coupling term (proportional to $\hat{\sigma}_z$) were absent, then the system can execute simple sinusoidal oscillations between the states $|1\rangle$ and $|2\rangle$ with frequency Δ_0. Once we turn on the interaction term, the behavior depends critically on the strength and frequency-dependence of the associated coupling spectrum $J(\omega) \equiv \sum_i |C_i|^2 |m_i\omega_i\delta(\omega - \omega_i)$; see Ref. [4]. However, there is one nontrivial limit in which the behavior is strikingly simple: Consider the case where $J(\omega) = 0$ for all frequencies ω less than some lower limit ω_{min}, which we choose to be much larger than Δ_0. Then, irrespective of the strength of the coupling, it is clear that the environment will adjust adiabatically to the behavior of the system, that is, the energy eigenfunctions of the "universe" will be to a good approximation of the form (a special case of the lowest-order Born–Oppenheimer approximation, see Ref. [2])

$$\Psi_{\mathrm{un}} = \frac{1}{\sqrt{2}}(|\uparrow\rangle|\chi(\xi)\rangle \pm |2\rangle|\chi_2(\xi)\rangle) \tag{16}$$

where $\chi_1(\xi)(\chi_2(\xi))$ is the groundstate of the last two terms in (15) for $\sigma_z = +1(-1)$, and their splitting will be given by the renormalized tunnelling matrix element

$$\Delta = \Delta_0\langle\chi_1(\xi)|\chi_2(\xi)\rangle \tag{17}$$

where the "Franck–Condon factor" $\langle\chi_1|\chi_2\rangle \equiv F$ is explicitly given by the expression

$$F = \exp -\int_{\omega_{\mathrm{min}}}^{\infty} \frac{J(\omega)}{\omega^2}d\omega \tag{18}$$

and thus can be very small even though $\omega_{\mathrm{min}} \gg \Delta_0$.

It is clear from Eqs (16) and (17) that we effectively now have a renormalized two-state system with (renormalized) tunneling splitting $\Delta \ll \Delta_0$. So, for example, if we start the "universe" in the state $|1\rangle|\chi_1(\xi)\rangle$, it will oscillate between this state and the state $|2\rangle|\chi_2(\xi)\rangle$ with frequency Δ. Now at a time $\pi/2\Delta$ the state of the universe will be

$$\Psi_n = \frac{1}{\sqrt{2}}(|1\rangle|\chi_1(\xi)\rangle + i|2\rangle|\chi_2(\xi)\rangle \tag{19}$$

so that the quantities ρ_{12} and $\mathcal{E}$ will be given by

$$\rho_{12} = \frac{1}{2}iF, \quad \mathcal{E} = 1 - F^2 \tag{20}$$

so that for small F ρ_{12} is small and $\mathcal{E}$ close to 1. If one were to believe a prescription which has been commonly used in the quantum measurement literature, to the effect that the value of ρ_{12} is a measure of the mutual "coherence" of the components $|1\rangle$ and $|2\rangle$ of the wave function, then for F small one would have to conclude that decoherence is nearly complete. This conclusion would of course be quite wrong, since it would imply, inter alia, that for all times subsequent to $\pi/2\Delta$ the system density matrix would remain $(1/2)\hat{1}$ to within terms of order F; whereas in fact, we can carry on with the time evolution and convince ourselves that at time π/Δ the state of the system is the pure state $|2\rangle$ (associated of course with environment states $|\chi_2(\xi)\rangle$), which is about as far as we can get from the above. This phenomena is sometimes called "false decoherence" [3]; note that while the system–environment entanglement does not change the system dynamics qualitatively from that of the isolated system, it does lengthen the time scale by a factor F^{-1}, which may be very large.

Let us briefly discuss the opposite limit of the spin-boson problem, in which the oscillator bath has an upper cutoff at a frequency $\omega_{\max}$ that is much less than Δ_0. In this case there is a second characteristic energy in the problem, the "solvation energy"

$$\kappa \equiv \int_0^{\omega_{\max}} \omega^{-1} J(\omega)\, d\omega \tag{21}$$

Generally speaking we have $\kappa \leq \omega_{\max}$ and thus $\kappa \ll \Delta_0$; the opposite case occurs only for the case of so-called "sub-ohmic" dissipation ($J(\omega) \sim \omega^n$ where $n < 1$) or "ohmic" dissipation ($J(\omega) = \alpha\omega$) with $\alpha \gg 1$, and in most cases of practical interest turns out to forbidden by the sum rules satisfied by $J(\omega)$ (cf. below). Thus I will assume for present purposes that $\kappa \ll \Delta_0$. In that case, after a transient period lasting for a time $\sim \omega_{\max}^{-1}$, the oscillators settle into their unperturbed groundstate $\chi_0(\xi)$ (i.e., the groundstate of H_{sho}), so that to a first approximation the wave function of the universe is the unentangled state

$$\Psi_{\text{un}}(t) = \psi_{\text{spin}}(t)\chi_0(\xi) \tag{22}$$

where $\psi_{\text{spin}}(t)$ corresponds in the generic case to an oscillation with the original frequency Δ_0. Corrections to the unentangled state (22) can be obtained by regarding the spin as providing a high-frequency ($\omega = \Delta_0$) field driving the oscillators; a straightforward calculation then shows that the degree of entanglement $\mathcal{E}$ is at most of order

$$\mathcal{E} \sim \Delta_0^{-2} \int_0^{\omega_{\max}} J(\omega)\, d\omega \lesssim \Delta_0^{-2} \kappa \omega_{\max} \ll 1 \tag{23}$$

Thus, whenever the interaction of a two-state system with its environment can be cast into the canonical spin-boson form, it follows generically that, except possibly in the unusual case $\kappa \gg \omega_{\max}$, interaction with environmental modes of frequency much less than the characteristic system frequency cannot induce appreciable entanglement. It should be noted that this conclusion does not follow if one adds to the standard spin-boson Hamiltonian (15) coupling terms proportional to σ_x ("pure dephasing" terms); in that case it is clear that since the energy eigenstates of the "universe" $\Psi_\pm$ are of the form $\psi_\pm \cdot \chi_\pm(\xi)$ where $\chi_\pm(\xi)$ are different oscillator states, a state corresponding to an oscillation of the system, that is, a superposition of the states $\psi_\pm$, can be strongly entangled irrespective of the ratio ω_c/Δ_0.

Finally, we note that modes of the environment with excitation energies (frequencies) of the order of the (renormalized) system tunnelling matrix Δ play a specially important role, since they can exchange energy *irreversibly* with the system, leading to dissipation and (true) decoherence. Thus these modes must be treated with special care in any calculation that attempts to get the system dynamics quantitatively correct; such a calculation is attempted, for example, in Ref. [4].

As we have seen in the case of "false decoherence", the mere observation of coherent behavior in a two-state system does not itself establish the absence of substantial entanglement with its environment (although in cases when the latter is present, one would generally prima facie expect a substantial renormalization of the two-state oscillation frequency). But are the two-state systems that are envisioned as possible qubits for quantum computation in fact so entangled? Two systems in particular are of interest: a Cooper pair tunnelling in and out of a small "box" [5] and a pair of states of the radiation field $|0\rangle_\gamma$ and $|1\rangle_\gamma$ occurring in a QED cavity. In both of these cases it is not infrequently argued that a substantial degree of entanglement must exist, in the Cooper-pair case with the other ($\sim 10^9$) electrons in the box, in the QED case with the electrons in the walls of the cavity. To be sure, the existence of such substantial entanglement is at first sight difficult to reconcile with the fact that the experimental two-state behavior seems in each case rather well predicted by the textbook quantum mechanics of an isolated system (and in particular that the two-state oscillation frequency does not seem to be substantially renormalized); however, this argument may not be totally foolproof, so that an explicit calculation of the degree of entanglement is desirable. I shall show that in both cases it is very small, and in particular that is the case of the QED cavity; the strong "confinement" of the photons by the electrons of the walls *does not* imply strong entanglement with them. I will confine myself here to order-of-magnitude arguments; I hope to give a more quantitative discussion elsewhere.

Let us start with the Cooper-pair box, and choose the basis $|1\rangle$ and $|2\rangle$ to correspond to the Cooper pair being in box 1 and the reservoir respectively; for zero bias the energy eigenstates are then the usual symmetric and antisymmetric combinations of $|1\rangle$ and $|2\rangle$ and are split by the tunnelling energy t, so that if we neglect the system–environment coupling the system (pair) can perform oscillations between the two boxes with frequency $t/\hbar$. I will assume for simplicity that the distance between the box and the reservoir is large compared to the size of the box and that the latter has characteristic dimension L. The most important part of the "environment" in this case is the many ($\sim 10^9$) electrons in the box that do not engage in tunnelling; the relevant system–environment interaction is simply the Coulomb interaction of the tunnelling pair with these electrons, and may be written in the form

$$\hat{H}_{\rm int} = \hat{\Omega}|1\rangle\langle 1|, \quad \hat{\Omega} \equiv \int^V dr|\psi_c(r)|^2 \int dr' \frac{\hat{\rho}(r')}{|r-r'|} \times 2e^2/4\pi\varepsilon_0 \tag{24}$$

where V is the volume of the box, $\psi_c(r)$ is the (normalized) groundstate center-of-mass wave function of the Cooper pair inside the box, and $\rho(r') \equiv \sum_i \delta(r' - r_i)$ is the density of the N electrons originally in the box. In writing (24) I have ignored both the finite extent of the pair and the indistinguishability of the electrons composing it from the N "environmental" electrons; it is fairly clear that taking these complications into account will not change the order of magnitude of the quantities calculated below. Let us define the spectral density

$$\chi(\omega) \equiv \sum_n |\hat{\Omega}|^2_{n0} \delta(\omega - (E_n - E_0)/\hbar) \tag{25}$$

where n labels the energy eigenstates of the system formed by the N_c electrons in the box. (To the extent that multiple excitation of a single mode can be neglected and the problem thus [4] cast in the "spin boson" form, $\chi(\omega)$ is nothing but the $J(\omega)$ defined above.) Then it is clear that to the lowest order in $\hat{\Omega}_c$ the degree of entanglement is simply given by

$$\mathcal{E} = \int_0^\infty \omega^{-2}\chi(\omega)\,d\omega \equiv K_{-2} \tag{26}$$

where we define the moments of $\chi(\omega)$ by

$$K_n \equiv \int_0^\infty \omega^n \chi(\omega)\,d\omega \tag{27}$$

Needless to say, we cannot calculate the quantity K_{-2} exactly without a detailed knowledge not only of the shape of the box but also of the many-body eigenfunctions. However, *provided* that the behavior of $\chi(\omega)$ is not "pathological" (see below), it is easy to estimate the order of magnitude of K_{-2}, as follows: K_{-2} should be of the order of $(K_{-1}^3 K_1^{-1})^{1/2}$. Now K_1 should be of order $e^4/\varepsilon_0^2 L^2$ times the f-sum rule expression for the density correlation function at wave vector $q \sim L^{-1}$ in infinite space, which is Nq^2/m; thus $K_1 \sim Ne^4/m\varepsilon_0^2 L^4$. On the other hand, K_{-1} should be of order $(e^4/\varepsilon_0^2 L^2)$ times the "compressibility" of the charged electron gas in the box, which is of order $C/e^2 \sim \varepsilon_0 L/e^2$. (Note that the "typical" excitation frequency, which is $(K_1 K_{-1})^{1/2}$, comes out reassuringly to be of the order of the bulk plasma frequency $\omega \equiv (Ne^2/mL^3\varepsilon_0)^{1/2}$, as it should.) Thus, $(n \equiv N/L^3)$

$$\mathcal{E} \sim K_{-2} \sim (na_0 L^2)^{-1/2} \tag{28}$$

where a_0 is the Bohr radius. For realistic box geometries this quantity is always small compared to 1 (typically $\lesssim \sim 10^{-5}$).

The above argument might conceivably fail if $\chi(\omega)$ should turn out to have a great deal of spectral weight at very low frequencies, then the quantity $(K_{-1}^3/K_1)^{1/2}$ could be a substantial underestimate of K_{-2}. I believe this to be extremely improbable, because the most important Fourier components of the response will be those corresponding to wave vector $q \sim L^{-1}$, and their low-frequency spectral density will be automatically suppressed by the strong Coulomb repulsion, according to the standard RPA formula

$$\chi(q\omega) = \frac{\chi_0(q\omega)}{1 + V(q)\chi_0(q\omega)} \tag{29}$$

which should be at least a good qualitative guide. Quite irrespective of this, it is clear that K_{-2} cannot be smaller than $\omega_{\min}^{-1} K_{-1}$, where $\omega_{\min}$ is the minimum frequency of excitation of the system of electrons at fixed N. Since this quantity is 2Δ in the (zero-temperature) superconducting state, and K_{-1} is λE_c $(E_c \equiv e^2/8\pi\varepsilon_0 C, \lambda \sim 1)$, it follows that K_{-2}, cannot be larger than $\lambda E_c/(2\Delta)$. The quantity E_c/Δ is about 0.5 for the experiment of Ref. [5] and 0.25 for that of Ref. [6], and hence by this argument alone the "purity" $\eta \equiv 1 - \mathcal{E}$ cannot be much smaller than 1; in fact, since the condition $\mathcal{E}_c < \Delta$ is necessary for a Cooper-pair box to "work" at all, the minimum purity is of the order $\lambda/2$

(or $\sim 1 - e^{-\lambda/2}$ for $\lambda \gtrsim 1$, compare the discussion above on the spin-boson problem). However, for the reason above I believe that the corresponding upper limit on $\mathcal{E}$ is almost certainly a gross overestimate of the entanglement. I hope to amplify this argument elsewhere.

I finally turn to the case of the alleged entanglement of the photons in a QED cavity with the atoms of the confining walls. This differs from the Cooper-pair box case in that it is superpositions of the (approximate) energy eigenstates $|0\rangle_\gamma$ and $|1\rangle_\gamma$, rather than the eigenstates themselves, which are allegedly entangled; moreover this is not strictly a "two-state" system, since as we shall see it is necessary for consistency to take into account also the state $|2\rangle_\gamma$, and this strictly speaking requires us to generalize the definition of the degree of entanglement $\mathcal{E}$. I will not bother to give such an extended definition here, but will simply ask the intuitive question: How "different" (orthogonal) are the states of the environment according to whether the electromagnetic field in the cavity is in the (nominal) state $|0\rangle_\gamma$ or $|1\rangle_\gamma$? As we shall see, the qualitative result is that they differ only very little, and this conclusion is independent of the technical definition of $\mathcal{E}$.

I will assume that the electrons in the walls are at all times in their groundstate except in so far as they are perturbed by the electromagnetic field. In terms of the electron variables ξ and the electromagnetic vector potential $A(r)$, the time-independent Schrödinger equation for the wave functional $\Psi\{A(r)\colon \xi\}$ is

$$\left\{\int dr\left\{\frac{\delta^2}{\delta A(r)^2} + (\nabla \times A)^2 + j(\mathbf{r}) \cdot \mathbf{A}(\mathbf{r}) + \frac{\rho(r)}{m}A^2(r)\right\} + H'_{\mathrm{el}}(\xi)\right\}\Psi[\mathbf{A}(\mathbf{r}) : \xi]$$
$$= E\Psi[A(r) : \xi] \tag{30}$$

where the integral runs over all space including the cavity walls and $H'_{\mathrm{el}}(\xi)$ is the part of the Hamiltonian of the electrons in the walls that is independent of $A(r)$. $j(r)$ is the electric current density operator of the electrons and $p(r)$ the charge density operator.

I will simply state the salient features of the outcome of an analysis of Eq. (30) without proof; the details will be given elsewhere. As we might perhaps intuitively expect, a fairly good approximation to the energy eigenstates is of the form

$$\Psi\{A(r), \xi\} = \prod_n \chi_n^{(\lambda)}(A_n) \cdot \Phi_0(\xi) \tag{31}$$

where $\Phi_0(\xi)$ is the groundstate of $H'_{\mathrm{el}}(\xi)$ and the A_n are amplitudes of normal modes of the electromagnetic field with frequency ω_n and space-dependence $\varphi_n(\mathbf{r})$. (For simplicity I have buried the polarization index in the notation n here). The $\chi_n^{(\lambda)}$ are the usual harmonic-oscillator eigenfunctions for an oscillator of frequency ω_n, so that with an obvious extension of the notation the energy corresponding to (31) is

$$E = \sum_n \left(\lambda_n + \frac{1}{2}\right)\hbar\omega_n \tag{32}$$

The crucial point to appreciate is that for (31) to be a good approximation, the space-dependence of the eigenfunction $\phi_n(r)$ must be determined by the usual equation, *which includes the response of the electrons* to the corresponding classical field; specializing for simplicity to the case where this response is local and thus can be described by the uniform

conductivity $\sigma(\omega)$, we have schematically for the eigenvalue equation with eigenfunctions $\phi_n(r)$ and eigenvalues ω_n

$$(\omega^2 - c^2\nabla^2 - \theta(r)i\omega\sigma(\omega))\varphi(r) = 0 \tag{33}$$

where $\theta(r)$ is defined to be zero inside the cavity and one in the walls. The differential equation (33) must be supplemental by the usual continuity conditions on the fields at the boundary of the cavity. The salient point is then that for ω less than the electron plasma frequency $\omega_p \equiv (ne^2/m\varepsilon_0)^{1/2}$ (n = electron density) the eigenfunctions fall off exponentially to zero within the walls in a skin depth $\lambda(\omega)$, which, except for ω very close to ω_p, is the order of the high-frequency skin depth $\lambda_0 \equiv c/\omega_p$; moreover the coefficient of the decaying exponential is related to the rms amplitude inside the cavity by a factor of order $(\lambda(\omega)/\lambda_{fs})$, where $\lambda_{fs}(\omega) \equiv 2\pi c/\omega$ is the free-space wavelength.

Any state of the form (31) is of course completely unentangled. In considering the corrections to this picture, I will specialize for simplicity to the case that the real part of the a.c. conductivity $\sigma(\omega)$ can be approximated by zero for the photons we wish to consider; this is a good approximation both for microwave radiation ($\omega \ll \Delta$) in a superconducting cavity and for infrared and possibly optical radiation ($\omega\tau \gg 1$) in a normal-metal or superconducting cavity. Moreover, I shall assume as above that the electrodynamics of the metal is local and so can be specificied by $\sigma(\omega)$ alone. We focus on a given mode j, whose frequency ω_j satisfies the above condition, and therefore neglect the perturbation to the other modes, writing

$$\Psi\{A(r), \xi\} = \prod_{n \neq j} \chi_n^{(\lambda)}(A_n)\psi^{(\lambda)}(A_j : \xi) \tag{34}$$

The states $\psi^{(\lambda)}(A_i : \xi)$ are found by doing perturbation theory in the relevant part of the coupling $\mathbf{j} \cdot \mathbf{A}$: to lowest order we expect for instance

$$\psi^{(0)}(A_j : \xi) = |0\rangle_i \Phi'(\xi) \tag{35}$$

where $\Phi'(\xi)$ is a linear combination of excited states of $H'(\xi)$ and $|0\rangle_j$, $|1\rangle_j$ refer to the unperturbed eigenstates of the radiation field. Similarly we expect that the "single-photon" state is given by

$$\psi^{(1)}(A_j : \xi) = |1\rangle_j \Phi_0(\xi) + |0\rangle_j \Phi''(\xi)\rangle + |2\rangle_j X(\xi) \tag{36}$$

and so on. Here the functions Φ'_1, Φ'', X are orthogonal to $\Phi_0(\xi)$ and are not normalized.

It is clear that independently of the precise definition of the "degree of entanglement" in a superposition of the physical zero-photon and one-photon states of the mode i, it will be of the order of magnitude of the quantity $\langle\Phi'|\Phi'\rangle$. In turn it is fairly straightforward, by inserting the explicit perturbation theoretic experiment for Φ' and comparing with the standard Kubo formula result, to see that $\langle\Phi'|\Phi'\rangle$ is given by an expression of the form

$$\langle\Phi'|\Phi'\rangle = \langle A_j^2\rangle \int dr |\varphi_j(r)|^2 Q(\omega) \tag{37}$$

where $Q(\omega)$ is a function that actually depends on the choice of gauge, but whose general order of magnitude is, independently of this, bounded above by ω_p^2/ω. The crucial point,

now, is that the dimensionless quantity $\int dr|\varphi_j(r)|^2$ (the "probability of finding the photon outside the cavity") is very small ($\sim(\lambda(\omega)/L)(\lambda(\omega)/\lambda_{sf})^2 \lesssim \lambda_0^3/\lambda_{sf}^2 L$, see above). Since the zero-point mean square amplitude $\langle A_j\rangle_0^2$ is of order ω_j^{-1}, we finally find

$$\langle\Phi'|\Phi'\rangle \lesssim \lambda_0/L \tag{38}$$

This quantity is very small for all realistic QED cavities used to date, and thus the above argument indicates that at least under the condition that $\mathrm{Re}\,\sigma(\omega)$ is negligible for the photons in question, their states are only very weakly entangled with those of the electrons in the walls. This is sufficient for my stated purpose of demonstrating that confinement does not imply entanglement; I hope to discuss the more general case in detail elsewhere.

This work was supported by the National Science Foundation under grant no. NSF-EIA01-21568. I thank Daniel Esteve, Bill Unruh and Michel Devoret for interesting me in these questions and for helpful discussions.

REFERENCES

[1] W. H. Zurek, S. Habib, and J. P. Paz, *Phys. Rev. Letters* **70**, 1187 (1993).
[2] A. J. Leggett, in *Applications of Statistical and Field Theory Methods to Condensed Matter*, ed. D. Baeriswyl, A. R. Bishop and J. Carmelo (Proc. 1989 NATO Summer School, Evora, Portugal).
[3] W. G. Unruh, in Relativistic Quantum Measurement and Decoherence, ed. H-P. Breuer and F. Petruccione, Springer Lecture Notes in Physics, vol. 559, Springer-Verlag, Berlin 2000, p. 125.
[4] A. J. Leggett, S. Chakravarty, A. T. Dorsey, M. P. A. Fisher, A. K. Garg, and W. Zwerger, *Revs. Mod. Phys.* **59** (1987).
[5] Y. Nakamura, Yu. A. Pashkin, and J. S. Tsai, *Nature* **398**, 786 (1999).
[6] D. Vion, A. Aassime, A. Cottet, P. Joyez, H. Pothier, C. Urbina, D. Esteve, and M. H. Devoret, *Science* **296**, 886 (2002).

MANIPULATION AND READOUT OF A JOSEPHSON QUBIT

D. Vion, A. Aassime, A. Cottet, P. Joyez, H. Pothier, M. H. Devoret*,
C. Urbina, and D. Esteve
Quantronics Group, Service de Physique de l'Etat Condensé, Division des Sciences de la Matière, CEA-Saclay, 91191 Gif-sur-Yvette, France

Abstract: We have operated a Josephson qubit device in which a long coherence time is obtained by decoupling the qubit from the readout circuit during manipulation. The achieved quantum coherence is sufficient to allow qubit manipulation with NMR-like techniques. We report pulsed microwave experiments that demonstrate the controlled manipulation of the qubit state.

Keywords: Quantum bits, Josephson junctions, Quantum coherence

1. ENGINEERING RULES FOR QUBITS

1.1 Qubit requirements

A two-level system can be used to implement a quantum bit provided it can be manipulated, projectively read out, and coupled to other similar ones in a controlled way (see Ref. [1] for a general review). The performance of a qubit device is measured by the numbers of single-qubit and two-qubit operations that can be performed during its coherence time, which is limited by its interaction with the other degrees of freedom of its environment, including the manipulation and readout systems. Achieving full control of the qubits and long coherence times are clearly somewhat incompatible goals since full isolation of the qubits is impossible. In particular, the readout of the qubit requires coupling it strongly to another physical system, which is itself measured at the macroscopic level. Although all qubit devices have specific features, their coupling to the environment can often be described in a generic way.

1.2 Manipulation, readout and decoherence

We consider here that the total Hamiltonian contains a term $H_c = \hat{X} \cdot \hat{\lambda}$, which couples a qubit variable $\hat{X}$ to an external variable $\hat{\lambda}$ of the qubit embedding circuit. This coupling

*Present address: Applied Physics, Yale University, New Haven, CT 06520, USA.

entangles the qubit and its environment, which results in decoherence of the qubit. The readout system performs the measurement of $\hat{X}$, and the signal to be measured is $\Delta X_{01} = \langle 1|\hat{X}|1\rangle - \langle 0|\hat{X}|0\rangle$. This signal is directly related to the variations of the qubit transition frequency ν_{01} with the average value of the external variable λ treated as a control parameter:

$$\Delta X_{01} = h\frac{\partial \nu_{01}}{\partial \lambda} \tag{1}$$

In the weak coupling regime, decoherence occurs without modifying the qubit states, and the qubit is projected in the eigenstate basis after a time called the coherence time [2]. Decoherence is fully described by relaxation processes, in which an energy $h\nu_{01}$ is exchanged between the qubit and its environment, and by dephasing processes, in which the relative phase between the two qubit states picks an extra random contribution. The entanglement between the qubit and its environment reduces then to a random dephasing arising from the modulation of the qubit transition frequency by the fluctuations of the control variable. The semi-classical approximation, which breaks down in the zero temperature limit, is valid for all the Josephson qubits operated up to now. After a time t, the random phase-shift accumulated between both qubit states is

$$\delta\varphi = 2\pi \int_0^t \frac{\partial \nu_{01}}{\partial \lambda}\, \delta\lambda(t')\, dt' \tag{2}$$

When the fluctuation spectrum $S_\lambda(\omega)$ is constant below a characteristic frequency ω_C, the coherence factor $\langle \exp(i\delta\varphi)\rangle$ decays exponentially at times longer than ω_C^{-1} with a decay time [3] given by

$$T_\varphi = \frac{1}{\pi(\partial \nu_{01}/\partial \lambda)^2 S_\lambda(\omega = 0)} \tag{3}$$

Note that a special treatment is required when the spectral density diverges at low frequency [3]. In general, the spectral density $S_\lambda(0)$ is the sum of contributions arising from:

- thermal fluctuations of the environment, whose contribution is proportional to temperature;
- nonequilibrium extra-noise, arising from uncontrolled variables or from the readout system.

The comparison of expressions (1) and (3) shows that the dephasing time T_φ and the signal to be measured ΔX_{01} are closely related, as can be anticipated. However, coupling the qubit to a readout system qubit opens a way to more noise than required by the measurement process itself. When other noise sources than the measurement system itself cannot be avoided, long dephasing times can nevertheless be achieved by operating the qubit at a stationary working point where $\partial \nu_{01}/\partial \lambda = 0$, so that the coupling to all noise sources is suppressed at first order. Since at such a point the signal vanishes, that is, $\Delta X_{01} = 0$, it has to be changed prior to readout. We have developed this readout strategy for a qubit circuit based on the Cooper-pair box [4], a device for which quantum coherence has already been demonstrated [5]. In this new device, nicknamed the quantronium, activating the readout automatically drives the qubit away from its optimal working point [6,7].

2. THE QUANTRONIUM CIRCUIT

The quantronium circuit, described in Fig. 1, consists of a superconducting loop interrupted by two adjacent small Josephson tunnel junctions with capacitance C_J and Josephson energy E_J each, which define a low capacitance C_Σ superconducting electrode called the "box island", and by a large Josephson junction with large Josephson energy E_{J0}; $20E_J$. The island is charge-biased by a voltage source U through a gate capacitance C_g, and the loop is flux-biased by an external field. In addition to E_J, the quantronium has a second energy scale which is the Cooper pair Coulomb energy E_C; $(2e)^2/2C_\Sigma$. This system has discrete quantum states which are in general quantum superpositions of several charge states with different number N of excess Cooper pairs in the island, and which carry different currents around the loop. In this device, at $E_J \approx E_C$, neither N nor its conjugated variable θ is a good quantum number. The eigenstates are determined by the dimensionless gate charge $N_g = C_g U/2e$ and by the phase $\delta = \gamma + \phi$, where γ is the phase across the large junction and $\phi = 2\pi\Phi/\Phi_0$, with Φ the external flux imposed through the loop and $\Phi_0 = h/2e$. The bias current I_b is zero except during readout of the state.

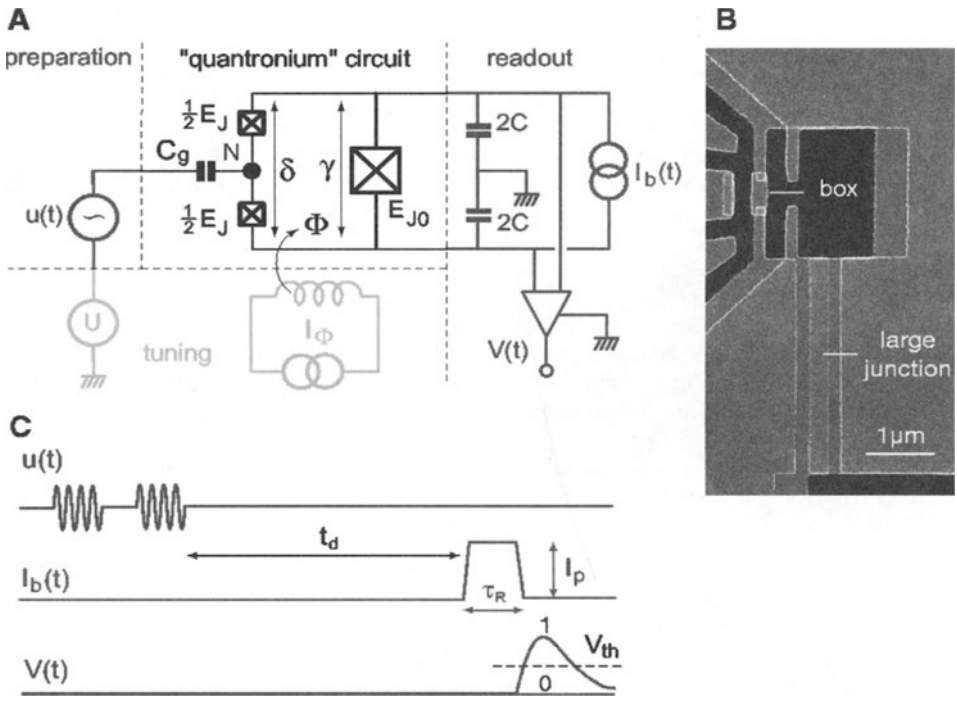

Figure 1. (A) Idealized circuit diagram of the "quantronium", with its tuning, preparation and readout blocks. (B) Scanning electron micrograph of a sample. (C) Manipulation and readout signals: Microwave pulses $u(t)$ applied to the gate manipulate the quantum state of the circuit. Readout is performed by applying a current pulse $I_b(t)$ to the large junction and by monitoring the voltage $V(t)$ across it.

The large junction is shunted by a large capacitor C so that γ is almost a classical variable. In the regime, the energy spectrum is sufficiently anharmonic for the two lowest energy states $|0\rangle$ and $|1\rangle$ to form a two-level system.

This system corresponds to an effective spin one-half with eigenstates $|0\rangle \equiv |s_z = +1/2\rangle$ and $|1\rangle \equiv |s_z = -1/2\rangle$. At $N_g = 1/2$, $I_b = 0$ and $\phi = 0$, its "Zeeman energy" $h\nu_{01}$, of the order of E_J, is stationary with respect to N_g and ϕ, making the system immune to fluctuations of the control parameters (at first order). This point is thus optimal for operating the device. The manipulation of the qubit state is performed by applying microwave pulses $u(t)$ with frequency ν; ν_{01} to the gate, and by applying bias-current pulses with a small amplitude. The resonant modulation of the gate voltage induces Rabi precession between both qubit states, and the bias current shifts the qubit transition frequency. Starting from $|0\rangle$, any superposition $|\Psi\rangle = \alpha|0\rangle + \beta|1\rangle$ can be prepared.

2.1 Qubit readout

For readout, we have implemented a strategy reminiscent of the Stern and Gerlach experiment: the information about the quantum state of the quantronium is transferred onto another variable, the phase γ and the two states are discriminated through the supercurrent in the loop. For this purpose, a trapezoidal readout pulse $I_b(t)$ with a peak value slightly below the critical current $I_0 = E_{J0}/\varphi_0$ is applied to the circuit. When starting from $\langle\delta\rangle \approx 0$ the phases $\langle\gamma\rangle$ and $\langle\delta\rangle$ grow during the current pulse, and consequently a state-dependent supercurrent develops in the loop. This current adds to the bias current in the large junction, and by precisely adjusting the amplitude and duration of the $I_b(t)$ pulse, the large junction switches during the pulse to a finite voltage state with a large probability p_1 for state $|1\rangle$ and with a small probability p_0 for state $|0\rangle$. The efficiency of this projective measurement is expected to exceed $\eta = p_1 - p_0 = 0.95$ for optimum readout conditions. The readout part of the circuit was tested by measuring the switching probability p as a function of the pulse height I_p for a current pulse duration of $\tau_r = 100$ ns, at thermal equilibrium. The discrimination efficiency was then estimated using the calculated difference between the currents of both states $|0\rangle$ and $|1\rangle$. Its value $\eta = 0.6$ is lower than the expected one, possibly due to noise coming from the large-bandwidth current-biasing line.

An actual "quantronium" sample is shown on the right side of Fig. 1. It was fabricated by aluminum deposition through a suspended mask patterned by e-beam lithography. The switching of the large junction to the voltage state is detected by measuring the voltage across it with an amplifier at room temperature. By repeating the experiment (typically a few 10^4 times), the switching probability is measured, which gives the weights of both states.

2.2 Qubit manipulation

First, spectroscopic measurements were performed by applying to the gate a weak continuous microwave irradiation suppressed just before the readout current pulse. The variations of the switching probability with the microwave frequency display a resonance whose center frequency evolves as shown in Fig. 2 as a function of the control parameters. These spectroscopic data allow the determination of the relevant circuit parameters. At the optimal working point, the linewidth was found to be minimal with a 0.8 MHz FWHM, corresponding to a quality factor $Q = 2 \times 10^4$.

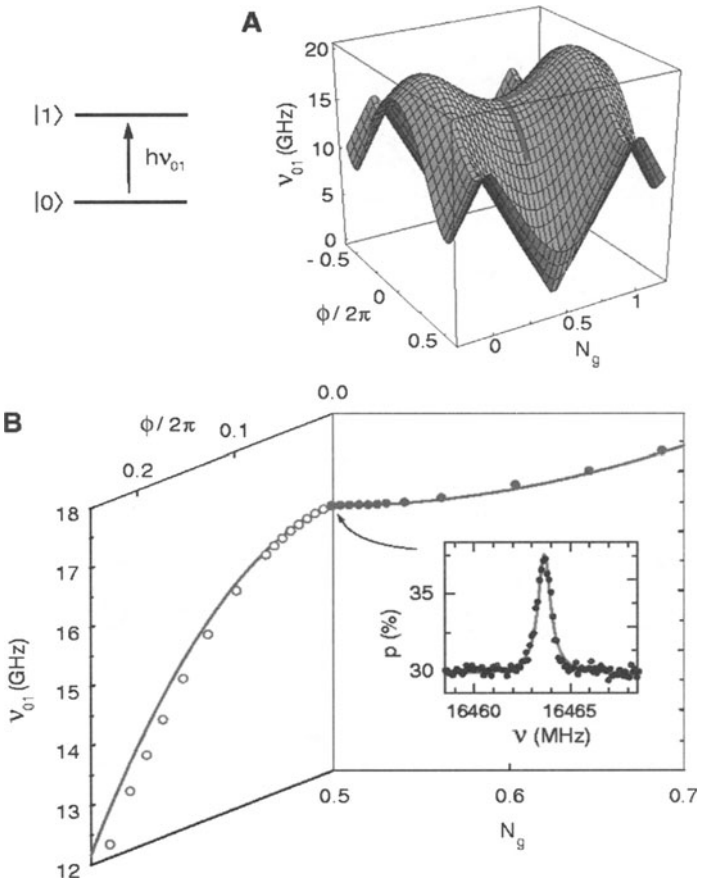

Figure 2. (A) Calculated transition frequency ν_{01} as a function of the control parameters N_g and ϕ. (B) Measured center transition frequency (symbols) as a function of reduced gate charge N_g for reduced flux $\phi = 0$ (right panel) and as a function of ϕ at $N_g = 1/2$ (left panel), at 15 mK. Spectroscopy is performed by measuring the switching probability p (10^5 events) when a continuous microwave irradiation of variable frequency is applied to the gate before readout. Continuous line: best fits used to determine circuit parameters. Inset: narrowest lineshape, obtained at the saddle point (Lorentzian fit with a FWHM of 0.8 MHz).

2.2.1 Preparation of a coherent superposition

Close to the optimal point, controlled rotations of the spin could be performed using large-amplitude microwave pulses at the transition frequency. The switching probability measured after a pulse varies sinusoidally with the pulse duration (see Fig. 3), in agreement with the theory of Rabi oscillations. The linear dependence of the Rabi frequency with the microwave amplitude was used to calibrate the rotation angle. It can be seen that the amplitude of the Rabi oscillations is smaller than the estimated efficiency. This loss of contrast is possibly due to a relaxation of the level

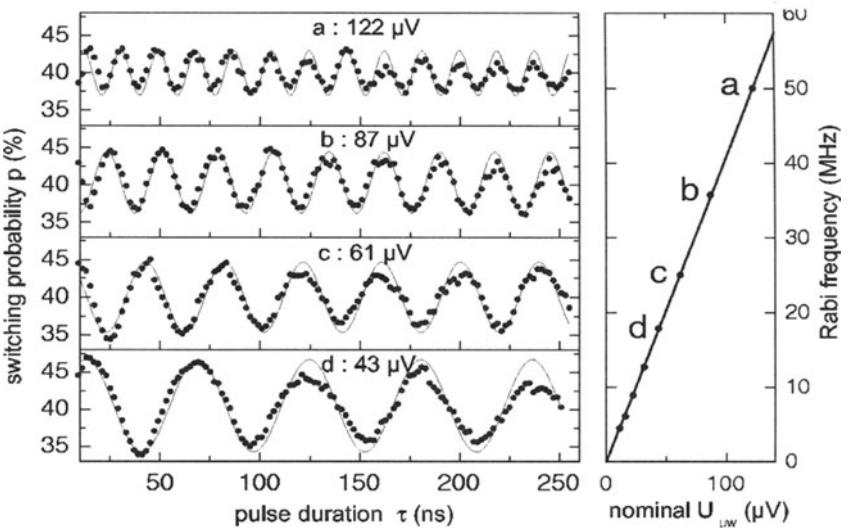

Figure 3. Left: Rabi oscillations of the switching probability p measured just after a resonant microwave pulse of duration τ. Data taken at 15 mK for nominal amplitudes (dots, from top to bottom). Solid lines are sinusoidal fits used to determine the Rabi frequency. Right: test of the linear dependence of the Rabi frequency with the microwave amplitude.

population during the measurement itself. A higher fidelity is needed for achieving perfect single-shot readout.

2.2.2 *Measurement of the coherence time*

The measurement of the coherence time during free evolution was obtained using a two-pulse sequence with a delay during which the qubit evolves freely. For a given detuning $\Delta\nu$ of the microwave frequency, the switching probability displays decaying oscillations of frequency $\Delta\nu$ (see Fig. 4), which correspond to the "beating" of the spin precession with the external microwave field. This experiment is analogous to the Ramsey-fringe experiment. The envelope of the oscillations yields the coherence time, which corresponds to 8000 coherent free precession turns on average.

This time is shorter than the relaxation time $T_1 = 1.8\ \mu$s deduced from the exponential decay of the switching probability when the readout is delayed after a single pulse. Decoherence of the quantum state is thus dominated by dephasing and not by relaxation from the excited state to the ground state.

2.2.3 *Full qubit state manipulation*

At the optimal point, the two-pulse sequence can be used to test the phase-shift between both qubit states induced by a small adiabatic change of the bias current during a pulse, as shown in Fig. 5. By combining bias current phases and microwave pulses, any unitary evolution of the qubit can then be achieved.

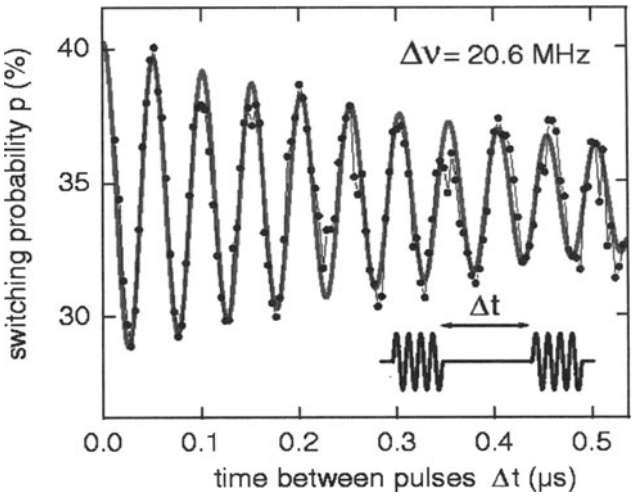

Figure 4. Dots: switching probability after a two-pulse sequence as a function of the pulse delay Δt, at 15 mK. The total acquisition time was 5′. Continuous grey line: fit by an exponentially damped sinusoid with frequency 20.6 MHz, equal to the detuning frequency $\Delta\nu$, and decay time constant $T_\varphi = 0.5$ μs.

2.2.4 Adding and removing decoherence

When departing from the optimal point, the coherence time T_φ decreases rapidly, as shown in the top panel of Fig. 6. By inserting a π pulse in a two $\pi/2$ pulse sequence, NMR-like echo experiments can be performed to probe the spectral density of the noise sources responsible for dephasing. In this sequence, the random phases accumulated

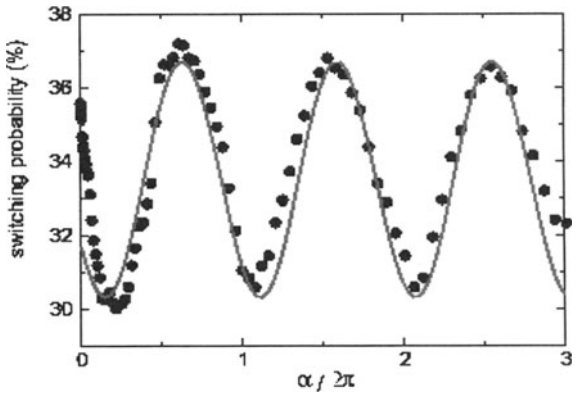

Figure 5. Switching probability following a two-pulse sequence as a function of the rotation angle α induced by a bias current pulse with variable amplitude. The 100 ns bias current pulse is applied between the two microwave pulses.

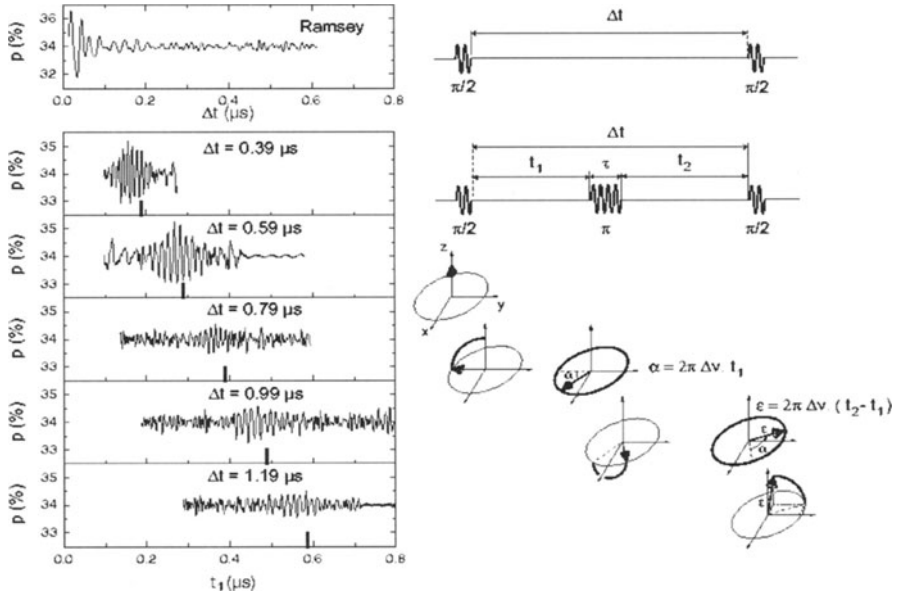

Figure 6. Top panel: Ramsey fringes measured at $N_g = 0.52$, $\phi = 0$. The decay time constant of the fringes is here $T\varphi$; 30 ns. Lower panels: echo signals obtained with the pulse sequence schematically described on the right side, for various sequence durations Δt. A first pulse brings the representative vector of the spin along the $-y$ axis. A free precession follows by an angle α during a time t_1. A subsequent pulse brings the spin in the symmetric position with respect to the x axis. A second free precession follows during time t_2 which brings the spin at an angle ε with the y axis. The last pulse results in a final component of the spin equal. The average switching probability obtained by repeating the sequence is an oscillating function of $(t_2 - t_1)$ with an amplitude peaking when t_2; t_1.

during the two free evolution periods, with durations t_1 and t_2, compensate at t_2; t_1 if the transition frequency does not change on this time-scale. As can be seen in Fig. 6, echoes can be observed at times for which Ramsey fringes are completely washed out. This indicates that in this situation decoherence was essentially due to charge fluctuations at frequencies lower than 1 MHz. At the opposite, no echo was seen in experiments attempting to probe the phase noise, suggesting the phase noise extends over a wide frequency range.

3. CONCLUSION AND PERSPECTIVES

Mastering the quantum evolution of an individual qubit is a first step towards functional quantum circuits. It is, however, still necessary to improve the coherence time by a factor $\approx$100 to achieve a high fidelity readout and to implement controlled qubit interactions. Coupling several quantronium circuits can in principle be achieved using on-chip capacitors and/or ultrasmall junctions, and various coupling schemes have been

proposed for other Josephson qubits [8–11]. Quantum gates could then be implemented and probed by measuring quantum correlations present in multi-qubit entangled states. In conclusion, there is no fundamental obstacle to the realization of an elementary quantum processor based on Josephson junctions.

Acknowledgements

The essential technical contribution of Pief Orfila and the support from the IST-10673 SQUBIT contract, and from the CNRS (Actions Concertée Nanosciences), are gratefully acknowledged.

REFERENCES

[1] M. A. Nielsen, and I. L. Chuang, *Quantum Computation and Quantum Information* (Cambridge University Press, Cambridge, 2000).
[2] Yu. Makhlin, G. Schön, and A. Shnirman, *Rev. Mod. Phys.* **73**, 357 (2001).
[3] A. Cottet, A. Steinbach, P. Joyez, D. Vion, H. Pothier, D. Esteve, and M. E. Huber, in *Macroscopic Quantum Coherence and Quantum Computing*, Edited by D. Averin, B. Ruggiero and P. Silvestrini. (New York, Kluwer Academic, 2001).
[4] A. Cottet, D. Vion, P. Joyez, D. Esteve, and M. H. Devoret, in *Macroscopic Quantum Coherence and Quantum Computing*, Edited by D. Averin, B. Ruggiero, and P. Silvestrini. (New York, Kluwer Academic, 2002).
[5] V. Bouchiat, D. Vion, P. Joyez, D. Esteve, and M. H. Devoret, *Phys. Scr.* **T76**, 165 (1998).
[6] Y. Nakamura, Yu. A. Pashkin, and J. S. Tsai, Nature **398**, 786 (1999); Y. Nakamura, Yu. A. Pashkin, T. Yamamoto, and J. S. Tsai, *Phys. Rev. Lett.* **88**, 047901 (2002).
[7] A. Cottet, D. Vion, P. Joyez, A. Aassime, D. Esteve, and M. H. Devoret, *Physica C* **367**, 197 (2002).
[8] D. Vion, A. Aassime, A. Cottet, P. Joyez, H. Pothier, C. Urbina, D. Esteve, and M. H. Devoret, *Science* **296**, 886 (2002).
[9] C. H. van der Wal A. C. J. ter Haar, F. K. Wilhelm, R. N. Schouten, C. J. P. M. Harmans, T. P. Orlando, Seth Lloyd, and J. E. Mooij, *Science* **290**, 773 (2000).
[10] Siyuan Han, Yang Yu, Xi Chu, Shih-I Chu, and Zhen Wang, *Science* **296**, 889 (2002).
[11] J. M. Martinis, S. Nam, J. Aumentado, and C. Urbina, *Phys. Rev. Lett.* **89**, 117901 (2002).

AHARONOV–CASHER EFFECT SUPPRESSION OF MACROSCOPIC FLUX TUNNELING

Jonathan R. Friedman[1,2,*] and D. V. Averin[1]
[1]*Department of Physics and Astronomy, The State University of New York at Stony Brook, Stony Brook, NY 11794-3800*
[2]*Department of Physics, Amherst College, P.O. Box 5000, Amherst, MA 01002-5000*

Abstract: We show theoretically that the Aharonov–Casher effect can be used to modulate flux tunneling. We study a variant of an rf-SQUID in which the Josephson junction is replaced by a Bloch transistor – two junctions separated by a small superconducting island on which the charge can be induced by an external gate voltage. When the Josephson coupling energies of the junctions are equal and the induced charge is $q = e$, destructive interference between tunneling paths brings the flux tunneling rate to zero. Destructive interference can still occur even if the two junctions are not equivalent, although the tunneling rate no longer goes precisely to zero. We analyze the system in two limits: when the Josephson energy E_J is much larger than the island charging energy E_C and vice versa.

Keywords: Flux tunneling, SQUIDs, Aharonov–Casher effect, Geometric phase

Recent experiments have shown that superconducting devices can behave as macroscopic quantum objects. Superconducting loops can be put into coherent superpositions of flux [1] and persistent-current [2] states. In the charge regime, Nakamura *et al.* [3] have observed quantum oscillations of the charge state on a superconducting island. Very recently, Rabi oscillations were observed in single Josephson junctions [4, 5] and in a hybrid charge-flux device [6]. Here we consider theoretically how flux tunneling in a SQUID can be modulated by a geometric-phase effect [7, 8], the Aharonov–Casher effect.

In the original formulation of the Aharonov–Casher effect [9], a magnetic moment moving around a line charge acquires a phase proportional to the linear charge density. In analogy, Reznik and Aharonov [10] showed that fluxons in a superconductor moving around an external charge q could acquire such a phase. There has been a fair amount of theoretical work concerning this effect in Josephson-junction arrays and devices [11–16]. Experimental evidence for the Aharonov–Casher effect in a Josephson system was first reported by Elion *et al.* [17].

*Corresponding author. E-mail: jrfriedman@amherst.edu

Quantum Computing and Quantum Bits in Mesoscopic Systems
Edited by Leggett *et al.*, Kluwer Academic/Plenum Publishers, 2004

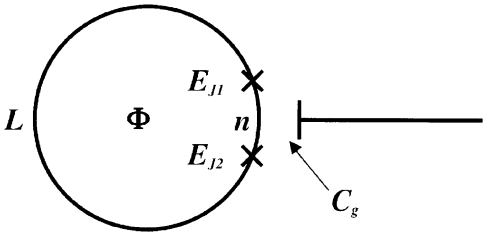

Figure 1. Schematic of the proposed device, an rf-SQUID with the single Josephson junction replaced by a Bloch transistor. The charge on the superconducting island of the transistor can be induced by a gate voltage.

In many studies of the Aharonov–Casher effect in Josephson-junction systems the resistance of the device or array is found to depend periodically on a gate voltage and, thus, the induced charge on the superconducting island(s). It is important to note that Coulomb blockade can produce qualitatively similar phenomena due to the quantization of charge on island(s) [18]. While Coulomb blockade can modulate flux tunneling rates, it cannot, however, completely turn off tunneling. We propose a simple device in which the Aharonov–Casher effect is predicted to suppress entirely flux tunneling [19], allowing the effect to be unambiguously distinguished from Coulomb-blockade oscillations.

Figure 1 shows a schematic of the proposed device, a variant of an rf-SQUID in which the single Josephson junction has been replaced by a Bloch transistor (see, e.g., Ref. [18]) – two small, closely spaced Josephson junctions. The charge on the island between the junctions can be varied by an external gate voltage V_g. The device is similar to those studied in recent experimental [6] and theoretical [20, 21] work. Coulomb blockade is expected to suppress flux tunneling because of the gate-voltage dependence of the critical current of the Bloch transistor. We show that, in fact, the flux tunneling rate can be entirely suppressed when the gate-voltage-induced charge $q = C_g V_g$ is e, an effect that cannot be explained in terms of Coulomb blockade.

The underlying physics of this effect is as follows. When flux tunneling occurs, the Josephson phase across one of the junctions slips, that is, the flux "passes through" one of the junctions. Since there are two junctions, there are two tunneling paths, which encircle the island of the Bloch transistor. Interference occurs between the two paths and when $q = e$, the relative phase of the two paths is π and the interference is destructive, suppressing tunneling. The induced charge q should not be mistaken for the actual charge on the island since it is a c-number linear in the voltage applied to the gate electrode. The amplitude of flux tunneling through a single junction depends on its Josephson coupling energy E_J. Thus, when the Josephson energies of the two junctions are equal,[1] $E_{J1} = E_{J2}$, the destructive interference is complete and the total amplitude of flux tunneling is exactly zero. The Aharonov–Casher effect in this system makes it possible to control the phase of the flux-tunneling amplitude, an effect that can simplify design of Josephson-junction qubits for quantum computing [1, 2, 21, 23–25].

[1]The Josephson energies can be made equal in practice by replacing at least one junction by a small dc-SQUID, as has been done in recent experiments [1, 22], where the effective Josephson energy can be tuned via the application of an external flux.

We consider a SQUID of inductance L (Fig. 1) that is small enough that the SQUID has only two metastable flux states. Each junction has Josephson phase difference ϕ_i, Josephson energy E_{Ji} and capacitance C_i ($i = 1, 2$). A gate electrode couples with capacitance C_g to the island between the junctions and an external flux Φ_x is applied to the SQUID loop. The Hamiltonian for this system is

$$H = \frac{Q^2}{2C} + \frac{(2en - q)^2}{2C_\Sigma} + \frac{(\Phi - \Phi_x)^2}{2L} - E_{J1}\cos\phi_1 - E_{J2}\cos\phi_2 \tag{1}$$

where n is the number of Cooper pairs charging the island, and C_Σ is its total capacitance relative to all other electrodes. The flux Φ in the SQUID is related to the phase differences across the junctions by $2\pi\Phi/\Phi_0 = \phi_1 + \phi_2$, where $\Phi_0 = h/2e$ is the flux quantum. Φ is conjugate to the charge Q on the capacitance C between the ends of the SQUID loop: $[\Phi, Q] = i\hbar$. (Because of the stray-capacitance contribution to C, it is not related directly to the island capacitance C_Σ.) Similarly, the phase $\theta = (\phi_1 - \phi_2)/2$ is conjugate to n: $[\theta, n] = i$. Thus, Φ and θ are the "coordinates" of the SQUID and Q and n are the "momenta". In Eq. (1), we implicitly assume that the junction capacitances are similar so that there is no coupling between the charge variables Q and n.

The Hamiltonian has five relevant energies. These comprise the inductive energy $E_L = \Phi_0^2/2L$, the island charging energy $E_C = (2e)^2/2C_\Sigma$, the "external" charging energy $E_Q = (2e)^2/2C$ and the two Josephson energies, or, more conveniently, their sum and difference: $E_{J+} \equiv (E_{J1} \pm E_{J2})/2$. In general, the shape of the potential is determined by the dimensionless parameter $\beta_L \equiv 2\pi^2 E_{J+}/E_L$, which determines the height of the barrier between stable flux states, and by the junction asymmetry E_{J-}/E_{J+}. For cases of experimental interest $\beta_L \approx 1$.

We analyze tunneling between different flux states in two limits, one in which $E_C \ll E_{J+}$ and the other in which $E_C \gg E_{J+}$. For both cases, in order for flux tunneling to be completely suppressed three conditions must be met: $\Phi_x = \Phi_0/2$, $q = e$, and $E_{J-} = 0$. The first of these simply ensures that the two flux wells are aligned so that levels are on resonance. As we show below, for the case $E_C \ll E_{J+}$, the requirement $E_{J-} = 0$ is more crucial for observing the suppression of tunneling. In the opposite limit, the $q = e$ condition is the more stringent.

The first two terms in the Hamiltonian represent the kinetic energy of the system and the remaining terms represent the potential energy, shown in Fig. 2 for the case $\Phi_x = \Phi_0/2$ and $E_{J-} = 0$. The potential has minima in a checkerboard-like pattern with minima on one side of $\Phi = \Phi_0/2$ shifted by π in the θ direction relative to minima on the other side. The minima are not separated by integer multiples of Φ_0 in the Φ direction because of the inductive term in Eq. (1). However, the potential is strictly periodic in the θ direction, even when $E_{J-} \neq 0$. In fact, since the number n of Cooper pairs on the island is an integer, one can impose periodic boundary conditions on θ, wrapping all points with $\theta = \pi$ to $\theta = -\pi$.

Let us first consider the case $E_C \ll E_{J+}$, in which θ is a good quantum number and one can employ a tight-binding picture in which the system is localized in one of the minima of Fig. 2. We calculate the tunnel splitting using an instanton approach in which the imaginary-time action S_I is evaluated along the least-action paths in the inverted potential [26]. The zero-temperature tunnel splitting is then given by

$$\Delta = \sum_j \omega_j e^{-S_I^j/\hbar} \tag{2}$$

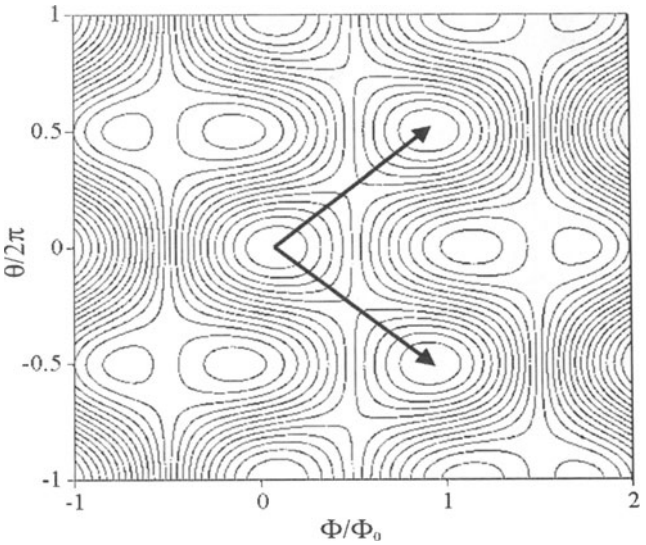

Figure 2. Two-dimensional potential for the system described by Eq. (1) with $E_{J1} = E_{J2} = 0.507\,\Phi_0^2/2L$. When $q = e$, destructive interference between the two paths shown leads to suppression of flux tunneling.

where the sum is over all least-action paths between two potential minima, and ω_j and S_I^j are the attempt frequency and imaginary-time action, respectively, for the jth path. The action is calculated by evaluating

$$S_I^j = \int_{-\infty}^{\infty} \mathcal{L}_E(\tau)\, d\tau \tag{3}$$

along the jth path, where $\mathcal{L}_E(\tau) \equiv -\mathcal{L}(t \to -i\tau)$ is the imaginary-time (Euclidean) Lagrangian obtained from the real-time Lagrangian $\mathcal{L}$, which in turn is obtained from the Hamiltonian by the usual transformation: $\mathcal{L} = \dot{\Phi}Q + ((\Phi_0/2\pi)\dot{\theta})(2en) - H$. For the case $E_{J-} = 0$ and using Hamilton's equations to obtain $\dot{\Phi} = Q/C$ and $(\Phi_0/2\pi)\dot{\theta} = (2en - q)/C_\Sigma$ we find

$$\mathcal{L}_E(\tau) = \frac{C}{2}\dot{\Phi}^2 + \frac{C_\Sigma}{2}\left(\frac{\Phi_0\dot{\theta}}{2\pi}\right)^2 + \frac{(\Phi - \Phi_x)^2}{2L} - 2E_{J+}\cos\left(\frac{\pi\Phi}{\Phi_0}\right)\cos\theta - iq\left(\frac{\Phi_0\dot{\theta}}{2\pi}\right) \tag{4}$$

where the dot represents differentiation with respect to τ. The last term in Eq. (4), being a total time derivative, has no effect on the classical dynamics of the system, but it is responsible for the interference effect that suppresses tunneling.

Let us consider the two tunneling paths illustrated schematically by the arrows in Fig. 2. The endpoints of the two paths are equivalent, since they merely differ in θ by 2π.

For the case $E_{J-} = 0$, every term in Eq. (4) except the last is symmetric under the reflection $\theta \to -\theta$. Hence, the actions of the two paths differ only because of the last term. The imaginary-time action for each path can then be separated into two parts: $S_I^j = \tilde{S}_I + S_{\text{geo}}^j$, where $\tilde{S}_I$ is the action obtained by using all but the last term in Eq. (4) and is the same for both paths. The geometric-phase action for each path is given by

$$S_{\text{geo}}^{1,2} = -iq\left(\frac{\Phi_0}{2\pi}\right)\int_{1,2}\dot{\theta}\,d\tau = \mp iq\left(\frac{\Phi_0}{2\pi}\right)\pi = \mp i\pi\left(\frac{q}{2e}\right)\hbar \tag{5}$$

From Eq. (2), the tunnel splitting is given by

$$\Delta = 2\Delta_0 \cos\left(\frac{q\pi}{2e}\right) \tag{6}$$

where $\Delta_0 = \omega_0 e^{-\tilde{S}_I/\hbar}$ is the tunnel splitting associated with one path. As Eq. (6) indicates, when the induced charge is e, the two tunneling paths interfere completely destructively and flux tunneling is wholly suppressed.

The above analysis is particularly simple because of the assumption $E_{J-} = 0$. If we relax this condition, the tunneling amplitude is modulated as $|\Delta|^2 = \omega_0^2(e^{-2\tilde{S}_I^{(1)}/\hbar} + e^{-2\tilde{S}_I^{(2)}/\hbar} + e^{-(\tilde{S}_I^{(1)}+\tilde{S}_I^{(2)})/\hbar}\cos(q\pi/2e))$, where $\tilde{S}_I^j$ is the nongeometric part of the action associated with the jth path. Here we can safely ignore the weak dependence of the attempt frequency ω_0 on path and take it to be the same for both paths. The fact that the cosine term is unaltered when $E_{J-} \neq 0$ is due to the periodicity of the potential along θ. The "depth" of the tunneling suppression can be characterized through the ratio

$$\left|\frac{\Delta(q=e)}{\Delta(q=0)}\right| = 2\tanh\left(\frac{\delta\tilde{S}_I}{2}\right) \tag{7}$$

where $\delta\tilde{S}_I = \tilde{S}_I^{(1)} - \tilde{S}_I^{(2)}$. With a change of variables and using the fact that energy is conserved along least-action paths, the actions $\tilde{S}_I^j$ can be reduced to a WKB-like expression:

$$\tilde{S}_I^j = \frac{2\hbar}{\pi}\sqrt{\frac{E_L}{E_Q}}\int_{\text{path}j}\sqrt{(E-\tilde{U})\left(1+\lambda\left(\frac{d\theta}{dx}\right)^2\right)}\,dx \tag{8}$$

where $x = \pi\Phi/\Phi_0$, $\lambda = E_Q/E_C$, $\tilde{U} = -\pi^2 U/E_L$ is the dimensionless inverted potential and E is the "energy" – the value of $\tilde{U}$ at the endpoints of the path. The integral was evaluated numerically along the two least-action paths and $\delta\tilde{S}_I$ was found to be linear in E_{J-}/E_{J+} when that parameter is on the order of a few percent. That is,

$$\delta\tilde{S}_I^j \approx \frac{2\hbar}{\pi}\sqrt{\frac{E_L}{E_Q}}\alpha(\beta_L, \lambda)(E_{J-}/E_{J+}) \tag{9}$$

The numerical coefficient $\alpha(\beta_L, \lambda)$ was found to be on the order of unity and changes by at most a factor of three as β_L and λ are both varied by an order of magnitude from experimentally relevant values (e.g., $\beta_L = 2$ and $\lambda = 0.2$). Because of this weak dependence of α, the most important factor in setting the scale for the effect of junction asymmetry is the

ratio E_L/E_Q: for small values of E_Q, one must have a very small junction asymmetry in order for the tunneling suppression at $q = e$ to be observable.

An interesting consequence of Eq. (6) is that when $e < q \bmod(4e) < 3e$ the tunnel splitting becomes negative. This means that the ground and excited states interchange roles: if the ground (excited) state can be approximated by $(|\phi_0\rangle + (-)|\phi_1\rangle)/\sqrt{2}$ when $-e < q \bmod(4e) < e$, where $|\phi_0\rangle$ and $|\phi_1\rangle$ are the distinct fluxoid states connected by the tunneling paths in Fig. 2, then it becomes $(|\phi_0\rangle - (+)|\phi_1\rangle)/\sqrt{2}$ for $e < |q| \bmod(4e) < 3e$.

Next, we consider the limit of large "internal" charging energy, $E_C \gg E_{J+}$. The physics of suppression of flux tunneling for $q \simeq e$ remains the same as for $E_C \ll E_{J+}$. The quantitative form of the tunneling amplitude is, however, quite different because for $E_C \gg E_{J+}$ the system wave function is delocalized in the θ-direction and flux trajectories with all values of $\Delta\theta$ contribute to the tunneling rate. Since the regime of flux tunneling requires the "external" charging energy E_Q to be smaller than E_{J+}, all energies of the flux dynamics are then smaller than the energies of the charge dynamics on the central island. In this case, when $q \simeq e$, only the two charge states of the island, $n = 0$ and $n = 1$, are relevant for the charge dynamics. The Hamiltonian of the system reduces to:

$$H = \frac{Q^2}{2C} + \frac{(\Phi - \Phi_x)^2}{2L} - E_{J+}\cos\left(\frac{\pi\Phi}{\Phi_0}\right)\sigma_z + \frac{e(q-e)}{C_\Sigma}\sigma_x - E_{J-}\sin\left(\frac{\pi\Phi}{\Phi_0}\right)\sigma_y \quad (10)$$

where the Pauli matrices σ_i act on the basis of $(|0\rangle \pm |1\rangle)/\sqrt{2}$, the symmetric and antisymmetric superpositions of the charge states.

The potential $U(\Phi)$ for the evolution of the flux Φ is then seen to have two branches, depending on the charge-space state of the system. For $\Phi < \Phi_0/2$, the symmetric charge state $(|0\rangle + |1\rangle)/\sqrt{2}$ provides the lower branch of the potential, whereas for $\Phi > \Phi_0/2$, the sign of $\cos(\pi\Phi/\Phi_0)$ changes and the lower branch of the potential is given by the antisymmetric state $(|0\rangle - |1\rangle)/\sqrt{2}$. This means that to avoid suppression of flux tunneling from a state localized in the region $\Phi < \Phi_0/2$ into the state with $\Phi > \Phi_0/2$, the system should make a transition between the symmetric and antisymmetric charge states in the course of flux tunneling. From the wave function of these states in the θ-representation: $|\psi_+| \propto \cos(\theta/2)$ and $|\psi_-| \propto \sin(\theta/2)$, one can see that such a transition corresponds to the shift in θ by $\pm\pi$, analogous to the similar shift in the limit of large E_{J+}.

The Hamiltonian (1.10) shows that the coupling between the two branches of the potential is provided by the difference E_{J-} of the Josephson energies and deviations of the induced charge q from e. In the absence of coupling, transitions between the two potential branches and, as a result, flux tunneling, are suppressed. When the coupling is weak (i.e., E_{J-} and $q - e$ are small), transitions between the potential branches take place near the degeneracy point $\Phi = \Phi_0/2$ and can be described in terms of Landau–Zener tunneling. The only difference from the standard situation of Landau–Zener tunneling is that the transition is not driven by a classical external force but by the flux motion under the tunnel barrier and therefore can be described as occurring in imaginary time. The amplitude of such an imaginary-time Landau–Zener transition has been found in the context of the dynamics of Andreev levels in superconducting quantum point contacts [27]. Adapted for the present problem, the expression for the transition amplitude is

$$\omega = \frac{1}{\Gamma(\lambda)}\left(\frac{2\pi}{\lambda}\right)^{1/2}\left(\frac{\lambda}{e}\right)^{\lambda} e^{i\phi}, \quad \lambda \equiv \frac{[e(q-e)/C_\Sigma]^2 + E_{J-}^2}{2E_{J+}[E_Q E]^{1/2}} \quad (11)$$

Here Γ denotes the Gamma function and E is the absolute value of the energy of the quasi-stationary flux state at $\Phi < \Phi_0/2$ measured relative to the effective top of the potential barrier formed by the crossing at $\Phi = \Phi_0/2$ of the two branches of the potential. The phase ϕ of the tunneling amplitude coincides with the phase of the coupling between the potential branches in the Hamiltonian (10) and is given by

$$\tan\phi = \frac{E_{J-}C_\Sigma}{e(q-e)} \tag{12}$$

Since the overall amplitude of flux tunneling is proportional to ω and since $\omega(\lambda) \simeq (2\pi\lambda)^{1/2}$ for $\lambda \ll 1$, Eq. (11) shows that, when E_{J-} is small, flux tunneling is suppressed at $q \simeq e$. Equation (12) also shows that, similarly to the limit of large E_{J+}, the sign of the tunneling amplitude at $E_{J-} \to 0$ changes abruptly when q moves through the point $q = e$. The absolute value of amplitude ω (11) is shown in Fig. 3 as a function of charge q for several values of E_{J-}. The curves in Fig. 3 indicate that the suppression of the flux tunneling amplitude at $q \simeq e$ remains pronounced for quite a large degree of asymmetry of the Josephson coupling energies. Note that this is in contrast to the case of $E_C \ll E_{J+}$ studied above, where the suppression of tunneling was very strongly dependent on E_{J-}. In the present case, however, the suppression depends quite strongly on q. The range of q over which tunneling is suppressed in Fig. 3 is set by the scale $q_0 \equiv 2e(2E_{J+})^{1/2}(E_Q E)^{1/4}/E_C$, which is much smaller than e. Thus, q must be quite close to e in this limit for the suppression of tunneling to be observable.

We have shown that the Aharonov–Casher effect can be used to suppress flux tunneling in an rf-SQUID-like device. We analyzed the flux tunneling rate in two limits: $E_C \ll E_{J+}$ and $E_C \gg E_{J+}$. For both cases tunneling is completely suppressed when $q = e$ and $E_{J-} = 0$. In the former case, the requirement that $E_{J-} = 0$ is crucial while in the latter, $q = e$ is more important. For actual experiments it might be wise to work away from either

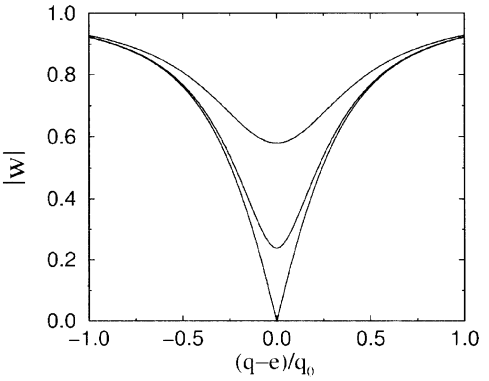

Figure 3. Absolute value of the transition amplitude between the two branches of the flux potential, which is proportional to the amplitude of flux tunneling, as a function of the induced charge q at $q \simeq e$. Note that the scale q_0 of variations of q is much smaller than e. From bottom to top, the curves correspond to increasing difference between the Josephson energies of the two junctions: $E_{J-}/(2E_{J+})^{1/2}(E_Q E)^{1/4} = 0.0, 0.1, 0.3$.

limit so that an overly strong dependence on q or E_{J-} does not prohibit observation of the effect. Elsewhere we have given [19] a general proof that the suppression of tunneling occurs for arbitrary values of E_{J+}/E_C. Thus, the effect should be observable within an experimentally realistic context.

Acknowledgements

We wish to thank J. Mannik, E. Chudnovsky, K. Jagannathan, W. Loinaz and A. Guillaume for useful discussions. This work was supported in part by the NSA and ARDA under ARO contract DAAD199910341.

REFERENCES

[1] J. R. Friedman *et al.*, *Nature* **406**, 43 (2000).
[2] C. H. van der Wal *et al.*, *Science* **290**, 773 (2000).
[3] Y Nakamura, Y A. Pashkin, and J. S. Tsai, *Nature* **398**, 786 (1999).
[4] Y. Yu, S. Han, X. Chu, S.-I. Chu, and Z. Wang, *Science* **296**, 889 (2002).
[5] J. M. Martinis, J. Aumentado, S. W. Nam, and C. Urbina, APS March Meeting, Indianapolis, IN, 2002.
[6] D. Vion, A. Aassime, A. Cottet, P. Joyez, H. Pothier, C. Urbina, D. Esteve, and M. H. Devoret, *Science* **296**, 886 (2002).
[7] A. Shapere and F. Wilczek, *Geometric Phases in Physics* (Singapore, World Scientific, 1989).
[8] M. V. Berry, Proc. R. Soc. London Ser. A-Math. *Phys. Eng. Sci.* **392**, 45 (1984).
[9] Y. Aharonov and A. Casher, *Phys. Rev. Lett.* **53**, 319 (1984).
[10] B. Reznik and Y. Aharonov, *Phys. Rev.* D **40**, 4178 (1989).
[11] B. J. van Wees, *Phys. Rev. Lett.* **65**, 255 (1990).
[12] T. P. Orlando and K. A. Delin, *Phys. Rev.* B **43**, 8717 (1991).
[13] R. Fazio, A. van Otterlo, and A. Tagliacozzo, *Europhys. Lett.* **36**, 135 (1996).
[14] E. Simanek, *Phys. Rev.* B **55**, 2772 (1997).
[15] A. Vourdas, Europhys. *Lett.* **48**, 201 (1999).
[16] D. A. Ivanov *et al.*, cond-mat/0102232.
[17] W. J. Elion *et al.*, *Phys. Rev. Lett.* **71**, 2311 (1993).
[18] D. V. Averin and K. K. Likharev, in *Mesoscopic Phenomena in Solids*, edited by B. L. Altshuler, P. A. Lee, and R. A. Webb p. 173 (Amsterdam, Elsevier, 1991).
[19] J. R. Friedman and D. V. Averin, *Phys. Rev. Lett.* **88**, 050403 (2002).
[20] A. B. Zorin, *Physica C* **368**, 284 (2002); A. B. Zorin, *Phys. Rev. Lett.* **86**, 3388 (2001).
[21] K. K. Likharev, private communication.
[22] R. Rouse, S. Han, and J. E. Lukens, *Phys. Rev. Lett.* **75**, 1614 (1995).
[23] D. V. Averin, *Fortschrit. der Physik* **48**, 1055 (2000).
[24] G. Falci *et al.*, *Nature* **407**, 355 (2000).
[25] Yu. Makhlin, G. Schøn, and A. Shnirman, *Rev. Mod. Phys.* **73**, 357 (2001).
[26] R. Rajaraman, *Solitons and Instantons: An Introduction to Solitons and Instantons in Quantum Field Theory* (Amsterdam, Elsevier Science, 1989).
[27] D. V. Averin, *Phys. Rev. Lett.* **82**, 3685 (1999); *Superlattices and Microstructures* **25**, 891 (1999).

SQUID SYSTEMS IN VIEW OF MACROSCOPIC QUANTUM COHERENCE AND ADIABATIC QUANTUM GATES

V. Corato[1,a], C. Granata, L. Longobardi[1,b], S. Rombetto[1], M. Russo[1], B. Ruggiero[1], L. Stodolsky[2], J. Wosiek[3], and P. Silvestrini[1,4,c]
[1]*Istituto di Cibernetica "E. Caianiello" del CNR, I-80078 Pozzuoli, Italy*
[2]*Max-Planck-Institut für Physik (Werner-Heisenberg-Institut), Fohringer Ring 6, 80805 Munich, Germany*
[3]*M. Smoluchowski Institute of Physics, Jagellonian University, Reymonta 4, 30-059 Cracow, Poland*
[4]*Seconda Università di Napoli, Dipartimento di Ingegneria dell'Informazione, I-81031, Aversa, Italy*

Abstract: We present the characterization of a fully integrated Josephson device consisting of an rf-SQUID coupled to a readout system based on a dc-SQUID sensor. In the classical regime, data on the decay rate from the metastable flux states of rf-SQUID are reported. The low dissipation level and the good insulation of the probe from the external noise are encouraging in view of macroscopic quantum experiments. Furthermore we examine the design of a quantum CNOT gate by adiabatic operations for rf-SQUID devices.

Keywords: Quantum computing, Josephson devices, SQUID

1. INTRODUCTION

The growing amount of theoretical interest in the area of quantum computing [1] has in recent years stimulated research with the aim of developing a corresponding technology [2].

One of the goals of any physical implementation of a quantum information-processing device is therefore to control systems of coupled qubits with a phase coherence time sufficiently long to permit the necessary manipulations. Qubit proposals based on Josephson devices both in the charge [3] and in the phase [4] spaces, have been suggested recently. Cooper pair number and phase are canonically conjugate dynamical variables.

---

[a]Also Universitá di Roma "La Sapienza", I-00185 Rome, Italy.
[b]Present address: Department of Physics and Astronomy, SUNY, NY 11794 3800, USA.
[c]E-mail: p.silvestrini@cib.na.cnr.it

Edited by Leggett *et al.*, Kluwer Academic/Plenum Publishers, 2004

Even though they are inherently restricted to work at extremely low temperatures, not only to guarantee the existence of superconductivity, Josephson junctions are expected to lend themselves to be arranged in extended arrays with very large numbers of gating elements; moreover, they appear to be quite robust with respect to decoherence, in that the range of frequencies characteristic of their (electromagnetic) coupling to the environment can be filtered out.

Recent experiments showing evidence of superposition of macroscopically distinct quantum states in Josephson systems open a new scenario in the field of devices for the quantum computation. The decoherence time is determined by temperature as well as by the effective dissipation parameter. If other sources of noise are filtered out, the intrinsic dissipation of the Josephson junctions is a result of the tunneling of thermally activated quasi-particles, and it is strongly decreasing with decreasing temperature. However, as solid-state qubits are by necessity coupled to many electromagnetic degrees of freedom through bias and reading wires, the measurement of the decoherence time requires careful circuit design [5].

In the present paper we review our efforts to use Nb Josephson structures for the realization of qubits based on the flux states of rf-SQUIDs. We present a planar chip working as a two-state system using the two magnetic flux states of an rf-SQUID measured by a magnetometer coupled to the probe by a superconducting flux transformer. In designing the device, special care has been devoted to obtaining the optimum coupling between the probe and the readout system in order to guarantee a good signal-to-noise ratio related to flux transitions, as well as to minimize the back-action due to the dc-SQUID readout into the quantum probe (this is an additional, often dominant source of decoherence [5]).

As a possible mechanism to measure the time-scale of the decoherence process, the adiabatic procedure has been proposed [6]. Now we want to extend the method to make a quantum CNOT gate by the interaction of two double-potential well systems undergoing adiabatic transformations. This can be realized with flux-coupled rf-SQUIDS with suitable design parameters.

From a theoretical point of view, we identify regions of the SQUID parameter space where stable behavior suitable for CNOT exists by finding essentially exact numerical solutions of the Schrödinger equation. The principle of the maintenance of the ordering of energy levels under adiabatic transformations – the "no level crossing theorem" – plays an important role in the analysis [6, 7].

2. SQUID SYSTEMS FOR MACROSCOPIC QUANTUM COHERENCE

In this section we present the design and measurement of a device using two magnetic flux states in an rf-SQUID (let us say $|0\rangle$ and $|1\rangle$) whose associated energies can be controlled by an external input. This device contains an rf-SQUID and a readout system based on a dc-SQUID sensor coupled to the probe via a flux transformer.

In Fig. 1 the picture of a SQUID device is shown. The rf-SQUID has an inductance of L=80 pH, a junction capacitance of $C = 2.3$ pF and a Josephson critical current $I_c = 15$ μA, corresponding to $\beta_L = 2\pi LI_c/\Phi_0 = 3.3$ ($\Phi_0 = 2.07 \times 10^{-15}$ Weber is the elementary quantum flux). The rf-SQUID is inductively coupled to a dc-SQUID by a superconductive flux transformer. The excitation flux is provided by a niobium single coil

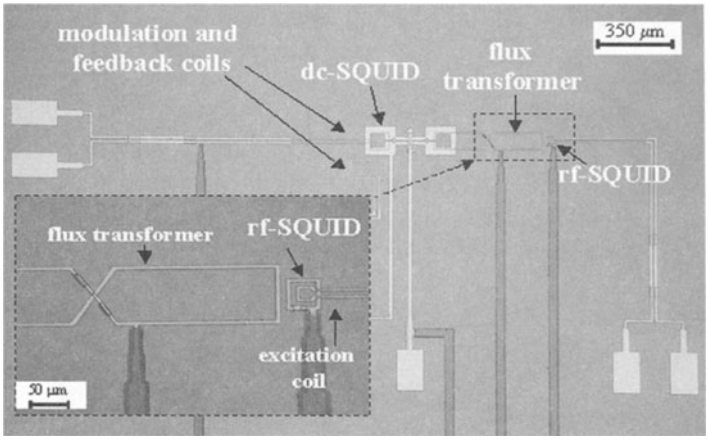

Figure 1. An rf-SQUID system. The rf-SQUID is the probe, whose state is read out by the dc-SQUID through a flux-transformer coil.

located inside the rf-SQUID hole (shown in the inset). Concerning the readout system, consisting of a dc-SQUID and the flux transformer, an excellent coupling is obtained using a gradiometric design. The whole device also includes single niobium coils for the modulation/compensation of the dc-SQUID and for the feedback in order to operate the readout system in Flux-Locked-Loop (FLL) configuration. Thin-film resistors have been inserted across all coils to realize integrated filtering stages.

Other details on the multilayer fabrication procedure based on $Nb/AlO_x/Nb$ technology have been reported elsewhere [8].

In order to evaluate the intrinsic dissipation of our system we measured the transitions between adjacent flux states of rf-SQUID as a function of the external flux Φ_x. In the absence of noise, the escape from the metastable well would occur at a critical value of the external flux Φ_c. Thermal noise induces transitions at random values of Φ_x smaller than Φ_c, whose probability distribution, namely $P(\Phi_x)$, was measured. Data were collected by standard time fly technique [9, 10]. We biased the excitation coil with a triangular-shaped waveform at a frequency of 100 Hz. The synchronism of the ramp generator was delayed and sent to the start input of a time-to-amplitude-converter (TAC). The dc-SQUID voltage, proportional to the flux enclosed by the rf-SQUID loop, was amplified and sent to a discriminator that provides the stop signal for the TAC at the time of the flux transition. The TAC then provides a voltage signal proportional to the time elapsed between the start and stop input that was sent to an analog to digital converter. The data, as recorded by multichannel system, are histograms showing the number of counts $P(K)$ in the channel K. In Fig. 2 we report the switching flux distribution $P(\Phi_x)$ of the rf-SQUID as a function of the external flux Φ_x at $T = 4.2$ K [11].

The fitting value of the effective resistance R, obtained from Kramers theory [12], is 700 Ω, corresponding to a Q factor of about 230 ($Q = \omega_j RC$; $\omega_j = (2eI_c/\hbar C)^{1/2}$). The fitting procedure shows a good agreement between the effective temperature T and the bath temperature T_b, with an experimental uncertainty lower than 100 mK.

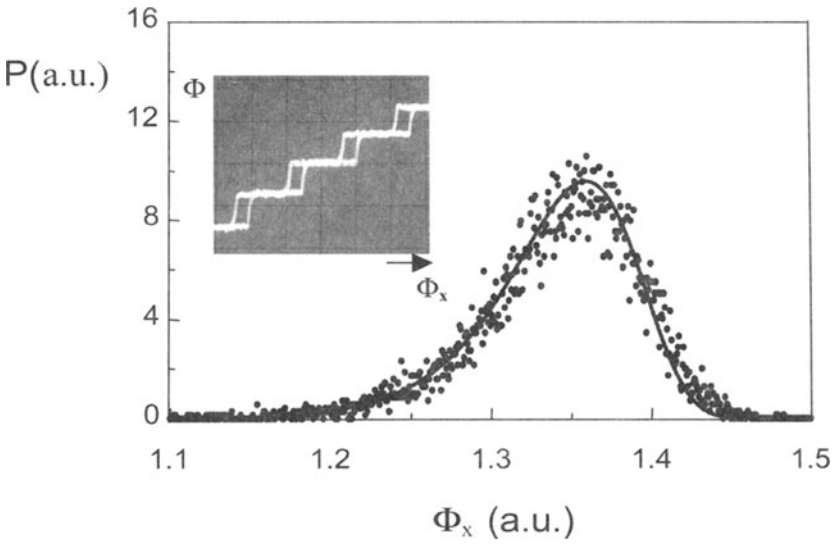

Figure 2. Switching flux distribution (circles) of the rf-SQUID as a function of the external flux at $T = 42$ K, P versus Φ_x. The solid line represents the theoretical prediction within Kramers theory [12] ($L = 80$ pH, $C = 2.3$ pF, $I_c = 15$ μA, $R = 700$ Ω). In the inset the dc-SQUID response is shown (x: a.u.; y: 3 mV/Φ_0).

From data down to 2.3 K, it is possible to calculate a very high value of the Q factor for the rf-SQUID device ($Q \sim 10^4$), leading to a very low dissipation level at low temperatures.

This result is encouraging estimating a decoherence time long enough to permit the quantum behavior of the system during an adiabatic manipulation.

3. ADIABATIC QUANTUM GATES

We examine the adiabatic procedure for manipulating coupled rf-SQUIDs in order to realize the two-qubits operation "controlled NOT" or CNOT.

The method works by varying an external flux in the SQUID Hamiltonian $H(t)$ that evolves in a time τ_{sweep} from an initial Hamiltonian, whose states are easily prepared, to a final configuration, that encodes the information on the quantum behavior of the system. During a NOT operation, which involves a single qubit, the evolution of an effective two-level system in one dimension occurs; if the system under consideration is a two-qubit system, as in the CNOT operation, this involves the evolution of a four-level system in two dimensions.

Experimentally, the time τ_{sweep} is freely adjustable, so it is possible to study situations ranging from a rapidly changing to a very slow, adiabatically changing Hamiltonian. For a pure quantum evolution in the adiabatic limit the correspondence between the initial and final state is of course complete, the ground state of the initial configuration producing the

ground state of the final one, the first excited producing the first excited and so on. The study of the fast sweep limit defines a first time scale, namely the shortest time τ_{adiab} in which an operation can be performed adiabatically. Deviation from the pure quantum behavior is expected if τ_{sweep} is longer than the decoherence time τ_{dec}. In this case during the interpolation the system loses quantum coherence. It is worth noting that to behave as in a quantum manner under adiabatic evolution, the device must have decoherence time τ_{dec} longer than τ_{adiab}. Compared to the fast switching operating mode, adiabatic manipulation of quantum states may be resilient to different kind of errors [13].

In the one-dimensional or single SQUID problem one has a Schrödinger equation in the variable Φ, the magnetic flux linked to the superconducting ring, with a potential term $V = V_0[(1/2)(\Phi - \Phi_x)^2 + \beta_L \cos\Phi]$. Both Φ and Φ_x, the external magnetic flux, are referred to $\Phi_0/2$ and normalized to $\Phi_0/2\pi$, so that the symmetric configuration of the potential is set at $\Phi_x = 0$. V_0 and β_L are constants depending on SQUID parameters.

When Φ_x is swept slowly as a function of time [6], an adiabatic inversion or level crossing can be induced, amounting to a realization of the NOT operation. If the state is originally in the left potential well it is transferred to the right well and vice versa, implying a reversal of current direction in the SQUID. Since we have a quantum system, a state which is a linear combination of left and right evolves into the NOT of the linear combination.

For a CNOT operation we have two flux-linked SQUIDs with inductances L_1, L_2 and a mutual inductance L_{12}. The system is described by a Schrödinger equation $i(\partial/\partial\tau)\psi = H\psi$, with $\tau = E_0 t$ a dimensionless time variable containing an overall energy scale E_0, or its stationary equivalent $H\psi = (E/E_0)\psi$, with

$$H = \frac{-1}{2\mu_1}\frac{\partial^2}{\partial\Phi_1^2} + \frac{-1}{2\mu_2}\frac{\partial^2}{\partial\Phi_2^2} + V \tag{1}$$

containing dimensionless "masses" μ and dimensionless position coordinates Φ_1, Φ_2.

With the definitions $1/L = \sqrt{L_1 L_2}/(L_1 L_2 - L_{12})$, $\beta_{L1} = [(2\pi)/(\Phi_0)]LI_{c1}$, $\beta_{L2} = [(2\pi)/(\Phi_0)]LI_{c2}$ and by introducing the reduced inductances $l_1 = L_1/\sqrt{L_1 L_2}$, $l_{12} = L_{12}/\sqrt{L_1 L_2}$, $l_2 = L_2/\sqrt{L_1 L_2}$, the potential has the form

$$\begin{aligned} V = \frac{1}{2} V_0 \{ & l_1(\Phi_1 - \Phi_{1x})^2 + l_2(\Phi_2 - \Phi_{2x})^2 - l_{12}(\Phi_1 - \Phi_{1x})(\Phi_2 - \Phi_{2x}) \\ & + \beta_{L1}\cos\Phi_1 + \beta_{L2}\cos\Phi_2 \} \end{aligned} \tag{2}$$

Further if C_1 and C_2 are the capacitances and we define $C = \sqrt{C_1 C_2}$ and $E_0 = 1/\sqrt{LC}$, we have for the "masses" $\mu_1 = C_1 E_0(\phi_0/(2\pi))^2$, $\mu_2 = C_2 E_0(\Phi_0/(2\pi))^2$ as well as $V_0 = \sqrt{C/L}(\Phi_0/(2\pi))^2$.

It will be recognized that our considerations can be used for realizations with other devices, after a similar identification of the general dimensionless parameters and overall energy scale E_0 is made.

CNOT is a two-bit operation and so is represented by four states. The potential in Eq. (2) has four distinct minima (Fig. 3), and we shall consider manipulations on the four lowest energy eigenstates (labeled 1–4), where initially and finally the wavefunctions of these states are well localized in distinct potential wells, thus furnishing a representation of the four logical states. Each corner of the picture represents one distinct physical configuration of (two current directions) $\otimes$ (two SQUIDs).

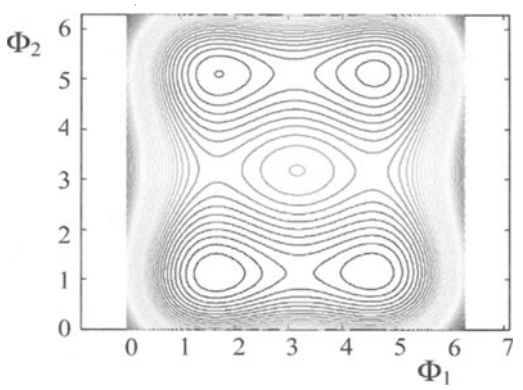

Figure 3. Potential as in Eq. (2), with its four wells. The coordinate Φ_1 (target hit) runs horizontally and Φ_2 (control bit) vertically.

For example let the parameters be chosen such that an initial configuration as visualized in Fig. 3 is

$$\begin{pmatrix} 3 & 4 \\ 1 & 2 \end{pmatrix}$$

CNOT is defined by the conditions: A) the control bit does not change its state, while B) the target bit is reversed or not reversed, according to whether the control bit is 1 or 0. If we now identify the top row of the pattern with control bit = 0 and the bottom row with control bit = 1, a physical embodiment of CNOT would be an adiabatic process where the energy levels rearrange as

$$\begin{pmatrix} 3 & 4 \\ 1 & 2 \end{pmatrix} \rightarrow \begin{pmatrix} 3 & 4 \\ 2 & 1 \end{pmatrix} \tag{3}$$

The restriction to slow, adiabatic changes is fundamental since it allows us to say that in the picture the state follows the labels. The no-level crossing property of adiabatic processes assures that a state initially in the first, or second, or third, ... energy level will end up in the first, or second, or third, ... energy level, while at the same time the physical properties associated with a given level may be changing.

Our task is now to find transformations of the parameters in Eq. (2) such that this adiabatic mapping of levels takes place. In analogy with the realization of the NOT operation [6] with one SQUID, we will investigate adiabatic changes of the Hamiltonian involving a sweep of the target bias Φ_{1x}.

For a two-level system, the theoretical estimate [6] gives that adiabatic behavior is obtained when the sweep time τ_{sweep} is long compared to

$$\tau_{\text{adiab}} = \varepsilon \tau_{\text{rabi}} \tag{4}$$

where ε is the energy difference between the two states at the beginning of the sweep and τ_{rabi} is the oscillation time associated with the coherent tunneling. In preliminary numerical tests we verify this estimate and so here we report on finding initial and final parameter sets for the stationary Schrödinger equation.

With a many dimensional parameter space and often nontrivial interactions between the parameters, one often finds states that are not "well defined". These are wave-functions that have large dispersions and that cannot be clearly attributed to a definite potential well. Or on the contrary one finds configurations where more than one of the four lowest states is localized in a given well. Nevertheless, using essentially exact numerical solutions of the Schrödinger equation, we are indeed able to find appropriate parameter regions.

A first requirement is that the control bit, Φ_2, should not change during the sweep (condition A). This must hold despite the perturbations communicated via the coupling l_{12} of the changing influences from the first device (Φ_1). We can try to assure this stability by "immobilizing" Φ_2 in making the external bias Φ_{2x} large relative to the varying influences. In the "spin" visualization this would correspond to putting the "spin" representing the second variable in a relatively strong "pseudo-magnetic field". This suggests studying the regions

$$|\Phi_{1x}| \ll |\Phi_{2x}| \tag{5}$$

It will turn out from the numerical solutions that the inequality need not be very strong. Now, if Φ_2 is indeed successfully "immobilized" it will be in one of its potential wells and can have just one of the two constant values $\Phi_2 \approx \pm 1$.

From the point of view of the other device, that is, Φ_1, this amounts to an extra bias whose value depends on whether we have the $(+)$ or $(-)$. That is, to linear order (since all Φ_{1x}, Φ_{2x} are small compared to 1 and Φ_1, Φ_2 are in the neighborhood of 1) the potential terms involving Φ_1 in Eq. (2) become

$$-2l_1\Phi_1\Phi_{1x} - 2l_{12}\Phi_1(\pm 1) = -l_1\Phi_1\left(\Phi_{1x} \pm \frac{l_{12}}{l_1}\right) = -2l_1\Phi_1\Phi_{1x}^{\text{eff}} \tag{6}$$

where we introduce the notation $\Phi_{1x}^{\text{eff}} = \Phi_{1x} \pm (l_{12}/l_1)$.

Thus there is an effective shift in the external bias on Φ_1 by $\pm l_{12}/l_1$. This is just as suggested by the "help" or "hindering" picture, and we find that the magnitude of the "help" is given by l_{12}/l_1.

We therefore try to analyze the behavior of SQUID 1 (target bit) as if it were simply under the external bias Φ_{1x}. We would expect that if there is a certain pattern of states, and Φ_{1x} is varied, the pattern should be maintained until there is a sign switch in Φ_{1x}^{eff}.

For $\Phi_{1x} = 0$ the sign of Φ_{1x}^{eff} is given by the $\pm$ sign alone, while for values of Φ_{1x} large enough, Φ_{1x}^{eff} does not change sign in any case.

There is therefore a region around $\Phi_{1x} = 0$ where the pattern is determined by the control bit, and another region for large $|\Phi_{1x}|$ where the pattern is determined only by the sign of Φ_{1x}. As we cross from one region to another, one pair of states will retain the sign it had for large $|\Phi_{1x}|$ and the other pair of states will switch. This would be the desired behavior, and CNOT is accomplished by a sweep of Φ_{1x}.

According to Eq. (6) the point where the switch from one pattern to another should take place is given by $|\Phi_{1x}| \approx l_{12}/l_1$. It is worth noting that for CNOT, asymmetric sweeps should be entertained for Φ_{1x}, unlike the simple symmetric sweeps for NOT.

We use a recently developed method [14] for numerical solution of the Schrödinger equation. A large basis of harmonic oscillator wavefunctions is used to reduce the problem to an array of fast algebraic manipulations. Because the method is particularly adapted to polynomial potentials we have used the expansion $\cos\Phi \approx 1 - (1/2)\Phi^2 + (1/24)\Phi^4$ for numerical work; this appears to give sufficient accuracy.

In Fig. 4 we show results for a part of the Φ_{1x}, Φ_{2x} plane. This shows three different regions where there are well-defined patterns (gray areas). At the boundary with the white area there is a breakdown in the patterns due to multiple states in a well or delocalization as manifested by large dispersions of the wavefunctions. The patterns are as follows.

In the intermediate gray region (left):

$$\begin{pmatrix} 3 & 4 \\ 1 & 2 \end{pmatrix}$$

In the darkest region (center):

$$\begin{pmatrix} 4 & 3 \\ 1 & 2 \end{pmatrix}$$

In the light gray region (right):

$$\begin{pmatrix} 4 & 3 \\ 2 & 1 \end{pmatrix}.$$

The patterns fit with the description arrived at in the previous section, where either the top or bottom row inverts as we go from the central region to large $|\Phi_{1x}|$. Hence a sweep from central region to the right region produces the mapping of Eq. (3). Similarly, sweeping from the right region to the center and from the left region to the central region

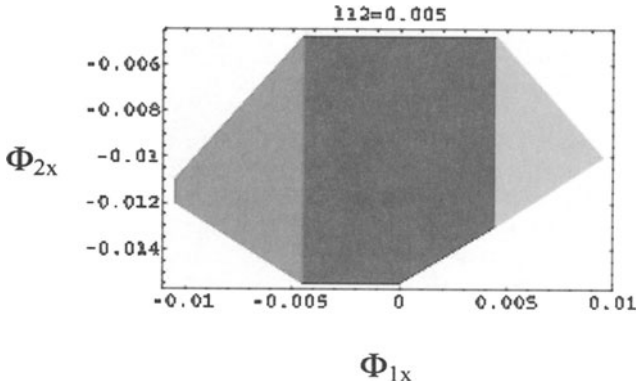

Figure 4. A region of the Φ_{1x}, Φ_{2x} plane with a well-defined pattern of solutions. The coupling parameter is $l_{12} = 0.0005$. Other parameters are $l_1 = l_2 = 1$, $\beta_{L1} = \beta_{L2} = 1.19$, $\mu_1 = \mu_2 = V_0 = 16.3$.

and vice versa can also serve as relatizations, differing simply in the assignment of (0, 1) for the bits or (1, 2) for the SQUIDs.

The figures show that the switch between patterns occurs quite close to $|\Phi_{1x}| = |I_{12}/I_1|$, as predicted. Also the breakdown at the boundaries can be understood in the model.

In terms of SQUID parameters, reasonable values for realization of the CNOT gate are $L_1 = 300$ pH, $L_2 = 280$ pH, $L_{12} = 1.8$ pH, $C_1 = C_2 = 0.1$ pF and $I_{c1} = I_{c2} = 1.45$ μA.

4. CONCLUSIONS

In conclusion, we have presented results in a thermal regime on the decay from the metastable flux states of an rf-SQUID-based device. The values of the effective dissipation derived by fitting experimental data are encouraging in view of macroscopic quantum coherence experiments. Work is in progress to improve the quality of the devices by suitable choice of the fabrication parameters to increase their application capability in the quantum regime. Finally, we propose the implementation of a quantum CNOT gate by adiabatic operations on rf-SQUID devices and provide values of SQUID parameters suitable for the experimental realization.

REFERENCES

[1] D. P. DiVincenzo, *Science* **270**, 255 (1995); C. H. Bennett and D. P. DiVincenzo, *Nature* **404**, 247 (2000).

[2] D. V. Averin, B. Ruggiero, and P. Silvestrini eds. *Macroscopic Quantum Coherence and Computing* (Kluwer Academic/Plenum Publishers, NY, U.S.A., 2001); J. Pekola, B. Ruggiero, and P. Silvestrini eds. *Superconducting Nano-Electronics Devices*. (Kluwer Academic/Plenum Publishers, NY, U.S.A., 2002).

[3] Y. Nakamura, Yu.A. Pashkin, and J. S. Tsai, *Nature* **398**, 786 (1999); V. Bouchiat, D. Vion, P. Joyez, D. Esteve, and M. H. Devoret, *Phys. Scripta T* **76**, 165 (1998); D. V. Averin, *Solid State Commun.* **105**, 659 (1998); Yu. Makhlin, G. Schon, and A. Schnirman, *Nature* **398**, 305 (1999); D. Vion, A. Aassime, A. Cottet, P. Joyez, H. Pothier, C. Urbina, D. Esteve, and M. H. Devoret, *Science* **296**, 886 (2002).

[4] J. R. Friedman, V. Patel, W. Chen, S. K. Tolpygo, and J. E. Lukens, *Nature* **406**, 43 (2000); J. E. Mooij, T. P. Orlando, L. Levitov, L. Tian, C. van der Wal, and S. Lloyd, *Science* **285**, 1036 (1999). Y. Yu, S. Han, X. Chu, S. I. Chu, Z. Wang, *Science* **296**, 889 (2002); J. M. Martinis, S. Nam, J. Aumentando, and C. Urbina, *Phys. Rev. Lett.* **89**, 117901 (2002).

[5] C. D. Tesche, *Phys. Rev. Lett.* **64**, 2358 (1990).

[6] P. Silvestrini and L. Stodolsky, *Phys. Lett.* **280**, 17 (2001); V. Corato, P. Silvestrini, L. Stodolsky, and J. Wosiek, cond-mat/0205514.

[7] E. Farhi, J. Goldstone, S. Gutmann, J. Lapan, A. Lundgren, and D. Preda, *Science* **292**, 472 (2001).

[8] C. Granata, C. Di Russo, A. Monaco, and M. Russo, *IEEE Trans. on Appl. Supercond.* **11**, 95 (2001).

[9] P. Silvestrini, O. Liengme, and K. E. Gray, *Phys. Rev.* B **37**, 1525 (1988); P. Silvestrini, V. G. Palmieri, B. Ruggiero, and M. Russo, *Phys. Rev. Lett.* **79**, 3046 (1997).

[10] B. Ruggiero, P. Silvestrini, C. Granata, V. G. Palmieri, A. Esposito, and M. Russo, *Phys. Rev.* B **57**, 134 (1998); V. Corato, E. Esposito, C. Granata, A. Monaco, B. Ruggiero, M. Russo, L. Stodolsky, and P. Silvestrini, *IEEE Trans. on Appl. Supercond.* **11**, 994 (2001).

[11] C. Granata, V. Corato, L. Longobardi, M. Russo, B. Ruggiero, and P. Silvestrini, *Appl. Phys. Lett.* **80**, 2952 (2002); C. Granata, V. Corato, L. Longobardi, S. Rombetto, M. Russo, B. Ruggiero, and P. Silvestrini, *IEEE Trans on Appl. Superconductivity*, 2003 (in press); and references therein.

[12] H. A. Kramers, *Physica* **7**, 284 (1940); M. Buttiker, E. P. Harris, and R Landauer, *Phys. Rev.* B **28**, 1268 (1983).
[13] A. R. Calderbank and P. W. Shore, *Phys. Rev.* A **54**, 1098 (1996); E. Knill and R. Laflamme, *Phys. Rev.* A **55**, 900 (1997); A. M. Stean, *Nature* **399**, 124 (1999).
[14] J. Wosiek, hep-th/0203116.

TEST OF AN rf-SQUID SYSTEM WITH STROBOSCOPIC ONE-SHOT READOUT UNDER MICROWAVE IRRADIATION

P. Carelli[1,2], M. G. Castellano[3,4], F. Chiarello[3,4], C. Cosmelli[4,5], R. Leoni[3,4], F. Sciamanna[5,6], C. Scilletta[5], and G. Torrioli[3,4]

[1]*Dipartimento di Energia Elettrica, Università de L'Aquila, Monteluco di Roio, 67040 L'Aquila, Italy*

[2]*INFN sez. Gran Sasso, 67040 L'Aquila, Italy*

[3]*Istituto di Fotonica e Nanotecnologie, CNR, Via Cineto Romano 42 00156 Rome, Italy*

[4]*INFN, sezione di Roma 1, 00185 Rome, Italy*

[5]*Dipartimento di Fisica, Università La Sapienza, 00185 Rome, Italy*

[6]*INFM, UdR L'Aquila, 67040 L'Aquila, Italy*

Abstract: An rf-SQUID under appropriate temperature and bias conditions can be used to perform tests on macroscopic quantum coherence, or as a qubit element for quantum computing. For both these purposes it is necessary a readout system allowing to discriminate stroboscopically the rf-SQUID state with high fidelity. This task can be performed by means of a hysteretic dc-SQUID inductively coupled to the rf-SQUID and turned on by a fast bias current pulse. We have proposed and realized an integrated system where all the devices, the rf-SQUID, the hysteretic dc-SQUID, and a SQUID magnetometer are on the same chip. This system can perform single-shot detection of the rf-SQUID state with a fidelity better than 98%. The rf-SQUID has been coupled to a high-frequency line working in the microwave region (2–26 GHz), and has been tested and characterized from 4.2 K to the mK region of temperatures.

Keywords: Macroscopic quantum coherence, Quantum computing, SQUID

1. INTRODUCTION

Solid-state superconducting quantum devices are ideal systems for the study of macroscopic quantum effects such as macroscopic quantum tunneling, resonant macroscopic quantum tunneling, energy level quantization (ELQ), all observed in past years [1–3]. Strong efforts are performed for the observation and study of macroscopic quantum coherence (MQC), probably the most important but also the most elusive among them [4–7]. The same superconducting quantum devices are suitable candidates for the engineering of quantum systems, in particular for quantum computing [8, 9]. We have

Quantum Computing and Quantum Bits in Mesoscopic Systems
Edited by Leggett *et al.*, Kluwer Academic/Plenum Publishers, 2004

realized an integrated system of SQUIDs for the observation and study of macroscopic quantum coherence, and for applications in quantum computing [10]. In this paper we present some recent developments and new ideas, in particular concerning the efficiency of the quantum state single-shot readout, and the effects of microwaves irradiating the system.

2. DESCRIPTION OF THE SYSTEM

Our system is composed of an rf-SQUID (radio frequency-superconducting quantum interference device), source of the magnetic flux quantum state, a SQUID amplifier, used for the state readout, and a hysteretic SQUID, used as flux discriminator for single-shot readout. These devices are coupled inductively by means of flux transformers, and all the elements are integrated on the same chip, realized by trilayer $Nb/AlO_x/Nb$ technology (Fig. 1).

The rf-SQUID can be schematized by a superconducting loop of inductance L interrupted by a Josephson junction of critical current I_0 and capacitance C, biased by an external magnetic flux ϕ_z. A small dc-SQUID (a low inductance loop with two junctions in parallel, biased by an applied flux ϕ_x) can be used instead of the single junction [11], allowing the control of the critical current according to the approximate expression

$$I_0(\phi_x) = I_{0\max}\left|\cos\left(\frac{\pi\phi_x}{\phi_0}\right)\right| \tag{1}$$

The rf-SQUID is described by the Hamiltonian

$$H = \frac{Q^2}{2C} + \frac{\phi_b^2}{2L}(\phi - \phi_z)^2 - \phi_b I_0(\phi_x)\sin\left(\frac{\phi}{\phi_b}\right) \tag{2}$$

where ϕ (the magnetic flux threading the loop) is the degree of freedom with conjugate momentum Q (the charge across the junction), and $\phi_b = \phi_0/(2\pi) = \hbar/(2e)$. For $\beta \equiv LI_0/\phi_b > 1$ the energy potential presents a series of wells and barriers. In this case the classical dynamics for a sweeping flux ϕ_z are characterized by jumps between wells.

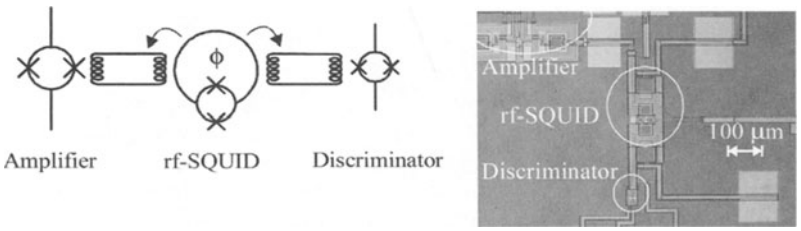

Figure 1. Scheme of the experimental apparatus (left), and microscope photography of the chip (right).

We have used the rf-SQUID $\phi - \phi_z$ characteristic to evaluate the rf-SQUID parameters $L = 85$ pH and $I_{0\max} = 12$ μA. From previous measurements the capacitance is estimated to be $C = 0.8$ pF.

In the quantum regime, under appropriate conditions of high barrier and low temperature and in a quasi-symmetric case (for ϕ_z near $\phi_0/2$), one can simplify the problem by considering a reduced dynamics, with a base consisting of just the two flux eigenstates localized in the left and right minima ($|L\rangle$ and $|R\rangle$) for the symmetric case ($\phi_z = \phi_0/2$). In this base the Hamiltonian can be written in terms of Pauli's matrices, by considering the spacing $h\Delta(\phi_x)$ between the two first energy levels in the symmetric case, and by introducing the energy asymmetry $h\varepsilon(\phi_z)$ between the two wells in the general case

$$H = -\frac{h\Delta(\phi_x)}{2}\sigma_x - \frac{h\varepsilon(\phi_z)}{2}\sigma_z \tag{3}$$

The Hamiltonian (3) has two eigenvalues, with spacing $h\Omega = h\sqrt{\Delta^2 + \varepsilon^2}$. The described system can be used to store and manipulate a single qubit, by mapping "0" and "1" states in the flux eigenstates. Quantum operations can be performed by changing the two bias fluxes, and by irradiating the system with microwave pulses of frequency $\Omega/(2\pi)$, in order to induce transitions between energy levels.

Quantum applications with such a system are possible only if the coherence time is long enough to perform all the required quantum operations before decoherence occurs. An indirect evaluation of coherence time, based on the study of ELQ, gives an order of magnitude of microsecond [12], compatible with other results on similar systems, and sufficient for quantum applications.

3. READOUT SCHEME

The flux state measurement can be performed by a standard dc-SQUID magnetometer, which we have integrated on the chip for control purposes. However, quantum computing and MQC experiments require the ability to perform fast one-shot measurements, with a detector normally turned off in a state not disturbing the system evolution, and turned on for a short time in order to have a precise state discrimination. For this purpose we have used a hysteretic dc-SQUID used as flux discriminator (Fig. 2) [13].

This device, inductively coupled to the rf-SQUID, can be turned on for a short time by applying a short current pulse of width I_b. The flux coming from the rf-SQUID modifies the dc-SQUID critical current according to Eq. (1). An accurate choice of the working point (set by adding a static bias flux to the input flux) allows having a transition to the normal state only when the rf-SQUID is in the right state and not for the left one, so that the rf-SQUID flux state can be discriminated by observing the voltage across the dc-SQUID. Recent measurements on our chip have shown the possibility to perform such measurements with fidelity better than 98%. In Fig. 3 it is reported the experimental three-dimensional plot that characterizes the coupled system rf-SQUID plus dc-SQUID discriminator, considering the sweeping of both bias fluxes, at 30 mK. The result shows the possibility to characterize the quantum state without the use of a magnetometer.

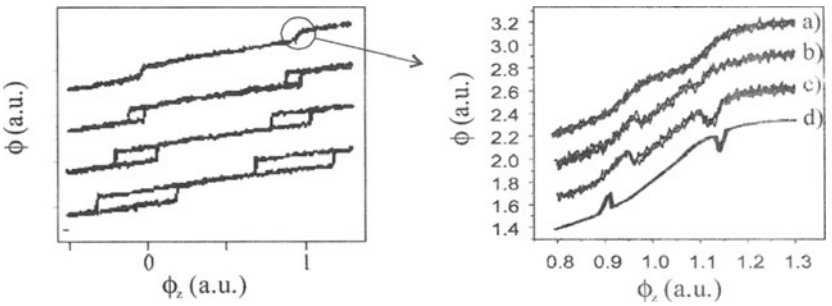

Figure 2. (Left) Example of the use of the dc-SQUID as discriminator: there are voltage transitions (V_{sw}) only in correspondence to current pulses I_b for which the input flux is in the up state. (Right) Switching probability of a dc-SQUID flux discriminator as a function of the input magnetic flux at different temperatures: (a) 18 mK; (b) 73 mK; (c) 150 mK; (d) 283 mK; (e) 373 mK; (f) 535 mK; (g) 626 mK.

4. APPLICATION OF MICROWAVES

A complete control of the SQUID qubit requires the possibility to apply microwave pulses of well-defined frequency and duration, in order to induce transition between energy levels, Rabi oscillations, and other similar phenomena. We are implementing the possibility to irradiate our rf-SQUID with microwave pulses. In first rough attempts we couple continuous microwaves (from 2 to 26 GHz) to the chip by means of a simple loop antenna placed nearby. Resonances in the rf-SQUID flux characteristics (Fig. 4, left) are expected when the microwave frequency ν is equal to energy levels spacing ν_{mn}, in order to induce transition between levels m and n. We have observed such resonances at 300 mK

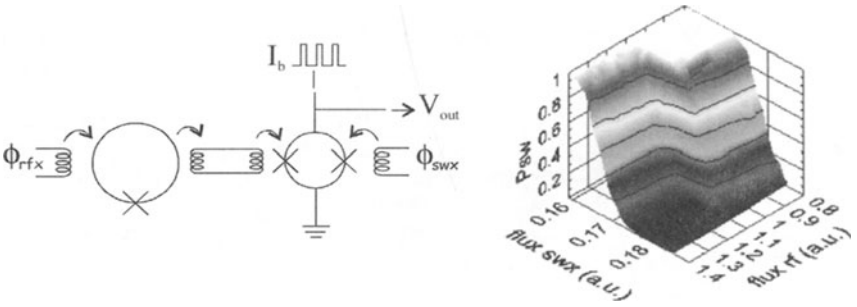

Figure 3. Characterization of the system rf-SQUID plus discriminator, sweeping both bias fluxes and observing the discriminator switching probability: scheme (left), and observations at 30 mK (right).

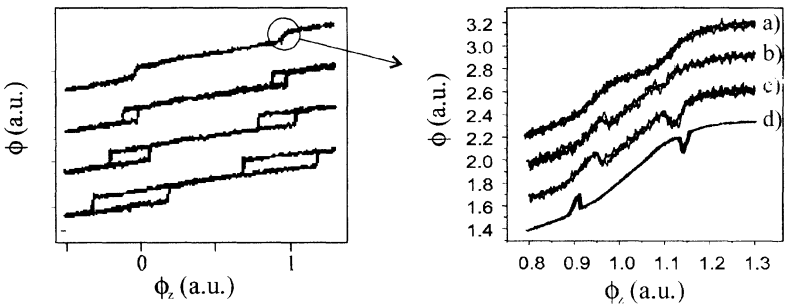

Figure 4. (On the left) Flux characteristic of an rf-SQUID obtained by sweeping the flux ϕ_z for different ϕ_x. (On the right) Resonances in the rf-SQUID flux characteristics at 300 mK, due to microwaves at different frequencies: (a) 12.250 GHz; (b) 13.00 GHz; (c) 14.233 GHz; (d) 15.00 GHz (strongly filtered).

(Fig. 4, right), with the expected behavior. Further attempts at lower temperatures and with microwave pulses are projected for the near future.

5. CONCLUSIONS

A full integrated SQUID system for the study of macroscopic quantum coherence and for quantum computing applications has been realized and well characterized both in the thermal and quantum regimes (down to 10 mK). The single-shot readout system works efficiently enough for the required operations, and first tests on the possibility to apply microwaves give satisfactory results. More work is now required for collecting together the different elements in order to perform coherent manipulations.

REFERENCES

[1] J. M. Martinis, M. H. Devoret, and J. Clarke, *Phys. Rev.* B **35**, 4682 (1987).
[2] R. Rouse, S. Han, and J. E. Lukens, *Phys. Rev. Lett.* **75**, 1614 (1995).
[3] C. Cosmelli *et al.*, *Phys. Rev. Lett.* **82**, 5354 (1999).
[4] A. J. Leggett, *Prog. Theor. Phys. Suppl.*, **69**, 80 (1980).
[5] A. J. Leggett, *Phys. Rev. Lett.* **54**, 587 (1985).
[6] C. D. Tesche, *Phys. Rev. Lett.* **64**, 2358 (1990).
[7] M. G. Castellano *et al.*, *J. Appl. Phys.* **80**, 2922 (1996).
[8] J. E. Mooij *et al.*, *Science* **285**, 1036 (1999).
[9] F. Chiarello, *Phys. Lett.* A, **277**, 189 (2000).
[10] M. G. Castellano *et al.*, *Appl. Supercond.* **5**, 405 (1998).
[11] S. Han, J. Lapointe, and J. E. Lukens, *Phys. Rev. Lett.* **63**, 1712 (1989).
[12] C. Cosmelli *et al.*, *Phys. Rev. Lett.* **82**, 5357 (1999).
[13] C. Cosmelli *et al.*, *Appl. Phys. Lett.* **80**, 3150 (2002).

SQUID RINGS AS DEVICES FOR CONTROLLING QUANTUM ENTANGLEMENT AND INFORMATION

M. J. Everitt[1,a], P. B. Stiffell[1,b], T. D. Clark[1,c], R. J. Prance[1], H. Prance[1], A. Vourdas[2,d], and J. F. Ralph[3,e]

[1]*The Quantum Circuits Group, Sussex University, Falmer, Brighton BN3 9QT, UK*
[2]*Department of Computing, Bradford University, Bradford, West Yorkshire BD7 1DP, UK*
[3]*Department of Electrical Engineering and Electronics, The University of Liverpool, Liverpool L69 3GJ, UK*

Abstract: We model a SQUID ring coupled to one or two electromagnetic field oscillator modes, each component being treated quantum mechanically. We show that the external flux on the SQUID ring can be used to control the exchange of energy, and level of entanglement, between the coupled systems. We then extend this model to include dissipation, and provide examples of the time evolution of these coupled, multicomponent systems. These dynamics demonstrate the manner in which decoherence due to an external environment may influence photon (energy) exchange and entanglement within these system.

Keywords: SQUID ring, Josephson devices, Entanglement, qubits

1. INTRODUCTION

SQUID rings (here taken to be a thick superconducting ring enclosing a single Josephson weak link device) are emerging as a strong contender for applications in proposed quantum technologies, such as quantum computing and information processing. This interest has certainly been promoted by the recent experimental work on the creation of quantum-mechanical superposition states in Josephson weak link systems. Here, we are particularly concerned with the existence of such states in SQUID rings [1, 2]. However, for these states to be of practical interest we must not only be capable of creating these in SQUID rings, but we must also be able to control and manipulate them in conjunction with quantum states in other circuit systems to which these rings are coupled.

[a]E-mail: m.j.everitt@sussex.ac.uk
[b]E-mail: p.b.stiffell@sussex.ac.uk
[c]E-mail: t.d.clark@sussex.ac.uk
[d]E-mail: a.vourdas@liverpool.ac.uk
[e]E-mail: jfralph@liverpool.ac.uk

As a first step to modelling quantum circuit systems built around SQUID rings, we present a theoretical model of a mesoscopic SQUID ring coupled to one or two quantum electromagnetic (em) field modes [3,4]. We show that by coupling these circuit components together we can control the exchange of energy (and therefore photons) between them via the (classical) magnetic flux applied to the ring. As an important consequence of this photon transfer we show that we can also control the level of entanglement between these system components.

In order to make use of such circuit systems in quantum computing, communications, and information processing, close attention has to be paid to the problem of decoherence arising through dissipative processes. In our approach we adopt the usual system plus reservoir model frequently applied to open quantum systems. For this we couple a reservoir to each component of the circuit system. We then model the total evolution by considering the master equation of the density matrix in the tensor product space formed from individual components of the system. We present results calculated from this model and compare these with those obtained in the absence of dissipation. These results demonstrate that dissipation need not destroy the quantum coherent effects such as entanglement and that, through the control available via the external flux, SQUID rings may well provide a robust solution to the manipulation of quantum information and entanglement in condensed matter circuits.

We now proceed to outline some of the background theory that needs to be introduced before we present our results.

2. THE SQUID RING

Central to this work is the nonlinear dependence of the SQUID ring on the external applied magnetic flux Φ_x. This dependence can be clearly seen in the well established lumped component SQUID ring Hamiltonian [8]

$$H_s = \frac{Q_s^2}{2C_s} + \frac{(\Phi_s - \Phi_x)^2}{2\Lambda_s} - \hbar\nu \cos\left(2\pi \frac{\Phi_s}{\Phi_0}\right) \tag{1}$$

where Φ_s, the magnetic flux threading the ring (inductance Λ_s), and Q_s, the electric displacement flux between the electrodes of the weak link (capacitance C_s) in the ring, are the conjugate variables [5,6] for the system (with $[\Phi_s, Q_s] = i\hbar$), $\hbar\nu/2$ is the matrix element for Josephson pair tunnelling through the weak link, Φ_x is the externally applied flux, and $\Phi_0 = (h/2e)$. In this paper we will only be considering the case in which the external flux is static and, to denote this, we will use $\Phi_{x\,\mathrm{stat}} = \Phi_x$. To illustrate explicitly the nonlinear dependence of the SQUID ring observables on the external magnetic bias flux, we show in Fig. 1 an example of the eigenvalues of the Hamiltonian as a function of $\Phi_{x\,\mathrm{stat}}$. In this example we have selected circuit parameters typical for a SQUID ring in the quantum regime [7], that is, $C_s = 1 \times 10^{-16}$ F, $\Lambda_s = 3 \times 10^{-10}$ H, and $\hbar\nu = 0.075\,\Phi_0^2/\Lambda_s$ ($\nu = 1.74\,\omega_s$, where the ring oscillator frequency is $\omega_s = 1/\sqrt{C_s\Lambda_s}$). These parameter values are used throughout the rest of this work.

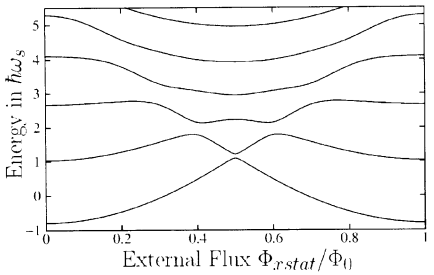

Figure 1. The first few energy eigenvalues E_κ, where $\kappa = 0, 1, \ldots, 5$, of a quantum mechanical SQUID ring as a function of static bias flux $\Phi_{x\,\mathrm{stat}}/\Phi_0$ over the range $0 \leq \Phi_{x\,\mathrm{stat}}/\Phi_0 \leq 1$ for $C_s = 1 \times 10^{-16}$ F, $\Lambda_s = 3 \times 10^{-10}$ H $(\hbar\omega_s = 0.043\,\Phi_0^2/\Lambda_s)$ and $\hbar\nu = 0.075\,\Phi_0^2/\Lambda_s = 1.74\,\hbar\omega_s$ $(\nu = 1.74\,\omega_s)$.

The ring Hamiltonian (1) can now be written in a more convenient form by invoking the unitary translation operator $\mathbb{T} = \exp(-i\Phi_x Q_s/h)$. The transformed Hamiltonian then reads

$$\mathscr{H}_s = \mathbb{T}^\dagger H_s \mathbb{T} = \frac{Q_s^2}{2C_s} + \frac{\Phi_s^2}{2\Lambda_s} - \hbar\nu\cos\left(2\pi\frac{\Phi_s + \Phi_x}{\Phi_0}\right) \tag{2}$$

The properties of this Hamiltonian have been studied in considerable detail, as can be found in the literature [7, 8].

3. COUPLING A SQUID RING TO EM-FIELD MODES

Our primary concern in this paper is to model the quantum mechanical behavior of circuit systems consisting of a SQUID ring coupled to one or more em-field oscillator modes (cavities). In this model we assume that the thermal energy $k_B T$ at the system temperature T is small compared with either $\hbar\omega_s$ or $\hbar\omega_e$, where ω_e is the oscillator mode(s) frequency. With this proviso, we study the interaction between the components both in the absence and presence of dissipation. Considering a quantum mechanical oscillator mode (cavity), represented as a parallel inductor-capacitor equivalent circuit, we can write the circuit Hamiltonian in the form

$$\mathscr{H}_e = \frac{Q_e^2}{2C_e} + \frac{\Phi_e^2}{2\Lambda_e} \tag{3}$$

where Λ_e and C_e are the equivalent circuit inductive and capacitive parameters and Φ_e and Q_e are, respectively, the cavity mode magnetic flux and charge operators for a field mode

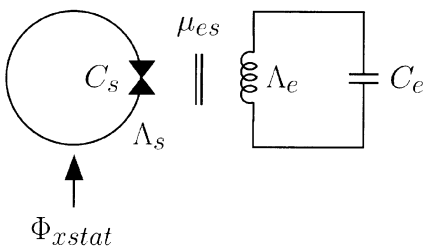

Figure 2. The most simple system, that is, a SQUID ring coupled to one em-field.

of frequency $\omega_e = 1/\sqrt{C_e \Lambda_e}$. As with the SQUID ring, these charge and flux operators are canonically conjugate and obey the commutation relation $[\Phi_e, Q_e] = i\hbar$.

As is common practice experimentally [9], we now consider systems in which the em-field modes are inductively coupled directly to a SQUID ring. The total system Hamiltonian for N em-field modes coupled to one ring can then be written as

$$\mathscr{H} = \mathscr{H}_s + \sum_{i=1}^{N} \left\{ \mathscr{H}_{e_i} + \frac{\mu_{se_i}}{\Lambda_s} \Phi_s \Phi_{e_i} \right\} \tag{4}$$

where μ_{se_i} is the fraction of em magnetic flux coupled between the ith field mode (subscript e_i) and the SQUID ring (subscript s). In this work we shall, in fact, deal only with the two simplest examples of such coupled systems (one or two modes), as depicted in Figs 2 and 3. Although apparently simple, these multicomponent systems present major computational difficulties. For this reason we choose, throughout this paper, to set $C_s = C_{e_i}$, $\Lambda_s = \Lambda_{e_i}$. This reduces the computational problem while preserving the physics of the situation.

By way of illustration, we show in Fig. 4 a computed set of the energy eigenvalues of the SQUID ring single oscillator mode system depicted in Fig. 2. These are plotted as a function of the normalized static magnetic flux $\Phi_{x\,\mathrm{stat}}/\Phi_0$ applied to the ring. Here, we have taken $C_s = C_e = 1 \times 10^{-16}$ F (with, from above, $\omega_e = \omega_s$) and the coupling factor $\mu_{es} = 1/100$. This sets $\omega_s/2\pi \approx 1$ THz and $\nu = 1.74\,\omega_s$. In Fig. 5, where the calculated time-averaged energy expectation values of $\mathscr{H}_s$ (in units of $\hbar\omega_s$) are shown as a function of $\Phi_{x\,\mathrm{stat}}/\Phi_0$, the em-field mode is in its first energy eigenstate state and the SQUID ring is in one of its first four energy eigenstates denoted by the label σ, that is, the initial states are $|1\rangle_e \otimes |\sigma\rangle_s$, $(\sigma = 0, 1, 2, 3)$.

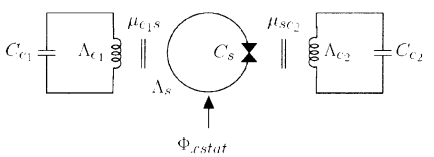

Figure 3. The next level of complexity, a SQUID ring coupled to two em-fields.

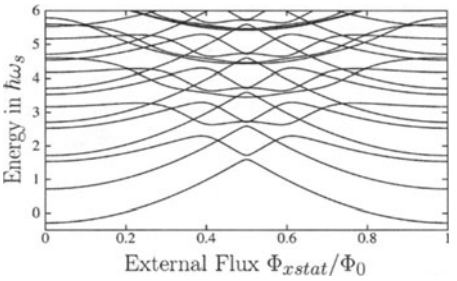

Figure 4. The eigenvalues for the Hamiltonian of the system shown in Fig. 2 with energy less than $6\,\hbar\omega_s$.

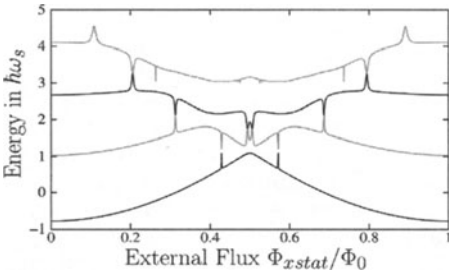

Figure 5. Time-averaged energy expectation values of $\mathscr{H}_s$. The initial states are $|1\rangle_e \otimes |\sigma\rangle_s$, ($\sigma = 0, 1, 2, 3$) (see text).

4. DESCRIBING EVOLUTION IN THE PRESENCE OF DISSIPATION

The results in this work extend the ideas developed by us in two of our recent publications [3,4] to include a preliminary study of the effects of dissipation on the quantum behavior of SQUID ring–oscillator mode systems. A standard and relatively simple approach, and one we adopt here, is to couple each component of the system to its own decohering, monochromatic, thermal bath.

With this assumption, the master equation for the evolution of the density operator of the system will then, in general, take the form [10]

$$\frac{\partial \rho}{\partial t} = -\frac{i}{\hbar}[\mathscr{H}, \rho] + \sum_i \frac{\gamma_i}{2\hbar}(M_i + 1)(2a_i \rho a_i^\dagger - a_i^\dagger a_i \rho - \rho a_i^\dagger a_i)$$
$$+ \frac{\gamma_i}{2\hbar} M_i (2a_i^\dagger \rho a_i - a_i a_i^\dagger \rho - \rho a_i a_i^\dagger) \tag{5}$$

where $i = s, e_1, \ldots, e_N$, the creation and annihilation operators for each of the components of the systems are denoted by $a_i^\dagger$ and a_i, respectively, M_i is related to the temperature T_i, and the frequency ω_{b_i} of each decohering bath via $M_i = (\exp(\hbar\omega_{b_i}/k_B T_i) - 1)^{-1}$ and γ_i is the coupling (damping rate) between each of the components to its respective thermal bath. For the examples we will calculate we set $T = 4.2$ K, with $\omega_{b_i} = \omega_s$ and, unless otherwise stated, $\gamma_i = 1 \times 10^{-5}\omega_s$.

5. MEASURES OF ENTANGLEMENT

In common with other researchers who have worked on entangled systems we have made use [3, 4] of the entropic quantity given by

$$I = \left\{ \sum_i S(\rho_i) \right\} - S(\rho) \tag{6}$$

to quantify the level of entanglement, where $I > 0$ implies entanglement. Here, $S(\rho) = -\mathrm{Tr}\,\rho \ln \rho$ is the von Neuman entropy and ρ_i is the reduced density operator for the ith component of the system. This measure of entanglement is very useful when we are dealing with a purely quantum system, that is, where $S(\rho) = 0$ at all times.

However, if the state of the system is not a pure quantum state, but a statistical mixture of states, this measure of entanglement will only provide information quantifying the level of correlation between the components of the system being studied. In particular, this measure is not able to distinguish between quantum or classical correlations. For this reason we now introduce another measure of entanglement, which is defined by

$$I_i = -S(\rho_i) + S(\rho) \tag{7}$$

This measure has the property that if $I_i < 0$, for any value of i, the system is entangled [11, 12]. It is important to note that this is a sufficient but not necessary condition for quantum correlation. Thus, explicitly, $I_i > 0$, for all i, does not imply that the system is not entangled.

Measures of entanglement are still very much an open topic and much work remains to be done in this field. However, since it is our aim to consider some of the effects of dissipation, so that the density operator for the system will evolve into a mixed state, we feel that Eq. (7) is a suitable measure of entanglement for the results presented in this paper.

6. SYSTEM EVOLUTION

As an illustration of the dynamical behavior of these systems we set the bias flux on the SQUID ring at an energy exchange point. We place one em-field oscillator mode in its first excited energy eigenstate and the remaining system components in their respective

ground states, that is, $|1\rangle_e \otimes |0\rangle_s$ for the two-mode system and $|1\rangle_{e_1} \otimes |0\rangle_s \otimes |0\rangle_{e_2}$ for the three-mode system.

In Fig. 6 we show the energy exchange between the em-field and the SQUID ring for the two-mode system. In Fig. 7 we present, for comparison with Fig. 6, the entanglement entropies, I_e and I_s. Here, as for Figs 4 and 5, the coupling factor μ_{es} is $1/100$ and the bias flux $\Phi_{x\,\mathrm{stat}}$, chosen to maximize the exchange of energy between the two components, is $0.42864\Phi_0$. In these two figures we can see quite clearly that as the em field loses energy so the SQUID ring gains it. We note that when the ring has gained the same amount of energy as the em field oscillator mode has lost, and vice versa, these two circuit components are maximally entangled.

In Figs 8 and 9 we show the equivalent evolution for the three-mode system. However, to show similar evolution over the same time scales as Figs 6 and 7 we have increased the coupling to $\mu_{e_1 s} = \mu_{e_2 s} = 0.316$. We have also moved the external bias flux on the SQUID ring to $0.42612\,\Phi_0$. Here we see that through the (static) bias flux the SQUID ring is acting as a tunable device mediating the transfer of energy, and the entanglement, between the two em-field modes. We note that had we chosen a smaller value of μ_{es}, together with a judicious choice of $\Phi_{x\,\mathrm{stat}}$, the result would have been a

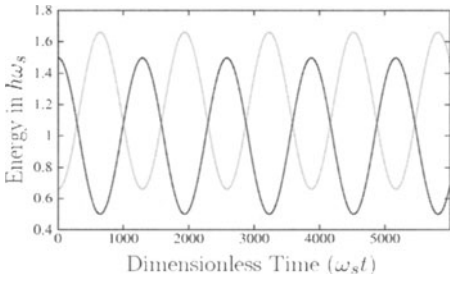

Figure 6. Energy exchange in the two-mode system with the initial state $|1\rangle_e \otimes |0\rangle_s$ at $\Phi_{x\,\mathrm{stat}} = 0.42864\,\Phi_0$.

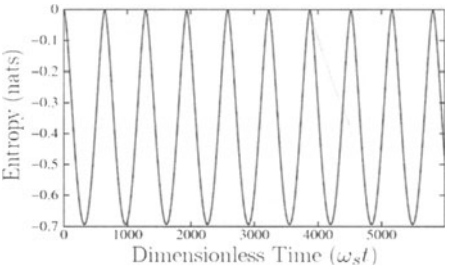

Figure 7. The entanglement entropies, I_e and I_s (which in this case are coincident), for comparison with Fig. 6.

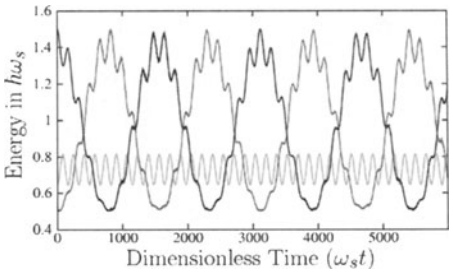

Figure 8. Energy in the first em field (black), the second em field (gray), and the SQUID ring (light gray) for the three-mode system with the initial state $|1\rangle_{e_1} \otimes |0\rangle_s \otimes |0\rangle_{e_2}$ at $\Phi_{x\,\mathrm{stat}} = 0.42612\,\Phi_0$.

system evolution with a strong quantum mechanical coupling between the field modes via the SQUID ring, but with negligible activity within the ring itself. However, the exchange of energy happens over much longer timescales and due to limitations on length in this paper no results of this phenomenon are presented. From these examples, therefore, it is apparent that a SQUID ring can be used as a switching device to control extended quantum effects such as entanglement and energy transfer in a complex, multicomponent, circuit system.

We now consider the consequences of coupling a thermal bath to each component of the two-mode system following the single frequency model introduced earlier [10]. The evolution is governed by the master Eq. (5), in which the temperature of each bath and the damping rate are again set at 4.2 K and $1 \times 10^{-5}\omega_s$, respectively. In Fig. 10 we show the evolution of the energy expectation values and the entropies I_s and I_e for comparison with Figs 6 and 7. Here we see that the exchange of energy is very similar to the case without dissipation. Moreover, the system is still definitely quantum mechanically correlated (entangled) throughout a significant part of the system evolution. If we extend this analysis to the three-mode system (two em modes plus one SQUID ring), as shown in Fig. 11, we once again see similar behavior to the case where dissipation is not present.

As the strength of the damping is increased it seems reasonable to assume that this will have an increasingly strong effect on the quantum correlations in an extended multi-

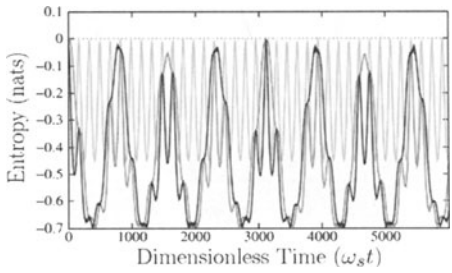

Figure 9. The entanglement entropies I_{e_1} (black), I_{e_2} (gray), and I_s (light gray) of the three-mode system for comparison with Fig. 8.

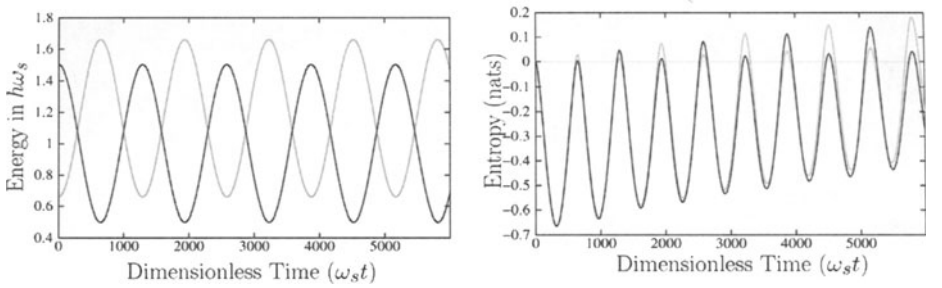

Figure 10. Energy exchange (left) and entanglement entropy (right) for comparison with Figs 6 and 7, respectively. Here the energy expectation value of the field and I_e is shown in black, while the energy expectation value of the SQUID ring and I_s are shown in gray. The results shown here were computed for $T = 4.2\,\mathrm{K}$ and a damping rate of $1 \times 10^{-5}\omega_s$.

component system. This is shown clearly in Figs. 12 and 13, where, after Figs 10 and 11, the two- and three-mode system evolution is again displayed but with the damping rate increased by an order of magnitude, from $1 \times 10^{-5}\omega_s$ to $1 \times 10^{-4}\omega_s$. We see here that after sufficient time, although some energy exchange is maintained, it is no longer obvious that any level of entanglement is retained.

7. CONCLUSION

In this paper we have presented some of the interesting nonperturbative phenomena associated with coupling electromagnetic field modes to a SQUID ring, where all the components were taken to behave quantum mechanically. This was extended, at a simple model level, to computing the consequences of introducing dissipation to such multi-component quantum circuits. This preliminary (thermal bath) model, borrowed from the field of quantum optics, goes some way to characterizing the effects of external

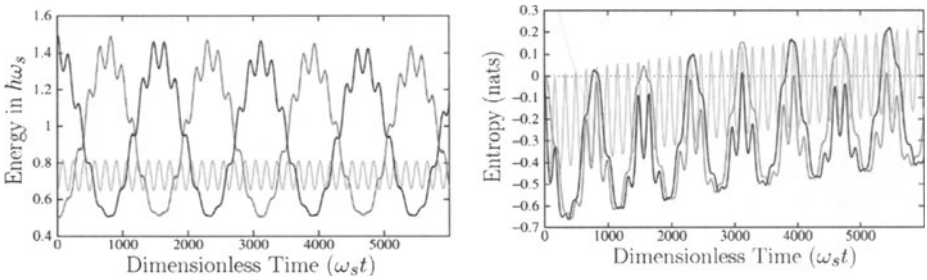

Figure 11. Energy exchange (left) and entanglement entropy (right) for comparison with Figs 8 and 9, respectively. Here the variables of the first field mode are shown in black, the second field mode in gray, and the SQUID ring in light gray. The results shown here were computed for $T = 4.2\,\mathrm{K}$ and a damping rate of $1 \times 10^{-5}\omega_s$.

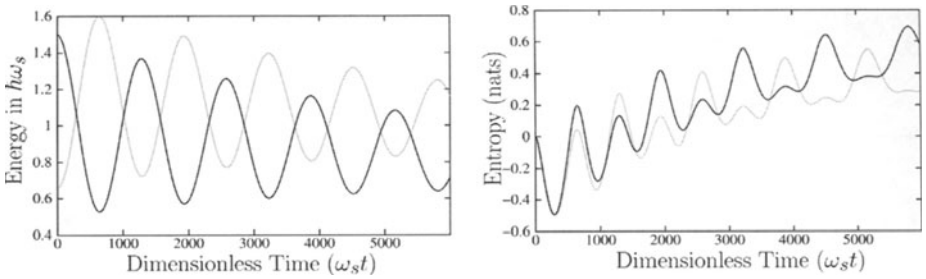

Figure 12. Energy exchange (left) and entanglement entropy (right) for comparison with Fig. 10. Here we have increased the damping rate by an order of magnitude, from $1 \times 10^{-5}\omega_s$ to $1 \times 10^{-4}\omega_s$.

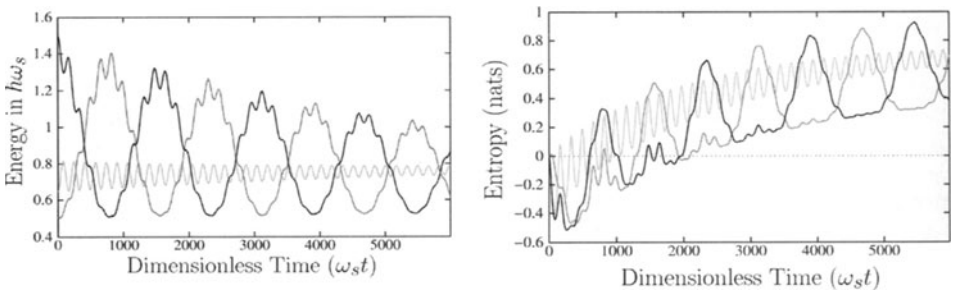

Figure 13. Energy exchange (left) and entanglement entropy (right) for comparison with Fig. 11. Here, as for Fig. 12, we have increased the damping rate from $1 \times 10^{-5}\omega_s$ to $1 \times 10^{-4}\omega_s$.

environments on the quantum properties of these circuit systems. However, we stress that this model is only a linear approximation to the processes that occur in quantum circuits based on SQUID rings with their inherently nonperturbative properties. The very strong nonperturbative nature of the quantum mechanical SQUID ring has already yielded many surprises [3, 4, 9]. It is not unlikely that when this is taken into account in more sophisticated descriptions of decoherence in SQUID-based systems that interesting, and nontrivial, new results will be revealed.

Acknowledgements

We would like to thank the NESTA Organisation and the EPSRC for their generous funding of this work. We would also like to express our thanks to Professors C.H. van de Wal and A. Sobolev for very useful discussions.

REFERENCES

[1] J. R. Friedman, V. Patel, W. Chen, S. K. Tolpygo, and J. E. Lukens, *Nature* **406** (2000).
[2] C. H. van der Wal, A. C. J. ter Haar, F. K. Wilhem, R. N. Schouten, C. J. P. M. Harmans, T. P. Orlando, S. Lloyd, and J. E. Mooij, *Science* **290** (2000).

[3] M. J. Everitt, P. Stiffell, T. D. Clark, A. Vourdas, J. F. Ralph, H. Prance and R.J. Prance, *Phys. Rev.* B **63** (2001).
[4] M. J. Everitt, T. D. Clark, P. Stiffell, H. Prance, R. J. Prance, A. Vourdas, and J. F. Ralph, *Phys. Rev.* B **64** (2001).
[5] A. Widom, *J. Low Temp. Phys.* **37**, 449 (1979).
[6] A. Widom and T. D. Clark, *Phys. Letters* A **90**, 280 (1982).
[7] T. D. Clark, J. Diggins, J. F. Ralph, M. Everitt, R. J. Prance, H. Prance, R. Whiteman, A. Widom, and Y. N. Srivastava, *Annals Phys.* **268**, 1 (1998).
[8] T. P. Spiller, T. D. Clark, R. J. Prance, and A. Widom, *Prog. Low Temp. Phys.* **13**, 219 (1992).
[9] R. Whiteman, T. D. Clark, R. J. Prance, H. Prance, V. Schollmann, J. F. Ralph, M. Everitt, and J. Diggins, *J. Modern Optics* **45**, 1175 (1998).
[10] U. Weiss, *Quantum Dissipative Systems* (Singapore, World Scientific, 1999).
[11] N. J. Cerf and C. Adami, *Phys. Rev. Lett.* **79**(26), 5194 (1997).
[12] N. J. Cerf and C. Adami, *Physica* D **120**, 62 (1998).

MANIPULATING QUANTUM TRANSITIONS IN A PERSISTENT CURRENT QUBIT

T. D. Clark[1], J. F. Ralph[2], M. J. Everitt[1], P. B. Stiffell[1], R. J. Prance[1], and H. Prance[1]
[1]*School of Engineering, The University of Sussex, Falmer, Brighton BN1 9QT, UK*
[2]*Department of Electrical Engineering and Electronics, The University of Liverpool, Liverpool L69 3GJ, UK*

Abstract: This paper discusses two methods for generating quantum transitions between energy eigenstates in a model persistent current qubit. The alternatives are compared and their advantages and disadvantages are considered. Of particular concern is the backreaction of the qubit on the magnetic flux bias coils, used to control the qubit, due to the large effective currents at or near to a quantum mechanical transition.

Keywords: Qubit, Josephson junction, SQUID

1. INTRODUCTION

This paper examines the behavior of a model persistent current qubit in the presence of a time-dependent electromagnetic field. The qubit under consideration has been proposed by Orlando *et al.* [1] and consists of a superconducting loop containing several Josephson weak link devices. The electromagnetic field is treated as a classical source of magnetic flux [2]. It consists of a quasi-static (near DC) bias field and a time-dependent field to induce transitions between the low-lying energy states of the qubit. Of particular concern is the effect that quantum transitions in the qubit can have on the quasi-static bias flux [3], which is often considered to be one of the external control parameters when the circuit operates as a qubit.

To ensure that the qubit is as insensitive as possible to any stray environmental fluctuations, the inductance of the superconducting loop in the qubit is small compared to the effective inductance of the weak links in the loop [1]. This ensures that the low-energy behavior of the qubit will be dominated by the weak links rather than the inductance. However, the loop inductance still plays a crucial role in coupling the qubit to the external fields. The magnetic flux bias is generated by passing a DC current through a coil that is inductively coupled to the loop. The current in the coil gives rise to a screening current in the qubit that couples back to the coil, modifying the true value of the applied DC flux.

Quantum Computing and Quantum Bits in Mesoscopic Systems
Edited by Leggett *et al.*, Kluwer Academic/Plenum Publishers, 2004

When a quantum transition is driven by an external field, it gives rise to a large screening current because it produces a comparatively large change in the average energy over a small range of the applied field. The large currents near to transitions lead to a significant backreaction from the qubit to the DC coil. The magnitude of this backreaction is inversely proportional to the inductance of the qubit loop. Although the effect should be present in all quantum devices based on superconducting persistent currents [3], the effect of the backreaction is accentuated by the small loop inductances that are required to ensure that the qubit is insensitive to environmental fluctuations.

This paper considers two methods that can be used to generate transitions between energy eigenstates of the persistent current qubit, and the problems associated with the control of the quantum circuit near to such transitions.

2. PERSISTENT CURRENT QUBITS

Two standard types of persistent current qubits have been proposed [1, 4]. Both use a superconducting inductive loop that encloses a quantum mechanical magnetic flux. Both contain weak link constrictions that allow the magnetic flux to tunnel into and out of the superconducting ring. The main distinction between the two types of persistent current qubit is the relative importance of the geometric inductance of the superconducting ring, and its contribution to the energy of the qubit.

The simplest type based around a radio-frequency (rf-)SQUID ring (superconducting loop with one weak link) is sometimes referred to as the quantum flux parametron [4]. It consists of rf-SQUID rings linked by switchable flux transformers. In a qubit, the rf-SQUID ring would be "tuned" so that only two energy states/current states are accessible, providing the zero/one logic states required for the qubit. Adjacent qubits could then interact via the flux transformers to produce superpositions and entanglements by appropriate manipulation of the DC magnetic flux and switching the flux transformers on and off. This paper concentrates on the second type of persistent current qubit, which is shown in Fig. 1. This type of qubit has a superconducting ring with four Josephson weak links, two of which are in parallel in a secondary superconducting loop. In this case, the geometrical inductance of the superconducting ring is small [1], typically around 10 pF, which makes the qubit less sensitive to the effects of stray electromagnetic fields. The zero/one logic states of the qubit correspond to current states whose energies are dominated by the weak links in the loop. By choosing appropriate values for the weak link critical currents, and hence energies, it is possible to reduce the behavior of the system to a simple two-level system [1]. This configuration has four control parameters: two magnetic fluxes in the two superconducting loops, and two voltages that can be applied via the two gate capacitors (see Fig. 1). All of these control fields can be used to manipulate the quantum states of the system, but this paper will concentrate on the applied magnetic fluxes.

3. TIME-DEPENDENT SCHRÖDINGER EQUATION

Quantum effects in superconducting circuits have been studied for over twenty years. The majority of this work has centred on solutions to the time-independent Schrödinger equation, calculating the energy eigenstates [5, 6] and looking at dissipative processes

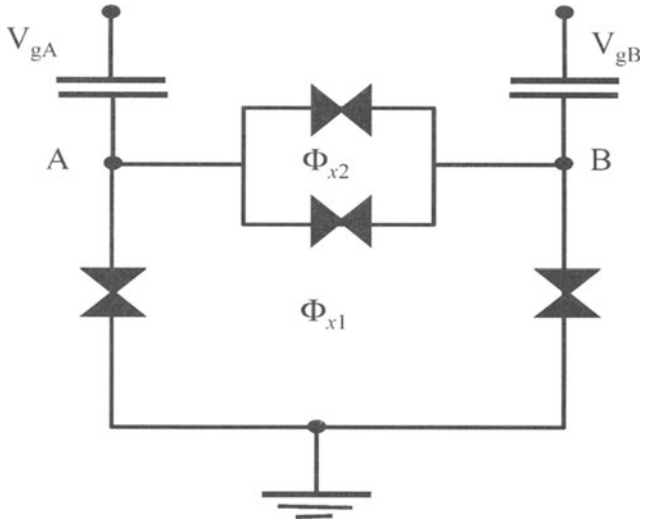

Figure 1. Schematic diagram of persistent current qubit proposed by Orlando *et al.* [1].

[7, 8] or perturbative transitions between energy eigenstates [9, 10]. Recently attention has shifted to the behavior of the time-dependent Schrödinger equation [11]. The behavior that the time-dependent equation predicts can be very different from that seen in optical or atomic systems. The coupling between the electromagnetic field and atomic or molecular systems is very weak compared to the coupling between the field and the superconducting ring. This means multiphoton excitations are comparatively easy to produce in superconducting systems [11].

The ability to reduce the system to a two-level system allows a number of simplifications to be made when calculating solutions to the Schrödinger equation, and the time-dependent Hamiltonian can be written in the matrix form [1]

$$H(t) = \begin{pmatrix} F(t) & -B(t) \\ -B(t) & -F(t) \end{pmatrix} \tag{1}$$

where the basis vectors

$$\begin{pmatrix} 1 \\ 0 \end{pmatrix} \quad \text{and} \quad \begin{pmatrix} 0 \\ 1 \end{pmatrix}$$

are persistent current states of the ring, and the functions $F(t)$ and $B(t)$ are defined by

$$F(t) = r_1 \frac{\Phi_{x1}(t)}{\Phi_0} + r_2 \frac{\Phi_{x2}(t)}{\Phi_0} \qquad B(t) = \frac{t_1 + s_1(\Phi_{x1}(t)/\Phi_0)}{1 - \eta\sqrt{E_J/E_C}} \tag{2}$$

where $\Phi_{x1}(t)$ and $\Phi_{x2}(t)$ are the (possibly time-dependent) magnetic flux biases that are applied to the two superconducting loops in Fig. 1 to control the behavior of the qubit, $\Phi_0 = (h/2e) = 2 \times 10^{-15}$ Wb is the superconducting flux quantum, $E_J = I_0\Phi_0/2\pi \equiv$ 200 GHz is the Josephson energy of the weak links (I_0 being the critical current of the weak links), $E_C = (e^2/2C) = E_J/80$ is the capacitive energy of the weak links, and the parameters $r_1 = 2\pi E_J\sqrt{1-(1/4\beta^2)}$, $r_2 = r_1/2$, $s_1 = 0$, $t_1 = 0.001E_J$, $\eta = 3.5$, and $\beta = 0.8$ have been taken from Ref. [1] (although the notation has been changed slightly, because Ref. [1] uses t instead of $B(t)$, but $B(t)$ is used here to avoid confusion with time t in the time-dependent equations). For simplicity, this paper will only consider examples where the magnetic flux in the secondary superconducting loop $\Phi_{x2}(t)$ is constant and the magnetic flux in the primary loop has a small sinusoidal term and a DC bias Φ_{DC1}, $\Phi_{x1}(t) = 0.001\Phi_0\sin(\omega t) + \Phi_{DC1}$, where the frequency of the time-dependent field $f = \omega/2\pi$ is chosen to be 10 GHz.

Using the matrix form of the Hamiltonian, the evolution of the qubit can be calculated using the unitary evolution operator

$$U(\delta t) = \cos\left(\frac{\delta t}{\hbar}\sqrt{F(t)^2 + B(t)^2}\right)I - \frac{i(F(t)\sigma_z + B(t)\sigma_x)}{\sqrt{F(t)^2 + B(t)^2}}\sin\left(\frac{\delta t}{\hbar}\sqrt{F(t)^2 + B(t)^2}\right) \quad (3)$$

where I is the identity matrix and σ_x and σ_z are Pauli matrices. Using this unitary operator for small finite time increments, the time-dependent Schrödinger equation can be integrated numerically for the qubit in a time-dependent electromagnetic field. To make use of these solutions, they need to be related back to a useful physical quantity. To do this, a time evolution operator (S) is defined such that

$$S|\psi\rangle = |\psi(t+T)\rangle \quad (4)$$

where $T = 2\pi/\omega$ is the period of oscillation of the electromagnetic field. The eigenvectors of this operator give a special set of initial conditions, for which the behavior of the system is periodic. This allows the time averages to be calculated for the energy expectation values for the ring which correspond to the Floquet (quasi-)energies

$$\langle\langle E(\Phi_{DC1})\rangle\rangle_\kappa = \frac{\omega}{2\pi}\int_0^{2\pi/\omega} \langle E(\Phi_{x1}(t))\rangle_\kappa \, dt \quad (5)$$

that are used in atomic and quantum optical calculations [12]. Example time-averaged energy levels are shown in Fig. 2. The figure shows three different types of transition. At zero bias, there are "rapid passage" (Landau–Zener) transitions where the energy gap between the two (time-independent) states is a minimum. To the right of zero bias there are single photon transitions and two-photon transitions. The applied field is relatively weak, so the width of each of the transitions is fairly small. The width of the single photon resonance is approximately 10^{-4}–$10^{-5}\Phi_0$.

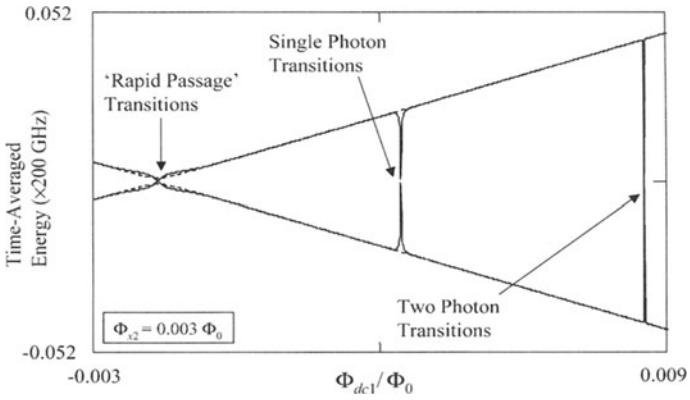

Figure 2. Time-averaged energy levels of the persistent qubit in the presence of a periodic field, showing three different types of transition.

4. GENERATING TRANSITIONS

The standard method for generating transitions in superconducting devices is to apply a pulse of electromagnetic radiation whose dominant frequency matches the quantum transition that is to be driven [9] (which is normally in the microwave energy range – 10 GHz for the cases considered in this paper). Two examples of transitions from pulsed fields are shown in Fig. 3: one for a 65 period pulse, and one for a 130 period pulse. The shorter pulse puts the qubit into a coherent superposition of the upper and lower energy levels, and the longer pulse puts the qubit into an almost pure excited state (the effect of

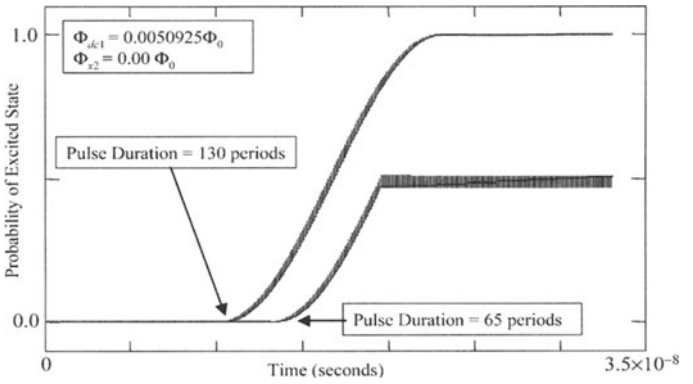

Figure 3. Two examples of transitions induced by a pulsed electromagnetic field: 130 period pulse and 65 period pulse.

dissipation is neglected for simplicity). This is a good method for generating transitions, but the fact that the pulse has a finite length does mean that some higher frequencies will be present, which could interfere with the operation of the qubit. The narrowness of the transition also requires that the bias/control fluxes be extremely stable (10^{-4}–$10^{-5}\Phi_0$).

An alternative method for generating transitions or superposition states from the ground state would be to use a continuous constant amplitude microwave field and to ramp the bias flux in such a way that the system passes through the transition region (see Fig. 4). The need for a shaped pulse, and the high frequencies that this requires, is removed and the requirement for a highly stable flux bias is reduced. As long as the flux rate is stable and the system is swept though a transition at the right rate, an excited state should be produced (again, ignoring dissipation effects for simplicity). The main problem with this type of controlled excitation is that the currents associated with transition region can be large. When these currents couple back to the bias coil, they can introduce nonlinear effects.

5. NONLINEAR BACKREACTION

The controllable parameter is the DC current flowing through the coil. The current in the coil gives rise to a screening current in the SQUID which couples back the coil, modifying the true value of the applied DC flux. The average screening current flowing in the SQUID ring is related to the derivative of the energy level with respect to the applied flux. (The use of the average is based on the Born–Oppenheimer approximation [13] and is justified because of the low frequencies associated with the DC coil.) If quantum transitions are driven by an external field, they give rise to a large screening currents because they produce a comparatively large change in the average energy over a small range of the applied flux. The currents associated with background energy levels in Fig. 2 (i.e., without the time-dependent field) are around 325 nA, while those near the single

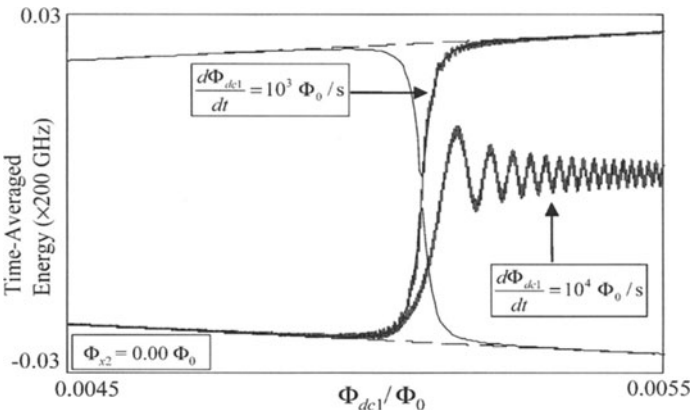

Figure 4. Two examples of transitions induced by linearly ramping the static magnetic flux through a transition.

photon resonance can be as much as 83 μA. These comparatively large currents near the transitions lead to a significant backreaction from the qubit to the DC coils.

Figure 5 shows the qubit circuit with an inductance in the main loop and the DC coil (represented as an oscillator). There is another DC coil providing the DC bias in the secondary loop. It is possible to include the backreaction on the second bias coil, but for simplicity only the main DC bias is considered here. However, if the backreaction on the second coil were to be included, the effect would be similar to that on the main flux bias.

The backreaction stems from the fact that the magnetic flux in each of the coils in Fig. 3 is defined in terms of the currents flowing though the coils

$$\begin{aligned} \Phi_{\mathrm{I}} &= \Lambda I_{\mathrm{I}} + M I_{\mathrm{DC}} \\ \Phi_{\mathrm{DC1}} &= L_{\mathrm{DC}} I_{\mathrm{DC}} + M I_{\mathrm{I}} \end{aligned} \tag{6}$$

where Φ_{I} is the total magnetic flux induced in the primary loop and I_{I} is the current flowing around the primary loop, Λ is the geometric inductance of the qubit (which is approximately 10 pF), L_{DC} is the inductance of the coil (which is assumed to be equal to that of the ring), and M is the mutual inductance between the two coils. The current flowing through the DC coil (I_{DC}) is the controllable parameter and the current flowing through the main qubit loop (I_{I}) is the time-averaged quantum mechanical current (the Born–Oppenheimer approximation).

The DC current is related to the static flux by the nonlinear equation [14]

$$\frac{\Phi_{\mathrm{DC}}}{L_{\mathrm{DC}}} = I_{\mathrm{DC}} + \frac{\mu \langle\langle I_{\mathrm{I}}(\mu \Phi_{\mathrm{DC}}) \rangle\rangle_{\kappa}}{1 - K^2} \tag{7}$$

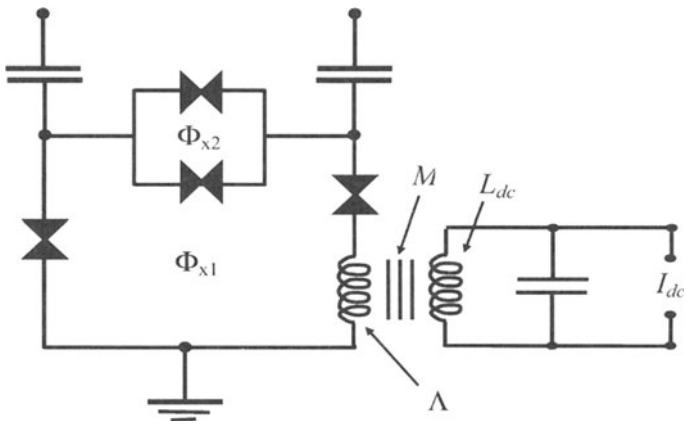

Figure 5. Schematic diagram of the persistent current qubit with bias coil for the applied magnetic flux.

where the time-averaged current in the superconducting loop can be found from

$$\langle\langle I_1(\Phi_{DC})\rangle\rangle_\kappa = -\frac{\partial\langle\langle E(\Phi_{DC})\rangle\rangle_\kappa}{\partial\Phi_{DC}} \tag{8}$$

and $K^2 = M^2/\Lambda L_{DC}$ and $\mu = M/\Lambda$ are coupling constants. This nonlinear equation can be solved numerically, and the time-averaged energy levels can be plotted against the DC current. Figure 6 shows a single photon transition as a function of the applied DC current, both with and without the effect of the backreaction. It is clear that the effect of the backreaction for $K^2 = 0.05$ is large enough to introduce a significant distortion into the apparent shape of the quantum resonance. In the ground state, there will also be hysteresis, where the apparent shape of the resonance differs depending on whether the DC current in the coil is (quasi-statically) increasing or decreasing.

6. CONCLUSIONS

This paper discusses the behavior of a persistent current qubit proposed by Orlando *et al.* [1]. It is an interesting vehicle for the exploration of quantum behavior in solid-state circuits. It shows a range of potentially useful behavior, including multiphoton excitations for comparatively low amplitude time-dependent fields ($\sim 0.001\Phi_0$). There are two methods that can be used to produce excited states or superposition states, either using pulsed electromagnetic fields or ramping the control flux through a driven transition. Lastly, the qubit control circuit can show interesting nonlinear effects that are due to quantum transitions in the qubit circuit. These nonlinear properties may make the control of the qubit more difficult but they offer an interesting mechanism with which to investigate the interface between the classical nonlinear regime and the linear quantum world.

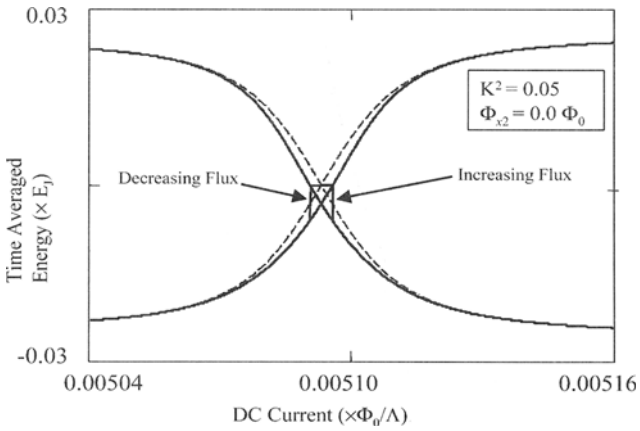

Figure 6. Example of hysteresis caused by the nonlinear backreaction of the qubit on the bias coil.

REFERENCES

[1] T. P. Orlando, J. E. Mooji, L. Tian, C. H. van der Wal, L. S. Levitov, S. Lloyd, and J. J. Mazo, *Phys. Rev.* B **60**, 15398 (1999).
[2] T. D. Clark, J. Diggins, J. F. Ralph, M. J. Everritt, R. J. Prance, H. Prance, and R. Whiteman, *Ann. Phys.* **268**, 1 (1998).
[3] J. F. Ralph, T. D. Clark, M. J. Everitt, and P. Stiffell, *Phys. Rev.* B **64**, 180504 (2001).
[4] M. F. Bocko, A. M. Herr, and M. J. Feldman, *IEEE Trans. on Appl. Superconduct.* **7**, 3638 (1997); F. Chiarello, *Phys. Lett.* A **277**, 189 (2000).
[5] A. Widom, *J. Low Temp. Phys.* **37**, 449 (1979); A. Widom and Y. Srivastava, *Phys. Rep.* **148**, 1 (1987).
[6] T. P. Spiller, T. D. Clark, R. J. Prance, and H. Prance, *Prog. Low Temp. Phys.* **XIII**, 219 (Elsevier, NY, U.S.A., 1992); R. J. Prance, T. D. Clark, R. Whiteman, J. Diggins, H. Prance, J. F. Ralph, T. P. Spiller, A. Widom, and Y. Srivastava, *Physica* **B203**, 381 (1994).
[7] A. O. Caldeira and A. J. Leggett, *Ann. Phys.* **149**, 374 (1983); A. J. Leggett, S. Chakravarty, A. T. Dorsey, M. P. A. Fischer, A. Garg, and W. Zweger, *Rev. Mod. Phys.* **59**, 1 (1987).
[8] G. Schön and A. D. Zaikin, *Phys. Rep.* **198**, 237 (1990).
[9] R. Rouse, S. Han, and J. E. Lukens, *Phys. Rev. Lett.* **75**, 1614 (1995); S. Han, R. Rouse, and J. E. Lukens, *Phys. Rev. Lett.* **76**, 3404 (1996).
[10] P. Silvestrini, B. Ruggiero, Y. N. Ovchinnikov, A. Esposito, and A. Barone, *Phys. Lett.* A **212**, 347 (1996); P. Silvestrini, B. Ruggiero, C. Granata, and E. Esposito, *Phys. Lett.* A **267**, 45 (2000).
[11] T. D. Clark, J. Diggins, J. F. Ralph, M. J. Everritt, R. J. Prance, H. Prance, and R. Whiteman, *Ann. Phys.* **268**, 1 (1998); J. Diggins, R.Whiteman, T. D. Clark, R. J. Prance, H. Prance, J. F. Ralph, A. Widom, and Y. Srivastava, *Physica* B **233**, 8 (1997).
[12] C. Cohen-Tannoudji, J. Dupont-Roc, and G. Grynberg, *Atom Photon Interactions* (New York, Wiley, 1992) Ch. III and Ch. IV; J. Shirley, *Phys. Rev.* B **138**, 979 (1965); S. I. Chu, *Adv. Atomic Molec. Phys.* **21**, 197 (1985).
[13] M. Born, Z. *Phys.* **38**, 803 (1926).
[14] J. F. Ralph, T. D. Clark, M. J. Everitt, and P. Stiffell, *Phys. Rev.* B **64**, 180504 (2001).

VORTICES IN JOSEPHSON ARRAYS INTERACTING WITH NONCLASSICAL MICROWAVES IN A DISSIPATIVE ENVIRONMENT

A. Konstadopoulou[1,a], J. M. Hollingworth[1], A. Vourdas[1,b], M. Everitt[2], T. D. Clark[2,c], and J. F. Ralph[3]
[1]*Department of Computing, University of Bradford, Bradford BD7 1DP, UK*
[2]*School of Engineering and Information Technology, University of Sussex, Falmer, Brighton BN1 9QT, UK*
[3]*Department of Electrical Engineering and Electronics, University of Liverpool, Liverpool L69 3GJ, UK*

Abstract: Vortices circulating in a ring made from a Josephson array in the insulating phase are studied. The ring contains a "dual Josephson junction" through which the vortices tunnel. External nonclassical microwaves are coupled to the device. The time evolution of this two-mode fully quantum mechanical system is studied, taking into account the dissipation in the system. The effect of the quantum statistics of the photons on the quantum statistics of the vortices is discussed. Entropic calculations quantify the entanglement between the two systems. Quantum phenomena in the system are also studied through Wigner functions. After a certain time (which depends on the dissipation parameters) these quantum phenomena are destroyed due to dissipation.

Keywords: Josephson array, Vortices, Entanglement, Dissipation

1. INTRODUCTION

Quantum information theory is the subject of extensive academic research in recent years, especially with the perspectives of quantum computation and communication. There has been a lot of interest in coherent electron behavior in Josephson devices for a long time. The new development in the last ten years [1] has been the experimental and theoretical study of mesoscopic Josephson devices (with capacitance lower than 10^{-6} F) where quantum phenomena are stronger. The field received new attention recently after it was recognised that suitable Josephson devices can serve as quantum

[a]E-mail: akonstad@bradford.ac.uk
[b]E-mail: a.vourdas@bradford.ac.uk
[c]E-mail: t.d.clark@sussex.ac.uk

Quantum Computing and Quantum Bits in Mesoscopic Systems
Edited by Leggett *et al.*, Kluwer Academic/Plenum Publishers, 2004

bits (qubits) in quantum information devices and that quantum logic operations could be performed.

Coherent vortex behavior in insulating systems (realized with Josephson arrays) has also been studied in the literature [2]. There is a duality between electrons in the superconducting phase and vortices in the insulating phase, which has been studied in Ref. [3]. In the same context, "dual Josephson junctions" for vortices have been studied [4]. They are weak links between two "super-insulators" and vortices tunnel through them in an analogous (dual) way to the tunneling of electron pairs through weak links between two superconductors (Josephson junctions).

In this paper we consider a ring made from a Josephson array in the insulating phase containing a dual Josephson junction through which the vortices tunnel. The system interacts with nonclassical microwaves (at GHz–THz frequencies) [5]. Nonclassical electromagnetic fields have been carefully prepared in a particular quantum state so that the amount of quantum noise is well defined and the statistics of photons is also well defined. This is a fully quantum mechanical system and we study explicitly how the quantum noise of the electromagnetic field affects the quantum noise of the vortex current. Our work in this paper extends that of Ref. [6] to include the effect of dissipation in the system. The results show that interesting quantum phenomena occur up to a certain time. They include nonclassical statistics (for both the device and the microwaves), entanglement between the two modes, and so on. After a certain time dissipation destroys these phenomena.

Josephson systems are good candidates for the development of amplifiers and frequency converters operating at THz frequencies. There is also a lot of work currently regarding their use as quantum gates in quantum technology and quantum computing [7].

2. INTERACTION OF JOSEPHSON ARRAYS WITH EXTERNAL NONCLASSICAL MICROWAVES

We consider a ring (Fig. 1) made from an array of Josephson junctions with Coulomb coupling constant E_C greater than the Josephson coupling constant E_J. For those values of

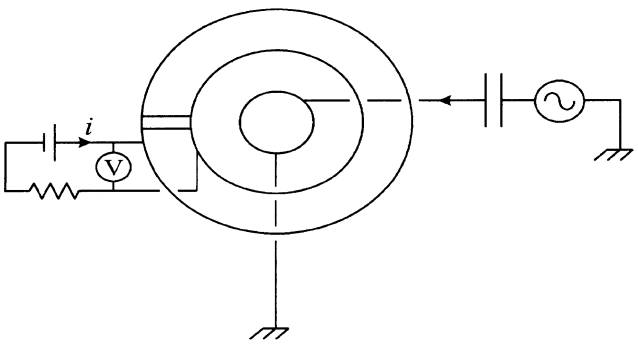

Figure 1. Ring made from array of Josephson junctions with a dual Josephson junction.

the parameters the array is in the insulating phase where vortices move with high mobility and charges are confined. Such rings have been considered experimentally in the context of the Aharonov–Casher effect in Ref. [8]. However, our ring has also a "dual Josephson junction" [4], which plays a similar role for vortices, as the ordinary Josephson junctions for electron pairs. The "dual phase" of the vortex wavefunction has a phase difference δ along the dual Josephson junction. This is analogous to the Cooper-pair wavefunction in superconducting rings with Josephson junctions, which has phase difference ϕ along the junction. The center of the ring contains charge $Q(t)$ induced through coupling with an external source of microwaves that are carefully prepared in a particular quantum state. For example, we can put the device of Fig. 1 in a cylindrical waveguide in the TM_{01} mode with the plane of the diagram perpendicular to the axis of the cylinder.

Microwaves in various quantum states have been produced experimentally in several laboratories. The system operates at low temperatures ($\hbar\Omega_1 > k_BT$ and $\hbar\Omega_2 > k_BT$), so that the thermal noise is less than the quantum noise in the microwaves and the device. The Hamiltonian describing the system is

$$H = \frac{1}{2}L(I - I_{\rm ex})^2 + \frac{(Q - Q_{\rm ex})^2}{2C} + E_{\rm dJ}(1 - \cos\delta) \tag{1}$$

where L is inductance of the device, $L_{\rm mw}$ is the inductance of the circuit that produces the external microwaves, and I and $I_{\rm mw}$ are the total and external (microwave) currents respectively[1]. C is the capacitance between the boundaries L_0 and L_1. Q and $Q_{\rm mw}$ are the total and external (microwave) charge, respectively, in the inner boundary of the ring. $E_{\rm dJ}$ is the dual Josephson coupling constant and $\delta = \Phi_0 Q$ the dual phase. $\Phi_0 = \pi/e$ is the flux quantum (in units where $\hbar = k_B = c = 1$). The sinusoidal term $E_{\rm dJ}(1 - \cos\delta)$ describes vortex tunnelling through the dual Josephson junction.

Quantization of the device and the electromagnetic field is done with the annihilation operators

$$a_1 = \left(\frac{1}{2\Omega_1 C}\right)^{1/2}[Q + i\Omega_1^{-1}I] \tag{2}$$

$$a_2 = \left(\frac{1}{2\Omega_2 C}\right)^{1/2}[Q_{\rm mw} + i\Omega_2^{-1}I_{\rm mw}] \tag{3}$$

and the corresponding creation operators. $\Omega_1 = (LC)^{-1/2}$ and $\Omega_2 = (LC)^{-1/2}$ are the oscillator frequency of the device and the microwaves. We note that for the parameters considered $\Omega_1 = \Omega_2$.

The Hamiltonian can now be written as

$$H = \Omega_1 a_1^\dagger a_1 + \Omega_2 a_2^\dagger a_2 - E_{\rm dJ}\cos[\mu(a_1^\dagger + a_1)] - \Omega_1(a_1^\dagger a_2 + a_1 a_2^\dagger) \tag{4}$$

where $\mu = \Phi_0(\Omega_1 C/2)^{1/2}$.

[1]For simplicity we assume that $L = L_{\rm mw}$ and that we have maximum coupling between the two circuits so that $g = \sqrt{LL_{\rm mw}} = L$.

3. TIME EVOLUTION

Assuming that the system is initially ($t = 0$) described by a density matrix $\rho(0)$, we have calculated numerically the evolution of the density matrix.

In the case that there is no dissipation present, the evolved density matrix $\rho(t)$ is given by

$$\rho(t) = \exp[iHt]\rho(0)\exp[-iHt] \tag{5}$$

The case with dissipation has been studied by several authors (e.g. [9]). In our analysis we use a very simple model. The derivative of the evolved density matrix is given by

$$\begin{aligned}\frac{\partial\rho}{\partial t} = {} & i[H, \rho] + \frac{\gamma_1}{2}(M+1)(2a_1\rho a_1^\dagger - a_1^\dagger a_1\rho - \rho a_1^\dagger a_1) \\ & + \frac{\gamma_1}{2}M(2a_1^\dagger\rho a_1 - a_1 a_1^\dagger\rho - \rho a_1 a_1^\dagger) \\ & + \frac{\gamma_2}{2}(M+1)(2a_2\rho a_2^\dagger - a_2^\dagger a_2\rho - \rho a_2^\dagger a_2) \\ & + \frac{\gamma_2}{2}M(2a_2^\dagger\rho a_2 - a_2 a_2^\dagger\rho - \rho a_2 a_2^\dagger),\end{aligned} \tag{6}$$

where γ_1 and γ_2 are the damping rates of the two modes respectively and M is the average number of bath quanta.

For both cases we have calculated numerically $\rho(t)$ and the reduced density matrices

$$\rho_1(t) = \mathrm{Tr}_2\rho(t); \quad \rho_2(t) = \mathrm{Tr}_1\rho(t) \tag{7}$$

Using these we calculated the average number of quanta in each mode

$$\langle N_i\rangle = \mathrm{Tr}[a^\dagger a\rho_i] \tag{8}$$

as functions of time.

For the purposes of numerical calculations, the infinite-dimensional matrix $\langle M_1, M_2|H|N_1, N_2\rangle$ has been truncated, with M_1, N_1 taking values from 0 to $N_{1\max}$ and M_2, N_2 taking values from 0 to $N_{2\max}$. Correspondingly, $N_{1\max}$ and $N_{2\max}$ were taken to be much greater than $\langle N_1\rangle$ and $\langle N_2\rangle$. As a measure of the accuracy of the approximation we calculated the traces of the truncated matrices. In the limit $N_{1\max} \to \infty$ and $N_{2\max} \to \infty$ they equal to 1; and in the truncated case the above sum was greater than 0.98 for both cases.

4. QUANTUM STATISTICS, NOISE, AND ENTANGLEMENT

The microwaves have been carefully prepared in a quantum state and this implies that the quantum statistics of the photons threading the ring is known.

We investigate how the quantum statistics and quantum noise of the photons affects the quantum statistics and quantum noise of the tunneling vortices. For this purpose we have calculated the second-order correlations

$$g_{ii}^{(2)} = \frac{\langle N_i^2\rangle - \langle N_i\rangle}{\langle N_i\rangle^2}; \quad i = 1, 2 \tag{9}$$

The $g_{11}^{(2)}$ and $g_{22}^{(2)}$ describe vortex and photon bunching or antibunching, respectively.

The quantum noise is quantified with the uncertainties

$$(\Delta x_i)^2 = \mathrm{Tr}(\rho x_i^2) - [\mathrm{Tr}(\rho x_i)]^2; \quad i = 1, 2 \tag{10}$$

In the initial state ($t = 0$) the system is not entangled. However, the microwaves become entangled with the Josephson array device as time evolves.

As a measure of the correlations between the two modes we have calculated the entropy [10]

$$I = S(\rho_1) + S(\rho_2) - S(\rho) \tag{11}$$

where $S = -\mathrm{Tr}\rho \ln \rho$ is the von Neumann entropy. The entanglement entropy I is positive according to the subadditivity property. The results show that although originally the two modes are uncorrelated, they become strongly correlated later. These correlations might be classical or quantum mechanical (entanglement). Reference [11] has used the conditional entropies

$$\begin{aligned} I_1 &= -S(\rho_1) + S(\rho) \\ I_2 &= -S(\rho_2) + S(\rho) \end{aligned} \tag{12}$$

as a criterion for entanglement.

When $I_i < 0$ ($i = 1, 2$) the system is entangled (although the converse is not true, i.e., an entangled system might have $I_i > 0$).

If the system is in a pure state at $t = 0$ and evolves unitarily in a dissipationless environment then $S(\rho) = 0$ and $S(\rho_1) = S(\rho_2)$. In this case $I = -2I_1 = -2I_2$ and therefore a positive value of I indicates negative value of I_i and hence entanglement.

5. RESULTS AND DISCUSSION

Initially, we assume that at time $t = 0$ the device is in the lowest (vacuum) state $|0\rangle$ ($a_1|0\rangle = 0$) and the microwaves in the coherent state $|A = 1.5\rangle$ ($a_2|A\rangle = A|A\rangle$). $\Omega_1 = \Omega_2 = 1.5 \times 10^{-4}$, $E_{\mathrm{dJ}} = 1.5 \times 10^{-4}$, $\mu = 2.8408$, and truncation $N_{i\max} = 10$. For these parameter values we have considered two cases; the first with no dissipation ($\gamma_1 = \gamma_2 = 0$) [6] (Fig. 2) and the second with dissipation $\gamma_1 = \gamma_2 = 2 \times 10^{-4}$ and $M = 1$ (Fig. 3).

The first graph shows $\langle N_1 \rangle$ (solid line) and $\langle N_2 \rangle$ (broken line) as functions of time. The second graph shows $g_{11}^{(2)}$ (solid line), $g_{22}^{(2)}$ (broken line). The third graph shows the uncertainties $\sqrt{\Omega}\Delta x_1$ (solid line) and $\sqrt{\Omega}\Delta x_2$ (dotted line) as functions of time. The fourth graph shows the entropies I (solid line), I_1 (broken line), and I_2 (dotted line) in natural units (nats) as a function of time.

In the absence of dissipation, results show the exchange of energy between the two modes. The plot of the second-order correlations shows that when one of the modes is described by Poissonian statistics ($g^{(2)} = 1$) the other mode is described by super-Poissonian statistics (strong bunching). These two statistics are exchanged almost periodically as functions of time. In a similar way the quantum noise of one mode affects that of the other mode periodically. Although the system starts with the two modes uncorrelated, after some time they become strongly correlated as is shown by the value of entanglement entropy.

However, the result for the simulation of the same system when dissipation is taken into account shows clearly the destructive role of dissipation on quantum

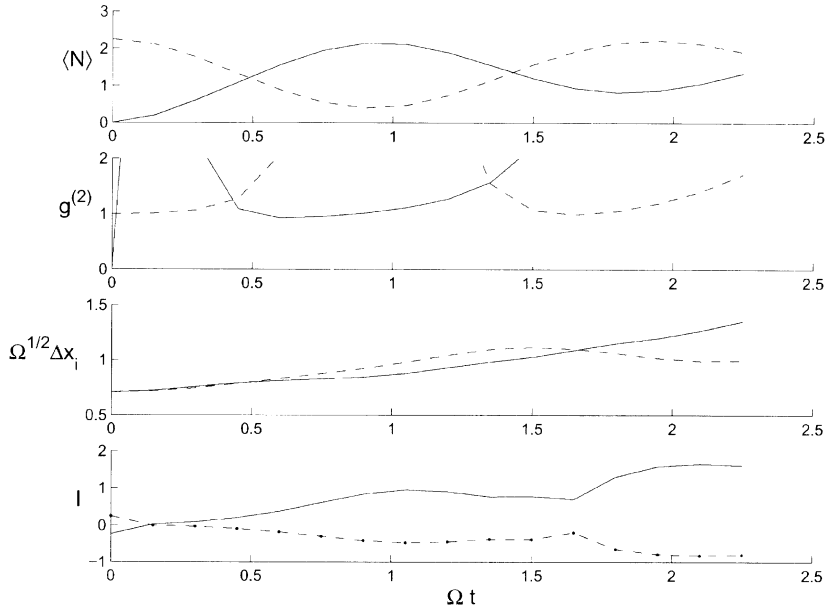

Figure 2. Evolution of the system in the absence of dissipation.

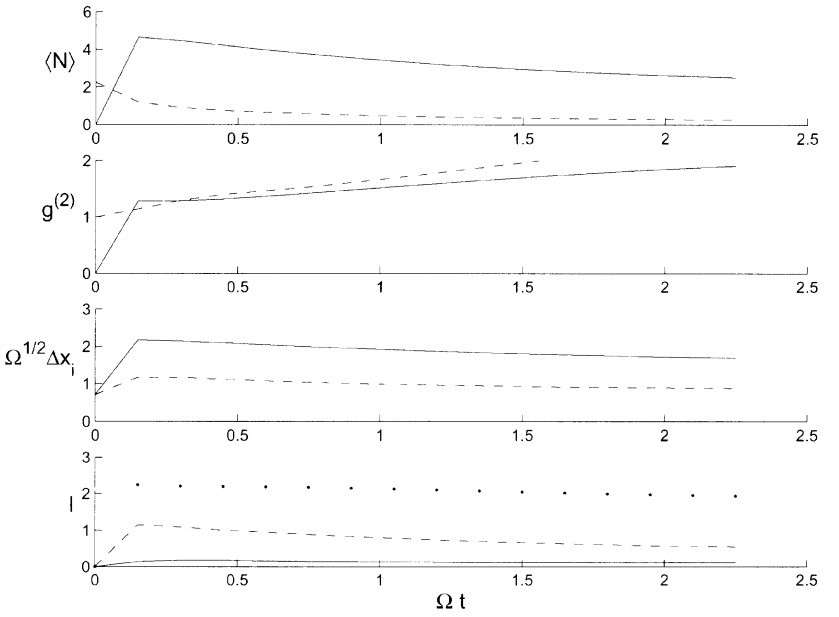

Figure 3. Evolution of the system in the presence of dissipation.

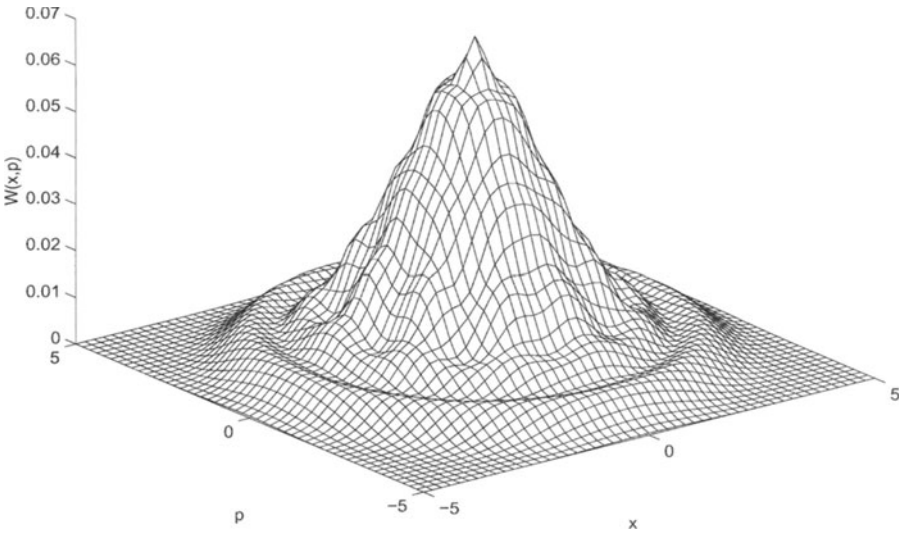

Figure 4. Wigner function of the evolved density matrix, dissipation has thermalised the state.

phenomena. After some time, there is no exchange of energy between the two modes, the statistics is thermal or even "super-thermal" and there is no entanglement. Indeed, in the absence of dissipation (Fig. 2) the quantity $I = -2I_1 = -2I_2$ is an increasing function of time. In contrast, in the presence of dissipation (Fig. 3) the same quantity very quickly becomes almost zero.

As a further demonstration of the effect of dissipation we have calculated the Wigner function [12] of the evolved density matrix of the vortices.

In Fig. 4 the Wigner function for the state of the device at $\Omega_1 t = 2.25$. It is described by almost Gaussian Wigner function which is characteristic of thermal states. Therefore, it is clearly demonstrated that after some time dissipation thermalises the mode. This can be seen from the values of $g^{(2)}$, but the Wigner function shows it very clearly in the position momentum plane.

Our model can be useful in the context of quantum gates based on Josephson technology, and also in the context of THz technology.

Acknowledgements

A. K. gratefully acknowledges support from EPSRC and the University of Bradford.

REFERENCES

[1] G. Schon, and A. D. Zaikin, (1990). *Phys. Rep.* **198**, 237.
[2] A. vanOudenaarden, and J. E. Mooij, (1996). *Phys. Rev. Lett.* **76**, 4947.
[3] T. P. Spiller, *et al.* (1990). *Nuovo Cim.* **105B**, 43.
[4] A. Vourdas, (1999). *Eurphys. Lett.* **48**, 201.
[5] A. Vourdas, and T. P. Spiller, (1997). *Z. Lett.* **B102**, 43.

[6] A. Konstadopoulou, *et al.* (2001). *IEE Proc. Science, Meas. Tech.* **148**, 229.
[7] Y. Makhlin, G. Schon, and A. Shnirman, (1999). *Nature* **398**, 305.
[8] T. P. Orlando, and K. A. Delin, (1991). *Phys. Rev.* B **43**, 8717.
[9] A. J. Leggett, *et al.* (1987). *Rev. Mod. Phys.* **1**, 59.
[10] G. Lindbland, (1973). *Commun. Math. Phys.* **33**, 305.
[11] N. J. Cerf, and C. Adami, (1998). This is a test. *Physica* D **120**, 62.
[12] S. Chountasis, and A. Vourdas, (1998). *Phys. Rev.* A, **58**, 1794.

REALIZATION OF UNIVERSAL QUANTUM CLONING AND OF THE NOT GATE BY OPTICAL PARAMETRIC AMPLIFICATION

F. Sciarrino, C. Sias, and F. De Martini
Dipartimento di Fisica, Universita' di Roma "La Sapienza", Istituto Nazionale di Fisica della Materia, Rome, Italy

Abstract: An arbitrary quantum state cannot be "cloned" perfectly, that is, reproduced with "fidelity" $F = 1$ into $M > 1$ states identical to the original by any conceivable physical device. The main root of this impossibility resides in the linearity of quantum mechanics. A second "quantum impossibility" process, based on the complete positivity character of any quantum operation, forbids the realization of a universal NOT gate that is, one that flips exactly *any* input qubit into an orthogonal one. A detailed investigation of these results, representing the most fundamental difference between classical and quantum information, can reveal the detailed structure of the latter. We report an experimental demonstration of the process of optimal cloning of $N = 1$ input qubit into $M = 2$ output qubits by a quantum-injected optical parametric amplifier (OPA). By the same apparatus the realization of a universal NOT gate is also demonstrated. The two processes will be found to be *universal* and *optimal*, that is, the measured *fidelity* of both processes $F < 1$ will be found close to the theoretical values.

Information encoded in a quantum system has to obey rules of quantum physics, which impose strict bounds on possible manipulations with quantum information. The common origin of these bounds is that all quantum-mechanical transformations have to be represented by completely positive maps [1], which in turn impose a constraint on the fidelity of the corresponding quantum-mechanical measurements. That is, an unknown state of a qubit cannot be precisely determined (reconstructed) from a measurement performed on a finite ensemble of identically prepared qubits [2–4]. In particular, the mean fidelity of the best possible (optimal) state estimation strategy based on the measurement of N identically prepared qubits is $F = (N + 1)/(N + 2)$. One of the obvious consequences of this bound on the fidelity of estimation is that unknown states of quantum systems cannot be cloned (copied) perfectly [5], that is, the perfect cloning transformation of the form $|\Phi\rangle \Longrightarrow |\Phi\rangle|\Phi\rangle$ is not permitted by the rules of quantum mechanics. This possibility would trigger dramatic changes in the present picture of the physical world, for example, it would be possible to utilize quantum nonlocality for superluminal signaling [6–8]. Another transformation that cannot be performed perfectly on an unknown state of

Quantum Computing and Quantum Bits in Mesoscopic Systems
Edited by Leggett *et al.*, Kluwer Academic/Plenum Publishers, 2004

a qubit is the spin-flip by the universal-NOT gate, that is, the operation $|\Phi\rangle \Longrightarrow |\Phi^{\perp}\rangle$, where the state $|\Phi^{\perp}\rangle$ is orthogonal to the original $|\Phi\rangle$ [9]. Spin-flipping is indeed an *anti-unitary*, time reversal transformation [3]. In spite of the fact that some quantum-mechanical transformations on unknown states of qubits cannot be performed perfectly, one still may ask that within the given structure of quantum mechanics [10] (i.e. the theory is linear and all maps are completely positive [8]) what are the best possible (optimal) approximations of these maps, that is, what is the "optimal" universal cloning and the "optimal" universal-NOT (U-NOT) gate. The *universality* condition is required to ensure that all inputs (in unknown states) are transformed with the same *fidelity*. Investigation of these universal optimal transformations, which are also called universal quantum machines [11], is extremely important since it reveals bounds on optimal manipulations with quantum information. Consequently, in recent years theoretical investigation on the Universal Optimal Quantum Cloning Machine (UOQCM) and on the U-NOT gate has been very thorough.

In spite of the success in the theoretical analysis of the bounds on optimal manipulations with individual qubits, it is extremely difficult to realize experimentally universal quantum machines. In the domain of quantum optics this is possible by associating a cloning machine with a photon amplification process, for example, involving inverted atoms in a laser amplifier or a nonlinear (NL) medium in an optical parametric amplifier (OPA). This can be done by virtue of the existing isomorphism between any logic state of a qubit and the polarization state of the photon qubit. In the OPA, mode non-degenerate case, it is generally supposed that N photons, prepared identically in an arbitrary quantum state $|\Phi\rangle$ of *linear-polarization* (π) are injected into the amplifier on the input mode k_1. The amplifier then generates on the same output "cloning mode" (C) $M > N$ copies, or "clones" of the input qubit $|\Phi\rangle$. Correspondingly, the OPA amplifier generates on the output "anticloning mode" (AC), $k_2 M - N$ states $|\Phi^{\perp}\rangle$, thus realizing a quantum NOT gate. According to this scheme, in the present work we report the experimental demonstration of the process of cloning $N = 1$ input photon into $M = 2$ output photons by a *quantum injected*, mode nondegenerate OPA operating in a $\vec{\pi}$-*entangled* configuration [12]. The process will be found *universal*, that is, implying equal quantum efficiencies for any arbitrary input $\vec{\pi}$-state, and *optimal*, that is, the loss of fidelity due to the amplification will agree with the limit values expected by the quantum analysis [13–15].

The first machine that was investigated theoretically was the *optimal universal quantum cloner* of qubits. The action of this cloner can be described by a simple covariant (ensuring universality) transformation [13]:

$$|\Phi\rangle|\downarrow\rangle_{\mathrm{C}}|\downarrow\rangle_{\mathrm{AC}} \Rightarrow \sqrt{\frac{2}{3}}|\Phi\rangle|\Phi\rangle|\Phi^{\perp}\rangle_{\mathrm{AC}} - \sqrt{\frac{1}{3}}|\{\Phi, \Phi^{\perp}\}\rangle|\Phi\rangle_{\mathrm{AC}} \tag{1}$$

where the first (unknown) state vector in the left-hand side of Eq. (1) corresponds to the system to be cloned, the second state vector describes the system on which the information is going to be copied ("blank" qubit), represented by the "cloning channel" (C) k_1, and the third state vector represents the cloner itself. The state $|\Phi^{\perp}\rangle$ is the *antipode* of $|\Phi\rangle$ on the Bloch sphere while $|\{\Phi, \Phi^{\perp}\}\rangle$ is the completely symmetric state of two qubits. In the present work the cloner is a qubit, associated with the "anti-cloning channel" (AC). Assume that the blank qubit and the cloner are initially in the known state $|\downarrow\rangle$. At the output of the cloner we find two qubits (the original and the copy) in the state $\rho = 2/3|\Phi\rangle|\Phi\rangle\langle\Phi|\langle\Phi| + 1/3|\{\Phi, \Phi^{\perp}\}\rangle\langle\{\Phi, \Phi^{\perp}\}|$. The density operator ρ describes the

best possible approximation of the perfect cloning process, that is, the state $|\Phi\rangle|\Phi\rangle$. The fidelity of this transformation does not depend on the state of the input and reads $F = \langle\Phi|\langle\Phi|\rho_{\text{out}}|\Phi\rangle|\Phi\rangle = 5/6$.

The cloner itself after the cloning transformation is in the state $\rho_{\text{AC}} = 1/3|\Phi^{\perp}\rangle\langle\Phi^{\perp}| + 1/3\mathbf{I}$, where $\mathbf{I}$ is the unity operator. This last density operator represents the best possible approximation of the action of the spin-flip (U-NOT) operation permitted by quantum mechanics and the fidelity of the U-NOT transformation is $F^* = \langle\Phi^{\perp}|\rho_{\text{out}}|\Phi^{\perp}\rangle = 2/3$, equal to the fidelity of estimation [8].

We may establish a closer connection of the above results for "cloning" with the adopted physical system, by considering for instance the *horizontal* (h) direction of the linear polarization, $\vec{\pi} = \mathbf{h}$, of a *single-photon* $N = 1$ injected into the OPA on the input mode k_1 (Fig. 1). By adopting for a moment the symbolic mathematical representation and some results of the general OPA theory given below, the amplification leads, by virtue of the transformation induced by the evolution operator $U_{AA'}$, to the output state: $|\Psi\rangle_{\text{out}} = U_{AA'}|\Psi\rangle_{\text{in}} = U_{AA'}|1\rangle_{1h}|0\rangle_{1v}|0\rangle_{2h}|0\rangle_{2v}$. This last expression means one photon on

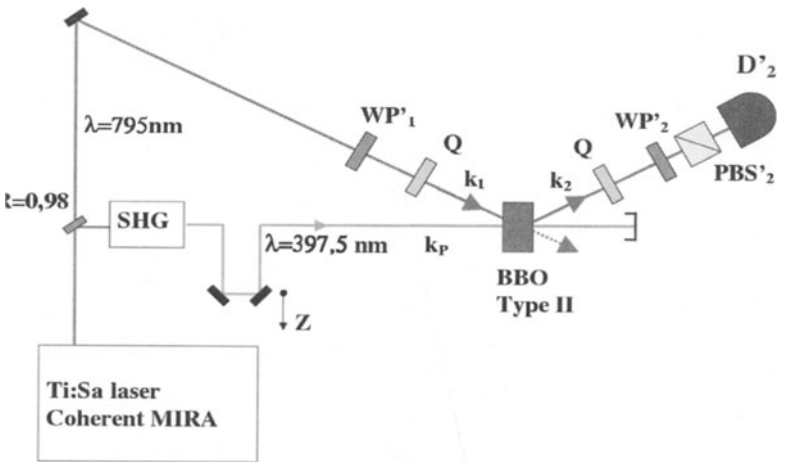

Figure 1. Schematic diagram of the optical parametric amplifier (OPA) in entangled configuration. The source was a Ti:Sa Coherent MIRA mode-locked pulsed laser providing by Second Harmonic Generation (SHG) the OPA "pump" field associated with the spatial mode with wavevectors (wv) k_p and wavelength λ_p. The OPA active element was an NL crystal slab (BBO: β-barium borate), 1.5 mm thick cut for Type II phase-matching (for more detail see Ref. [18]). A small portion of the laser radiation at wl λ was directed along the OPA injection mode k_1 The parametric amplification, with calculated gain $g \simeq 0.11$, was detected at the OPA output mode k_2 by D_2', a Si linear photodiode SGD100. An interference filter (IF) with bandwidth 3 nm was placed in front of the photodiode. The time superposition in the NL crystal of the "pump" and of the "injection" pulses was assured by micrometric displacements of a two-mirror optical "trombone". The time duration of the "pump" and of the "injected" pulses was 150 fs. Various π-states of the injected pulse were prepared by the wave-plate (either $\lambda/2$ or $\lambda/4$) WP_1' inserted on mode k_1 before injection. These states were then analyzed after amplification and before detection on mode k_2 by a π-analyzer $WP_2' + PBS_2'$, the last device being a polarizing beam splitter. In all experiments reported in the present work, fixed 4.8 mm thick X-cut quartz plates Q inserted on input and output modes k_1 and k_2 provided the compensation of unwanted beam walk-off effects due to the birefringence of the NL crystal.

the input k_j-*mode* with $j = 1$, **h** polarization, and zero photons on the three other input modes $j = 1, 2$ with **h** or **v** (vertical) polarizations. If we adopt the isomorphism: $|\Phi\rangle|\downarrow\rangle = |1\rangle_{1h}|0\rangle_{1v}$, $|\Phi^{\perp}\rangle|\downarrow\rangle = |0\rangle_{1h}|1\rangle_{1v}$ and $|\{\Phi, \Phi^{\perp}\}\rangle = |1\rangle_{1h}|1\rangle_{1v}$, we shall find that $|\Psi\rangle_{\text{out}}$, the output state of the OPA amplifier, is identical, in the first order of the small parameter g, to the output of the cloner transformation expressed by Eq. (1). Furthermore, and more generally by using the analog of the isomorphism discussed above we find that the amplification process $U_{AA'}$ in each order of the decomposition into the parameter g corresponds to the $N \rightarrow M$ cloning process, that is M (where $M \geq N$) output particles are detected over the C mode, k_1. Correspondingly, $M - N$ particles are detected over the output AC mode, k_2. Indeed the *optimum cloning* output state determined by the theory of the *quantum-injected* OPA is found [12,16,17]:

$$|\Psi_N\rangle_M = \sum_{m=0}^{M-N} (-1)^m P_N^M \begin{pmatrix} |M-m\rangle_{1h}|m\rangle_{1v} \\ |m\rangle_{2h}|M-N-m\rangle_{2v} \end{pmatrix} \tag{2}$$

where $P_N^M \equiv P_N^M(m) = \left[\binom{M-m}{N} / \binom{M+1}{N+1}\right]^{1/2}$ is a normalization constant. The result given by Eq. (2) agrees exactly with the expression evaluated by a general quantum analysis of the UOQCM and implies the *optimal cloning fidelity* to be $F = (NM + M + N)/(MN + 2M)$ [3].

A necessary common property of the UOQCM and U-NOT systems is their *universality* (U), that is, implying the same "quantum efficiency" (QE) of the apparatus for the input qubits spanning the entire Bloch sphere. In our experiment these qubits are assumed to represent states of polarization ($\vec{\pi}$), and QE is expressed by the OPA parametric "gain" g. Let us investigate the "microscopic" side of the universality property by first outlining the theory of the OPA in *entangled configuration* and making reference to Fig. 3 and to Ref. [12].

By virtue of the U-condition it is convenient to cast the interaction Hamiltonian in the following form:

$$\hat{H}_{\text{int}} = ih\chi(\hat{a}_{\Psi}^{\dagger}\hat{b}_{\Psi\perp}^{\dagger} - \hat{a}_{\Psi\perp}^{\dagger}\hat{b}_{\Psi}^{\dagger}) + h.c. \tag{3}$$

where the new field operators $\hat{a}$ and $\hat{b}$ act on the C and AC modes, respectively. Assume the input single photon, $N = 1$, in the mode k_1 to have a polarization Ψ. We will describe this polarization state as $\hat{a}_{\Psi}^{\dagger}|0, 0\rangle_{k_1} = |1, 0\rangle_{k_1}$ where the state $|m, n\rangle_{k_1}$ represents a state with m photons on the mode k_1 having the polarization Ψ, while n photons have the polarization $\Psi^{\perp}$ on the same mode. Initially there are no excitations in the mode k_2, the input state is then $|1, 0\rangle_{k_1}|0, 0\rangle_{k_2}$ and evolves according to the Hamiltonian in Eq. (3):

$$U_{AA'}|1, 0\rangle_{k_1}|0, 0\rangle_{k_2} \simeq |1, 0\rangle_{k_1}|0, 0\rangle_{k_2} + g(\sqrt{2}|2, 0\rangle_{k_1}|0, 1\rangle_{k_2} - |1, 1\rangle_{k_1}|1, 0\rangle_{k_2})(-2) \tag{4}$$

where $g = \chi t$ is the gain of the parametric amplifier. The approximation for the state vector describing the two modes at times $t > 0$ is sufficient in all cases in which the coupling value is small, as in our experiment: $g \sim 0.11$. The two addenda in Eq. (4), corresponding to the first two terms of the general sum given by Eq. (2), represent respectively the process when the input photon in mode k_1 did not interact in the nonlinear medium, followed by the first-order amplification process in the OPA. Here the state

$|2, 0\rangle_{k_1}$ describing two photons of the mode k_1 in the polarization state Ψ corresponds to the state $|\Psi\Psi\rangle$. This state vector describes the cloning of the original photon. The vector $|0, 1\rangle_{k_2}$ describes the state of mode k_2 with a single photon in with the polarization $\Psi^{\perp}$. This state vector represents the *flipped* version of the input. To see that the stimulated emission is responsible for creation of the flipped qubit, let us compare the state (4) with the output of the OPA when the vacuum is injected into the nonlinear crystal. In this case, we obtain to the same order of approximation

$$U_{AA'}|0, 0\rangle_{k_1}|0, 0\rangle_{k_2} \simeq |0, 0\rangle_{k_1}|0, 0\rangle_{k_2} + g(|1, 0\rangle_{k_1}|0, 1\rangle_{k_2} - |0, 1\rangle_{k_1}|1, 0\rangle_{k_2}) \qquad (5)$$

The two-photon condition on the C mode k_1 is described by the state vectors in the right-side of Eq. (5) $|2, 0\rangle_{k_1}$ and $|1, 1\rangle_{k_1}$, which do appear with different amplitudes corresponding to the probability ratio (signal-to-noise ratio) $R = 2$. Likewise, the *flipping qubit* condition on the AC mode k_2 is described by the state vector $|0, 1\rangle_{k_2}$, which appears with different amplitudes on the right-hand sides of Eqs (4) and (6) and is realized with signal-to-noise ratio $R^* = 2$. Precisely, R is the probability ratio of detecting on mode k_1, $M = 2$ particles with the same polarization ($\vec{\pi}$) against detecting two particles with different $\vec{\pi}$ on the same mode. On the other hand, R^* is the probability ratio of detecting on mode k_2, $M - N = 1$ *flipped* particle contributed by the cloning process against the one contributed by noise. The signal-to-noise ratios R and R^* were indeed the quantities directly measured by the present experiment, respectively on the output modes k_1 and k_2. As we shall see, by this result the values of the *fidelities* F and F^* corresponding to the universal cloning and to the NOT-gate were easily determined.

Universality. In spite of the microscopic analysis just given, we should note that in the present context the *universality* property is indeed a *macroscopic* classical feature of the OPA device. As a consequence, it can be tested equally well either by injection of *classical*, for example, *coherent* (Glauber) fields, or of *quantum* states of radiation, for example, single-photon Fock states. We report here the ones obtained by injection of an attenuated *coherent* laser field with wavelength (wl) $\lambda = 795$ nm using the set-up shown in Fig. 1. The *universality* condition is demonstrated by the plots of Fig. 2 showing the amplification pulses detected by D_2' on the OPA output mode k_2 (AC channel). Each plot

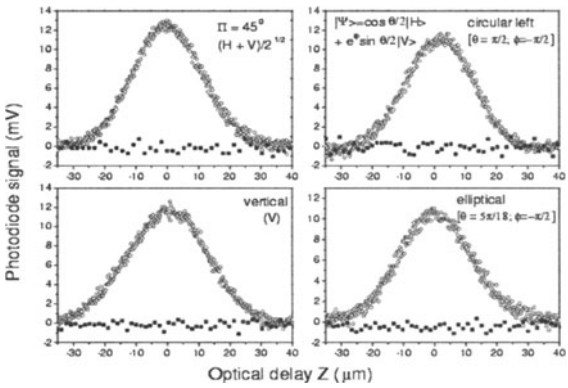

Figure 2. Experimental verification of the universality of the OPA system by injection of polarization $\vec{\pi}$-*qubits* represented by some significant points on the Bloch sphere.

corresponds to a definite state of polarization ($\vec{\pi}$) of the field injected on k_1. We may check that, in spite of different input $\vec{\pi}$-states, the amplification curves are almost identical. Each coherent pulse injected on the mode k_1 was amplified into an average photon number $M \approx 5 \times 10^3$ on the output mode k_2. The demonstration of the universality property is implied by the insensitivity to the $\vec{\pi}$-rotation angles of the gain g of the *quantum-injected* OPA.

Optimality. Figure 3 shows the *self-injected* OPA apparatus that realized the UOQCM process. To perform the cloning experiment PBS_2^* has been removed. By virtue of the tested universality of the OPA amplification, we consider here the OPA injection by a single photon in just one $\vec{\pi}$-state, for example, in the horizontal one $|H\rangle$. The measurement of R was carried out by a four-coincidence technique, involving all $D's$ of the apparatus, and by suitable changes of the settings of the $\vec{\pi}$-filtering devices on the C channel. By the value of the signal-to-noise ratio $R = 1.65 \pm 0.05$ determined on the basis of the data shown in Fig. 4, and by the theoretical results given by Eqs (4) and (5), the value of the UOQCM *fidelity* was found to be

$$F = \langle\Phi|\langle\Phi|\rho_{\text{out}}|\Phi\rangle|\Phi\rangle = \frac{2R+1}{2R+2} = 0.810 \pm 0.008$$
$$F_{\text{th}} = \frac{5}{6} = 0.833 \tag{6}$$

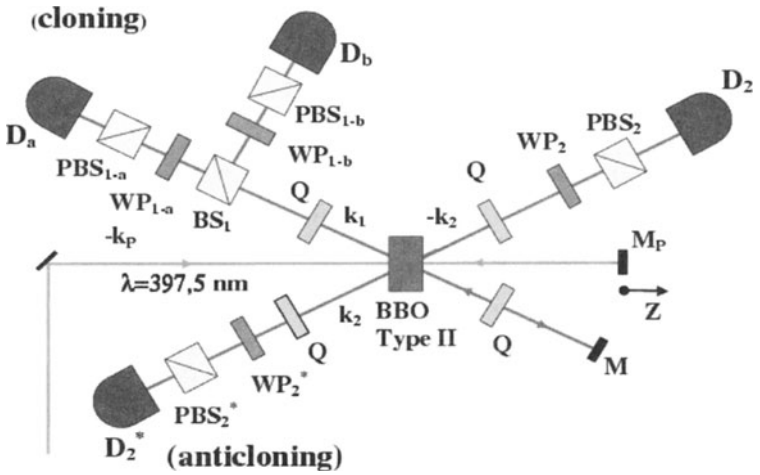

Figure 3. Schematic diagram of the set-up used to demonstrate the UOQCM and the U-NOT gate. A single photon pair with wavelength $\lambda = 795$ nm, was emitted by the SPDC process in a BBO towards the right side of the figure. One of the particles was detected, after polarization $\vec{\pi}$-filtering by D_2, and provided the *trigger* signal, that is, the *signature* of the injection event. The twin particle, back reflected by the mirror M with $\vec{\pi} = \mathbf{h}$, provided the $N = \mathbf{1}$ *quantum injection* into the OPA. All detectors D were SPCM-AQR14. Equal interference filters with bandwidth $\Delta\lambda = 6$ nm were placed in front of all $D's$. Micrometric adjustments of the coordinate **Z** of the UV mirror M_p ensured the time superposition in the NL crystal of the UV pump pulse and of the single photon pulse injected via back reflection by the mirror M.

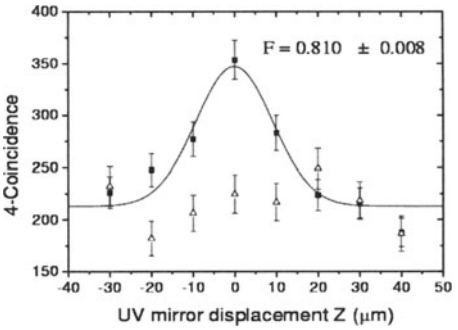

Figure 4. Demonstration of the UOQCM realized by the cloning (C) output channel, k_1.

An $N \simeq 1, M \simeq 2$ cloning experiment with OPA injection provided by an attenuated coherent pulsed laser field has been performed very recently by A. Lamas-Linares *et al.* [19], with the fidelity corresponding to different input $\vec{\pi}$-states equal to 0.80, 0.81, 0.80.

The set-up in Fig. 3 has also been used to perform U-NOT experiment. The only difference with the cloning experiment consists of the different measurement devices coupled to the output C and AC channels. Here the C channel, k_1, is simply coupled by a *normal* beam splitter (BS) to the detectors D_a and D_b: indeed a coincidence event involving these is the *signature* for a *cloning* event. The AC channel k_2 is coupled to a $\vec{\pi}$-analyzer consisting of the set $(PBS_2^* + WP_2^* + D_2^*)$. The signal-to-noise ratio determined by the four-coincidence data shown in Fig. 5 was $R^* = 1.69 + 0.06$ leading to the related value of the U-NOT *fidelity*:

$$F^* = \langle \Phi^\perp | \rho_{\text{out}} | \Phi^\perp \rangle = \frac{R^*}{(R^* + 1)} = 0.630 \pm 0.008 \tag{7}$$

$$F_{\text{th}}^* = \frac{2}{3} = 0.666$$

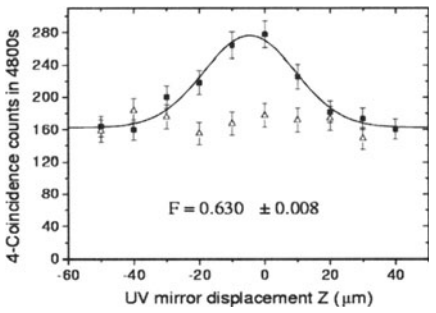

Figure 5. Demonstration of the U-NOT gate realized by the anticloning (AC) output channel, k_2.

As a concluding remark, it is well known that a method for flipping qubits alternative to the U-NOT gate consists in manufacturing the orthogonal qubits on the basis of the result of the measurement on the input qubits. The fidelity F^* of the two alternative methods is the same [9]. However, in the U-NOT gate the information encoded in the input qubit is not lost in the irreversible state reduction implied by the measurement. It is just redistributed into several qubits at the output. Since this redistribution of information is governed by a unitary transformation, the process is in principle reversible, which is definitely not true in the case of measurement-based flipping operation. We also want to stress that, to the best of our knowledge, the present U-NOT experiment is the first systematic attempt to realize an anti-unitary gate. Obviously, the fidelity of the gate is strictly determined by the structure of quantum mechanics.

A remarkable, somewhat intriguing aspect of the present work is that both the quantum cloning and the U-NOT gate are realized by the *same* physical apparatus, by the same unitary transformation, and correspondingly by the same quantum logic network [4]. To the best of our knowledge it is not well understood yet why these two processes are so closely related.

In summary the adopted OPA apparatus is an ideal system to demonstrate the relevant features of quantum cloning. It also establishes an interesting connection between the technical *engineering* of parametric amplifiers and abstract quantum measurement theory. Indeed, following this parallelism, it is found that the intrinsic noise due to the injected vacuum field into *any* universal OPA device is in exact correspondence with, and must be interpreted as, the amount of quantum fluctuations that determines the upper bounds to the *fidelity* determined by the CP-map structure of quantum mechanics [8].

Acknowledgements

We are indebted to V. Buzek, S. Popescur and C. Simon for very enlightening discussions and suggestions. This work has been supported by the FET European Network on Quantum Information and Communication (Contract IST-2000-29681: ATESIT) and by INFM (Contract PRA-CLON-02).

REFERENCES

[1] J. Preskill, Lecture Notes on Quantum Computation, http://www.theory.caltech.edu/people/ph229/#lecture.
[2] A. S. Holevo, *Probabilistic and Statistical Aspects of Quantum Theory* (Amsterdam, North-Holland, 1982)
[3] S. Massar and S. Popescu, *Phys. Rev. Lett.* **74**, 1259 (1995). N. Gisin and S. Popescu, *Phys. Rev. Lett.* **83**, 432 (1999).
[4] R. Derka, V. Buzek, and A. Ekert, *Phys. Rev. Lett.* **80**, 1571 (1998).
[5] W. K. Wootters and W.K. Zurek, *Nature* (London) **299**, 802 (1982).
[6] N. Herbert, *Found. of Phys.* **12**, 1171 (1982). L. Mandel, *Nature* (London), **304**, 188 (1983).
[7] N. Gisin, *Phys. Lett. A*, **259** (1999).
[8] C. Simon, V. Buzek, and N. Gisin, *Phys. Rev. Lett.* **87**, 170405 (2001).
[9] V. Buzek, M. Hillery, and R. F. Werner, *Phys. Rev.* A **60**, R2626 (1999).
[10] A. Peres, *Quantum Theory: Concepts and Methods* (Dordrecht, Kluwer, 1993).
[11] A. Alber *et al. Quantum Information: An Introduction to Basic Theoretical Concepts and Experiments*, Springer Tracts in Modern Physics Vol. 173 (Berlin, Springer-Verlag, 2001).
[12] F. De Martini, *Phys. Rev. Lett.* **81**, 2842 (1998).

[13] V. Buzek and M. Hillery, *Phys. Rev.* A **54**, 1855 (1996).
[14] N. Gisin and S. Massar, *Phys. Rev. Lett.* **79**, 2153 (1997); D. Bruss, A. Ekert, and C. Macchiavello, *Phys. Rev. Lett.* **81**, 2598 (1998).
[15] R. F. Werner, *Phys. Rev.* A **58**, 1827 (1998).
[16] C. Simon, G. Weihs, and A. Zeilinger, *Phys. Rev. Lett.* **84**, 2993 (2000).
[17] F. De Martini, V. Mussi, and F. Bovino, *Opt. Comm.* **179**, 581 (2000).
[18] F. De Martini, G. Di Giuseppe, and S. Padua, *Phys. Rev. Lett.* **87**, 150401 (2001).
[19] A. Lamas-Linares, C. Simon, J. C. Howell, and D. Bouwmeester, *Science* **296**, 712–714 (2002).

NEW QUANTUM NANOSTRUCTURES

Boron-based metallic nanotubes and geometric phases in carbon nanocones

V. H. Crespi, P. Zhang, and P. E. Lammert
Department of Physics and Materials Research Institute, University Park, PA, 16802-6300, USA

Abstract: Several new metallic and semiconducting nanostructures may provide interesting substrates for observations involving quantum coherence. Boron-based nanotubes with beryllium atoms in the hexagonal faces should exhibit uniformly metallic properties with multiple conduction channels of disparate character. The apical dislocation in a carbon nanocone mixes the low-energy electronic states of a graphene sheet and produces a geometrically derived effective flux through the apex which suppresses the Aharonov–Bohm effect.

Keywords: Nanotube, Boron, Metallic, Cone, Graphene, Geometric phase

1. BORON-BASED NANOTUBES

We propose several new nanostructures with the potential to show interesting physics due to coherence of the wavefunction either along a tubular structure or around the apex of a conical structure. Within band theory, carbon nanotubes are metals semiconductors depending on the wrapping indices (n, m), which express the tube circumference in graphitic lattice coordinates [1–4]. Boron nitride tubes, in contrast, are uniformly large-gap ($\backsim$5 eV) semiconductors [2–4]. Other tubular sp^2 structures previously proposed include ordered alloys of boron, carbon, and nitrogen such as BC_3, BC_2N; related multi-layered structures have also been proposed [5]. We describe the theory of boron oxide and beryllium diboride nanotubes, systems that have unique electronic properties that are unattainable in the currently known systems. Both systems already exist in bulk form [6–8]. The energetic cost against curving them into tubes is less than that for carbon and boron nitride.

We use the *ab initio* pseudopotential method [9] in the local density approximation (LDA) to study the structural and electronic properties of these new classes of nanotubes. The energy cut-offs of the plane-wave expansions for B_2O and BeB_2 are 120 and 60

Quantum Computing and Quantum Bits in Mesoscopic Systems
Edited by Leggett *et al.*, Kluwer Academic/Plenum Publishers, 2004

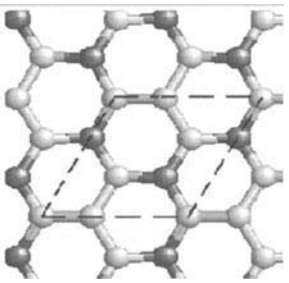

Figure 1. Structure of the lowest-energy allotrope of single-layer B_2O.

Rydbergs, respectively. Brillouin zone k-point sampling grids are either $8 \times 8 \times 1$ or $10 \times 6 \times 1$ for planar structures, depending on the shape of the unit cells. The density of the k-point sampling along the axial direction of the tubes is similar to that in the planar structures.

The destruction of sublattice symmetry in B_2O opens a bandgap, but one smaller than that in BN. The lowest energy allotrope of B_2O that we considered is a relatively high-symmetry structure with six atoms per unit cell and C_3 symmetry. Out-of-plane relaxation is signicant; the distance from the upper oxygen layer to the lower boron layer is about 1.5 atomic units. Within the local density approximation, the planar form of B_2O is a semiconductor with a valence band maximum at Γ. Due to C_3 symmetry, there is only one type each of B—B and B—O bonds; the B—B bonds have length 1.54 Å and the B—O bonds have length 1.47 Å. When wrapped into a nanotube, the relatively weak B—B bonds buckle substantially in preference to the formation of a more planar B—O structure. The curvature energy of a (3, 0) B_2O nanotube is very small (almost zero). For comparison, the curvature energies of carbon and boron nitride tubes of similar diameter are 0.15 and 0.1 eV/atom, respectively.

Single-layer planar B_2O has a nearly direct band gap of about 2.8 eV (since this is an LDA bandgap, it is likely underestimated). Curvature-induced hybridization reduces the bandgap in the (3, 0) nanotube to 1.63 eV, direct at Γ. This moderate (and at least in some cases, direct) band gap for B_2O nanotubes is potentially appealing for electronic or optical applications. The band gaps of corresponding carbon nanotubes are smaller and depend quite sensitively on both tube diameter and helical pitch, while the bandgaps of boron nitride nanotubes are larger, in the order of 5 eV.

Table 1. Structure properties of single-layer and bulk BeB_2 and MgB_2. Values in parentheses are for the bulk materials.

	Bond length B—B (Å)	*B-(Be, Mg) layer distance (Å)*	*Interlayer interaction (eV/atom)*
MgB_2	1.746 (1.742)	1.532 (1.711)	0.7
BeB_2	1.722 (1.662)	0.496 (1.398)	0.1

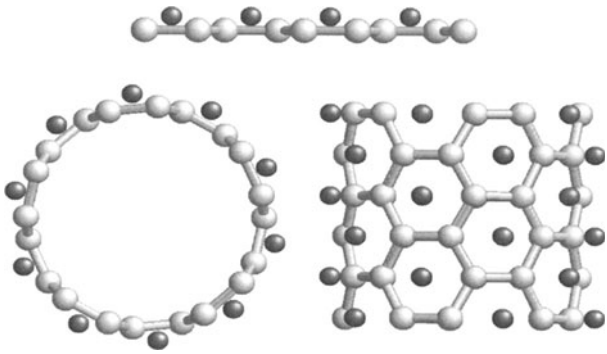

Figure 2. Structure of single-layer and tubular BeB_2.

In addition to these semiconducting B_2O tubes, boron might also form the basis for one-dimensional metallic structures based on the known planar material BeB_2. The exfoliation energy of bulk BeB_2 into a single-layer material is surprisingly low, only twice that in graphite, since upon exfoliation the Be atoms fall nearly coplanar with the boron planes. The Be atom drops to only 0.50 Å above the plane in single-layer BeB_2, as shown in Fig. 2. The B—B bonds elongate accordingly, from 1.66 Å to 1.72 Å, to accommodate the nearly coplanar Be atom. The related Mg compound does not show this distortion and therefore has a much higher exfoliation energy.

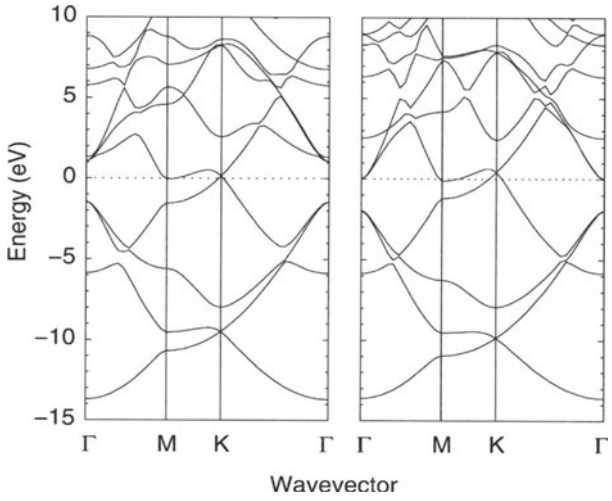

Figure 3. Band structures of single-layer BeB_2 in both the relaxed planar structure (left) and with Be atoms forced into the same plane as the boron atoms (right), which forces the conduction bands at Γ down to the Fermi level.

Figure 3 shows the band structure of relaxed single-layer BeB_2. Graphene is well-known for its unusual pointlike Fermi surface at the K points. BeB_2 retains this fascinating low-energy idiosyncracy and adds a second one: the π band at M drops below E_F and produces three new nearly point like Fermi circles. Straightforward band-folding arguments then suggest that *all* BeB_2 nanotubes are metallic. Does curvature-induced rehydridization in nanotubes remove these degeneracies? Curvature can actually enhance the metallicity: density functional calculations show that the (5, 5) and (8, 0) BeB_2 tubes are both metallic, with several bands crossing E_F.

The simple band-folding picture is complicated by curvature-induced shifts in the bandstructure. The single-layer structure with the Be atoms pressed into the boron plane can explain this effect. In the optimized structure, the p_{xy} and p_z bands of Be are nearly degenerate at Γ and lie about 1 eV above E_F. When the Be atoms are pushed into the B layer, the energy of the p_{xy} bands at Γ drops to E_F, as shown in Fig. 3. When the BeB_2 sheet curves into a tube, these same two bands also shift downwards and contribute to the uniform metallicity of the BeB_2 tubes. At larger diameters, the simple band-folding picture should reassert itself. The densities of states at the Fermi level for both (5, 5) and (8, 0) BeB_2 tubes are significantly higher than those for typical metallic carbon nanotubes. Note that distortions of the Be atoms could be softer than displacements of carbon in graphene sheets, so that the BeB_2 system may be more prone to Peierls-like distortions, although multiple bands crossing the Fermi energy at different incommensurate wavevectors could not be gapped by a single low-period static distortion. The possibility of a quasi-periodic Peierls-like distortion is interesting.

These two new classes of tubular structures promise to offer several interesting new properties. For example, B_2O possesses an intermediate and relatively uniform semiconducting bandgap. The single-layer BeB_2 family, in addition to being metallic (within a single-particle picture), offers the potential for large electron–phonon coupling matrix elements and relatively high density of states.

2. ELECTRONIC STRUCTURE OF GRAPHENE NANOCONES

Graphitic cones were discovered in 1997 [10]. The topological nature of the apical defect in a cone modifies the low-energy electronic structure, with remarkable consequences for electronic properties. Here we focus primarily on the single-pentagon cones. A semiconducting nanotube is a translational phase defect: the gap of a semiconducting carbon nanotube [11–13] arises from a frustration in the phase of the graphitic Fermi-level states as they pass around the tube circumference. A cone forms a rotational defect whose phase frustration constitutes a generalized topological phase. In contrast to a nanotube, the topological phase in a cone entwines the two Fermi points.

Starting from a continuum theory [14–16] of graphene, defects can be represented as pure gauge fields. In the continuum picture the pentagonal defect is shrunk to a point and the entire surface assumes graphene-like properties locally. The zero-energy graphene states can be labelled by the direction of a wavevector $\boldsymbol{K}$ and a sublattice index A or B (see Fig. 4). We can take $|\boldsymbol{K}_+, A\rangle$ and $|\boldsymbol{K}_+, B\rangle$ as a basis of the four-dimensional space, with $\boldsymbol{K}_- = -\boldsymbol{K}_+$. Under rotation counterclockwise about any hexagon center by 120° these states pick up simple phases: $R_6{}^2|\boldsymbol{K}A\rangle = \eta|\boldsymbol{K}A\rangle$, and $R_6{}^2|\boldsymbol{K}B\rangle = \overline{\eta}|\boldsymbol{K}B\rangle$, where $\eta = \exp(2\pi i/3)$.

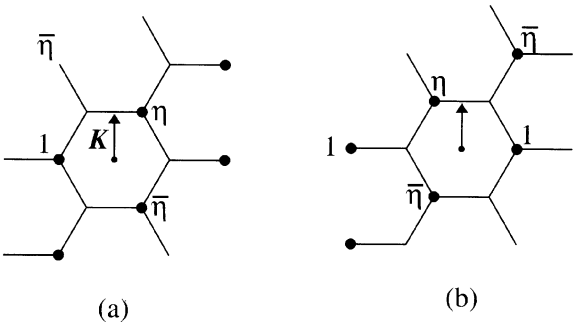

Figure 4. The phases of the Fermi-level states in graphene. Picking a direction $\boldsymbol{K}$ pointing from the center of a hexagon to the middle of one side, we assign amplitudes as shown, where $\eta = \exp(2\pi i/3)$. If (a) the nonzero amplitudes are on the right-hand atoms of bonds cut by $\boldsymbol{K}$, the state is $|\boldsymbol{K}A\rangle$; if (b) on the left-hand atoms $|\boldsymbol{K}B\rangle$. There are only two distinct $\boldsymbol{K}$.

$\boldsymbol{K}$ labels only the orientation of the amplitude pattern; momentum is not a good quantum number in cones. Low-energy states consist of slowly varying envelope functions multiplying these four patterns, written as a four-component envelope wavefunction

$$\Psi(x) = \begin{pmatrix} \psi_A \\ \psi_B \end{pmatrix}, \qquad \psi_{A,B}(x) = \begin{pmatrix} \psi_{A,B+} \\ \psi_{A,B-} \end{pmatrix} \tag{1}$$

where the $\pm$ subscripts refer to $\boldsymbol{K}_+$ and $\boldsymbol{K}_-$. A *globally consistent* choice of $\boldsymbol{K}_+$, $\boldsymbol{K}_-$, A, B is required.

To avoid complicating distractions, we first consider the Hamiltonian of a simple graphene wherein crystal momentum is a good quantum number and we can work with just the $\boldsymbol{K}_+$ components. The Hamiltonian is [14,16]

$$H_0 = -iv_F(\sigma_1\partial_x + \sigma_2\partial_y) = -iv_F\boldsymbol{\sigma}\cdot\boldsymbol{\partial} \tag{2}$$

The σ values are Pauli spin matrices operating in the A/B indices; A is 'up,' B is 'down,' and the x axis is along $\boldsymbol{K}_+$. The $\boldsymbol{K}_-$ components of the wavefunction have a similar Hamiltonian, but with x and y axes rotated through 180 . If the $|\boldsymbol{K}_-, A\rangle$ and $|\boldsymbol{K}_-, B\rangle$ patterns are multiplied by i and $-i$ respectively, thus inducing a compensatory change in the corresponding components of the spinor wavefunction ψ, the Hamiltonian in Eq. (2) acts on the $\boldsymbol{K}_+$ and $\boldsymbol{K}_-$ pieces in precisely the same fashion, using the $\boldsymbol{K}_+$ coordinate axes. This is an example of a frame rotation.

Multiply connected topologies require gauging of the symmetries in Eq. (2): that is, the familiar electromagnetic $U(1)_{\text{em}}$ symmetry, an $SU(2)_K$ symmetry operating on the $\pm$ indices, and the $SO(2)_{\text{spin}}$ symmetry. We will write the Pauli matrices acting on the $\pm$ indices as τ_μ. The three gauge fields yield a Hamiltonian:

$$H = -iv_F\boldsymbol{\sigma}\cdot\left(\boldsymbol{\partial} - ie\boldsymbol{A} - \frac{i}{2}\sigma_3\boldsymbol{\omega} - i\boldsymbol{b}^\mu\tau_\mu\right) \tag{3}$$

Details of this derivation are available elsewhere [17].

Consider a loop encircling a pentagonal disclination counterclockwise when viewed from above. We will use the Dirac notation to indicate components (in A, B or $\pm$) of the wavefunction *at a given point* along the path. The holonomy associated with a disclination is a rotation by the deficit angle of the disclination. Suppressing the A/B labels for clarity, we write the basis vectors at the beginning of the loop by $|1\rangle$ and $|2\rangle$. These take a slightly unfamiliar form

$$|1\rangle = |\boldsymbol{K}_+\rangle, \quad |2\rangle = \exp\left(-\frac{i\pi}{2}\sigma_3\right)|\boldsymbol{K}_-\rangle \tag{4}$$

since we have rotated the frame for $\boldsymbol{K}_-$. Using the phase factors for the action of 120 rotations, parallel transport on $|1\rangle$ and $|2\rangle$ is

$$|1\rangle \to R_6|\boldsymbol{K}_+\rangle = e^{-2\pi i\sigma_3/3}|\boldsymbol{K}_-\rangle = e^{-2\pi i\sigma_3/12}|2\rangle \tag{5}$$

and

$$|2\rangle = \exp\left(-\frac{i\pi}{2}\sigma_3\right)|\boldsymbol{K}_-\rangle \to -\exp\left(-\frac{2\pi i}{12}\sigma_3\right)|1\rangle \tag{6}$$

The holonomy associated to a pentagonal disclination can then be written as

$$T(1) = \exp\left[2\pi i\left(-\frac{\sigma_3}{12} - \frac{\tau_2}{4}\right)\right] \tag{7}$$

This holonomy measures the failure of Fermi-level states naively continued around a non-contractible loop to match up with themselves upon closing the loop. Since the complete wavefunction (i.e. the envelope times the Fermi-level pattern) must be continuous, this requires an inconvenient discontinuity in the envelope wavefunction. The gauge fields introduced for the wave equation of the envelope Ψ remove this restriction so that Ψ becomes continuous again, just as the vector potential does for an electron on a flux-threaded ring.

Turning attention to the eigenstates on a cone in this continuum picture, the Hilbert space can be decomposed into partial waves in the usual way ($\mathcal{H} = \bigoplus_j \mathcal{H}_j$) so that a general spinor decomposes into

$$\psi(r,\phi) = \sum_j \chi^{(j)}(r)e^{ij\phi} \tag{8}$$

where the Hamiltonian is $H = \sum_j h^{(j)}$. The total angular momentum takes on all half integer values, $j = \ldots, -3/2, -1/2, 1/2, \ldots$. The radial Hamiltonians take the form

$$h_\nu = v_F\begin{pmatrix} 0 & \partial_r + \left(\nu + \frac{1}{2}\right)\frac{1}{r} \\ -\partial_r + \left(\nu - \frac{1}{2}\right)\frac{1}{r} & 0 \end{pmatrix} \tag{9}$$

The value of ν depends upon j and whether one is in graphene or the single-pentagon cone:

$$\nu = \begin{cases} j + \dfrac{\Phi}{\Phi_0}, & \text{flat;} \\ \dfrac{6}{5}\left(j + \dfrac{\Phi}{\Phi_0} + \dfrac{\tau_2}{4}\right), & \text{pentagon.} \end{cases} \tag{10}$$

The flat sheet (no disclination) provides a control. The magnetic flux Φ through the disclination allows one to compute the magnetoconductance, at least in the case of a flux restricted to the immediate vicinity of the apex. $\Phi_0 = h/e$ is the normal flux quantum.

For brevity's sake we do not here consider the solutions to this partial-wave Hamiltonian (they are ordinary Bessel functions with some special boundary conditions) but instead consider the magnetotransport around a graphene annulus that encompasssed a disclination before the center of the cone was removed. The elastic scattering length, ℓ_p, in single-wall nanotubes [18] is believed to range up to many microns and the phase coherence length (ℓ_ϕ) at room temperature seems also to be long [19]. A graphitic ring would be expected to have a somewhat reduced ℓ_p, due to rough edges, but ℓ_ϕ is likely comparable to that in the tube. A mesoscopic normal metal ring in a perpendicular magnetic field exhibits oscillations as the flux through the ring is varied [20]. The longest period of oscillation is one normal flux quantum $\Phi_0 = h/e$, corresponding essentially to the Aharonov–Bohm effect, and first observed in this context in the mid-1980s [21].

Equation (10) is valid for a ring. For a flat gaphene sheet the Hamiltonian is $SU(2)_K$ invariant, so that the two Fermi points produce two independent branches of excitations that respond identically to a magnetic flux, their individual responses being just as in an ordinary metal. The total response therefore also has fundamental period Φ_0. In an $n_\Omega = 1$ ring, on the other hand, *the Φ_0 component of the oscillations is completely extinguished.* From Eq. (10), we see that the $\tau_2 = +1$ ($\tau_2 = -1$) branch behaves as though it were subjected to a flux of $\Phi = \Phi_0/4$ ($\Phi = -\Phi_0/4$). This relative shift of the magnetoconductance curves results in a complete cancellation of the Φ_0 periodic component. Cones with intact apices will also show novel magnetic phenomena, including the prospect for radial charge density waves. Structures with multiple disclinations promise to exhibit additional interesting physics, since a translation does not commute with the transformation in $\pm K$.

REFERENCES

[1] S. Iijima, *Nature* **354**, 56 (1991).

[2] A. Rubio, J. L. Corkill, and M. L. Cohen, *Phys. Rev.* B **49**, 5081 (1994).

[3] X. Blase, A. Rubio, S. G. Louie, and M. L. Cohen, *Europhys. Lett.* **28**, 335 (1994).

[4] N. G. Chopra, R. L. Luyken, K. Cherrey, V. H. Crespi, M. L. Cohen, S. G. Louie, and A. Zettl, *Science* **269**, 966 (1995).

[5] Z. Weng-Sieh, K. Cherrey, N. G. Chopra, X. Blase, Y. Miyamoto, A. Rubio, M. L. Cohen, S. G. Louie, A. Zettl, and R. Gronsky, *Phys. Rev.* B **51**, 11229 (1995); L. A. Chernozatonskii, *JETP Lett.* **74**, 335 (2001); I. Boustani, A. Quandt, E. Hernández and A. Rubio, *J. Chem. Phys.* **110**, 3176 (1999); A. Quandt, A. Y. Liu, and I. Boustani, *Phys. Rev.* B **64**, 125422 (2001).

[6] H. T. Hall and L. A. Compton, *Inorg. Chem.* **4**, 1213 (1965).

[7] M. P. Grumbach, O. F. Sankey, and P. F. McMillan, *Phys. Rev.* B **52**, 15807 (1995).

[8] Diamond-like forms have also been observed for B_2O. T. Endo, T. Sato, and M. Shimada, *J. Mater. Sci. Lett.* **6**, 683 (1987). BeB_2: L. Y. Markovskii, Y. D. Kondrashev, and G. V. Kaputovskais, *J. Gen. Chem. USSR* **25**, 1007 (1955); D. E. Sands, C. F. Cline, A. Zalkin, and C. L. Hoenig, *Acta Cryst.* **14**, 309 (1961); M. S. Borovikova, V. V. Fesenko, and J. Less, *Common. Metals* **117**, 287 (1986).
[9] J. Ihm, A. Zunger, and M. L. Cohen, *J. Phys. C* **12**, 4409 (1979).
[10] A. Krishnan, E. Dujardin, M. M. J. Treacy, J. Hugdahl, S. Lynum, and T. W. Ebbesen, *Nature* **388**, 451 (1997).
[11] R. Saito, M. Fujita, G. Dresselhaus, and M. S. Dresselhaus, *Appl. Phys. Lett.* **60**, 2204 (1992).
[12] N. Hamada, S. Sawada, and A. Oshiyama, *Phys. Rev. Lett.* **68**, 1579 (1992).
[13] B. I. Dunlap and C. T. White, *Phys. Rev. Lett.* **68**, 631 (1992).
[14] D. P. DiVincenzo and E. J. Mele, *Phys. Rev.* B **29**, 1685 (1983).
[15] C. L. Kane and E. J. Mele, *Phys. Rev. Lett.* **78**, 1932 (1997).
[16] P. E. Lammert and V. H. Crespi, *Phys. Rev.* B **61**, 7308 (2000). Beware a different convention regarding A/B labelling.
[17] P. E. Lammert and V. H. Crespi, *Phys. Rev. Lett.* **85**, 5190 (2000).
[18] C. T. White and T. N. Todorov, *Nature* **393**, 240 (1998).
[19] S. J. Tans, M. H. Devoret, H. Dai, A. Thess, R. E. Smalley, L. J. Geerligs, and C. Dekker, *Nature* **386**, 474 (1997).
[20] A. G. Aronov and Yu. V. Sharvin, *Rev. Mod. Phys.* **59**, 755 (1987).
[21] R. A. Webb, S. Washburn, C. P. Umbach, and R. B. Laibowitz, *Phys. Rev. Lett.* **54**, 2696 (1985).

TRANSPORT INVESTIGATIONS OF CHEMICAL NANOSTRUCTURES

W. Liang, M. Bockrath, and H. Park[a]
Department of Chemistry and Chemical Biology, Harvard University, Cambridge, MA 02138, USA

Abstract: In this chapter, fabrications and characterizations of nanometer-sized transistors that incorporate individual molecules and carbon nanotubes will be described. In the first part of the presentation, we describe transport measurements of single-nanotube transistors that allow the characterization of electronic shell filling and exchange coupling as well as Fabry–Perot interference between traveling electron waves in metallic nanotubes. In the second part of the chapter, we describe fabrication and characterization of single-molecule transistors incorporating individual inorganic molecules. Transport investigation provides detailed insight into the electron motion through a molecule, as demonstrated by the observation of Kondo resonance and spin filling in a di-vanadium molecule.

Over the past five years, single-electron transistors of individual chemical nanostructures, such as molecules [1, 2], nanocrystals [3–5], and single-walled carbon nanotubes (SWNTs) [6–12], have emerged as a powerful experimental probe of the electronic motion through these structures. When an individual nanostructure is attached to metallic electrodes via tunnel barriers, electron transport is dominated by single-electron charging and energy-level quantization [13]. As the coupling to the electrodes increases, however, higher-order tunneling and correlated electron motion give rise to new phenomena, including inelastic cotunneling and Kondo resonance [2, 10, 14–19]. Our understanding of electron transport through chemical nanostructures is still in its infancy, however, and much work needs to be done to develop detailed insight into this problem.

In this chapter, we discuss our recent studies on the fabrication and characterization of nanometer-sized transistors that incorporate individual molecules and carbon nanotubes [2, 12, 19]. In the first part of the presentation, we discuss a systematic transport study of metallic nanotube quantum dots with conductance ranging from 0 to $4e^2/h$ (the value of e^2/h is 38.8 μS or $(25.8\ \mathrm{k\Omega})^{-1}$), which enables a unified characterization of the electronic structure in metallic nanotubes, including single-electron charging, electronic shell filling

[a]E-mail: hpark@chemistry.harvard.edu

Quantum Computing and Quantum Bits in Mesoscopic Systems
Edited by Leggett *et al.*, Kluwer Academic/Plenum Publishers, 2004

and exchange couplings [19], and Fabry–Perot interference between traveling electron waves [12]. In the second part of the presentation, we describe the fabrication and characterization of single-molecule transistors incorporating individual inorganic clusters [2]. Molecules incorporating transition metal atoms provide powerful new probes for Kondo physics because the spin and orbital degrees of freedom can be controlled through well-defined chemistry [20, 21]. In the example presented here an individual di-vanadium molecule [20] serves as a spin impurity, and the Kondo resonance is tuned reversibly using the gate voltage to alter the charge and spin state of the molecule [2]. The resonance persists at temperatures up to 30 K and when the energy separation between the molecular state and the Fermi level of the metal exceeds 100 meV.

Isolated SWNTs were synthesized by chemical vapor deposition using a procedure reported previously [11, 12, 22]. Nanotubes with a diameter of ≤ 1 nm were located relative to alignment marks, and electrical leads were defined by electron-beam lithography by depositing a thin layer of chromium, followed by gold. Electrical characterization was performed as a function of bias voltage (V) and gate voltage (V_g). The degenerately doped silicon substrate acted as a gate electrode to modulate the charge density within the nanotubes. Figure 1 shows an example of differential conductance ($\partial I/\partial V$) plot as a function of V and V_g obtained from representative metallic nanotube devices. The nanotube devices typically exhibit a V_g-averaged linear-response conductance (G_{av}) that varies from 0.01 to 3.2 e^2/h depending on the contact resistance between nanotubes and metallic electrodes.

The qualitative characteristics of nanotube devices fall into three distinct categories depending on the value of G_{av}. The first category consists of nanotube devices with $G_{\mathrm{av}} \ll e^2/h$ where a SWNT makes tunnel contact to the metallic electrodes. Nanotube devices in this weak coupling regime exhibit diamond-shaped conductance-gap regions in the V–V_g plane characteristic of single-electron charging that can be understood well by the Coulomb blockade model. Nanotube devices in this regime have been extensively studied previously, providing experimental evidence for energy level quantization [7, 8] and Luttinger-liquid behavior [9].

The second category consists of nanotube devices with G_{av} approaching the theoretical maximum ($4e^2/h$) [12, 23]. In this strong coupling regime, the nanotube makes near-ohmic contact to the metallic electrodes, and transport measurements reveal a regular

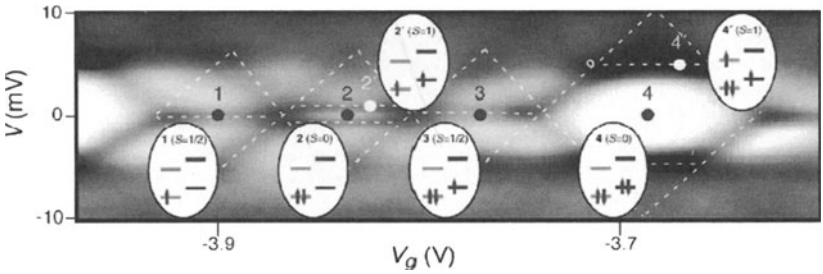

Figure 1. Plot of $\partial I/\partial V$ plots as a function of V and V_g for a nanotube device measured at $T = 1.5$ K. Here, the white color corresponds to 0, and the darkest color corresponds to 1.5 e^2/h. The sloping white dashed lines delineate conductance-gap regions. The electronic configurations are shown at the positions marked by numbered dots.

pattern of criss-crossing $\partial I/\partial V$ peaks and dips. This behavior originates from quantum interference between traveling electron waves that are multiply reflected by the nanotube–metal interface [12].

Finally, the third category consists of nanotube devices with $G_{av} \sim 1-2e^2/h$, as shown in Fig. 1, that represent a transition from the weak to strong coupling regimes. Inspection of Fig. 1 shows that the device characteristics in this intermediate coupling regime evolves smoothly as a function of G_{av} with several new transport features that do not appear in the weak or strong coupling regimes, including four-electron periodicity, the Kondo resonance, and inelastic cotunneling [19]. These features can be explained in a unified fashion using a shell-filling model that incorporates the band structure of metallic SWNTs as well as the exchange and Coulomb interactions between electrons [24–27]. The analysis of the experimental data allows the quantitative determination of all the Hartree–Fock parameters that completely determine the electronic structure of metallic nanotubes. Values of the energy parameters obtained from this analysis compare favorably with the theoretically predicted exchange and Coulomb energies for (10,10) armchair nanotubes [19, 24].

We now turn our discussion to the fabrication and characterization of single-molecule transistors where an individual molecule attached to two electrodes serves as an active element [2]. Devices were prepared by an extension of the methods previously employed in constructing single-C_{60} [1] and single-nanocrystal transistors [5]. Using electron-beam lithography, a narrow gold bridge was fabricated on an aluminum pad with a ~3 nm oxide layer serving as a gate electrode [28]. The electromigration-induced break-junction technique [1, 5] was then used to create two closely spaced gold electrodes. Depositing a dilute methanol solution of di-vanadium (V_2) molecules ([(*N*,*N*′,*N*″-trimethyl-1,4,7-triazacyclononane)$_2$V$_2$(CN)$_4$(μ-C$_4$N$_4$)] [20] onto the gold bridge completes the fabrication of single-V_2 transistors.

Figure 2 shows plots of $\partial I/\partial V$ as a function of V and V_g for a representative single-V_2 transistor [2]. Two distinct characteristics, which are shared by all single-V_2 transistors studied to date, are evident in Fig. 2. The device displays two conductance-gap regions, I and II, bounded by two broad $\partial I/\partial V$ peaks that slope linearly as a function of V_g. These peaks cross at $V_g = V_c$, at which point the conductance gaps vanish. This behavior is a clear signature of the Coulomb blockade phenomenon. The device also exhibits a sharp zero-bias $\partial I/\partial V$ peak in region I, signifying the occurrence of a Kondo resonance, while it is clearly absent in region II. Most notably, the Kondo resonance in region I generally persists up to $T \geq 10$ K.

These observations can be understood in a straightforward fashion by considering the spin states of the V_2 molecule. In the neutral V_2 molecule, both vanadium atoms exist in a +4 oxidation state, each possessing one valence *d* electron [20]. Previous bulk measurements show that in organic solvents three oxidation states of the V_2 molecule are accessible [20]: neutral V_2^0, positive V_2^{1+}, and negative V_2^{1-}. Magnetic measurements indicate that the ground state of V_2^0 is a spin-singlet ($S = 0$) due to the antiferromagnetic coupling between vanadium centers, while that of V_2^{1-} is a spin-quadruplet ($S = 3/2$) due to the resonant exchange of the added electron [20]. The ground state of V_2^{1+} is a spin-doublet ($S = 1/2$) since it possesses only one *d* electron. These results, combined with the transport data presented in Fig. 2, indicate then that the V_2^{1+} and V_2^0 species are responsible for the device behavior in regions I and II, respectively. Moreover the detailed analysis of transport data, such as that shown in Fig. 2, indicate that the Kondo resonance persists at

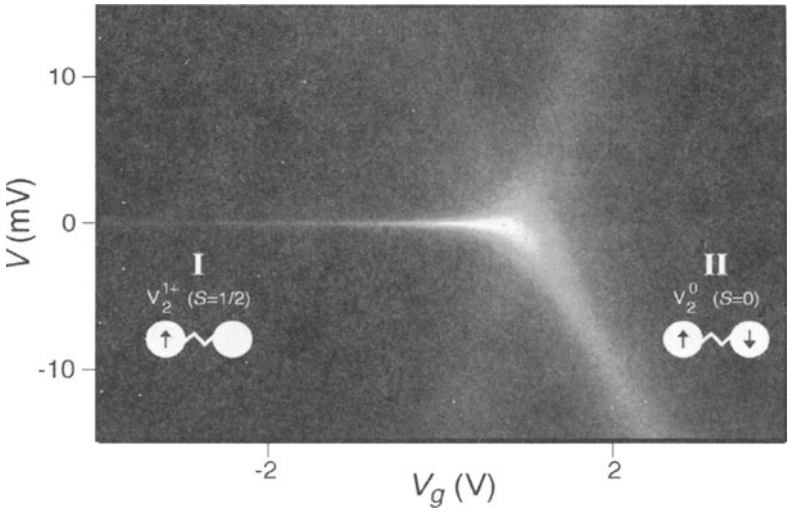

Figure 2. Plot of $\partial I/\partial V$ as a function of V and V_g obtained from a single-V_2 transistor measured at $T = 300$ mK. The $\partial I/\partial V$ values change from dark (0) to bright ($1.55\ e^2/h$). The labels, I and II, mark two conductance-gap regions, and the diagrams indicate the charge and spin states of the V_2 molecule in each region.

temperatures up to 30 K and when the energy separation between the molecular state and the Fermi level of the metal exceeds 100 meV.

This example clearly demonstrates that molecules can provide a new mesoscale system where critical parameters of Kondo physics, such as the spin and orbital degrees of freedom, are defined by chemical synthesis [2]. With the recent advances of synthetic methodology, the preparation of molecular clusters possessing adjustable magnetic properties is becoming feasible [21]. Future investigations of such species are expected to provide detailed insight into electron transport through a molecular system where the spin and orbital degeneracies are precisely controlled.

Acknowledgements

We gratefully acknowledge support from NSF, DARPA, the US Army, the Packard Foundation, the Sloan Foundation, and the Dreyfus Foundation.

REFERENCES

[1] H. Park, J. Park, A. K. L. Lim, E. H. Anderson, A. P. Alivisatos, and P. L. McEuen. Nano-mechanical oscillations in a single-C_{60} transistor. *Nature* **407**, 57–60 (2000).

[2] W. Liang, M. P. Shores, M. Bockrath, J. R. Long, and H. Park. Kondo resonance in a single-molecule transistor. *Nature* (2002) in press.

[3] D. C. Ralph, C. T. Black, and M. Tinkham. Gate-voltage studies of discrete electronic states in aluminum nanoparticles. *Phys. Rev. Lett.* **78**, 4087–4090 (1997).

[4] D. L. Klein, R. Roth, A. K. L. Lim, A. P. Alivisatos, and P. L. McEuen. A single-electron transistor made from a cadmium selenide nanocrystal. *Nature* **389**, 699–701 (1997).
[5] H. Park, A. K. L. Lim, A. P. Alivisatos, J. Park, and P. L. McEuen. Fabrication of metallic electrodes with nanometer separation by electromigration. *Appl. Phys. Lett.* **75**, 301–303 (1999).
[6] S. J. Tans, M. H. Devoret, H. Dai, A. Thess, R. E. Smalley, L. J. Geerligs, and C. Dekker. Individual single-wall carbon nanotubes as quantum wires. *Nature* **386**, 474–476 (1997).
[7] M. Bockrath, D. H. Cobden, P. L. McEuen, N. G. Chopra, A. Zettl, A. Thess, and R. E. Smalley. Single-electron transport in ropes of carbon nanotubes. *Science* **275**, 1922–1925 (1997).
[8] S. J. Tans, M. H. Devoret, R. J. A. Groeneveld, and C. Dekker. Electron–electron correlations in carbon nanotubes. *Nature* **394**, 761–764 (1998).
[9] M. Bockrath, D. H. Cobden, J. Lu, A. G. Rinzler, R. E. Smalley, L. Balents, and P. L. McEuen. Luttinger-liquid behaviour in carbon nanotubes. *Nature* **397**, 598–601 (1999).
[10] J. Nygard, D. H. Cobden, and P. E. Lindelof. Kondo physics in carbon nanotubes. *Nature* **408**, 342–346 (2000).
[11] M. Bockrath, W. Liang, D. Bozovic, J. H. Hafner, C. M. Lieber, M. Tinkham, and H. Park. Resonant electron scattering by defects in single-walled carbon nanotubes. *Science* **291**, 283–285 (2001).
[12] W. Liang, M. Bockrath, D. Bozovic, J. H. Hafner, M. Tinkham, and H. Park. Fabry–Perot interference in a nanotube electron waveguide. *Nature* **411**, 665–669 (2001).
[13] H. Grabert and M. H. Devoret, *Single Charge Tunneling* (New York, Plenum, 1992).
[14] D. Goldhaber-Gordon, H. Shtrikman, D. Mahalu, D. Abusch-Magder, U. Meirav, and M. A. Kastner. Kondo effect in a single-electron transistor. *Nature* **391**, 156–159 (1998).
[15] S. M. Cronenwett, T. H. Oosterkamp, and L. P. Kouwenhoven. A tunable Kondo effect in quantum dots. *Science* **281**, 540–544 (1998).
[16] D. Goldhaber-Gordon, J. Gores, M. A. Kastner, H. Shtrikman, D. Mahalu, and U. Meirav. From the Kondo regime to the mixed-valence regime in a single-electron transistor. *Phys. Rev. Lett.* **81**, 5225–5228 (1998).
[17] J. Schmid, J. Weis, K. Eberl, and K. v. Klitzing. Absence of odd–even parity behavior for Kondo resonances in quantum dots. *Phys. Rev. Lett.* **84**, 5824–5827 (2000).
[18] W. G. van der Wiel, S. D. Franceschi, T. Fujisawa, J. M. Elzerman, S. Tarucha, and L. P. Kouwenhoven. The Kondo effect in the unitary limit. *Science* **289**, 2105–2108 (2000).
[19] W. Liang, M. Bockrath, and H. Park. Shell filling and exchange coupling in metallic single-walled carbon nanotubes. *Phys. Rev. Lett.*, (2002) in press.
[20] M. P. Shores and J. R. Long. Tetracyanide-bridged divanadium complexes: Redox switching between strong antiferromagnetic and strong ferromagnetic coupling. *J. Am. Chem. Soc.* ASAP (2002).
[21] M. P. Shores, J. J. Sokol, and J. R. Long. Nickel(II)-molybdenum(III)-cyanide clusters: Synthesis and mangetic behavior of species incorporating [(Me3tacn}Mo(CN)3]. *J. Am. Chem. Soc.* ASAP (2002).
[22] J. H. Hafner, M. J. Bronikowski, B. R. Azamian, P. Nikolaev, A. G. Rinzler, D. T. Colbert, K. A. Smith, and R. E. Smalley. Catalytic growth of single-wall carbon nanotubes from metal particles. *Chem. Phys. Lett.* **296**, 195–202 (1998).
[23] C. T. White and T. N. Todorov. Carbon nanotubes as long ballistic conductors. *Nature* **393**, 240–242 (1998).
[24] Y. Oreg, K. Byczuk, and B. I. Halperin. Spin configurations of a carbon nanotube in a nonuniform external potential. *Phys. Rev. Lett.* **85**, 365–368 (2000).
[25] S. Tarucha, D. G. Austing, T. Honda, R. J. v. d. Hage, and L. P. Kouwenhoven. Shell filling and spin effects in a few electron quantum dot. *Phys. Rev. Lett.* **77**, 3613–3616 (1996).
[26] L. P. Kouwenhoven, T. H. Oosterkamp, M. W. S. Danoesastro, M. Eto, D. G. Austing, T. Honda, and S. Tarucha. Excitation spectra of circular few-electron quantum dots. *Science* **278**, 1788–1792 (1997).
[27] S. Tarucha, D. G. Austing, Y. Tokura, W. G. v. d. Wiel, and L. P. Kouwenhoven. Direct Coulomb and exchange interaction in artificial atoms. *Phys. Rev. Lett.* **84**, 2485–2488 (2000).
[28] A. Bachtold, P. Hadley, T. Nakanishi, and C. Dekker. Logic circuits with carbon nanotube transistors. *Science* **294**, 1317–1320 (2001).

LONG-RANGE COHERENCE IN BOSE–EINSTEIN CONDENSATES

F. S. Cataliotti
LENS, Dipartimento di Fisica, Università di Firenze, via Nello Carrara 1, I-50019, Sesto Fiorentino (FI), Italy

Abstract: We create a one-dimensional array of Josephson junctions by condensing ^{87}Rb atoms in the combined potential of an optical standing wave superimposed on a harmonic magnetic trap. The array realizes at the same time an atom interferometer, which allows monitoring coherence across the system and obtaining via some simple theoretical assumptions the most relevant parameters of the ground state. We can introduce the analogous of an external voltage across the junctions by non-adiabatically displacing the magnetic potential. In this way we have induced an oscillating atomic current related to coherent tunneling of the Bose–Einstein condensates through the optical barriers. The frequency of the oscillations is a direct measurement of the critical current allowed to flow through the junctions. By changing the height of the optical barriers we can externally control the critical current. The experimental results confirm the predictions of a one-dimensional theoretical treatment based on the Josephson current–phase relations. We have observed a disruption of the coherent atomic oscillations when the displacement is increased above a critical value. This is interpreted as a dynamical transition from a superfluid to an insulator state accompanied by a loss of long-range coherence across the array. The height of the optical barriers is now used to control the critical displacement. The experimental results are compared with the predictions of the same model used for the coherent oscillations underlining some crucial discrepancies.

Keywords: Bose–Einstein condensates, Josephson junctions, Superfluidity

1. INTRODUCTION

The coherent nature of Bose–Einstein condensates (BEC) was proven soon after the first experimental realization of a dilute alkali condensate using atom interferometry. In a pioneering experiment Ketterle and collaborators split a sodium condensate with a laser beam and observed spatial interference fringes recombining the two condensates [1]. Bragg diffraction from optical standing waves allowed the measurement of phase coherence across a BEC showing that the coherence length of a condensate is equal to its size [2]. The use of Bragg diffraction has also allowed the demonstration of other coherent effects like matter wave amplification [3], four-wave mixing [4], and super-radiant Raleigh scattering [5]. Loading BECs in one-dimensional optical lattices the group of Kasevich has demonstrated a mode-locked atom laser [6] and the possibility to obtain number squeezing [7]. In two- and

Quantum Computing and Quantum Bits in Mesoscopic Systems
Edited by Leggett *et al.*, Kluwer Academic/Plenum Publishers, 2004

three-dimensional optical lattices the group of Hänsch have explored phase coherence in the array [8] and observed the quantum phase transition known as Mott-insulator phase transition [9]. In our group we have produced condensates inside a one-dimensional optical lattice aligned horizontally to exploit long-range coherence effects in BEC-like superfluidity [10] and the DC Josephson effect in a one-dimensional array of neutral Josephson junctions [11]. In this chapter, I will describe some experiments performed in an array of Josephson junctions in various limits. In successive sections, I will report the method for the production and characterization of the array, based on atomic interferometry; small amplitude dipole oscillations in the array at zero temperature; and the large amplitude oscillations, which will be shown demonstrating a classical superfluid–insulator transition caused by a modulational instability.

2. ONE-DIMENSIONAL ARRAY OF BECS

The procedure for producing Bose–Einstein condensates of alkali atoms can be found in Ref. [1] together with references to the early works in the field of coherent atomic samples. In our experiment we load cold ^{87}Rb atoms in the $|F = 1, m_F = -1\rangle$ state from a double magneto-optical trap system into an Ioffe-type harmonic magnetic trap [12]. The trap is cylindrically symmetric with an axial frequency of $\omega_x/2\pi =$ 9 Hz and a radial frequency of $\omega_\perp/2\pi = 92$ Hz. We cool the atoms in this trap via rf-forced evaporation until they reach a temperature below 300 nK, just above the critical temperature for condensation, which is around 150 nK dependent on the number of atoms we load in the trap. At this stage of evaporation we suddenly switch on an optical standing wave formed by retroreflecting light from a laser blue detuned of ~3 nm with respect to the D1 transition at $\lambda = 795$ nm. The laser beam is aligned horizontally along the axis of the magnetic trap. The laser beam waist is much larger than the atomic cloud transverse size and does not produce any appreciable radial force forming, together with the magnetic potential, an array of disc-shaped traps. The potential is therefore $V = 1/2m(\omega_x^2 x^2 + \omega_\perp^2 r_\perp^2) + sE_R \cos^2(2\pi x/\lambda)$. The periodic optical potential is given in units s of the energy $E_R = h^2/2m\lambda^2$ gained by an atom (of mass m) absorbing one lattice photon. This energy corresponds to a temperature of ~170 nK. In our experiments we could vary the optical potential up to $s = 15$. When $s > 1$ the atoms are confined in an array of classically independent traps since the optical potential barriers are much higher than the thermal energy of the atoms. Indeed it is possible to "freeze" the degree of freedom associated with the motion along the axis and study condensation in this quasi-two-dimensional system [13]. After switching on the laser light we continue the evaporation ramp until the desired temperature is reached. This ensures that the atoms reach the equilibrium state in the combined trap. When we evaporate to well below the critical temperature, so that no thermal fraction is experimentally visible, we typically obtain ~200 condensates separated by a distance of $\lambda/2$, each containing ~1000 atoms. Due to the blue detuning of the laser beam the atoms are trapped in the nodes of the standing wave, reducing light scattering below 1 Hz.

When the height of the optical barriers is much larger than the condensate's chemical potential we are justified in describing the condensate as a sum of wavefunctions localized in each potential well

$$\Psi_0(\mathbf{r}) = \sum_{k=0,\pm 1\pm\cdots\pm k_M} \frac{\sqrt{2}}{g}\mu_k \left[1 - \frac{r_\perp^2}{R_{\perp k}^2}\right] \exp\left[-\frac{(x - k\lambda/2)^2}{2\sigma^2} + i\phi_k\right] \tag{1}$$

where $R_{\perp k}^2 = \sqrt{2\mu_k/m\omega_\perp^2}$ is the radial size of the kth condensate, g depends on the scattering length a through the relation $g = 4\pi\hbar^2 a/m$, while $\mu_k = 1/2\, m\omega_x^2 d^2(k_M^2 - k^2)$ plays the role of an effective k-dependent chemical potential. The value of k_M is fixed by the normalization condition $N = \sum N_k$ to

$$k_M^2 = \frac{2\hbar\bar{\omega}}{m\omega_x^2 d^2}\left(\frac{15}{8\sqrt{\pi}} N \frac{a}{a_{ho}} \frac{d}{\sigma}\right)^{2/5} \tag{2}$$

with $\bar{\omega} = (\omega_x \omega_\perp^2)^{1/3}$ the geometrical average of the magnetic frequencies, $a_{ho} = \sqrt{\hbar/m\bar{\omega}}$ is the corresponding oscillator length and a is the s-wave scattering length. From the above equations one also obtains the result $N_k = N_0(1 - k^2/k_M^2)$ with $N_0 = (15/16)N/k_M$. These equations generalize the well-known Thomas–Fermi results holding for magnetically trapped condensates [14] to include the effects of the optical lattice. This generalization is justified by the fact that the optical confinement along the optical lattice is much stronger than the magnetic potential; therefore it is more suitable to use a harmonic approximation for the wavefunction along the x-direction and a Thomas–Fermi approximation in the radial direction [15].

When the atoms are released from the combined trap they spread out and overlap producing an interferogram, which will depend on the relative phases ϕ_k of the individual condensates. Figure 1 show a typical image of the cloud taken after an expansion time $t_{\exp} = 29.5\,\text{ms}$, corresponding to a total number of atoms $N \sim 20\,000$ and to an optical potential $s = 5$. The image shows a clear structure with three interference peaks separated by $2h/m\lambda \cdot t_{\exp}$, that is, by the distance corresponding to the reciprocal of the lattice constant. I remark that, differently from the case of two separated condensates, interference fringes appear only if the initial configuration is coherent. In other words, since one single interference experiment with an array of condensates is equivalent to averaging a series of interference experiments with two condensates, an interference pattern will appear only in presence of a fixed relative phase between condensates belonging to consecutive wells. What is locking the phase difference across the array of BEC is tunneling through the optical barriers; in a classical picture no interference peaks

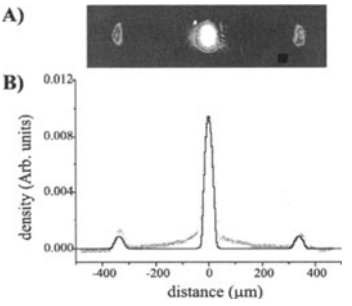

Figure 1. (A) Absorption image of the density distribution of the expanded array of condensates. (B) Experimental density profile (crosses) obtained from the absorption image (A) integrated along the vertical direction. The wings of the central peak result from a small thermal component. The continuous line corresponds to the calculated density profile for the expanded array of condensates for the experimental parameters ($s = 5$ and $t_{\exp} = 29.5$ ms).

would arise. The width of the central peak ($n = 0$) of the interferogram is of the order $\Delta p_x \approx \hbar / m R_x \cdot t_{\exp}$ where $R_x \approx k_M d$ is half of the length of the whole sample in the x-direction. The occurrence of these peaks is the analog of multiple order interference fringes in light diffraction.

The relative population of the $n \neq 0$ peaks with respect to the central one ($n = 0$) obeys the simple law

$$P_n = \exp\left(\frac{-16\pi^2 n^2 \sigma^2}{\lambda^2}\right) \tag{3}$$

holding also in the presence of a smooth modulation of the atomic occupation number N_k in each well. This means that by measuring P_n from the experimental data we can deduce the size σ of the individual condensates, hence the overlap between condensates and the tunneling rate as will be described in Section 3.

3. SMALL-AMPLITUDE OSCILLATIONS OF THE ARRAY

In the preceding section, I have shown that the BECs produced in our combined trap are phase locked by the tunneling of atoms through the optical barriers. The system indeed realizes a one-dimensional array of Josephson junctions (JJ) as I wish to demonstrate in this section.

A Josephson junction is a simple device made of two coupled macroscopic quantum fluids [16]. If the coupling is weak enough, an atomic mass current I flows across the two systems, driven by their relative phase $\Delta\phi$ with a limiting current I_c, the "Josephson critical current", namely the maximal current allowed to flow through the junction. The relative phase dynamics, on the other hand, are sensitive to the external and internal forces driving the system being driven by the chemical potential difference between the two quantum fluids [17]. The arrays of JJs are made of several simple junctions connected in various geometrical configurations. In the last decade such systems have attracted much interest, due to their potential for studying quantum phase transitions in systems where the external parameters can be readily tuned [9, 18]. Recently, the creation of simple quantum-logic units and more complex quantum computer schemes have also been discussed [19].

The condensates in two neighboring sites of the array have a significant interaction via the tunneling through the barrier; we can therefore rewrite the Gross–Pitaevskii equation, normally used to describe weakly interacting condensates, as a discrete nonlinear Schrödinger equation (DNLS) in a parabolic potential [20]. I remark that the model used here is one dimensional as we are now only concerned with the motion along the array; we write the condensate order parameter as

$$\Psi(x, t) = \sum_j \sqrt{N_j(t)} \exp(i\phi_j(t))\Phi_j(x) \tag{4}$$

and obtain

$$i\hbar \frac{\partial \psi_n}{\partial t} = -K(\psi_{n-1} + \psi_{n+1}) + (\varepsilon_n + \Lambda|\psi_n|^2)\psi_n \tag{5}$$

where $\varepsilon_n = 1/2 m\omega_x^2 (\lambda/2)^2 n^2$ and $\Lambda = g_0 N_T \int dx \Phi_j^4$.

The tunneling rate is

$$K \approx -\int dx \left[\frac{\hbar^2}{2m} \vec{\nabla}\Phi_j \cdot \vec{\nabla}\Phi_{j+1} + \Phi_j V \Phi_{j+1} \right] \tag{6}$$

I observe that the wavefunctions Φ_j, as well as the tunneling rate K, depend on the height of the energy barrier.

In the ground-state configuration the Bose–Einstein condensates are distributed among the sites at the bottom of the parabolic trap. If we suddenly displace the magnetic trap along the lattice axis by a small distance $\sim$30 μm (the dimension of the array is $\sim$100 μm) the cloud will be out of equilibrium and will start to move. As the potential energy that we give to the cloud is still smaller than the inter-well barrier, each condensate can move along the lattice only by tunneling through the barriers. A collective motion can only be established at the price of well definite phase coherence among the condensates. In other words, the relative phases among all adjacent sites should remain locked together in order to preserve the ordering of the collective motion. The locking of the relative phases will again show up in the expanded cloud interferogram.

For not too large displacements, we observe a coherent collective oscillation of the condensates, that is, we see the three peaks of the interferogram of the expanded condensates oscillating in phase, thus showing that the quantum mechanical phase is maintained over the entire condensate (Fig. 2, left). The top part of Fig. 2 (left) show the positions of the three peaks as a function of time spent in the combined trap after the displacement of the magnetic trap, compared with the motion of the condensate in the same displaced magnetic trap but in absence of the optical standing wave (I refer to this as

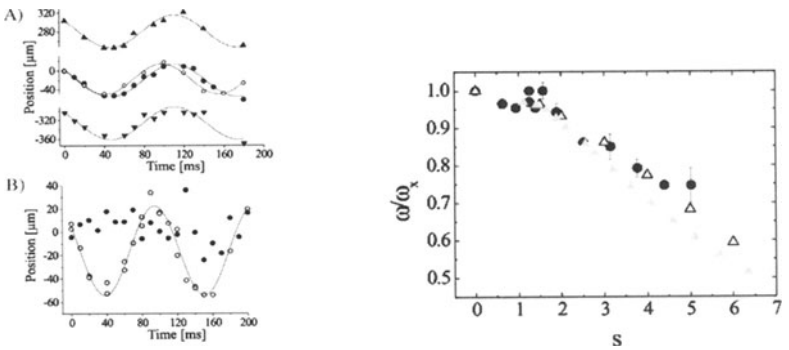

Figure 2. (A) Center of mass positions of the three peaks in the interferogram of the expanded condensate as a function of the time spent in the combined trap after displacement of the magnetic field. Up and down triangles correspond to the first-order peaks, filled circles to the central peak. Open circles show the center of mass position of the BEC in absence of the optical lattice. The continuous lines are the fits to the data. (B) Center of mass positions of the thermal cloud as a function of time spent in the displaced magnetic trap with the standing wave turned on (filled circles) and off (open circles). Right: The ratio of the frequency of the atomic current in the array of Josephson junctions to the harmonic trap frequency as a function of the inter-well potential height. Experimental data (circles) are compared to the values calculated with Eq. (8) (gray triangles) and to a numerical simulation of the one-dimensional GPE (open triangles).

"harmonic" oscillation). The motion performed by the center of mass of the condensate is an undamped oscillation at a substantially lower frequency than in the "harmonic" case. I remark that in a thermal cloud, although individual atoms are allowed to tunnel through the barriers, no macroscopic phase is present and no motion of the center of mass should be observed. The center of mass positions of the thermal clouds are also reported in Fig. 2 (left) together with the "harmonic" oscillation of the same cloud in absence of the optical potential. As can be clearly seen the thermal cloud does not move from its original position in the presence of the optical lattice.

The current flowing through the junction between two quantum fluids has a maximum value, the critical Josephson current I_c, which is directly proportional to the tunneling rate K. The existence of such a condition essentially limits the maximum velocity at which the condensate can flow through the inter-well barriers and therefore reduces the frequency of the oscillations. As a consequence we expect a dependence of the oscillation frequency on the optical potential through the tunneling rate. If we rewrite the DNLS Eq. (5) in terms of the canonically conjugated variables population/phase and use collective coordinates we arrive to a phase–current relation.

$$\begin{aligned} \hbar \frac{d}{dt}\xi(t) &= 2K \sin \Delta\phi(t) \\ \hbar \frac{d}{dt}\Delta\phi(t) &= -m\omega_x^2 \left(\frac{\lambda}{2}\right)^2 \xi(t) \end{aligned} \tag{7}$$

where $\xi(t)$ is the center of mass of the array and $\Delta\phi(t)$ the relative phase across the junction. I remark that, in the regimes we are considering, the current–phase dynamics do not depend explicitly on the interatomic interaction. However, it is clear that the non-linear interaction is crucial in determining the superfluid nature of the coupled condensates, by locking the overall phase coherence against perturbations.

From Eq. (7) we can see that the small-amplitude oscillation frequency ω of the current $I \equiv N_T d/dt\xi$ gives a direct measurement of the critical Josephson current $I_c \equiv 2KN_T/\hbar$ and, therefore, of the atomic tunneling rate of each condensate through the barriers. The critical current is related to the frequency ω of the atomic oscillations in the lattice and to the frequency ω_x of the condensate oscillations in absence of the periodic field by the relation

$$I_c = \frac{4\hbar N_T}{m\lambda^2}\left(\frac{\omega}{\omega_x}\right)^2 \tag{8}$$

Figure 2 (right) shows the experimental values of the oscillation frequencies together with the result of a variational calculation. It must be noted that, due to mean field interactions, in our system only for potentials higher than $\sim E_R$ does a bound state exist in the lattice.

4. MODULATIONAL INSTABILITY IN A JJ ARRAY

In the preceding two sections, I have shown that, for small-amplitude oscillations across the optical lattice, the motion of a pure condensate is undamped and only shows damping in presence of a significant thermal fraction. This behavior is due to macroscopic coherence across the array established and maintained by tunneling of atoms through the

optical barriers. In this section, I will consider the large-amplitude oscillations where the induced dynamics disrupts phase coherence across the array and the system undergoes a classical dynamical transition from superfluid to insulator.

When we increase the displacement of the magnetic trap center for a fixed height of the optical barriers, we observe that the center of mass of the atomic sample no longer oscillates, but slowly moves towards the center of the magnetic potential. This is shown in Fig. 3 (left) where I report the evolution of the atomic cloud center-of-mass position for a barrier height of $s = 5$ and displacements of 30 and 120 μm.

In the latter case we observe the loss of long-range coherence across the array in the interferogram of the expanded cloud. Indeed the interference peaks, present immediately after the displacement, are quickly washed due to the evolution in the combined trap as shown in Fig. 3 (center) where I report absorption images taken at different evolution times compared with the corresponding images in the absence of the optical lattice.

The one-dimensional model, introduced in Section 3 gives an estimate for the onset of the pinning of the condensates and illuminates the nature of the two regimes [21].

In the theoretical model the system undergoes a sharp transition from a regime with coherent oscillations (*superfluid regime*) to another one with pinning (*insulator*). The transition occurs at a critical displacement

$$\xi_{cr} = \sqrt{\frac{2K}{\Omega}} \tag{9}$$

Because the tunneling rate K depends on the height of the optical barriers, the critical displacement should depend on the height of the inter-well potential: precisely, the larger the height, the lower is the tunneling rate and the critical displacement. The reason for such a transition relies on the activation of a dynamical instability, called *modulational instability*, which was first discussed for the DNLS without external field in Ref. [22]. The modulational instability refers to an exponential growth of small perturbations of a carrier wave, as a result of the interplay between dispersion and nonlinearity [23]. Modulational instability "unlocks" the relative phases, which start to run independently with different

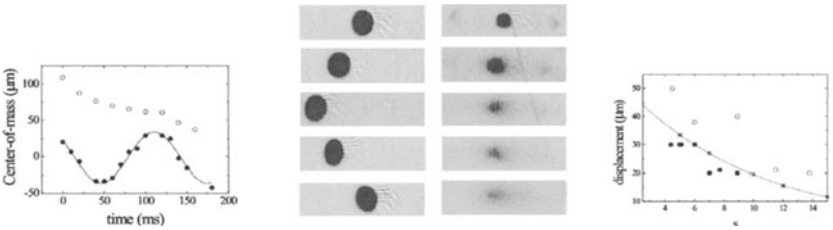

Figure 3. Position of the center of mass of the atomic cloud in the trap for a barrier height of 5 E_R. Filled circles: displacement of 30 μm; open circles: displacement of 120 μm. The continuous line represents a fit to the "small displacement" data with a sine function. Center: Absorption images taken every 20 ms starting just after the sudden displacement of the harmonic trap by 120 μm. The atoms have expanded for 27.8 ms after release from the pure harmonic trap (left row) or from the combined trap (right row). Right: Comparison of experimental results with Eq. (9). Filled circles represent coherent oscillations (with coherent interferogram featuring the three peaks), empty circles pinned motions; stars connected with a continuous line show results of Eq. (9).

velocities. Phase coherence through the array is quickly lost and the system behaves as an insulator. This transition occurs for classical fields and it is qualitatively different from the quantum Mott insulator–superfluid transition [9, 24]. In the modulational instability the insulator regime is associated with a vanishing temporal correlation among the phases of each condensate in each site even if each site still contains a coherent state. In the quantum transition the insulator regime is associated with the emergence, driven by quantum phase fluctuations, of squeezed atom number states in each site and cannot be reproduced by a Gross–Pitaevskii type equation. In our one-dimensional system the atom numbers in each well and the tunneling rate between adjacent wells are too large to observe an effect of quantum phase fluctuations.

In order to evidence the dependence of the critical displacement on the optical barriers' height and verify the theoretical prediction, we have followed the evolution of the condensates in the combined trap for different values of the displacement and of the optical potential. The experimental findings are summarized in Fig. 3 (right) compared with Eq. (9) for different values of s: filled circles denotes coherent oscillations (with coherent interferogram featuring the three peaks) and empty circles pinned motions, while the results of Eq. (9) are shown as stars connected with a continuous line. However, for values of displacement just above ξ_{cr} we could not observe a complete disruption of the interferogram but rather the appearance of more complex structures within the three visible peaks. I remark that the one-dimensional DNLS gives an estimate for the onset of loss of the coherence, but it does not quantitatively describe the breaking of the wave packet. We attribute this to the fact that our DNLS is based on the tight-binding approximation, which is obtained with the assumption that the transverse degrees of freedom are frozen, which is not completely true [15]. Neglecting the radial dynamics does not affect the description of the coherent motion significantly. But at the point in which the wave packet starts to breaks, the inclusion of radial oscillations could be important, causing only damping of the BEC motion, without breaking down the three peaks structure [25]. We believe that the quantitative analysis of the breakdown process is a very interesting topic, which deserves further investigations: here I limit this discussion to the consideration that the one-dimensional DNLS gives a reasonable estimate of the onset of the condensates' pinning.

Another point to stress is that the effective dimensionality of the BECs trapped in each well can modify the degree of nonlinearity of the DNLS. Such corrections can be included with site-dependent parameters in the DNLS, but can ultimately complicate its structure. We can ignore such corrections when we explore bulk properties of the system, as the small oscillations, where the details of the (tail) density profile are irrelevant. In this respect, the DNLS equation can be seen as a zero-order (perturbative) approximation of more complicate discrete, nonlinear equations.

5. CONCLUSIONS

In this paper, I have described a one-dimensional array of Josephson junctions realized with Bose–Einstein condensates produced in an optical lattice. The junction critical current can be controlled by changing the intensity of the light beam producing the optical lattice. This was shown studying small-amplitude dipole oscillations of the array in a harmonic magnetic potential. Dipole oscillations of the array have been investigated in various limits. In the finite temperature limit we have been able to study interactions between the condensed and normal components of a cloud of ^{87}Rb atoms under T_c. The use

of the array has allowed in this limit full separation in the dynamics of the coherent and incoherent components, thus realizing an atom-optical coherence filter, which could be used to obtain "spectrally pure" atom lasers. In the large amplitude limit the array undergoes a classical dynamical transition between a superfluid and an insulator state. The transition is due to a modulational instability caused by the interplay between dispersion and nonlinearity, which disrupts long-range phase coherence across the array. The critical amplitude for this transition can be controlled again with the intensity of the light beam producing the optical lattice. The transition, sharp in the one-dimensional theory, is indeed broadened in the actual experiment, opening up the possibility to control the phase dynamics in the array.

The full control and characterization of a one-dimensional array of neutral Josephson junctions could be of interest for quantum logic experiments. Neutral junctions should be far less sensitive to perturbations than charged systems like those realized with superconductors. Furthermore I have shown that is possible to accurately control most of the parameters of the system with simple experimental operations.

REFERENCES

[1] M. Inguscio, C. E. Wieman, and S. Stringari, Eds. *Bose–Einstein Condensation in Atomic Gases* (Oxford, Tokyo, Washington, IOS Press Amsterdam, 1999).

[2] J. Stenger *et al., Phys. Rev. Lett.* **82**, 4569 (1999); Y. B. Ovchinnikov *et al., Phys. Rev. Lett.* **83**, 284 (1999); E. W. Hagley *et al., Phys. Rev. Lett.* **83**, 3112 (1999); J. E. Simsarian *et al., Phys. Rev. Lett.* **85**, 2040 (2000).

[3] M. Kozuma *et al., Science* **286**, 2309 (1999), S. Inouye *et al., Nature* **402**, 641 (1999).

[4] I. Deng *et al., Nature* **398**, 218 (1999).

[5] S. Inouye *et al., Science* **285**, 571 (1999).

[6] B. P. Anderson and M. A. Kasevich, *Science* **282**, 1686 (1998).

[7] C. Orzel, A. K. Tuchman, M. L. Fenselau, M. Yasuda, and M. A. Kasevich, *Science* **291**, 2386 (2001).

[8] M. Greiner, I. Bloch, O. Mandel, T. W. Hänsch, and T. Esslinger, *Phys. Rev. Lett.* **87**, 160405 (2001).

[9] M. Greiner, O. Mandel, T. Esslinger, T. W. Hänsch, and I. Bloch, *Nature* **415**, 39 (2002).

[10] S. Burger, F. S. Cataliotti, C. Fort, F. Minardi, M. Inguscio, M. L. Chiofalo, and M. P. Tosi, *Phys. Rev. Lett.* **86**, 4447 (2001).

[11] F. S. Cataliotti, S. Burger, C. Fort, P. Maddaloni, F. Minardi, A. Trombettoni, A. Smerzi, and M. Inguscio, *Science* **293**, 843 (2001).

[12] C. Fort *et al., Europhys. Lett.* **49**, 8 (2000).

[13] S. Burger, F. S. Cataliotti, C. Fort, P. Maddaloni, F. Minardi, and M. Inguscio, *Europhys. Lett.* **57**, 1 (2002).

[14] F. Dalfovo, S. Giorgini, L. P. Pitaevskii, and S. Stringari, *Rev. Mod. Phys.* **71**, 463 (1999).

[15] P. Pedri *et al., Phys. Rev. Lett.* **87**, 220401 (2001).

[16] A. Barone, *Weakly Coupled Macroscopic Quantum Systems: Likeness with Difference*, I. O. Kulik and R. Ellialtioglu, Eds. (Kluwer Academic Publishers, 2000) pp. 301–320; A. Barone, and G. Paterno, *Physics and Applications of the Josephson Effect* (New York, Wiley, 1982).

[17] D. R. Tilley and J. Tilley, *Superfluidity and Superconductivity* (New York, Hilger, 1990).

[18] R. Fazio and H. van der Zant, cond-mat/0011152.

[19] Y. Makhlin, G. Schön, and A. Shnirman, *Rev. Mod. Phys.* **73**, 357 (2001).

[20] A. Trombettoni and A. Smerzi, *Phys. Rev. Lett.* **86**, 2353 (2001).

[21] A. Smerzi, A. Trombettoni, P. G. Kevrekidis, and A. R. Bishop, to appear in *Phys. Rev. Lett.*

[22] M. Peyrard and M. Kruskal, *Physica* **14D**, 88 (1984).

[23] A. C. Scott, *Nonlinear Science: Emergence and Dynamics of Coherent Structures*, Oxford, Oxford Univ. Press, 1999.

[24] D. Jaksch *et al.*, *Phys. Rev. Lett.* **81**, 3108 (1998).

[25] M. Modugno, private communication.

A SIMPLE QUANTUM EQUATION FOR DECOHERENCE THROUGH INTERACTION WITH THE ENVIRONMENT

E. Recami[1,a] and R. H. A. Farias[2,b]
[1]*Facoltà di Ingegneria, Università statale di Bergamo, Dalmine, Italy and INFN — Sezione di Milano, Milan, Italy*
[2]*LNLS — Synchrotron Light National Laboratory, Campinas, S.P. Brazil*

Abstract: Within the density matrix formalism, it is shown that a simple way to get decoherence is through the introduction of a "quantum" of time (*chronon*): thus replacing the differential Liouville–von Neumann (LvN) equation with a finite-difference version of it. In this way, one is given the possibility of using a rather simple quantum equation to describe the decoherence effects due to interaction with the environment.

In other words, the mere introduction (not of a "time-lattice", but simply) of a "chronon" allows us to go on from differential to finite-difference equations; and in particular to write down the Schrödinger equation (as well as the LvN equation) in three different ways: "retarded", "symmetrical", and "advanced". One of such three formulations—the *retarded* one—describes in an elementary way a system that is exchanging (and losing) energy with the environment. In its density-matrix version, indeed, it can be easily shown that all nondiagonal terms go to zero very rapidly. [A much larger presentation of this work appeared c/o the Laid Archives as the e-print quant-ph/9706059, and as the preprint IC/98/74, ICTP; Trieste, 1998].

Keywords: Quantum decoherence, Interaction with the environment, Quantum measurement theory, Finite-difference equations, Chronon, Caldirola, Density-matrix formalism, Liouville–von Neumann equation, Proceedings

1. INTRODUCTION

In this Chapter, we briefly mention the consequences of the introduction of a quantum of time τ_0 in the formalism of nonrelativistic quantum mechanics, by referring ourselves, in particular, to the theory of the *chronon* as proposed by P. Caldirola. Let us recall that such an interesting "finite difference" theory, forwards—at the classical level—a solution

[a]E-mail: recami@mi.infn.it
[b]E-mail: ruy@lnls.br

Quantum Computing and Quantum Bits in Mesoscopic Systems
Edited by Leggett *et al.*, Kluwer Academic/Plenum Publishers, 2004

for the motion of a particle endowed with a non-negligible charge in an external electromagnetic field, overcoming all the known difficulties met by Abraham–Lorentz's and Dirac's approaches (and even allowing a clear answer to the question whether a free-falling charged particle does or does not emit radiation), and—at the quantum level—yields a remarkable mass spectrum for leptons.

In unpublished work [cf. the e-print quant-ph/9706059, and the subsequent Report IC/98/74 (ICTP; Trieste, 1998), where also extensive references can be found], after having reviewed Caldirola's approach, we [1] worked out, discussed, and compared to one another the *new* representations of quantum mechanics (QM) resulting from it, in the Schrödinger, Heisenberg, and density-operator (Liouville–von Neumann) pictures, respectively.

Let us stress that, for each representation, three (*retarded, symmetric*, and *advanced*) *formulations* are possible, which refer either to times t and $t - \tau_0$, or to times $t - \tau_0/2$ and $t + \tau_0/2$, or to times t and $t + \tau_0$, respectively. It is interesting to note that, when the chronon tends to zero, the ordinary QM is obtained as the limiting case of the "symmetric" formulation only, while the "retarded" one does naturally appear to describe QM with friction, that is, to describe *dissipative* quantum systems (like a particle moving in an absorbing medium). In this sense, *discretized* QM is much richer than the ordinary one.

In the mentioned unpublished work [1], we have also obtained the (retarded) finite-difference Schrödinger equation within the Feynman path integral approach, and studied some of its relevant solutions. We have then derived the time-evolution operators of this discrete theory, and used them to get the finite-difference Heisenberg equations.[1] Afterwards, we have studied some typical applications and examples: as the free particle, the harmonic oscillator and the hydrogen atom; and various cases have been pointed out for which the predictions of discrete QM differ from those expected from "continuous" QM. We want here to give our attention to the fact that, when applying the density matrix formalism to the solution of the *measurement problem* in QM, very interesting results are met, as, for instance, a natural explication of "decoherence" [2], which seem to reveal the power of discretized (in particular, *retarded*) QM.

2. OUTLINE OF THE CLASSICAL APPROACH

If ρ is the charge density of a particle on which an external electromagnetic field acts, the famous Lorentz's force law

$$\mathbf{f} = \rho\left(\mathbf{E} + \frac{1}{c}\mathbf{v} \wedge \mathbf{B}\right) \tag{1}$$

is valid only when the particle charge q is negligible with respect to the external field sources. Otherwise, the classical problem of the motion of a (non-negligible) charge in an electromagnetic field is still an open question. For instance, after the known attempts by

[1]When discussing therein the mutual compatibility of the various pictures listed above, we found that they *can* actually be written in a form such that they result to be equivalent (as it happens in the "continuous" case of ordinary QM), even if the Heisenberg picture cannot be derived by "discretizing" directly the ordinary Heisenberg representation.

Abraham and Lorentz, in 1938 Dirac [3] obtained and proposed his famous classical equation

$$m\frac{du_\mu}{ds} = F_\mu + \Gamma_\mu \tag{2}$$

where Γ_μ is the Abraham four-vector

$$\Gamma_\mu = \frac{2}{3}\frac{e^2}{c}\left(\frac{d^2u_\mu}{ds^2} + \frac{u_\mu u^\nu}{c^2}\frac{d^2u_\nu}{ds^2}\right) \tag{3}$$

that is, the (Abraham) reaction force acting on the electron itself, and F_μ is the four-vector that represents the external field acting on the particle

$$F_\mu = \frac{e}{c}F_{\mu\nu}u^\nu \tag{4}$$

At the nonrelativistic limit, Dirac's equation goes formally into the one previously obtained by Abraham–Lorentz:

$$m_0\frac{dv}{dt} - \frac{2}{3}\frac{e^2}{c^3}\frac{d^2\mathbf{v}}{dt^2} = e\left(\mathbf{E} + \frac{1}{c}\mathbf{v}\wedge\mathbf{B}\right) \tag{5}$$

The last equation shows that the reaction force equals $(2/3)(e^2/c^3)(d^2\mathbf{v}/dt^2)$.

Dirac's dynamical Eq. (2) presents, however, many problem, related to the infinite many nonphysical solutions that it possesses. Actually, it is a third-order differential equation, requiring three initial conditions for singling out one of its solutions. In the description of a *free* electron, for example, it yields "self-accelerating" solutions (*runaway solutions*), for which velocity and acceleration increase spontaneously and indefinitely. Moreover, for an electron submitted to an electromagnetic pulse, further nonphysical solutions appear, related this time to *pre-accelerations*: If the electron comes from infinity with a uniform velocity v_0 and, at a certain instant of time t_0, is submitted to an electromagnetic pulse, then it starts accelerating *before* t_0. Drawbacks like these motivated further attempts to find out a coherent (not pointlike) model for the classical electron.

Considering elementary particles as points is probably the sin plaguing modern physics (a plague that, unsolved in classical physics, was transferred to quantum physics). One of the simplest ways for associating a discreteness with elementary particles (let us consider, for example, the electron) is just via the introduction (not of a "time-lattice", but merely) of a "quantum" of time, the *chronon*, following Caldirola [4]. Like Dirac's theory, Caldirola's theory is also Lorentz invariant (continuity, in fact, is not an assumption required by Lorentz invariance). This theory postulates the existence of a universal interval τ_0 of *proper* time, even if time flows continuously as in the ordinary theory. When an external force acts on the electron, however, the reaction of the particle to the applied force is not continuous: The value of the electron velocity u_μ is supposed to jump from $u_\mu(\tau - \tau_0)$ to $u_\mu(\tau)$ *only at certain positions* s_n along its world line; *these "discrete positions" being such that the electron takes a time* τ_0 *for travelling from one position* s_{n-1} *to the next one* s_n. The electron, in principle, is still considered as pointlike, but the Dirac relativistic equations for the classical radiating electron are

replaced: (i) by a corresponding *finite-difference* (retarded) equation in the velocity $u^{\mu}(\tau)$

$$\frac{m_0}{\tau_0}\left\{u_\mu(\tau) - u_\mu(\tau - \tau_0) + \frac{u_\mu(\tau)u_\nu(\tau)}{c^2}[u_\nu(\tau) - u_\nu(\tau - \tau_0)]\right\} = \frac{e}{c}F_{\mu\nu}(\tau)u_\nu(\tau) \qquad (6)$$

which reduces to the Dirac Eq. (2) when $\tau_0 \to 0$; and (ii) by a second equation [the *transmission law*] connecting this time the discrete positions $x^{\mu}(\tau)$ along the world line of the particle:

$$x_\mu(n\tau_0) - x_\mu[(n-1)\tau_0] = \frac{\tau_0}{2}\{u_\mu(n\tau_0) - u_\mu[(n-1)\tau_0]\} \qquad (6a)$$

which is valid inside each discrete interval τ_0, and describes the *internal* motion of the electron. In these equations, $u^{\mu}(\tau)$ is the ordinary four-vector velocity, satisfying the condition $u_\mu(\tau)u^\mu(\tau) = -c^2$ for $\tau = n\tau_0$, where $n = 0, 1, 2, \ldots$ and $\mu, \nu = 0, 1, 2, 3$; while $F^{\mu\nu}$ is the external (retarded) electromagnetic field tensor, and the chronon associated with the electron (by comparison with Dirac's equation) resulted to be

$$\frac{\tau_0}{2} \equiv \theta_0 = \frac{2}{3}\frac{ke^2}{m_0c^3} \simeq 6.266 \times 10^{-24}\ \text{s}$$

depending, therefore, on the particle (internal) properties [namely, on its charge e and rest mass m_0].

As a result, the electron happens to appear eventually as an extended-like [5] particle, with internal structure, rather than as a pointlike object. For instance, one may imagine that the particle does not react instantaneously to the action of an external force because of its finite extension (the numerical value of the chronon is of the same order as the time spent by light to travel along an electron classical diameter). As already said, Eq. (6) describes the motion of an object that happens to be pointlike only at discrete positions s_n along its trajectory; even if both position and velocity are still continuous and well-behaved functions of the parameter τ, since they are differentiable functions of τ. It is essential to note that a discreteness character is given in this way to the electron without any need of a "model" for the electron. Actually it is well known that many difficulties are met not only by the strictly pointlike models, but also by the extended-type particle models ("spheres", "tops", "gyroscopes", and so on). We deem the answer stays with a third type of model, the "extended-like" one, like the present approach; or like the (related) theories [5] in which the center of the pointlike charge is spatially distinct from the particle center of mass. Let us repeat that the worst also met in quantum field theory, like the presence of divergencies, are due to the pointlike character still attributed to (spinning) particles; since—as we already remarked—the problem of a suitable model for elementary particles was transported, *unsolved*, from classical to quantum physics. One might consider that problem to be the most important even in modern particle physics. Equations (6) and (6a), together, provide a full description of the motion of the electron, but they are *free* from pre-accelerations, self-accelerating solutions, and problems with the hyperbolic motion.

In the *nonrelativistic limit* the previous (retarded) equations are simplified into the form

$$\frac{m_0}{\tau_0}[\mathbf{v}(t) - \mathbf{v}(t - \tau_0)] = e\left[\mathbf{E}(t) + \frac{1}{c}\mathbf{v}(t) \wedge \mathbf{B}(t)\right] \tag{7}$$

$$\mathbf{r}(\mathbf{t}) - \mathbf{r}(\mathbf{t} - \tau_0) = \frac{\tau_0}{2}[\mathbf{v}(\mathbf{t}) - \mathbf{v}(\mathbf{t} - \tau_0)] \tag{7a}$$

The important point is that Eqs (6) and (6a), or (7) and (7a), allow us to overcome the difficulties met with the Dirac classical equation. In fact, the electron *macroscopic* motion is completely determined once velocity and initial position are given. The explicit solutions of the above relativistic equations for the radiating electron—or of the corresponding non-relativistic equations—verify that the following questions can be regarded as having been solved within Caldirola's theory: (A) *exact relativistic solutions*: (1) free electron motion; (2) electron under the action of an electromagnetic pulse; (3) hyperbolic motion; (B) *non-relativistic approximate solutions*: (1) electron under the action of time-dependent forces; (2) electron in a constant, uniform magnetic field; (3) electron moving along a straight line under the action of an elastic restoring force.

In Ref. [1] we studied the electron radiation properties as deduced from the finite-difference relativistic Eq. (6), and their series expansions, with the aim of showing the advantages of the present formalism with respect to the Abraham–Lorentz–Dirac one.

2.1 The three alternative formulations

Two more (alternative) formulations are possible for Caldirola's equations, based on different discretization procedures. In fact, Eqs (6) and (7) describe an intrinsically radiating particle. And, by expanding Eq. (6) in terms of τ_0, a radiation reaction term appears. Caldirola called those equations the *retarded* form of the electron equations of motion.

On the contrary, by rewriting the finite-difference equations in the form

$$\frac{m_0}{\tau_0}\left\{u_\mu(\tau + \tau_0) - u_\mu(\tau) + \frac{u_\mu(\tau)u_\nu(\tau)}{c^2}[u_\nu(\tau + \tau_0) - u_\nu(\tau)]\right\} = \frac{e}{c}F_{\mu\nu}(\tau)u_\nu(\tau) \tag{8}$$

$$x_\mu[(n+1)\tau_0] - x_\mu(n\tau_0) = \tau_0 u_\mu(n\tau_0) \tag{8a}$$

one gets the *advanced* formulation of the electron theory, since the motion is now determined by advanced actions. At variance with the retarded formulation, the advanced one describes an electron that absorbs energy from the external world.

Finally, by adding together retarded and advanced actions, Caldirola wrote down the *symmetric* formulation of the electron theory

$$\frac{m_0}{2\tau_0}\left\{u_\mu(\tau + \tau_0) - u_\mu(\tau - \tau_0) + \frac{u_\mu(\tau)u_\nu(\tau)}{c^2}[u_\nu(\tau + \tau_0) - u_\nu(\tau - \tau_0)]\right\}$$

$$= \frac{e}{c}F_{\mu\nu}(\tau)u_\nu(\tau) \tag{9}$$

$$x_\mu[(n+1)\tau_0] - x_\mu((n-1)\tau_0) = 2\tau_0 u_\mu(n\tau_0) \tag{9a}$$

which does not include any radiation reactions, and describes a nonradiating electron.

Before closing this brief introduction to the classical "chronon theory", let us recall at least one more result derivable from it. If we consider a free particle

and look for the "internal solutions" of Eq. (7a), we get—for a periodical solution of the type

$$\dot{x} = -\beta_0 c \sin\left(\frac{2\pi\tau}{\tau_0}\right); \quad \dot{y} = -\beta_0 c \cos\left(\frac{2\pi\tau}{\tau_0}\right); \quad \dot{z} = 0$$

(which describes a uniform circular motion) and by imposing the kinetic energy of the internal rotational motion to equal the intrinsic energy m_0c^2 of the particle—that the amplitude of the oscillations is given by $\beta_0^2 = 3/4$. Thus, the magnetic moment corresponding to this motion is exactly the *anomalous magnetic moment* of the electron, obtained in a purely classical context: $\mu_a = ((1/4\pi)\, e^3/(m_0c^2))$. This shows, by the way, that the anomalous magnetic moment is an intrinsically classical, and not quantum, result; and the absence of h in the last expression is a confirmation of this fact.

3. DISCRETIZED QUANTUM MECHANICS

Let us pass to a topic we are more interested in, which is a second step towards our eventual application of the discretization procedures for a possible solution of the measurement problem in QM, without having to make recourse to the reduction (wave-packet instantaneous collapse) postulate. Namely, let us focus our attention, now, on the consequences for QM of the introduction of a chronon. In our (unpublished) Ref. [1], we have extensively examined such consequences. Here, we shall recall only some useful results.

There are physical limits that, even in ordinary QM, seem to prevent the distinction of arbitrarily close successive states in the time evolution of a quantum system. Basically, such limitations result from the Heisenberg relations; in such a way that, if a discretization is to be introduced in the description of a quantum system, it cannot possess a universal value (since those limitations depend on the characteristics of the particular system under consideration). In other words, the value of the fundamental interval of time has to change a priori from system to system. All these points are in favor of the extension of Caldirola's procedure to QM. Time will still be a continuous variable, but the evolution of the system along its world line will be regarded as discontinuous. In analogy with the electron theory in the nonrelativistic limit, one has to substitute the corresponding finite-difference expression for the time derivatives; for example

$$\frac{df(t)}{dt} \to \frac{f(t) - f(t - \Delta t)}{\Delta t} \tag{10}$$

where proper time is now replaced by the local time t. The chronon procedure can then be applied to obtain the finite-difference form of the Schrödinger equation. As for the electron case, there are three different ways to perform the discretization, and three "Schrödinger equations" can be obtained:

$$i\frac{h}{\tau}[\Psi(\mathbf{x}, \mathbf{t}) - \Psi(\mathbf{x}, \mathbf{t} - \tau)] = \hat{H}\Psi(\mathbf{x}, \mathbf{t}) \tag{11}$$

$$i\frac{h}{2\tau}[\Psi(\mathbf{x}, \mathbf{t} + \tau) - \Psi(\mathbf{x}, \mathbf{t} - \tau)] = \hat{H}\Psi(\mathbf{x}, \mathbf{t}) \tag{11b}$$

$$i\frac{h}{\tau}[\Psi(\mathbf{x}, \mathbf{t} + \tau) - \Psi(\mathbf{x}, \mathbf{t})] = \hat{H}\Psi(\mathbf{x}, \mathbf{t}) \tag{11c}$$

which are, respectively, the *retarded*, *symmetric*, and *advanced* Schrödinger equations, all of them transforming into the (same) continuous equation when the fundamental interval of time (that can now be called just τ) goes to zero.

Because the equations are different, the solutions they provide are also fundamentally different. As we have already seen, in the classical theory of the electron the symmetric equation represented a nonradiating motion, providing only an approximate description of the motion (without taking into account the effects due to the self fields of the electron). However, in the quantum theory it plays a fundamental role. In the discrete formalism too, the symmetrical equation constitutes the only way to describe a bound nonradiating particle. Let us remark that, for a time-independent Hamiltonian, the outputs obtained in the discrete formalism by using the symmetric equation resulted to be [1] very similar to those obtained in the continuous case. For these Hamiltonians, the effect of discretization appears basically in the frequencies associated with the time-dependent term of the wave-function, and, in general, seems to be negligible.

However, the solutions of the *retarded* (and *advanced*) equations show a completely different behavior. For a Hamiltonian explicitly independent of time, the solutions have a general form given by

$$\Psi(\mathbf{x}, \mathbf{t}) = \left[1 + i\frac{\tau}{\hbar}\hat{H}\right]^{-t/\tau} f(\mathbf{x})$$

and, expanding $f(x)$ in terms of the eigenfunctions of $\hat{H}$:

$$\hat{H}u_n(\mathbf{x}) = W_n u_n(\mathbf{x})$$

that is, writing $f(\mathbf{x}) = \sum_n c_n u_n(\mathbf{x})$, with $\sum_n |c_n|^2 = 1$, one can obtain that

$$\Psi(\mathbf{x}, \mathbf{t}) = \sum_n c_n \left[1 + i\frac{\tau}{\hbar}W_n\right]^{-t/\tau} u_n(\mathbf{x}).$$

The norm of this solution is given by

$$|\Psi(\mathbf{x}, \mathbf{t})|^2 = \sum_n |c_n|^2 \exp(-\gamma_n t)$$

with

$$\gamma_n = \frac{1}{\tau}\ln\left(1 + \frac{\tau^2}{\hbar^2}W_n^2\right) = \frac{W_n^2}{\hbar^2}\tau + O(\tau^3)$$

where it is apparent that the damping factor depends critically on the value τ of the chronon. This *dissipative* behavior originates from the character of the *retarded* equation; in the case of the electron, the retarded equation possesses intrinsically dissipative solutions, representing a radiating system. The Hamiltonian has the same status as in the ordinary (continuous) case. It is an observable, since it is a Hermitian operator and its eigenvectors form a basis of the state space. However, as we have seen, the norm of the

state vector is not constant any longer, due to the damping factor. An opposite behavior is observed for the solutions of the advanced equation, in the sense that they increase exponentially.

One of the most impressive achievements due to the introduction of the chronon hypothesis in the realm of QM has been obtained in the description of a bound electron by using the new formalism. In fact, Caldirola found for the excited state of the electron the value $E \simeq 105.55$ MeV, which is extremely close (with an error of 0.1%) to the measured value of the rest mass of the muon. For this, and similar questions, we just refer the reader to the quoted literature.

4. DISCRETIZED (RETARDED) LIOUVILLE EQUATION, AND A SOLUTION OF THE MEASUREMENT PROBLEM: DECOHERENCE FROM INTERACTION WITH THE ENVIRONMENT

Suppose we want to measure [6] the dynamical variable R of a (microscopic) object $\mathcal{O}$, by utilizing a (macroscopic) measuring apparatus $\mathcal{A}$. The eigenvalue equation $R|r\rangle_{\mathcal{O}} = r|r\rangle_{\mathcal{O}}$ defines a complete eigenvector basis for the observable R; so that any state $|\psi\rangle_{\mathcal{O}}$ of $\mathcal{O}$ can be given by the expansion $|\psi\rangle_{\mathcal{O}} = \sum_r c_r|r\rangle_{\mathcal{O}}$.

As to the apparatus $\mathcal{A}$, we are interested only in its observable A, whose eigenvalues α represent the value indicated by a *pointer*; then, we can write $A|\alpha, N\rangle_{\mathcal{A}} = \alpha|\alpha, N\rangle_{\mathcal{A}}$, quantity N representing the set of internal quantum numbers necessary to specify a complete eigenvector basis for it. Let the initial state of $\mathcal{A}$ be $|0, N\rangle_{\mathcal{A}}$; in other words, the pointer is assumed to indicate initially the value zero. The interaction between $\mathcal{O}$ and $\mathcal{A}$ is expressed by a time-evolution operator U, which is expected to relate the value of r with the measurement α.

In conventional ("continuous") quantum mechanics, the *density operator*, ρ, obeys the Liouville–von Neumann (LvN) equation

$$\frac{d\rho}{dt} = -\frac{i}{\hbar}[H, \rho] \equiv -i\mathcal{L}\rho(t)$$

where $\mathcal{L}$ is the Liouville operator; so that, if the Hamiltonian H is independent of time, the time evolution of ρ is

$$\rho(t - t_0) = \exp\left(-\frac{i}{\hbar}H(t - t_0)\right)\rho_0 \exp\left(\frac{i}{\hbar}H(t - t_0)\right)$$

It is known that, if the compound system $\mathcal{O}$ plus $\mathcal{A}$ is initially, for instance,[2] in the mixed state

$$\rho^{\text{in}} = \sum_M C_M |\psi_M^{\text{in}}\rangle\langle\psi_M^{\text{in}}|$$

[2]By contrast, if we consider as initial state for the system $\mathcal{O}$ plus $\mathcal{A}$ the pure state $|\psi_N^{\text{in}}\rangle = |\psi\rangle_{\mathcal{O}} \otimes |0, N\rangle_{\mathcal{A}} \equiv |\psi\rangle_{\mathcal{O}}|0, N\rangle_{\mathcal{A}}$, then, within the ***ordinary*** "continuous" approach, the time evolution leads necessarily to a coherent superposition of (macroscopically distinct) eigenvectors: $U(t, t_0)|\psi\rangle_{\mathcal{O}}|0, N\rangle_{\mathcal{A}} = \sum_r c_r|\alpha_r; r, N\rangle \equiv |\psi_N^{\text{fin}}\rangle$. As a consequence, as is well known, one has to postulate a state collapse from $|\psi_N^{\text{fin}}\rangle$ to $|\alpha_{r_0}; r_0, N\rangle$, where r_0 is the value indicated by the pointer after the measurement.

where quantities C_M are (classical) probabilities associated with the states $|\psi_M^{\text{in}}\rangle$, then the "continuous" approach is known to forward

$$\rho^{\text{fin}} \equiv U_\rho U^\dagger = \sum_M C_M |\psi_M^{\text{fin}}\rangle\langle\psi_M^{\text{fin}}| = \sum_{r_1, r_2} c_{r_1}^* c_{r_2} \sum_M C_M \{|\alpha_{r_1}; r_1, M\rangle\langle\alpha_{r_2}; r_2, M|\}$$

where the off-diagonal terms yield a coherent superposition of the corresponding eigenvectors. In this case, the reduction postulate has to imply that, in the measurement process, the nondiagonal terms do instantaneously vanish.

On the contrary, in the discrete case, with the interaction embedded in the Hamiltonian H, the situation is completely different. Let us consider the energy representation, where $|n\rangle$ are the states with defined energy: $H|n\rangle = E_n|n\rangle$. Since the time evolution operator is a function of the Hamiltonian, and commutes with it, the basis of the energy eigenstates will be a basis also for this operator.

The discretized (*retarded*) LvN equation is

$$\frac{\rho(t) - \rho(t - \tau)}{\tau} = -i\mathcal{L}\rho(t) \tag{12}$$

which reduces to the LvN equation when $\tau \to 0$. The essential point is that, following, for example, a procedure similar to Bonifacio's [7], one gets in this case a *nonunitary* time-evolution operator:

$$V(t, 0) = \left[1 + \frac{i\tau\mathcal{L}}{\hbar}\right]^{-t/\tau} \tag{13}$$

which, as for all nonunitary operators, does not preserve the probabilities associated with each of the energy eigenstates (that make up the expansion of the initial state in such a basis of eigenstates). We are interested in the time instants $t = k\tau$, with k an integer.[3]

Thus, the time-evolution operator (13) takes the initial density operator ρ^{in} to a final state for which the nondiagonal terms decay exponentially with time, namely to

$$\rho_{rs}^{\text{fin}} = \langle r|V(t, 0)|s\rangle = \rho_{rs}^{\text{in}}[1 + i\omega_{rs}\tau]^{-t/\tau} \tag{14}$$

where

$$\omega_{rs} \equiv \frac{1}{\hbar}(E_r - E_s) \equiv \frac{1}{\hbar}(\Delta E)_{rs} \tag{15}$$

Expression (14) can be written

$$\rho_{rs}(t) = \rho_{rs}(0)e^{-\gamma_{rs}t}e^{-i\nu_{rs}t} \tag{16}$$

[3]Let us emphasize that the appearance of nonunitary time-evolution operators is not associated with the *coarse graining* approach only, since they also come out of the discrete Schrödinger equations.

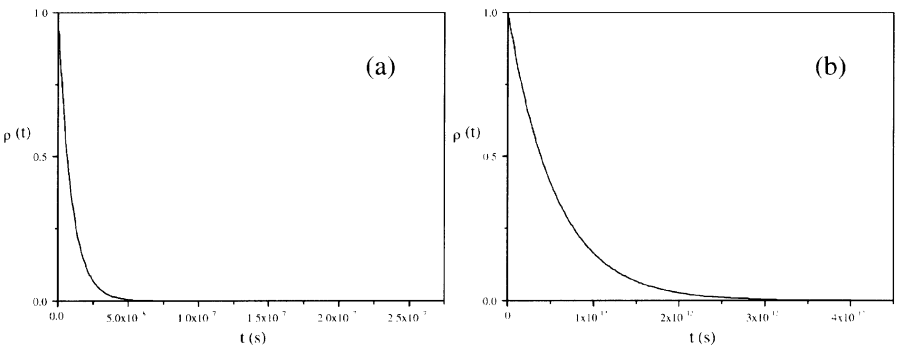

Figure 1. Damping of the nondiagonal terms of the density operator for two different values of τ. For both cases we used $\Delta E = 4\,\text{eV}$. (a) Slower damping for $\tau = 6.26 \times 10^{-24}$ s; (b) faster damping for $\tau = 1 \times 10^{-19}$ s.

with

$$\gamma_{FS} \equiv \frac{1}{2\tau}\ln(1 + \omega_{FS}^2\tau^2) \tag{17}$$

$$\nu_{FS} \equiv \frac{1}{\tau}\tan^{-1}(\omega_{FS}\tau) \tag{18}$$

One can observe, indeed, that the nondiagonal terms tend to zero with time, and that the larger the value of τ, the faster the decay becomes. Actually, the chronon τ is now an interval of time related no longer to a single electron, but to the whole system $\mathcal{O} + \mathcal{A}$. If one imagines the time interval τ to be linked to the possibility of distinguishing two successive, different states of the system, then τ can be significantly larger than 10^{-23} s, implying an extremely faster damping of the nondiagonal terms of the density operator (Fig. 1).

5. COMMENTS AND CONCLUSIONS

It should be noted that the time-evolution operator (13) preserves trace, obeys the semigroup law, and implies an irreversible evolution towards a stationary diagonal form. In other words, notwithstanding the simplicity of the present "discrete" theory, that is, of the chronon approach, an intrinsic relation is present between *measurement process* and *irreversibility*. Indeed, the operator (13), meeting the properties of a semigroup, does not possess in general an inverse (and noninvertible operators are, of course, related to irreversible processes). For instance, in a measurement process in which the microscopic object is lost after the detection, one is just dealing with an irreversible process that could be well described by an operator like (13).

In our (discrete and retarded) theory, the "state reduction"

$$\rho(t) \xrightarrow{t \to 0} \sum_n \rho_{nn}(0)|n\rangle\langle n|$$

is not instantaneous, but depends—as we have already seen—on the characteristic value τ. More precisely, the nondiagonal terms tend exponentially to zero according to a factor which, to the first order, is given by

$$\exp\left|\frac{-\omega_{nm}^{2}\tau t}{2}\right| \tag{19}$$

Thus, the reduction to the diagonal form occurs, provided that τ possesses a finite value, no matter how small, and provided that $\omega_{nm}\tau$, for every n, m, is *not* much smaller than 1, where

$$\omega_{nm} = \frac{(E_n - E_m)}{\hbar}$$

are the transition frequencies between the different energy eigenstates (the last condition being always satisfied, for example, for nonbounded systems).

It is essential to note that *decoherence has been obtained* above, *without having recourse to any statistical approach, and in particular without assuming any "coarse graining" of time*. The reduction to the diagonal form illustrated by us is a consequence of the discrete (retarded) LvN equation only, once the inequality $\omega_{nm}\tau \ll 1$ is *not* verified.

Moreover, the measurement problem is still controversial even with regard to its mathematical approach. In the simplified formalization introduced above, however, we have not included any consideration beyond those common to the quantum formalism, allowing an as clear as possible recognition of the effects of the introduction of a chronon.

Let us repeat that the introduction of a fundamental interval of time in the description of the measurement problem made possible a simple but effective formalization of the state reduction process (through a mechanism that can be regarded as a decoherence caused by interaction with the environment [2]) only for the retarded case. This is not obtainable, when taking into account the symmetric version of the discretized LvN equation.

It may be important to stress that the retarded form (12) of the direct discretization of the LvN equation is the *same equation* obtained via the *coarse grained* description (extensively adopted in [7]). This leads us to consider such an equation as a basic equation for describing *complex systems*, which is always the case when a measurement process is involved.

Let us add some brief remarks. First, the "decoherence" does not occur when we use the time evolution operators obtained directly from the retarded Schrödinger equation; the dissipative character of that equation, in fact, causes the norm of the state vector to decay with time, leading again to a nonunitary evolution operator. However, this operator (after having defined the density matrix) yields damping terms that act also on the diagonal terms! We discussed this point, as well as the question of the compatibility between Schrödinger's picture and the formalism of the density matrix; these points have been analyzed by us in an Appendix of our (unpublished) Ref. [1]. Secondly, the new discrete formalism allows not only the description of the stationary states, but also a (space–time) description of transient states. The retarded formulation yields a natural quantum theory for dissipative systems, and it is not without meaning that it leads to a simple solution of the measurement problem in QM. Thirdly, since the composite system $\mathcal{O} + \mathcal{A}$ is a complex system, it is suitably described by the *coarse grained* description (exploited by Bonifacio in some important papers of his Ref. [7]): it would be quite useful to increase our understanding of the relationship between the two mentioned pictures in order to get a deeper insight on the decoherence processes involved.

Acknowledgements

One of the authors (ER) wishes to thank Anthony Leggett, Berardo Ruggieri, Paolo Silvestrini, and all the Organizers, for their kind invitation to participating in the MQC2 Workshop and to contributing to these Proceedings, as well as for some discussions. For stimulating discussions, or kind collaboration over the years, the authors are moreover very grateful to Rodolfo Bonifacio, Mauro Brambilla, Christian Cocca, Gianni Degli Antoni, Salvatore Esposito, Flavio Fontana, Antony Legget, Giovanni Salesi, Michel Zamboni-Rached, Marisa T. Vasconselos, and Daniel Wisniwesky. Finally, they acknowledge useful discussions with V. Abate, E. O. Capelas, R. Colombi, G. C. Costa, G. Giuffrida, H. E. Hernández, F., L. C. Kretly, P. Leal-Ferreira; F. Pisano, L. Salvo, M. Santini, J. W. Swart, C. Ussami, J. Vaz, and M. Villa.

REFERENCES

[1] R. H. A. Farias and E. Recami, *Introduction of a quantum of time (chronon), and its consequences for quantum mechanics*, Report IC/98/74 (JCTP; Trieste, 1998), appeared in preliminary form c/o the Lanl Archives as the e-print quant-ph/9706059. Cf. also R. H. A. Farias: *Introduction of a 'quantun' of time into the formalism of quantum mechanics*, PhD Thesis, E. Recami supervisor (Campinas, S.P.; UNICAMP; 1994).

[2] H. D. Zee, *Found. Phys.* **1** (1970) 69; W. H. Zurek, *Phys. Rev.* **D26** (1982) 1862; J. A. Wheeler and W. H. Zurek (eds.), *Quantum Theory and Measurement* (Princeton NJ, Princeton, U.P., 1983); A. O. Caldeira and A. J. Leggett, *Physica* **A121** (1983) 587; *Phys. Rev.* **A31** (1985) 1057; E. Joss and H. D. Zee, *Z. Phys.* **B59** (1985) 223; P. Bush, P. J. Lahti, and P. Mittelstaed, *The Quantum Theory of Measurement* (Berlin, Springer, 1991); W. G. Unruh and W. H. Zurek, *Phys. Rev.* **D40** (1989) 1071; W. H. Zurek, *Physics Today* **44** (Oct. 1991), p. 36; L. Davidovich *et al.*, *Phys. Rev. Lett.* **71** (1993) 2360; M. Namiki and S. Pascazio, *Phys. Reports* **232** (1993) 301; A. J. Leggett: in *Foundations of Quantum Mechanics*, ed. by M. Tsukada *et al.* (Tokyo, 1993), p. 10; Y. Ne'eman, *Phys. Lett.* **A186** (1994) 5.

[3] P. A. M. Dirac, The classical theory of electron, *Proc. Royal Soc.* **A167** (1938) 148; *Ann. Inst. Poincaré* **9** (1938) 13. Cf. also M. Schönberg *et al.*, *Phys. Rev.* **69** (1945) 211; and *Anais Ac. Brasil. Cie.* **19** (1947) issue no. 3, pp. 46–98.

[4] P. Caldirola, *Nuovo Cimento* **10** (1953) 1747; *Suppl. Nuovo Cim.* **3** (1956) 297; *Rivista Nuovo Cim.* **2** (1979), issue no. 13, and refs. therein; *Revista Brasil. de Física*, special vol. (1984, July), p. 228. See also R. Cirelli, *Nuovo Cimento* **1** (1955) 260; L. Lanz, *Nuovo Cimento* **23** (1962) 195; F. Casagrande and E. Montaldi, *Nuovo Cimento* **A40** (1977) 369; **A44** (1978) 453; P. Caldirola and E. Montaldi, *Nuovo Cimento* **B53** (1979) 291; P. Caldirola, G. Casati and A. Prosperetti, *Nuovo Cimento* **A43** (1978) 127; P. Caldirola, *Nuovo Cimento* **A49** (1979) 497; A. Prosperetti, *Nuovo Cimento* **B57** (1980) 253; L. Belloni, *Lett. Nuovo Cim.* **31** (1981) 131; V. Benza and P. Caldirola, *Nuovo Cimento* **A62** (1981) 175; G. C. Ghirardi and T. Weber, *Lett. Nuovo Cim.* **39** (1984) 157; and in particular R. Bonifacio and P. Caldirola, *Lett. Nuovo Cim.* **38** (1983) 615; **33** (1982) 197. At last, cf. A. D. Yaghjian, *Relativistic Dynamics of a Charged Sphere* (Berlin, Springer, 1992).

[5] E. Recami and G. Salesi, *Phys. Rev.* **A57** (1998) 98; *Found. Phys.* **28** (1998) 763; *Adv. App. Cliff. Ag.* **6** (1996) 27; G. Salesi and E. Recami, *Found. Phys. Lett.* **10** (1997) 533; *Phys. Lett.* **A190** (1994) 137; **A195** (1994) E389; and refs. therein.

[6] L. E. Ballantine, What is the point of the quantum theory of measurement?, in *Fundamental Questions in Quantum Mechanics*, ed. by L. Roth and A. Inomata (Gordon & Breach, 1986).

[7] R. Bonifacio, *Lett. Nuovo Cim.* **37** (1983) 481; *Nuovo Cimento* **B114** (1999) 473; *Z. für Naturf.* **A57** (2001) 41. See also R. Bonifacio *et al.*, in [4].

SEARCHING FOR A SEMICLASSICAL SHOR'S ALGORITHM

P. Giorda[1,a], A. Iorio[2,b], S. Sen[3,c], and G. Vitiello[2,d]
[1]*Institute for Scientific Interchange, Villa Gualino, Viale Settimio Severo 65, 10133-Torino, Italy*
[2]*Dipartimento di Fisica "E.R. Caianiello" Università di Salerno, 84081 Baronissi (SA), Italy, and I.N.F.N.*
[3]*School of Mathematics, Trinity College Dublin, Dublin 2, Ireland*

Abstract: We explore the feasibility of a two-step semiclassical approximation of Shor's quantum algorithm based on coherent states. The first step is the implementation of a classical time-evolution for the spin 1/2 system making the computation. The second step is the coherent states approximation of the Shor's algorithm itself, in particular of the quantum Fourier transform (QFT). One of the aims is to eventually give an estimate of the new complexity arising from this approximation, and compare it with Pollard–Strassen's (classical) and Shor's (quantum) algorithm.

1. INTRODUCTION

Shor's quantum algorithm [1] determines the prime factors of a composite l-bit number N in[1] $O[l^2 \log l \log\log l]$ steps, while the best classical algorithm due to Pollard and Strassen [2] requires a number of steps of the order $O[\exp\{cl^{1/3} \log^{2/3} l\}]$, for some c. This was a landmark event in quantum computing and quantum cryptography. It suffices to note that, if one performs 10^{10} operations per second, easily accessible on a (classical) personal computer, the time required for the factorization of an $N \sim 10^{99}$ would improve from $\sim 10^{14}$ years to $\sim 10^{-6}$ seconds!

Nonetheless the difficulty of constructing quantum computers with the required power makes Shor's algorithm a theoretically important work which, at present, cannot be implemented. It is then of strong interest to explore *semiclassical* limits of Shor's algorithm, and to see how much these approximations affect the efficiency of the algorithm. The important problem to solve is what is a semiclassical approximation in

[a]E-mail: giorda@isiosf.isi.it
[b]E-mail: iorio@sa.infn.it
[c]E-mail: sen@maths.tcd.ie
[d]E-mail: vitiello@sa.infn.it
[1]Here, and in what follows $\log \equiv \log_2$ and $\ln = \log_e$, unless otherwise stated.

Quantum Computing and Quantum Bits in Mesoscopic Systems
Edited by Leggett *et al.*, Kluwer Academic/Plenum Publishers, 2004

this framework. In this paper, we take the first steps in that direction, while the precise computation of the correction are currently under investigation [3].

In Section 2, we shall briefly introduce the notation and review the key ideas of Shor's algorithm. In Section 3, we shall explain the first of the two steps of our semiclassical approximation based on coherent states: the classical time-evolution for the spin $1/2$ system making the computation. Finally in Section 4, we shall outline the coherent states approximation of the Shor's algorithm itself, in particular of the quantum Fourier transform (QFT).

2. NUMBER FACTORING AND QUANTUM MECHANICS

Given an l-bit integer number N, the fastest way to factor it into relative co-primes $N = n_1 \cdot n_2 \cdot \ldots$ is to find t_1 and t_2 such that $t_1^2 = t_2^2 (\text{mod } N)$, and $t_1 \neq \pm t_2 (\text{mod } N)$; thus one can write

$$(t_1 + t_2)(t_1 - t_2) = 0 \ (\text{mod } N) \tag{1}$$

and neither $(t_1 + t_2)$ nor $(t_1 - t_2)$ is zero (mod N). It is then matter of finding the greatest common divisors (gcd): $\gcd(t_1 + t_2, N)$, and $\gcd(t_1 - t_2, N)$ to have two of the factors, and so on. This approach is the same for classical and quantum algorithms.

In the quantum case a further result of number theory is used. Given the integer to be factored N, if one randomly picks an integer $1 < x < N$, and $\gcd(x, N) = 1$ (otherwise we would have been so lucky to have already found a factor of N), then the period L of the function

$$f(a) = x^a \ (\text{mod } N), \quad \text{with} \quad f(a + L) = f(a) \ (\text{mod } N) \tag{2}$$

determines the factors of N, provided L is even and $x^{L/2} \neq -1 (\text{mod } N)$. This is easily seen from the fact that $x^a = x^{a+L} (\text{mod } N)$ implies

$$x^L = 1 (\text{mod } N) \tag{3}$$

and, for L even, both sides are squares. Thus, since $x^{L/2} \neq -1 (\text{mod } N)$, one can proceed as before, and compute $\gcd(x^{L/2} + 1, N)$. This procedure would take a polynomial time on a computer that makes use of quantum superposition, and QFT. This is the Shor's method, to determine L *quickly*, that is, in polynomial time.

Let us now introduce the mathematical and physical framework to describe a quantum computer, give some of details of Shor's algorithm, and introduce the notation.

As any quantum system, a quantum computer is described by a Hilbert space [4], and its operations are implemented by operators ("quantum gates") acting on this Hilbert space. One possibility is to consider the tensor product of spin $\hbar/2$ states, to represent information in a binary digit form. As is well known, a state of such a quantum system is a string of two-level states, each spin state with $s = -\hbar/2$ (spin down) representing the binary integer zero, each spin state with $s = +\hbar/2$ (spin up) representing the binary

integer one. These states are the basis of the two-level Hilbert space $\mathcal{H}_2$, and are usually represented as

$$\left|\frac{1}{2}, -\frac{1}{2}\right\rangle \quad \text{or} \quad |0\rangle \quad \text{or} \quad \begin{pmatrix} 0 \\ 1 \end{pmatrix} \tag{4}$$

for the spin down, and

$$\left|\frac{1}{2}, +\frac{1}{2}\right\rangle \quad \text{or} \quad |1\rangle \quad \text{or} \quad \begin{pmatrix} 1 \\ 0 \end{pmatrix} \tag{5}$$

for the spin up. The full Hilbert space to represent an l-bit number is then

$$\bigotimes_{i=0}^{l-1} \mathcal{H}_2^i \tag{6}$$

Clearly such two-level systems can be physically realized in many other ways. However, in all cases, the bone structure can be represented in such a tensor product space. It is clear that the spin states introduced form a representation of the Lie algebra SU(2) of angular momentum. As is well known, this Lie algebra has three generators J_0, J_1, and J_2, and one can introduce the so-called step-up, $J_+ = J_1 + iJ_2$, and step-down, $J_- = J_1 - iJ_2$, generators to write the defining commutation relations of SU(2) as

$$[J_+, J_-] = 2\hbar J_0, \quad [J_0, J_\pm] = \pm \hbar J_\pm \tag{7}$$

also known as the Cartan–Weyl form of the Lie algebra. In the next section we shall present a semiclassical version of this quantum system.

We now want to summarize briefly the quantum factoring algorithm of Shor. Let us start with the state

$$|s\rangle = \frac{1}{\sqrt{q}} \sum_{a=0}^{q-1} |a\rangle |x^a (\text{mod } N)\rangle \tag{8}$$

where N is the number to be factored, $|a\rangle = |a_{l-1}, \ldots, a_0\rangle$, $a_i = 0,1\ \forall i = 0, \ldots, l-1$, is the quantum representative of the l-bit number $a = \sum_{i=0}^{l-1} a_i 2^i$, $a_{\max} = 2^l - 1 \equiv q - 1$, hence $q = 2^l$.

The key step in Shor's approach was to replace $|a\rangle$ by its quantum Fourier transformed

$$|a\rangle \to \frac{1}{\sqrt{q}} \sum_{c=0}^{q-1} |c\rangle \exp\left\{2\pi i \frac{a \cdot c}{q}\right\} \tag{9}$$

where, as for $|a\rangle$, $|c\rangle$ is the quantum representative of the binary number $c = \sum_{j=0}^{l-1} c_j 2^j$, $c_i = 0, 1\ \forall i = 0, \ldots, l-1$. This is achieved by acting on $|a\rangle$ with the string of $l(l-1)/2$ operators in the left-to-right order

$$\Phi = R_{l-1} S_{l-2,l-1} R_{l-2} S_{l-3,l-1} S_{l-3,l-2} R_{l-3} \cdots R_1 S_{0,l-1} S_{0,l-2} \cdots S_{0,1} R_0 \tag{10}$$

where the operators R_i act on the ith two-states Hilbert space $\mathcal{H}_2^i$, as

$$R_i = \frac{1}{\sqrt{2}}\left[|0_i\rangle\langle 0_i| + |0_i\rangle\langle 1_i| + |1_i\rangle\langle 0_i| + e^{i\pi}|1_i\rangle\langle 1_i|\right] \tag{11}$$

or

$$R_i = \frac{1}{\sqrt{2}}\begin{pmatrix} 1 & 1 \\ 1 & -1 \end{pmatrix} \tag{12}$$

depending on the notation, and the operators $S_{i,j}$, $j > i$, act on tensor products of two-states Hilbert spaces $\mathcal{H}_2^i \otimes \mathcal{H}_2^j$, and are given by

$$\begin{aligned} S_{ij} = {} & |0_i, 0_j\rangle\langle 0_i, 0_j| + |0_i, 1_j\rangle\langle 0_i, 1_j| + |1_i, 0_j\rangle\langle 1_i, 0_j| \\ & + e^{i\theta_{ij}}|1_i, 1_j\rangle\langle 1_i, 1_j| \end{aligned} \tag{13}$$

or

$$S_{i,j} = \begin{pmatrix} 1 & 0 & 0 & 0 \\ 0 & 1 & 0 & 0 \\ 0 & 0 & 1 & 0 \\ 0 & 0 & 0 & e^{i\theta_{ij}} \end{pmatrix} \tag{14}$$

depending on the notation, where $\theta_{ij} = \pi/2^{j-i}$. The string of operators in Φ can be shown to generate the required state (9) after a step of "reversing the labels" has been carried out: $b_j \to c_{l-1-j}$. The final result of acting with Φ on $|s\rangle$ is then

$$|s'\rangle = \frac{1}{q}\sum_{a,c=0}^{q-1} \exp\left\{2\pi i \frac{a \cdot c}{q}\right\}|c\rangle|x^a (\mathrm{mod}\ N)\rangle \tag{15}$$

The probability of observing c_0, and $x_k (\mathrm{mod}\ N)$ is easily computed

$$\begin{aligned} \mathbf{P}(c_0, x^k (\mathrm{mod}\ N)) &\equiv |\langle c_0, x^k (\mathrm{mod}\ N)|s'\rangle|^2 \\ &= \left|\frac{1}{q}\sum_{a=0}^{q-1} \exp\left\{2\pi i \frac{a \cdot c_0}{q}\right\}\right|^2_{a=k(\mathrm{mod}\ L)} \end{aligned} \tag{16}$$

The probability (16) is a function of the period L we want to determine, hence the measure of c_0, and $x^k (\mathrm{mod}\ N)$ turns into a measure of L. This is seen by noticing that $a = k (\mathrm{mod}\ L)$ means $a = k + bL$ for some integer b, hence

$$\mathbf{P}(c_0, x^k (\mathrm{mod}\ N)) = \left|\frac{1}{q}\sum_{b=0}^{[(q-k-1)/L]} \exp\left\{\pi i b \frac{\{Lc_0\}_q}{q/2}\right\}\right|^2 \tag{17}$$

where $[A]$ indicates the integer part of A, $Lc_0 = dq + \{Lc_0\}_q$ for some integer d. We also want this probability to be as close as possible to 1, and this is obtained by requiring

$$-\frac{q}{2} < \{Lc_0\}_q < \frac{q}{2} \tag{18}$$

which gives

$$\left|\frac{c_0}{q} - \frac{d}{L}\right| < \frac{1}{2L} \tag{19}$$

It is then matter of picking up the right c_0, see, for instance, Ref. [1] for a plot of **P** as a function of c_0. It turns out [1, 2] that the probability is

$$\mathbf{P}(c_0, x^k(\text{mod } N)) > \frac{1}{3L^2} \tag{20}$$

By looking at Eq. (19) one immediately sees that we have found L: c_0 was measured, q is known, and d/L is the best rational representation of the real number c_0/q, and can be determined by using the continuous fraction approximation.

We can estimate the leading contributions to the complexity of this algorithm. There are two relevant operations: (i) the quantum Fourier transform Φ, and (ii) the measure of c_0 and $x^k(\text{mod } N)$.

(i) By counting how many operators enter the expression (10) of Φ, we notice that this part of the algorithm involves $O(l^2)$ steps.

(ii) From Eq. (20) the number of measurements that have to be performed in order to have the overall probability close to 1 is $O(L^2)$. From Eq. (3) we see that $L \sim O(\log N) \sim O(l)$. Thus we find that the complexity of this part is again $O(l^2)$.

3. SYMPLECTIC STRUCTURE AND CLASSICAL TIME-EVOLUTION

We want now to exploit the semiclassical nature of the coherent states associated with the Lie algebra SU(2), to present our semiclassical approximations in two separate steps. First we shall construct the phase-space associated with the Lie algebra of the angular momentum (7). After that standard step has been taken, we shall outline our coherent states approximation of Shor's algorithm, with special emphasis on the QFT Φ [3].

Mathematically a semiclassical representation of the Lie algebra SU(2) corresponds to determining the phase-space, with its symplectic structure, such that commutators of the Lie algebra are realized as Poisson brackets of appropriate functions derived in this phase-space. The procedure for doing this is well known. Let us briefly summarize the steps involved.

The basic idea is to introduce the coherent state [5]

$$|\lambda\rangle = \exp\left\{\lambda \frac{J_+}{\hbar}\right\} \left|\frac{1}{2}, -\frac{1}{2}\right\rangle, \tag{21}$$

where λ is a complex number, we use the basis $|1/2, -1/2\rangle$, $|1/2, +1/2\rangle$, and we have made the angular momentum operators dimensionless. Note that this last point is of some importance since we are going to introduce dimensionless Poisson brackets, while the standard Poisson brackets have dimension of [action]$^{-1}$. Thus we shall eventually end up

with a symplectic structure where $\hbar$ is hidden in the dimensionless operators, which we shall still call J_0, J_+, and J_-. In the coherent state representation these operators, suitably normalized, are the complex functions [5]

$$\begin{aligned} \mathcal{J}_0 &\equiv \frac{\langle\lambda|J_0|\lambda\rangle}{\langle\lambda|\lambda\rangle} = -\frac{1}{2}\frac{1-|\lambda|^2}{1+|\lambda|^2} \\ \mathcal{J}_+ &\equiv \frac{\langle\lambda|J_+|\lambda\rangle}{\langle\lambda|\lambda\rangle} = \frac{\bar{\lambda}}{1+|\lambda|^2} \\ \mathcal{J}_- &\equiv \frac{\langle\lambda|J_-|\lambda\rangle}{\langle\lambda|\lambda\rangle} = \frac{\lambda}{1+|\lambda|^2} \end{aligned} \tag{22}$$

They have the property that $\mathcal{J}_+\mathcal{J}_-\mathcal{J}_0^2 = 1/4$, that is, the vector $(\mathcal{J}_0, \mathcal{J}_1, \mathcal{J}_2)$ has length $j = 1/2$, and it represents a point on the surface of the sphere $S^2 \sim SU(2)/U(1)$ of radius $1/2$.

We can now introduce the Kähler potential $V(\lambda, \bar{\lambda}) = \ln\langle\lambda|\lambda\rangle = \ln(1+|\lambda|^2)$, to construct the associated symplectic form [6] ω on the phase-space defined by the complex variables λ, and $\bar{\lambda}$. This form is given by

$$\omega = \omega_{\lambda,\bar{\lambda}} d\lambda \wedge d\bar{\lambda} \tag{23}$$

where

$$\omega_{\bar{\lambda},\lambda} = -\omega_{\lambda,\bar{\lambda}} \equiv \frac{\partial^2 V}{\partial\lambda\partial\bar{\lambda}} = (1+|\lambda|^2)^{-2} \tag{24}$$

and of course $(\omega^{-1})_{\lambda,\bar{\lambda}} = (1+|\lambda|^2)^2$. The Poisson brackets of two functions on the λ, $\bar{\lambda}$ phase-space, $f(\lambda, \bar{\lambda})$, $g(\lambda, \bar{\lambda})$ can now be defined as

$$\{f, g\} \equiv (\omega^{-1})_{\lambda,\bar{\lambda}} \partial_\lambda f \partial_{\bar{\lambda}} g + (\omega^{-1})_{\lambda,\bar{\lambda}} \partial_{\bar{\lambda}} f \partial_\lambda g \tag{25}$$

The Poisson brackets of $\mathcal{J}_0$, $\mathcal{J}_+$, $\mathcal{J}_-$ can be easily computed, and are

$$\{\mathcal{J}_+, \mathcal{J}_-\} = 2\mathcal{J}_0, \quad \{\mathcal{J}_0, \mathcal{J}_\pm\} = \pm\mathcal{J}_\pm \tag{26}$$

They give back the Lie algebra SU(2) we started with in a dimensionless semiclassical form. This establishes the fact that the phase-space corresponding to SU(2) is $S^2 \sim SU(2)/U(1)$ with stereographic coordinates $\mathcal{J}_+$, $\mathcal{J}_-$, and $\mathcal{J}_0$.

We can move further to define the Hamiltonian H associated with the symplectic form ω. One starts by introducing a vector field v that keeps ω invariant

$$\mathbf{L}_v \omega = 0 \tag{27}$$

where $\mathbf{L}_v$ is the Lie derivative [6] associated with the vector field v. One can also write the Lie derivative as $\mathbf{L}_v = d \cdot i_v + i_v \cdot d$, where d and i_v act on p-forms Ω^p as d: $\Omega^p \to \Omega^{p+1}$, and i_v: $\Omega^p \to \Omega^{p-1}$. To be more explicit let us write a p-form in local coordinates on a

symplectic manifold M of even dimension $2n$

$$\Omega^p = \frac{1}{p!} \sum_{i_1,\ldots,i_p=1}^{2n} \Omega_{i_1,\ldots,i_p}(x_1, \ldots, x_{2n})\, dx_{i_1} \wedge \cdots \wedge dx_{i_p} \tag{28}$$

where $\Omega_{i_1,\ldots,i_p}$ is a totally antisymmetric tensor field, and $x_1, \ldots, x_{2n}$ are the local coordinates on the $2n$-dimensional symplectic manifold M. Thus

$$d\Omega^p = \frac{1}{(p+1)!} \sum_{k,i_1,\ldots,i_p=1}^{2n} \frac{\partial \Omega_{i_1,\ldots,i_p}}{\partial x_k}(x_1, \ldots, x_{2n})\, dx_k \wedge dx_{i_1} \wedge \cdots \wedge dx_{i_p} \tag{29}$$

while

$$i_v\Omega^p = \frac{1}{(p-1)!} \sum_{i_1,\ldots,i_p=1}^{2n} (-1)^j \Omega_{i_1,\ldots,j,\ldots,i_p}(x_1, \ldots, x_{2n})\, dx_{i_1} \wedge \cdots \wedge d\hat{x}_j \wedge \cdots \wedge dx_{i_p} \tag{30}$$

where $d\hat{x}_j$ means that dx_j is missing.

With the help of these definitions it is now easy to make use of the condition (27) to write

$$\mathbf{L}_v\omega = (d \cdot i_v + i_v \cdot d)\omega = 0 \tag{31}$$

but from the definition of symplectic forms it follows that $d\omega = 0$, hence $d \cdot (i_v\omega) = 0$, that is, the one-form $i_v\omega$ is closed. According to the lemma of Poincaré it follows that locally the one-form is equal to d acting on a function (a zero-form):

$$i_v\omega = dH \tag{32}$$

where H is a function locally defined on the phase-space of the system. If H can be globally defined then it can be taken as the Hamiltonian corresponding to the vector field v.

In our case, we can follow the above outlined procedure to obtain

$$H = -\frac{1}{2}\frac{1-\lambda\bar{\lambda}}{1+\lambda\bar{\lambda}} \tag{33}$$

as a possible classical Hamiltonian. Once H is chosen it determines the dynamics in the phase-space, and the "time-evolution" of any function $f(\lambda, \bar{\lambda})$ is given by

$$\dot{f} \equiv \{H, f\} \tag{34}$$

it is straightforward to check that $\dot{f} = i\partial f/\partial\phi$, where $\lambda = re^{i\phi}$ hence the dimensionless time parameter of the semiclassical evolution is $t = -i\phi$.

By noting that $\mathcal{J}_0 = H$, and using Eq. (26) one has

$$\dot{\mathcal{J}}_\pm = \mathcal{J}_\pm, \quad \dot{\mathcal{J}}_0 = 0 \tag{35}$$

Thus in the semiclassical limit the quantum spin system we started out with has been replaced by coordinates on S^2 with the associated symplectic form. Consistently with this symplectic form a Hamiltonian can be introduced, which leads to the coordinates $\mathcal{J}_+$, and $\mathcal{J}_-$ precessing uniformly, always preserving the length of the vector. This is a classical spinning vector. Note also that

$$\{\mathcal{J}_+, \mathcal{J}_-\} = 2H \tag{36}$$

The first step towards our attempt to construct a semiclassical version of Shor's algorithm is now complete.

4. COHERENT STATE APPROXIMATION OF SHOR'S ALGORITHM

We now want to describe the strategy of the second stage of the semiclassical approximation, leaving to a following paper [3] the exact computation of the feasibility.

The key step we propose to modify in the original quantum algorithm of Shor is the one involving the QFT Φ. We recall that the Fourier transformation consists in the following replacement

$$|a\rangle \to \sum_{c=0}^{q-1} |c\rangle\langle c|\Phi|a\rangle \tag{37}$$

with $\langle c|\Phi|a\rangle = q^{-1/2} \exp\{2\pi i a \cdot c/q\}$. As noted earlier this transformation is at the core of the factorization algorithm.

What we intend to do [3], is to implement the QFT in the coherent state basis $|\lambda\rangle$. This represents the most crucial point of our semiclassical approximation, and we claim that such an approach could shed some light on the implementation of Shor's algorithm on *macroscopic quantum* devices. This would represent a major breakthrough, since nowadays those devices are experimentally feasible.

Of course a crucial issue is to eventually give an estimate of the new complexity arising from this approximation, and compare it with Pollard–Strassen's (classical) and Shor's (quantum) algorithm [3]. Only then we can say whether this semiclassical approximation is of any practical use.

Acknowledgements

A.I. and G.V. acknowledge the financial support of the European Science Foundation, Network COSLAB.

REFERENCES

[1] P. Shor, *SIAM J. Sci. Statist. Comput.* 26 (1997) 1484. LANL e-print archive: quant-ph/9508027 available on line at http://xxx.lanl.gov

[2] P. Shor, *Introduction to Quantum Algorithms*, LANL e-print archive: quant-ph/0005003 (July 2001) available on line at http://xxx.lanl.gov

[3] P. Giorda, A. Iorio, S. Sen, and G. Vitiello, *Semi-Classical Shor's Algorithm*, in preparation.

[4] P. A. M. Dirac, *The Principles of Quantum Mechanics*, Clarendon Press (Oxford), 1958; Yu. Manin, *Computable and Uncomputable* (in Russian), Sovetskoye Radio, Moscow (1980); R. P. Feynman, Simulating physics with computers, *Int. J. Theo. Phys.* **21** (1982), 467; R. P. Feynman, Quantum Mechanical Computers, *Found. Phys.* **16** (1986), 507.

[5] A. Perelomov, *Generalized Coherent States* (Springer-Verlag, 1986).

[6] M. Nakahara, *Geometry, Topology and Physics* (Adam Hilger, 1990); C. Nash and S. Sen, *Topology and Geometry for Physicists* (Academic Press, 1983).

LOW T_c JOSEPHSON JUNCTION RESPONSE TO AN ULTRAFAST LASER PULSE

P. Lucignano[1,a], A. Tagliacozzo[1,b], and F. W. J. Hekking[2,c]
[1]*INFM, unita' di Napoli, Dipartimento di Scienze Fisiche Universita Federico II' Napoli, Monte S. Angelo, Via Cintia 80126 Napoli, Italy*
[2]*Laboratoire de Physique et Modélisation des Milieux, Condensés, Maison des Magistères Jean Perrin, BP 166,38042 Grenoble, Cedex 9, France*

Abstract: We study the interaction of ultrafast laser radiation (<100 fs pulses) with a Josephson junction. For very weak radiated power, heating of the junction is assumed to be negligible and relaxation of the order parameter is disregarded. The time evolution of the order parameter phase $\varphi(t)$, after the arrival of the pulse, is studied within a time-dependent Bogoliubov–de Gennes mean field theory. While the effect of the optical frequency of the laser is averaged out, two characteristic time scales arise in the Josephson current. The first is related to the pair breaking time $\hbar/\Delta_0$, while the second is related to the pulse duration. The latter marks the time scale for oscillations in the envelope function of the Josephson current.

1. INTRODUCTION

The characteristic frequency in the dynamics of a Josephson junction (JJ) is the so-called Josephson plasma frequency ω_J, which is in the range of microwaves. Coupling a JJ to a microwave field leads to the well-known lock-in conditions, which show up as Shapiro steps in the I/V characteristic. On the other hand, photoresponse to laser radiation induces heat relaxation (bolometric effect) and nonequilibrium generation of quasiparticles. Both phenomena are extensively studied since they are relevant for the fabrication of fast and sensitive detectors. The model used, involving different temperatures associated with separate distributions of electrons and phonons out of equilibrium is essentially phenomenological [1–3].

In recent years, laser light with pulses of many femtoseconds duration has become available as a source to test the photoresponse of a JJ. This type of tool can be extremely useful, in that it allows studying an unexplored regime in non-equilibrium superconductivity. Also, it is quite valuable for future applications,

[a]E-mail: procolo@na.infn.it
[b]E-mail: arturo@na.infn.it
[c]E-mail: hekking@polycnrs-gre.fr

Quantum Computing and Quantum Bits in Mesoscopic Systems
Edited by Leggett *et al.*, Kluwer Academic/Plenum Publishers, 2004

because fast pulses in flux and gate voltages are extremely important when processing information in superconducting quantum computing devices (qubits) [4]. Indeed, finite rise and fall times of pulses may result in a significant error in dynamic computation schemes [5].

We take a low T_c JJ as the reference case. Although the laser optical frequency ($\omega \sim 100$ THz) is quite high compared to ω_J, the power of the laser can be reduced enough, so that the energy released by the radiation on the junction is quite small. If the time interval between two pulses is long enough, the bolometric response can be neglected. On the other hand, the duration τ_c of the laser pulses ($\sim$80–140 fs) is short compared to the pair-breaking time $\hbar/\Delta_0 \sim 1$–5 ps. However, the evolution time of the order parameter, $\tau_\psi \sim \tau_{e-e} \sim \tau_{e-ph}$, which is strongly material dependent and $\sim$20 ps in the case of Nb, will be a relevant comparison time scale for our picture, because it regulates the superconductive behavior in the nonequilibrium regime. In our approach, we assume that, on a time scale intermediate between the pulse length and the relaxation time $\sim\tau_\psi$, the order parameter behaves coherently and acquires an extra phase due to the coupling to the pulse. The quasi-particles (qp) coherence factors enter the definition of the superconducting order parameter and their dynamics is studied within a Bogoliubov–de Gennes time-dependent formalism, sticking, however, to an equilibrium qp distribution. At low temperatures the response of the coherence factors of the superconducting electrode to the radiation is averaged over the period of the optical frequency ω.

This chapter is organized as follows. In Section 2, we set up the general formalism, to calculate the time-dependent phase $\varphi(t)$ of the superconducting order parameter after the impinging of the pulse, within the time-dependent Bogoliubov–de Gennes equations (TdBdGE). In Section 3, the TdBdGE is averaged with respect to the frequency ω, and the Josephson current is calculated, which is found to oscillate with frequency $\Delta_0/\hbar$. In addition, the perturbation to the Josephson current has an envelop, slowly oscillating in time, whose period is, in our approximation, the same as the pulse duration.

2. TIME-DEPENDENT BOGOLIUBOV–DE GENNES EQUATIONS

An idealized Josephson overlap tunnel junction is sketched in Fig. 1. As explained in the introduction the device operates in a regime characterized by $\omega \gg \omega_c \gg \Delta_0/\hbar \gg \tau_\psi^{-1}$. Here ω is the optical frequency, ω_c is the inverse of the pulse duration τ_c, Δ_0 is the

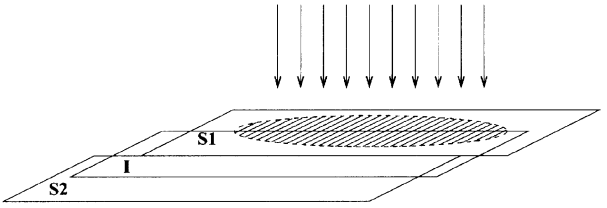

Figure 1. Irradiated Josephson tunnel junction.

magnitude of the gap in the unperturbed excitation spectrum, and τ_ψ is the order parameter relaxation time.

The penetration depth of the laser light λ in the topmost layer $S1$ is assumed to be shorter than its thickness, so that any modification induced by the radiation field only involves $S1$ (see the idealized geometry in Fig. 1). At $T \ll T_c$, we assume that superconducting coherence is not affected by the pulse. However,the pulse itself induces a nonequilibrium dynamics of the order parameter, which we describe by the TdBdGE [6]. These equations assume slow space and time dependence of the superconducting coherence factors u_k, v_k entering the self-consistent definition of the order parameter:

$$\Delta(\vec{r}, t) = \lambda \sum_k u_k(\vec{r}, t) v_k^*(\vec{r}, t)[1 - 2f_k(\vec{r}, t)] \tag{1}$$

In Eq. (1), λ is the strength of the electron–phonon coupling and $f_k(\vec{r}, t)$ is the space and time-dependent qp nonequilibrium distribution function for the excitation mode of wave vector k. The TdBdGE are:

$$i\hbar \frac{\partial}{\partial t} u_k = \left\{ \frac{1}{2m} [\vec{p} - e\vec{A}(\vec{r}, t)]^2 + V(\vec{r}, t) - \mu \right\} u_k + \Delta(\vec{r}, t) v_k \tag{2}$$

$$i\hbar \frac{\partial}{\partial t} v_k = -\left\{ \frac{1}{2m} [\vec{p} + e\vec{A}(\vec{r}, t)]^2 + V(\vec{r}, t) - \mu \right\} v_k + \Delta(\vec{r}, t) u_k \tag{3}$$

We neglect the scalar potential $V(\vec{r}, t)$ and we measure all energies with respect to the Fermi level μ, which we assume to be unperturbed by the radiation on average. The TdBdGE can be derived as a mean field limit of the semiclassical equations for the nonequilibrium Green's functions, for example, in the Usadel approximation [7]. The nonequilibrium distribution functions should be self-consistently determined from the appropriate kinetic equations. In the present discussion, we will not consider nonequilibrium in the distribution functions and use the zero temperature Fermi factors f_k instead. In Eqs (2) and (3) the vector potential $A(\vec{r}, t)$ couples the radiation to the coherence factors u_k and v_k. In addition, we consider a small size JJ, that is, we do not take into account spatial variation of the order parameter in $S1$. The k-vector that appears in Eqs (2) and (3) is the relative momentum of the pair. The TdBdGE are intended to be solved for each k, but this label will be suppressed when possible hereafter.

3. RESPONSE TO A SHORT LASER PULSE

In the case of a short pulse laser radiation, we expect that the response of the system to the optical frequencies ($\omega \sim 100$ THz) is very weak and the dynamics, on that time scale, can be averaged out. Hence the superconducting coherence is not severely affected, but the order parameter enters a nonequilibrium dynamical state, which we analyze in this paper.

The laser vector potential is

$$A(r, t) = \sum_{\pm} a_{\pm}(r, t) e^{\pm i\omega t} \tag{4}$$

where $a_\pm$ is a slowly varying "envelope" function, corresponding to the femtosecond pulse, and the terms $e^{\pm i\omega t}$ oscillate at optical frequencies ($\pm\omega$). We look for solutions of Eqs (2) and (3) in the form

$$u_k = U_k + \sum_{\pm} \chi_k^{\pm} e^{\pm i\omega t}, \quad v_k = V_k + \sum_{\pm} \eta_k^{\pm} e^{\pm i\omega t} \tag{5}$$

where U_k is a slowly varying function of space and time (on the ω^{-1} scale); while χ_k and η_k vary on the fast scale. The same form is assumed in the gap Δ of Eq. (1).

A decomposition of TdBdGE into harmonics arises. We define the zero-order harmonic equation to be the one that does not contain exponentials $e^{\pm i\omega t}$. We neglect harmonic equations of order two, or higher. The zero-order harmonic equations also include the fast varying components $\chi^{\pm}$ and $\eta^{\pm}$, which appear in Eq. (5). One can use the first-order harmonic equation to relate $\chi^{\pm}$ and $\eta^{\pm}$ to the derivatives of the slowly varying components U_k and V_k. These derivatives are of order $1/R$, where R is the transverse dimension of the laser beam on the sample. In addition, these derivatives are multiplied by a (small) factor $1/\omega$. We thus see that the terms including $\chi^{\pm}$ and $\eta^{\pm}$ in the zero-order equation can be neglected if $\hbar\omega \gg \hbar^2/4mR$.

As a result, only the intensity of the electromagnetic field appears in the zero-order harmonic equation. Because a large spot size, R, is assumed in the following, we drop any r-dependence whatsoever. Under these conditions, we obtain the zero-order harmonic equations:

$$\begin{cases} \left[-i\hbar\dfrac{\partial}{\partial t} + \xi_k + Q\delta(t)\right] U_k(t) + \Delta(t) V_k(t) = 0 \\ \left[-i\hbar\dfrac{\partial}{\partial t} - \xi_k - Q\delta(t)\right] V_k(t) + \Delta^*(t) U_k(t) = 0 \end{cases} \tag{6}$$

where

$$\xi_k = \frac{\hbar^2 k^2}{2m} - \mu$$

and

$$a_+ a_- \approx \frac{\mathcal{E}}{m\omega^2 R^2}\,\delta(t) \equiv Q\delta(t) \tag{7}$$

where $\mathcal{E}$ is the energy per particle released by the radiation. Because the pulse is very short, on the time scales of the order parameter dynamics, we have approximated the time dependence of the light intensity with a Dirac-delta in time, $Q\delta(t)$. Its amplitude is anyhow small: $Q \sim (0.01\text{–}0.1)\hbar$.

It is a hard task to solve Eq. (6) together with Eq. (1) self-consistently. An approximate solution is based on the physical Ansatz that the gap parameter of the superconductor exposed to the radiation is

$$\Delta(t) = \Delta_0 e^{-i\varphi(t)} \tag{8}$$

where $\Delta_0 = \sum_k u_k^0 v_k^0$ is the unperturbed gap parameter of the BCS theory, with

$$u_k^{0^2} = \frac{1}{2}\left(1 + \frac{\xi_k}{E_k}\right), \quad v_k^{0^2} = \frac{1}{2}\left(1 - \frac{\xi_k}{E_k}\right) \tag{9}$$

where $E_k = \sqrt{\xi_k^2 + \Delta^2}$ is the quasi-particle energy spectrum.

Inserting Eq. (8) into Eq. (6), we get the equation satisfied by $\varphi(t)$:

$$\dot{\varphi}(t) = iQ \sum_k (|v_k^0|^2 e^{i(E_k + \xi_k)t} - |u_k^0|^2 e^{i(\xi_k - E_k)t}) \tag{10}$$

for $t > 0$ with the initial condition $\varphi(t \leq 0) = 0$.

In order to perform the sum over k vectors in Eq. (10) we change it into an integral over energies by introducing a density of states $N(\xi)$. We approximate $N(\xi)$ with its value at the Fermi energy $N(\mu)$. Two contributions are singled out, which we represent symbolically as

$$\sum_k \rightarrow \sum_{|\xi_k| < \Delta_0} + \sum_{\omega_c > |\xi_k| > \Delta_0} \tag{11}$$

The first term includes changes in the coherence of the Cooper pair condensate, but no changes due to real excitation processes. On the contrary, the second one in the right-hand side includes the effect of real pair-breaking processes and contributes to the imaginary part of φ, that is, to the damping of the order parameter.

A δ-like pulse in time would imply that all frequencies up to infinity are involved in the second sum. Of course this is unphysical and the finite time duration of the pulse τ_c acts as a phenomenological cut-off for the energies involved: $\omega_c \approx \tau_c^{-1}$.

As a result, a change of the phase in the upper superconductor produces a change in the Josephson current flowing across the junction given by

$$\delta J(t) = -\frac{e^*}{m^* d} \frac{|\Delta_0|}{k_B T_c} e^{-\Im m \varphi} \sin(\Re e \varphi) \tag{12}$$

We find that $\Im m \varphi$ modulates the envelope of this current correction on the (long) time scale $\theta \sim 4\pi\omega_c/\Delta_0^2$, while $\Re e \varphi$ is responsible for fast oscillations in the Josephson current dynamics on the much shorter pair-breaking scale $\Delta_0^{-1} \ll \theta$. The Josephson current is plotted in Fig. 2 divided by the prefactor $J_0 = |\Delta_0| e^*/k_B T_c m^* d$ as a function of time for two values

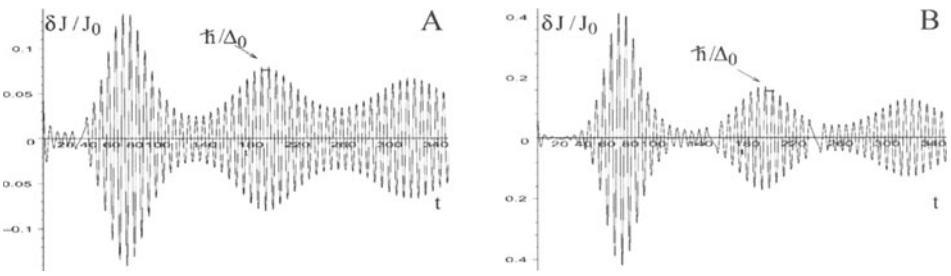

Figure 2. Josephson current vs. time in arbitrary unit of time. The control parameter Q for the laser intensity is $Q = 0.01(A)$ and $Q = 0.1(B)$.

of the energy released by the laser (with $Q = 0.01(A)$ and $Q = 0.1(B)$). The time scales θ and Δ_0^{-1} do not depend on Q because nonlinear terms do not show up in our approximation. However, the oscillations of the envelope function are much more prominent when Q is increased. The cut-off frequency ω_c of Eq. (11) is also responsible for the delay in the response of the system to the pulse. The consequence of a finite duration of the pulse is the appearance of a delay time $\tau_d \sim 2\omega_c/\Delta_0^2$ after which the first current peak starts.

4. DISCUSSION

Relaxation processes are not included in our model. We expect, however, that the oscillations at later times in Fig. 2, which are due to a coherent interference, will be washed out when relaxation processes are taken into account. Relaxation typically occurs on time scales of the order of τ_ψ. For instance, in the case of Nb ($\Delta_0 \sim 9$ K) the pair in breaking time $\hbar/\Delta_0$ is about 1 ps, whereas the time scale of the oscillation of the order parameter envelope function θ is of the order 20 ps. Because in Nb $\tau_\psi \sim \tau_{e-ph} \sim 20$ ps we expect that only the first few oscillations will be visible.

The model should be improved taking into account corrections to the qp distribution functions due to nonequilibrium. This will be done supplementing the TdBdGE and self-consistent gap equations with a kinetic relaxation type equation for the nonequilibrium distribution functions $f_k(t)$ [8]. This allows us to check the main assumption underlying our calculation, that is, the persistence of superconducting coherence also in presence of the pulse and the absence of sizeable bolometric effects caused by the perturbation.

An experimental test is planned at INFM laboratories *Coherentia* in Napoli.

Acknowledgement

We acknowledge important discussions with E. Santamato and A. Barone.

REFERENCES

[1] A. V. Sergeev and M. Yu. Reizer, *J. Mod. Phys.* B **6**, 635 (1996), M. Yu. Reizer, *Phys. Rev.* B **39**, 1602 (1989), A. V. Sergeev and M. Yu. Reizer, *Zh. Eks. Teor. Fiz.* **90**, 1096 (1986) [*Sov. Phys. JETP* **63**, 616 (1986)].

[2] M. Lindgren, M. Currie, C. Williams, T. Y. Hsiang, P. M. Fauchet, R. Sobolewski, S. H. Moffat, R. A. Hughes, J. S. Preston, and F. A. Hegmann, *Appl. Phys. Lett.* **74**, 853 (1999).

[3] A. D. Semenov, R. S. Nebosis, Yu. Gousev, M. A. Heusinger, and K. F. Renk, *Phys. Rev.* B **52**, 581 (1995).

[4] Yu. Makhlin, G. Schön, and A. Shnirman, *Rev. Mod. Phys.* **73**, 357 (2001).

[5] M. S. Choi, R. Fazio, J. Siewert, and C. Bruder, *Europhys. Lett.* **53**, 251 (2001).

[6] R. Kümmel, *Z. Physik* **218**, 472 (1969); R. Kümmel, in *Physics and Applications of Mesoscopic Josephson Junctions*, edited by H. Ohta and G. Ishii (Tokyo, The Physical Society of Japan, 1999).

[7] J. Rammer and H. Smith, *Rev. Mod. Phys.* **58**, 323 (1986).

[8] R. Kümmel, U. Gunsenheimer, and R. Nicolsky, *Phys. Rev.* B **42**, 3992 (1990).

INFLUENCE OF THE MEASUREMENT PROCESS ON THE STEP WIDTH IN THE COULOMB STAIRCASE

R. Schäfer[1], B. Limbach[1,2], P. vom Stein[1,2], and C. Wallisser[1,2]
[1]*Forschungszentrum Karlsruhe, Institut für Festkörperphysik, D-76121 Karlsruhe, Germany*
[2]*Universität Karlsruhe, Fakultät für Physik, D-76128 Karlsruhe, Germany*

1. INTRODUCTION

Recently the single-electron electrometer has gained new attention as it might serve as the primary readout device of the coherent state of a charge qubit represented by a superconducting single-electron box. Already in the early 1990s it became clear by pioneering experiments of the Saclay group (e.g., Ref. [1]) that the single-electron transistor can serve as the most sensitive electrometer known today. However, only the recently grown interest in the device has stimulated a more detailed look at the performance of the device in the actual measurement process from the theoretical side [2, 3]. For fundamental reasons that are at the heart of quantum mechanics a detector sensitive at the quantum level intermingles inextricably with the quantum system it observes. So it is natural to expect that the couplings between a single-electron box and a single-electron electrometer as it was realized, for example, in Ref. [4], have a strong mutual influence on each other. In this paper we describe experiments on a capacitively coupled system of two single-electron transistors made of aluminum with aluminum-oxide tunnel barriers in a layout very similar to the one used in Ref. [1]. One of the transistors is operated as a single-electron box by connecting source and drain to ground in parallel. The other is used as an electrometer to detect the charge state of the box. We take a close look at the mutual influence, which becomes easily noticeable at the degeneracy points of the box, where two box-charge states differing by an elementary charge e are energetically equivalent. Such degeneracy points can be crossed periodically by ramping up the box-gate voltage at a constant rate. In an isolated box, driving the box-gate voltage across a degeneracy point would result in a sharp jump of the mean box charge. The width of the jump is expected to be related to the temperature $T = 1/k_B\beta$ of the system by

$$f(m_b) = \frac{1}{1 + \exp(\beta E_b(1 - 2m_b))} \tag{1}$$

Quantum Computing and Quantum Bits in Mesoscopic Systems
Edited by Leggett *et al.*, Kluwer Academic/Plenum Publishers, 2004

where m_b is the gate charge in units of e, and we denote the charging energy of the box by E_b. In this paper we demonstrate that relation (1) is not applicable for a coupled system when information about the box state is actually accessed by the electrometer. This is evident from our experimental data as well as from an analysis of the complete system consisting of the box and the electrometer in the framework of the sequential tunneling approach [5].

We study our sample in the normal conducting state (suppressing the superconductivity of aluminum by a sufficiently high magnetic field) as well as in the superconducting state. Most of the paper deals with the normal conducting case where a simple description by the sequential tunneling of single electrons is presumably applicable. The superconducting case is considerably more complex as tunneling of quasiparticles as well as Cooper-pair tunneling plays a role.

Our sample is relatively simple and does not include quasi-particle traps used in more elaborate experiments (e.g. Ref. [4]). So it is not surprising that we do not observe $2e$-periodic behavior expected for the Cooper-pair box even at 26 mK. e-Periodicity signals that we are dealing with a nonequilibrium situation where more quasi-particles are present than accounted for by thermal equilibrium. Essentially a single quasi-particle in the volume of the sample is enough to switch from the proper $2e$-periodic ground-state behavior to the nonequilibrium e-periodic behavior. As the recombination rate for quasiparticles can be rather long, even a very low generation rate for quasi-particles can perpetuate the non-equilibrium situation. Nevertheless, we do observe a saturation behavior of the transition width at low temperatures very similar to the results of Ref. [4]. In this former publication the saturation of the transition width in the superconducting box has been attributed to the lifting of the degeneracy due to the Josephson coupling. In our situation the reasoning used in Ref. [4]—based on a two-state Hamiltonian where the states coupled by Josephson tunneling differ by two elementary charges on the box island—is obviously not applicable. In Section 4 we argue that the nonequilibrium leading to the e-periodicity serves as a natural mechanism for the observed saturation, too.

2. SEQUENTIAL MODEL

In the description of the most relevant properties of the system we restrict ourselves to the so-called sequential model, which is known to describe systems of small tunnel junctions with conductances G small compared to $G_K = e^2/h$ to lowest order in $g = G/G_K$. The system of interest is sketched in Fig. 1 and the notation used in this section is introduced in Table 1. The total charge on the box and transistor island is given by $Q_b = U_b C_b - em_b - U_t C_g$ and $Q_t = U_t C_t - en_t - U_b C_g$, respectively, where U_b and U_t are the electrical potentials on the box and transistor island. In the experiment C_d and C_c' represent the primary gates of the box and the transistor, respectively, while C_c and C_d' are considerably smaller and represent the unavoidable stray capacitances. The relations for Q_b and Q_t yield $eU_b = 2E_b(Q_b/e + m_b) + 2E_g(Q_t/e + n_t)$ and $eU_t = 2E_t(Q_t/e + n_t) + 2E_g(Q_b/e + m_b)$. In the sequential model the states of the system are classified by the number of excess electrons on the box and transistor island, m and n, respectively. The total charging energy of the system depends on the dimensionless polarization charges m_b and n_t as well as on m and n and may be evaluated from $E_{(m,n)}(m_b, n_t) = \int_{-em_b}^{-em} U_b(Q_t = -en_t)\,dQ_b + \int_{-en_t}^{-en} U_t(Q_b = -em)\,dQ_t$:

$$E_{(m,n)}(m_b, n_t) = E_b(m - m_b)^2 + E_t(n - n_t)^2 + 2E_g(m - m_b)(n - n_t) \tag{2}$$

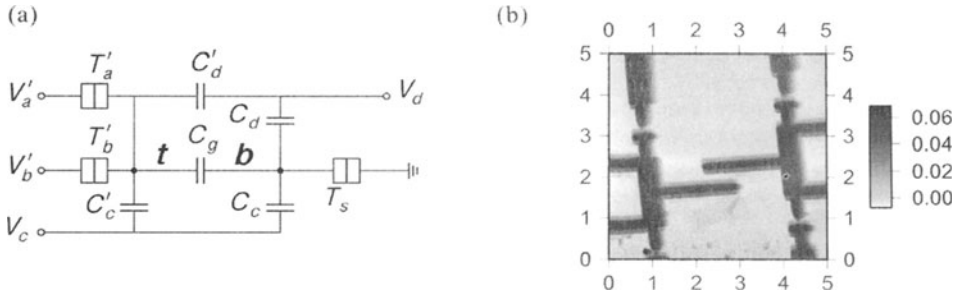

Figure 1. (a) Transistor t and box b coupled by the capacity C_g. The tunnel contacts T'_i, $i \in \{a, b, s\}$ are characterized by a capacity C'_i and a conductance G'_i. The tunnel contact T_s is built from two contacts in parallel, namely T_a and T_b. (b) Atomic-force microscope picture of the sample. In the center of the picture are the islands of the two transistors. The coupling is adjusted by varying the length of the two fingers pointing inwards. The gates of the two transistors are realized via electrodes not visible in the picture. Units: μm.

Transitions between the states occur via tunneling of electrons across the tunneling barriers. In the normal-conducting case only the sequential tunneling of single electrons is taken into account. In the superconducting case the sequential tunneling of quasi-particles is exponentially suppressed for energies within the gap. In this region the coherent tunneling of Cooper pairs has to be taken into account as it might be the leading mechanism for changing the island charge. In this section we restrict ourselves to the normal-conducting case for the sake of simplicity. Tunneling across T'_a and T'_b onto the transistor island is associated with an energy consumption of $\Delta E_i(n) = \int_{-ne}^{-(n+1)e} (U_t - V'_i)\, dQ_t = 2E_t(n + 1/2 - n_t) + 2E_g(m - m_b) + eV'_i$, $i \in \{a, b\}$. These tunneling events mediate between states differing in n by one. Similarly $\Delta E_s(m) = \int_{-me}^{-(m+1)e} U_b\, dQ_b = 2E_b(m + 1/2 - m_b) + 2E_g(n - n_t)$ describes tunneling across T_s mediating between states differing in m by one. Tunneling rates for the individual junctions can be deduced using Fermi's golden rule [5] which in the normal-conducting case yields $\Gamma_i(k \to k + 1) = (g_i/h)\Delta E_i/(\exp(\beta \Delta E_i) - 1)$, $i \in \{a, b, s\}$. Here g_i is the dimensionless conductance $g_i = G_i/G_K$ of the corresponding contact, k has to be identified with m if $i = s$ or with n otherwise. The inverse processes of tunneling from the islands to the leads is associated with an energy of the same magnitude but

Table 1. Shorthands used in this chapter (see Fig. 1(a)).

Box island capacity	$C_b = C_c + C_d + C_g + C_s$
Transistor island capacity	$C_t = C'_a + C'_b + C'_c + C'_d + C_g$
Dimensionless box-gate charge	$m_b = (V_c C_c + V_d V_d)/e$
Dimensionless transistor island charge	$n_t = (V_c C'_c + V_d C'_c + V'_a C'_a + V'_b C'_b)/e$
Effective box charging energy	$E_b = (e^2/2)/(C_b - C_g^2/C_t)$
Effective transistor charging energy	$E_t = (e^2/2)/(C_t - C_g^2/C_b)$
Coupling energy	$E_g = (e^2/2)(C_g/C_b C_t - C_g^2)$

opposite sign. The master equation for the occupation probabilities of the states (m, n) reads:

$$\begin{aligned}\dot{p}_{(m,n)} = &(\Gamma_a(n+1 \to n) + \Gamma_b(n+1 \to n))p_{(m,n+1)} \\ &+ (\Gamma_a(n-1 \to n) + \Gamma_b(n-1 \to n))p_{(m,n-1)} \\ &+ \Gamma_s(m+1 \to m)p_{(m+1,n)} + \Gamma_s(m-1 \to m)p_{(m-1,n)} \\ &- (\Gamma_a(n \to n+1) + \Gamma_b(n \to n+1) \\ &+ \Gamma_a(n \to n-1) + \Gamma_b(n \to n-1) \\ &+ \Gamma_s(m \to m+1) + \Gamma_s(m \to m-1))p_{(m,n)} \\ = &\ 0 \end{aligned} \tag{3}$$

where the last equality explicitly states that one looks for stationary solutions. The physical quantities that matter in the framework of this chapter are the mean box charge $\bar{m} = \sum_{m,n} m p_{(m,n)}$ and the transistor current $I_{sd} = \sum_{m,n} -e(\Gamma_a(n \to n+1) - \Gamma_a(n \to n-1)) \times p_{(m,n)}$. For given n_t and m_b only a limited number of states have to be taken into account, as Eq. (3) in conjunction with Eq. (2) describes an exponentially small occupation probability for states (m, n) with $E_{(m,n)}(m_b, n_t) \gg \beta^{-1}$. Furthermore we can restrict ourselves to the range $-0.5 \leq m_b \leq 0.5$ and $0 \leq n_t \leq 1$, as larger variations in m_b and n_t can be incorporated in successive readjustments of $m \to m \pm 1$ and $n \to n \pm 1$ each time n_t or m_b have changed by more than unity, as apparent from (2). At low temperatures it therefore turns out that one has to consider the occupation of six states only. At $m_b = 0$ only states (m, n) with $m = 0$ are occupied with considerable probability. On changing m_b towards $m_b = 1$ the probability is successively shifted to states (m, n) with $m = 1$. The current I_t in the transistor at $n_t \in [-0.5, 0.5]$ and at source-to-drain voltages $V_{sd} = V'_a - V'_b \lesssim 2E_t/e$ is dominantly sustained by states (m, n) with $n \in \{-1, 0, 1\}$. Taking only six states into account Eq. (3) takes the form $\sum_j M_{ij} p_j = 0$ where $i, j \in \{(0, 0), (0, 1), (1, 1), (1, 0), (1, -1), (0, -1)\}$. The one-dimensional null-space of the matrix M_{ij} is most easily found with modern computer algebra systems. So we will do without writing down the lengthy expressions for p_i here. At elevated temperature more states are involved and we have to fall back upon numerical methods in solving Eq. (3). In this case after an initial guess for the probabilities $p_{(n,m)}$ the time evolution described by the master Eq. (3) is used in an iterative relaxation procedure, which in general converges towards a stationary solution.

3. EXPERIMENTAL DETAILS

Our sample is fabricated by standard e-beam lithography in conjunction with a shadow evaporation technique from aluminum with aluminum oxide barriers. The sample parameters can be found by analyzing the behavior of the transistor current at high V_{sd} (E_c, E'_c and the tunnel conductances are determined this way) and from various periods seen in Coulomb oscillation measurements: $E_c = 2.03 \pm 0.05 k_B$ K, $E'_c = 1.93 \pm 0.05 k_B$ K, $E_g = 0.112 \pm 0.0009 k_B$ K, $C_d = 69$ aF, $C'_c = 66$ aF, $C_c = 23.2$ aF, $C'_d = 20.8$ aF, $g_a \sim g_b = 0.120 \pm 0.002$, and $g'_a \sim g'_b = 0.130 \pm 0.002$.

The measurements are performed in the mixing chamber of a top-loading dilution refrigerator. The sample is mounted within a well-shielded metallic cavity. All electrical

wiring into the cavity is made from highly resistive leads (32 Ω/m, diameter 0.23 mm), which are fed through stainless steel capillaries with an inner diameter of 0.34 mm and a length of 1 m. The capillaries are wound up in a compact coil, which is completely held in thermal equilibrium with the sample. These feedthroughs form resistive co-axial cables. They provide a damping exceeding 200 dB in the frequency range from 20 GHz to 6 THz, as calculated by classical electrodynamics taking the skin effect into account [6]. The validity of the used formulae was checked experimentally in the frequency range up to 20 GHz using a spectrum analyzer. During each measurement one of the transistors is operated as a single-electron box while the other one is used as electrometer. The working point of the latter is selected by applying a voltage V_{sd} slightly above the threshold of the Coulomb blockade and choosing a constant n_t. To gain resolution a lock-in technique has been used. The mean value of m_b, which is varied slowly with a rate of about 0.2 min^{-1}, is superimposed by an AC signal of small amplitude with a frequency of 34.15 Hz. The AC component of the current response is detected by a lock-in amplifier. This signal is to a good approximation proportional to the derivative of the current dI_{sd}/dm_b. The derivative has peaks where jumps in the current signal the transition of the box charge between neighboring states. The width of the peaks may be related to an effective temperature T_{eff} by comparing it to the ideal behavior of a single-electron box. To do so the measured curves are fitted to a function of the form $h(m_b) = cf'(m_b) + d$, where c accounts for the sensitivity by which variations of the box charge are transferred to variations of the electrometer current via the coupling capacity C_g. Similarly, d accounts for the fact that the step-like change of the box charge is transferred to a saw-tooth-like current variation by adding an appropriate tilt dm_b. Finally

$$f(m_b) = \frac{\sum_m m \exp(-\beta_{eff} E_m)}{\sum_m \exp(-\beta_{eff} E_m)} \tag{4}$$

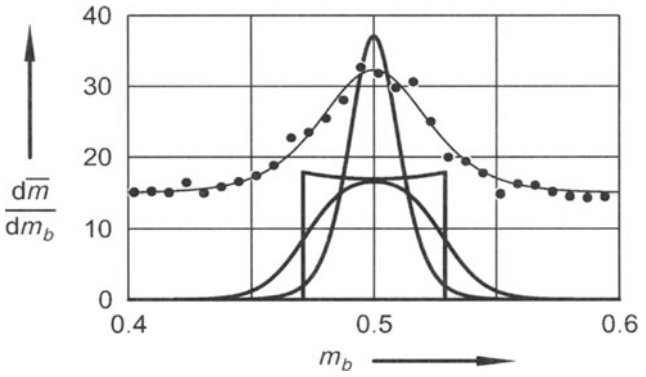

Figure 2. The derivative of the mean box charge with respect to m_b as a function of m_b as calculated from the six-state approximation (thick lines). Highest peak: $n_t = 0$ and $k_B T = 0.0135 E_b$ ($\sim$26 mK). Curve with discontinuities: $n_t = 0.5$ and $T = 0$. Broad curve: $n_t = 0.5$ and $k_B T = 0.0135 E_b$. The dots are taken from a measurement at 26 mK normalized to yield a unity integral, and offset for clarity. Thin line: Best fit of Eq. (4) to the experimental data corresponding to $T_{eff} = 56$ mK.

is the step function of the single-electron box not coupled to any measuring device. Note that Eq. (1) is a low temperature approximation of Eq. (4). Here $E_m = E_b(m - m_b)^2$ is the electrostatic energy of the box island charged by m electrons. In Fig. 2 a part of a measurement in the normal-conducting state is shown together with the least-squares fit of $h(m_b)$ to these data. Measurements have been taken in the temperature range from 26 mK, the lowest temperature we could reach, up to 500 mK. With increasing temperature the peaks in dI_{sd}/dm_b get wider and their amplitude decreases. Above 500 mK the signal gets buried in the experimental noise.

4. RESULTS

Figure 3 summarizes our main finding. At each temperature we took measurements of dI_{sd}/dm_b at up to 100 different values of n_t. By varying n_t we change the working point of the electrometer. At $n_t = 0$ and $n_t = 0.5$ the electrometer current takes its minimal and maximal value for a given source-to-drain voltage. At these points the electrometer has no sensitivity; small changes of the box charge do not result in a variation of the electrometer current. In between the electrometer's sensitivity is finite. Of all measurements taken we selected those for a further analysis where a periodic peak structure is clearly visible. For these measurements the parameter T_{eff} is determined. The difference between the mean of T_{eff} and the temperature T in the mixing chamber of our dilution refrigerator is depicted as dots in Fig. 3, while the root-mean-square deviation from the mean value is indicated by the error bars.

In the superconducting state the effective temperature saturates at about $0.08E_c \sim 160$ mK (see Fig. 3(a)). This behavior can be understood taking the following route of arguments. At elevated temperatures the number of quasi-particles exited above the gap

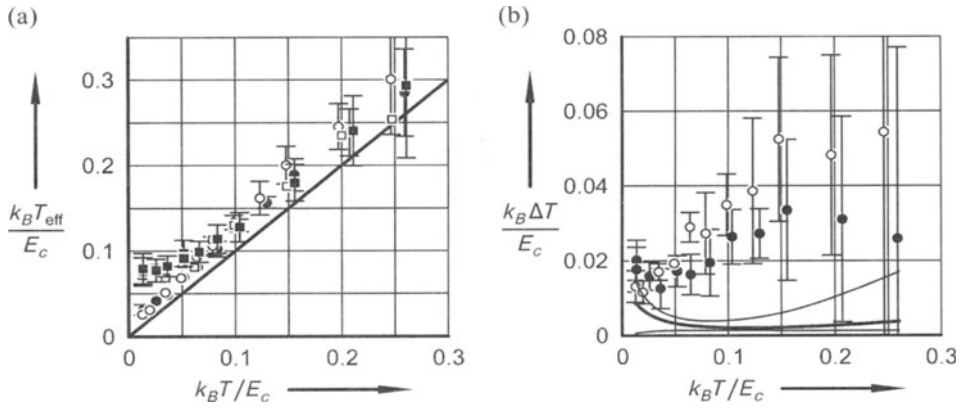

Figure 3. (a) T_{eff} as a function of the bath temperature T. Circles: normal-conducting state. Squares: superconducting state. Open symbols: configuration with $E_b = 2.03k_B$ K. Closed symbols: configuration with $E_b = 1.93k_B$ K. (b) $\Delta T = T_{eff} - T$ as a function of T. Open circles: configuration with $E_b = 2.03k_B$ K. Closed circles: configuration with $E_b = 1.93k_B$ K. Lines: result for the sequential model (see text).

energy can be evaluated as $N_{eq} = N_0 V \int N(E) f(\beta E)\, dE$, which describes the thermal equilibrium situation. Here $N(E) = |\Delta|/\sqrt{(E^2 - \Delta^2)}$ is the reduced superconducting density of states $f(\beta E) = (\exp(\beta E) + 1)^{-1}$ is the Fermi function, Δ is the superconducting gap energy, N_0 is the normal-conducting density of states supposed to be constant at the Fermi edge, and V is some effective volume of the sample. For temperatures $T \ll \Delta/k_B$ we have $N_{eq} \propto \exp(-\Delta/k_B T)$. $2e$-Periodicity is expected below $k_B T^* = \Delta/\ln N_{eff}$, where $N_{eff} = \sqrt{2\pi k_B T \Delta N_0 V_i}$ is the effective number of available quasi-particle states at the box island (V_i is the box island volume) [7, 8]. However, this requires thermal equilibrium in the leads. In the nonequilibrium situation of the present experiment the actual number of quasi-particles N_{neq} exceeds N_{eq} at $T < T^*$ considerably. A phenomenological ansatz to describe this situation is

$$N_{neq} = N_0 V \int N(E) f(\beta_{eff} E)\, dE \tag{5}$$

At this point it should be noted that an N_{neq} of order unity suffices to switch to e-periodicity. Since β_{eff}, which can be deduced by inverting relation (5), depends only logarithmically on N_{neq} it is reasonable to assume $\beta_{eff} \approx (k_b T^*)^{-1}$. This explains the saturation of the transition width found in our experiment qualitatively. The simple reasoning of this paragraph suggests identifying the saturation value of $T_{eff} \approx 160\,\text{mK}$ with T^*. As the islands of our transistors are relatively large ($V_i \approx 5 \times 10^{-20}\,\text{m}^3$ corresponding to $\ln N_{eff} \sim 12$) this is in good agreement with theoretical predictions for T^*.

In the normal-conducting state the effective temperature continues to decrease below T^*. However, it lies significantly above the temperature of the heat bath in which the sample is immersed. In principle this could have several reasons. One may argue that our single-electron box is not in thermal equilibrium with the heat bath or that a small fraction of black body radiation from parts of the experimental equipment that is at higher temperatures than the sample itself enters the metallic cavity containing the sample and spoils the experimental results by triggering photo-assisted tunneling events. However, even though it is almost impossible to rule out pollution effects with certainty, their signature is in general different from our findings. Usually those effects are less important at elevated temperature and cause the saturation of certain physical quantities below some threshold indicating that cooling the system by further decreasing the temperature of the heat bath gets inefficient. A good example for this behavior is our finding in the superconducting state, where even a tiny fraction of nonequilibrium quasi-particles leads to a saturation of the transition width below T^*. In the normal-conducting case we find an ongoing decrease of T_{eff} to the lowest bath temperatures available. Yet in the whole temperature range T_{eff} exceeds the bath temperature significantly.

5. DISCUSSION

Further evidence that the enhancement of T_{eff} above the bath temperature is an intrinsic effect is gained by analyzing the sequential model for the normal-conducting state. In qualitative agreement with our experimental data it yields a broadening of the width of the transition between neighboring charge states in the box, which might be

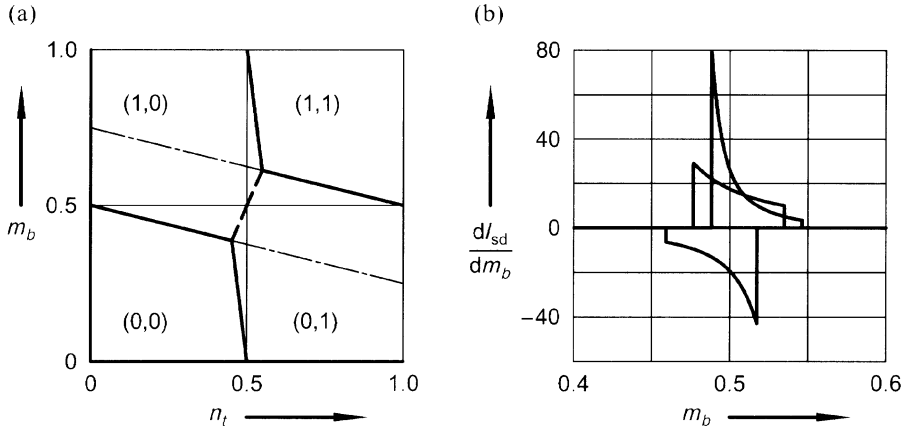

Figure 4. (a): Stability diagram for the system at zero V_{sd} for $E_t/E_b = 2$ and $E_b/E_g = 4$. Thick lines separate regions where certain states (m, n) have the lowest electrostatic energy. A direct transition between state (1, 0) and state (0, 1) across the dashed line is possible only via a higher order process. The thin dot-dashed lines are explained in the text. (b): The derivative of the electrometer current with respect to m_b as a function of m_b at zero temperature for different values of n_t ($n_t \in \{0.2, 0.4, 0.7\}$ from top to bottom) as calculated from the six states approximation. The curves have been normalized to give a total area of unity.

described by an enhanced T_{eff}. Figure 4(a) shows the stability diagram of the system depicted in Fig. 1 for $V_a' = V_b' = 0$. The tilt of the thick lines and the occurrence of the dashed line are due to the coupling; without coupling, $E_g = 0$, the thick lines would be exactly horizontal and vertical. At finite $V_{sd} = V_a' - V_b'$ each of the almost vertical lines which correspond to $\Delta E_a(n) = \Delta E_b(n) = 0$ has to be replaced by two lines whose distance increases with V_{sd}. On the other hand, the borders between neighboring *box* states stay sharp at zero temperature. The border between state (0, 0) and (1, 0) is described by $m_b = 0.5 - (E_g/E_b)n_t$. In Fig. 4(a) it is extended by a thin dot-dashed line to $n_t = 1$; this line we name border I. For the border between state (0, 1) and (1, 1) the relation $m_b = 0.5 + E_g/E_b(1 - n_t)$ holds. The corresponding line has been outstretched down to $n_t = 0$; we call it border II. In an experiment where m_b is swept from zero to one at constant $n_t = 0$ the transition between $m = 0$ and $m = 1$ occurs at $m_b = 0.5$ where border I is crossed. At finite temperature the transition is broadened in exactly the same way as for an isolated box (see highest peak in Fig. 2). The situation is quite different when n_t is held constant at $n_t = 0.5$. $\bar{m}$ starts to increase as soon as m_b crosses border I and reaches $\bar{m} = 1$ only when border II is reached (see the curve with discontinuities in Fig. 2). The distance of the two borders is given by $\delta m = E_g/E_b$. At finite temperature the discontinuities in $d\bar{m}/dm_b$ are removed as shown by the broader peak in Fig. 2. If n_t is neither too close to 0 nor to 0.5, the electrometer current is a good measure of the box charge state. Figure 4(b) shows the result of our six-state approximation at zero temperature. As in the case of $n_t = 0.5$ (Fig. 2) the transition from $\bar{m} = 0$ to $\bar{m} = 1$ occurs between the borders I and II. But for $n_t < 0.5$ border II is less important than border I and vice versa at $n_t > 0.5$. At finite temperatures the discontinuities of Fig. 4(b) are removed, too.

The result for the sequential model is incorporated in Fig. 3(b) as lines. As in the experiment we have determined $I_{sd}(m_b)$ for different values of n_t at varying temperatures. From $I_{sd}(m_b)$ an effective temperature describing the width of the transition between neighboring box states can be deduced. The thick line in Fig. 3 corresponds to the average of T_{eff} over n_t. The thin lines correspond to the maximal and minimal T_{eff} found. At low temperature and in the normal-conducting state the calculation are in fairly good agreement with the experimental findings. However, as the temperature increases, the sequential model predicts a nonmonotonic behavior with a minimal additional broadening (with model parameter chosen in accordance with the experiment) at about $0.1E_c$. In this region the experimentally found broadening exceeds the predictions considerably. At the present stage of our knowledge we do not understand this discrepancy. A conceivable explanation would be that fluctuation of the potential at the box island assists tunneling between neighboring charge states not accounted for by the sequential tunneling model [9]. Fluctuation of the box-island potential result from the sequential tunneling of electrons on and off the electrometer island, by which the current through the electrometer—the actual measured quantity—is sustained. The major effect of these fluctuations on the transition width is naturally included in the sequential model for the total system as calculated in this paper. However, it is supposable that the spectral density of the fluctuations contains considerable weight at frequencies ω to assist tunneling between two charge states differing in energy by $\hbar\omega$ missed by the sequential model. This may result in principle in additional broadening, but the mechanism yields too small a contribution to account for the complete transition width, too [10]. In our opinion it is worthwhile to calculate higher-order contributions as that might lead to a more appropriate theoretical description.

6. SUMMARY

We presented experimental data taken on a mesoscopic sample consisting of two single-electron transistors coupled capacitively. The transistors are built from aluminum with aluminum oxide tunnel barriers. One transistor at a time is operated as a single-electron box whose charge state is measured by the other transistor operated as an electrometer. The sample has been measured in the superconducting state as well as in the normal-conducting state, where the superconductivity of aluminum has been suppressed by a sufficiently strong magnetic field. For an isolated box the transition between two charge states is expected to be thermally broadened. We find experimentally an additional broadening due to the coupling to the electrometer. We solved the sequential-tunneling model for the coupled system and were able to calculate the additional broadening resulting from fluctuations of the potential on the box island. While the theoretical predictions of the sequential model are too small at elevated temperatures to give a quantitative explanation for the observed broadening, we find a fairly good conformity at low temperatures.

In the superconducting state we find e-periodic behavior even at 26 mK. This signals that more quasi-particles are present than accounted for by thermal equilibrium expressions. As our sample does not include quasi-particle traps, this behavior is not surprising. The presence of nonequilibrium quasi-particles in the superconducting state leads to a saturation of the transition width between the e-periodic charge states below a characteristic temperature $T^* = 160\,\text{mK}$.

Acknowledgements

We acknowledge fruitful discussions with G. Göppert, G. Johansson, H. v. Löhneysen, and G. Schön.

REFERENCES

[1] P. Lafarge, H. Pothier, E. R. Williams, D. Esteve, C. Urbina, and M. H. Devoret, Direct observation of macroscopic charge quantization, *Z. Phys. B—Condensed Matter* **85**, 327 (1991).
[2] G. Johansson, A. Käck, and G. Wendin, Full frequency back-action spectrum of a single-electron transistor during qubit readout, *Phys. Rev. Lett.* **88**, 046802-1–4 (2002).
[3] Y. Makhlin, G. Schön, and A. Shnirman, Quantum-state engineering with Josephson-junction devices, *Rev. Mod. Phys.* **73**, 357–400 (2001).
[4] V. Bouchiat, D. Vion, P. Joyez, D. Esteve, and M. H. Devoret, Quantum coherence with a single Cooper pair, *Physica Scripta* **T76**, 1665 (1998).
[5] G.-L. Ingold and Y. V. Nazarov, in *Single Charge Tunneling*, edited by H. Grabert and M. H.Devoret (New York, Plenum Press, 1992), pp. 21–107.
[6] A. B. Zorin, The thermocoax cable as the microwave frequency filter for single electron circuits, *Rev. Sci. Instrum.* **66**(8), 4296 (1995).
[7] G. Schön and A. D. Zaikin, Parity effects on electron tunneling through small superconducting islands, *Euro-Phys. Lett.* **22**, 695 (1994).
[8] M. T. Tuominen, J. M. Hergenrother, T. S. Tighe, and M. Tinkham, Experimental evidence for parity-based 2*e* periodicity in a superconducting single-electron tunneling transistor, *Phys. Rev. Lett.* **69**, 1997 (1992).
[9] G. Johansson, A. Käck, and G. Wendin, Full frequency back-action spectrum of a single-electron transistor during qubit readout, *Phys. Rev. Lett.* **88**, 046802 (2002).
[10] G. Johansson, private communication.

JOSEPHSON JUNCTION TRIANGULAR PRISM QUBITS COUPLED TO A RESONANT LC BUS

Qubits and gates for a holonomic quantum computer

S. P. Yukon
Air Force Research Laboratory, Electromagnetics Technology Division, Hanscom AFB, MA 01731, USA

Abstract: We investigate the properties of Josephson junction triangular prism qubits coupled by mutual inductance to a resonant LC bus. We show how the symmetries of the qubit potential may be used to implement the Duan Cirac Zoller scheme for holonomic quantum computation.

Keywords: Josephson junction qubit, Geometric gates, Holonomic quantum computation

1. INTRODUCTION

A geometric approach for achieving quantum computation using non-Abelian holonomic gate operations has been recently proposed by Pachos *et al.* [1]. An implementation of (non-Abelian) holonomic quantum computation using a trapped ion quantum computer [2] has subsequently been proposed by L. M. Duan, J. I. Cirac, and P. Zoller (DCZ) [3]. We propose here an alternative physical implementation of holonomic quantum computation based on a previously described quantum computer employing Josephson junction (JJ) triangular prism qubits coupled to a resonant LC bus [4]. For the ion trap system the excitation of different transitions can be distinguished by polarization or by frequency. For qubits based on the symmetric potential well of a JJ triangular prism, symmetric and antisymmetric excitations of prism's two JJ triangles using external magnetic flux take the place of laser pulse polarization. Because the qubit potential well and qubit's interaction with external flux are defined by Bohm Aharonov vector potential integrals around each cell circuit (yielding an Abelian holonomy or Berry phase), the basis for both qubit and gate properties can be said to be of geometric origin.

The DCZ qubits are atomic ions that have the desirable feature that all of the qubits possess identical properties when they are isolated from local environmental perturbations. The JJ qubits that we propose to employ have inherent fabrication errors and no two qubits

Quantum Computing and Quantum Bits in Mesoscopic Systems
Edited by Leggett *et al.*, Kluwer Academic/Plenum Publishers, 2004

will be exactly identical. To overcome this variability, the local microwave rf sources that provide the gate pulses at each qubit need to have their frequencies adjusted to match the transition frequencies needed for that particular qubit. A desirable aspect of holonomic quantum computing for such nonidentical qubits is that once the local rf source frequencies have been adjusted, it is possible to carry out a set of global (or multi-local) logic operations as the holonomic gates depend only on relative phases and amplitudes of the rf gate sources and not on their absolute amplitudes. Because the gate rotation angle for a holonomic gate depends on the solid angle subtended by the closed path in parameter space, holonomic gates should be relatively immune to small random fluctuations in external magnetic flux since the integral of the fluctuations they induce on a closed path should average to zero.

1.1 Josephson junction triangular prism qubits

In Fig. 1 we have sketched the three alternative versions of the flattened JJ prism qubit proposed in Ref. [4]. Of these the four- and five-cell versions have similar properties except that the five-cell version has an extra constraint condition (on the sum of the fluxes through the five cells) that gives rise to unwanted combinations of second-order excitations. Of the two, the simpler four-cell version is thus preferable.

The three- and four-cell versions may be distinguished by the circulating currents in the outer cells when the system is at a potential well minimum. The expressions for the effective one-dimensional potential for both the three- and four-cell versions may be written as $V_r(\chi) = -2\cos(\chi) + r\cos(2\chi)$ (shown in Fig. 3 for $r = 0.675$). The expression for the phase ζ^* of a (dotted) junction at a potential minimum in one of the triangular cells may be written as $\zeta^* = \pm\chi^* + f(\Phi_i)$ where $\pm\chi^*$ are the two minima for $V_r(\chi)$, and $f(\Phi_i)$ represents a function of Φ_is (where Φ_i is the external flux in the ith cell). The circulating current in the left- and right-hand JJ triangular cells at the two minima may be represented as $I_{\mathrm{MEAN}} \pm \Delta I$ (left-hand cell) and $I_{\mathrm{MEAN}} \mp \Delta I$ (right-hand cell). For the three-cell circuit (with $\Phi_s = 0$ defined below) $I_{\mathrm{MEAN}} = 0.415$, $\Delta I = 0.415$ at $r = 1$, and $I_{\mathrm{MEAN}} = 0.65$, $\Delta I = 0.32$ at $r = 0.65$. For the four-cell circuit (with $\Phi_s = 2\Phi_q$ defined below) $I_{\mathrm{MEAN}} = 0.0$, $\Delta I = 0.87$ at $r = 1$, and $I_{\mathrm{MEAN}} = 0.0$, $\Delta I = 0.65$ at $r = 0.65$. The four-cell circuit yields a larger ΔI for gradiometer coupling to a SQUID detector and is therefore the circuit that we choose for the qubit.

The computational basis states for the qubit are taken to be the ground and first excited state of the potential $V_r(\chi)$. Because the ground and first excited states wavefunctions of a symmetric potential are purely symmetric and antisymmetric, respectively, there is an equal probability of the current being in the right- or left-hand JJ triangle. To perform a measurement, a Hadamard gate or a $\pi/2$ Y-rotation on a qubit in one of the basis states will lead to a superposed wavefunction that is centered around the left or right potential well

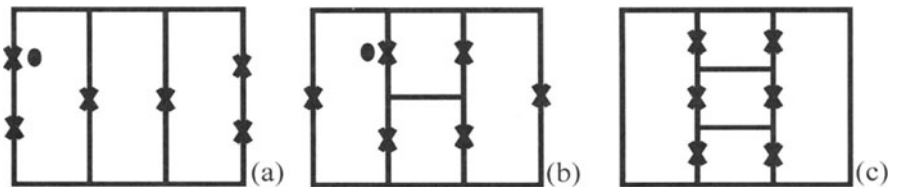

Figure 1. Sketch of three versions of the flattened triangular JJ prism.

minima. This in turn will lead to one of the previously described current patterns that can then be measured by a SQUID detector. A measurement performed without the Hadamard gate would be able to measure symmetric or antisymmetric combinations of the qubit basis states.

While we have used the symmetric properties of the potential $V_r(\chi)$ to define the qubit, we have used the results of Mooij *et al.* with regard to the low inductance properties of the qubit [5–7] and the necessity for suppressing transitions to other charge states [5, 6]. We will not discuss the aspects of coupling the qubit to detectors and the environment here, but the results of Refs [5] and [6] have addressed these issues and are applicable to the qubit proposed here.

The DCZ Hamiltonian employs three ground or metastable states plus a common excited state for each ion qubit. The Hamiltonian in the rotating frame for the jth ion with rf sources for each needed transition turned on, is given by

$$H_j = \hbar\Omega_0|e\rangle_j\langle 0| + \hbar\Omega_1|e\rangle_j\langle 1| + \hbar\Omega_b|e\rangle_j\langle b| + h.c. \tag{1}$$

where Ω_i are the Rabi frequencies for the transition from state $|i\rangle$ to state $|e\rangle$. Transcription of the DCZ holonomic quantum computation scheme to Josephson junction qubits requires: (1) qubits with three degenerate states (in the rotating frame) that couple to a common excited state; (2) a way of exciting each of the three states without exciting the others (and being able to control the amplitude and relative phase of the separate excitation modulation envelopes); and (3) a bus having harmonic oscillator energy levels that can couple to all of the qubits. In the next two sections we demonstrate how this may be accomplished using four-cell JJ prism qubits coupled to a resonant LC bus.

The Hamiltonian (in units of $2E_J$) for the four-cell qubit in Fig. 2, derived in Ref. [4], may be written as

$$\frac{H}{(2E_J)} = -\frac{\partial^2}{\partial\chi^2}2M_\chi - \left\{2\eta_H\cos\left(\frac{\phi_q}{2}\right)\cos\left(\chi+\frac{\phi_a}{2}\right) + \rho\cos(2\chi)\cos(\phi_s+\phi_q)\right\} \tag{2}$$

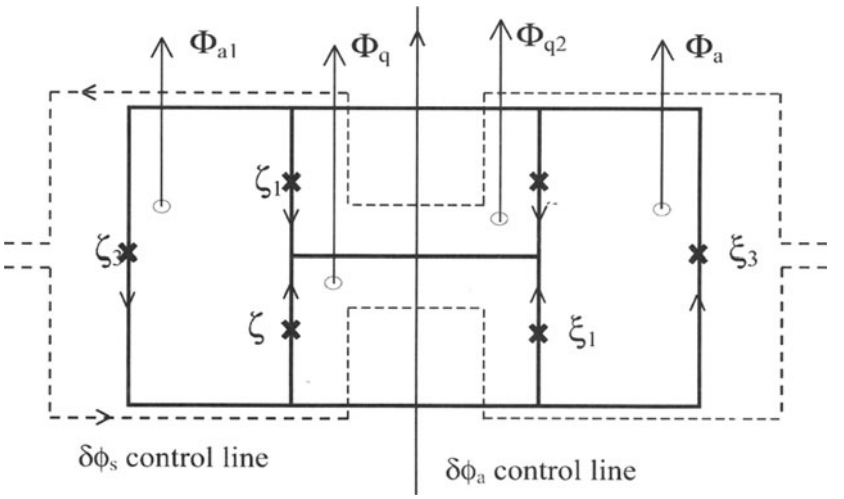

Figure 2. Flattened Josephson junction prism qubit with $\delta\phi_a$ and $\delta\phi_s$ control lines.

where we have defined $\theta = \theta_1 - \phi_r/2$ and $\chi = \psi_1 + (\phi_q - \phi_a)/2$ with $\phi_{q,r} = (\phi_{q1} \pm \phi_{q2})/2$, along with the diagonalizing $\pm$ combinations; $\psi_1 = (\zeta_1 - \zeta_2)/2$, $\psi_2 = (\xi_1 - \xi_2)/2$, $\theta_1 = (\zeta_1 + \zeta_2)/2$, $\theta_2 = (\xi_1 + \xi_2)/2$, as well as $\phi_{s,a} = (\phi_{a1} \pm \phi_{a2})/2$ with the definitions $\phi_{q,s,a} = 2\pi\,\Phi_{q,s,a}/\Phi_0$, $E_J = I_C\Phi_0/2\pi$ and $\Phi_0 = h/2e$. We have used the zero inductance limit Bohm–Aharonov phase constraint equations $\{\zeta_1 - \zeta_2 - \zeta_3 = \phi_{a1}$, $\xi_1 - \xi_2 - \xi_3 = \phi_{a2}$, $-\zeta_1 + \xi_2 = \phi_{q2}$, $\zeta_2 - \xi_1 = \phi_{q1}\}$ for the gauge invariant ζ_i and ξ_i junction phases. For junctions ζ_1, ζ_2, ξ_1, and ξ_2, the junction capacitances and critical currents have been taken equal to C and I_C, respectively. For junctions ζ_3 and ξ_3, the junction capacitances and critical currents have been taken equal to ρC and ρI_C respectively, allowing the mass term M_χ, to be written as $M_\chi = (2E_J)M = (1 + 2\rho)\,(2E_J)/(4(E_C/2))$, with $E_C = e^2/(2C)$. The η_H term comes from the Hartree replacement $\cos(\theta) \to \langle 0_\theta|\cos(\theta)|0_\theta\rangle \equiv \eta_H$. For the ground state $|0_\theta\rangle$, $\eta_H \approx 1$. In order to introduce the terms of the Hamiltonian that can be utilized for qubit gates, we further divide ϕ_q, ϕ_a, and ϕ_s into constant and small excursion constituents as $\phi_q = \phi_q^0 + \delta\phi_q$, $\phi_a = \phi_a^0 + \delta\phi_a$, and $\phi_s = \phi_s^0 + \delta\phi_s$. We take $\phi_r = 0$ (i.e. no constant or time-varying antisymmetric component of the flux threading the middle two cells).

For this Hamiltonian, the time-independent Schrödinger equation is equivalent to the Whittaker Hill equation, for which exact solutions have been found [8]. The lowest even and odd solutions are denoted by $gc_0(\chi)$, $gs_1(\chi)$, $gc_2(\chi)$, and $gs_3(\chi)$ and are defined in terms of continued fractions. If we identify the computational basis states $\langle\chi|1\rangle$ and $\langle\chi|0\rangle$ with $gc_0(\chi/2)$ and $gs_1(\chi/2)$, the assignment of $gc_2(\chi/2)$ and $gs_3(\chi/2)$ to the DCZ auxiliary states $\langle\chi|e\rangle$ and $\langle\chi|b\rangle$ will allow all of the DCZ one and two qubit holonomic gates to be carried out. The two basis states and auxiliary states are shown in the inset of Fig. 3 along

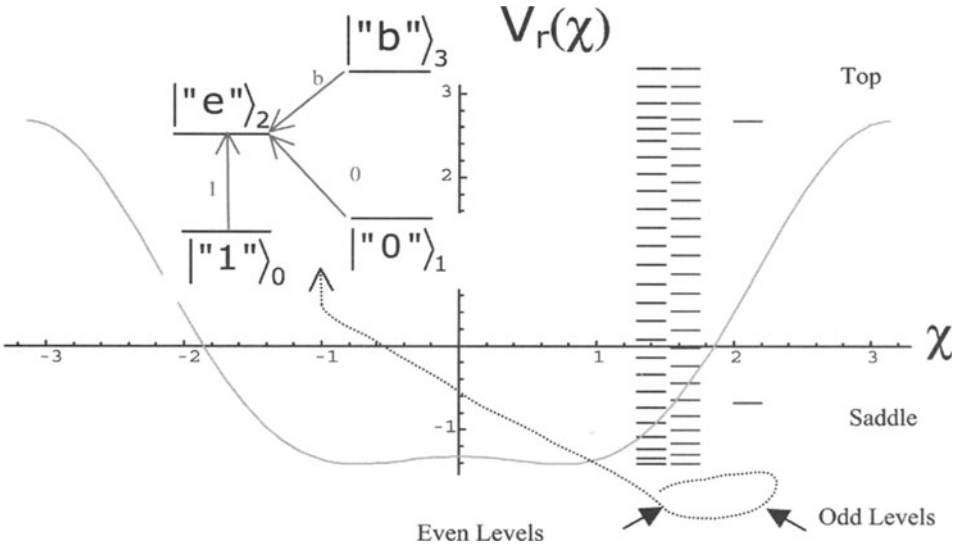

Figure 3. Energy levels and qubit transitions (inset) for $V_r(\chi)$ (in units of $2E_J$) with $r = 0.675$.

with the complete set of bound state levels for the qubit potential of Eq. (2) written as $V_r(\chi) = \cos(\chi + \phi_a/2) - r\cos(2\chi)$ with $r = -\rho\cos(\phi_s^0 + \phi_q^0)/(\eta_H \cos(\phi_q^0/2)) = 0.675$.

Since we have chosen to use the excited states $gc_2(\chi/2)$ and $gs_3(\chi/2)$ as the DCZ auxiliary states, their energy eigenvalues (and that of $gc_4(\chi/2)$, which is a possible transition from $gs_2(\chi/2)$) must lie appreciably below the potential well saddle that separates unit cells in the two-dimensional periodic potential (in order to prevent the excitation of different charge states) [5, 6]. There is a range of values of ϕ_s^0, ϕ_q^0, and η_H for which this is possible. As an example for the choice $r = 0.675$, $M_\chi = 100$, the saddle lies $0.74 \times (2E_J)$ above the potential minimum, while the $gc_4(\chi/2)$ and $gs_3(\chi/2)$ states lie respectively at $0.18 \times (2E_J)$ and $0.12 \times (2E_J)$ above the minimum.

A second requirement for the potential is that the transition frequencies $\omega_{21} = (E_2 - E_1)/\hbar$ and $\omega_{43} = (E_4 - E_3)/\hbar$ be separated by at least $10 \times \Omega_b$, where Ω_b is the Rabi frequency for the $gs_1(\chi/2) \leftrightarrow gc_2(\chi/2)$ transition, in order not to excite the $gs_3(\chi/2) \leftrightarrow gc_4(\chi/2)$ transition.

To model the inclusion of rf forcing and coupling to other qubits, we expand the potential in a power series around $\phi_a^0 = 0$, $\phi_q^0 \neq 0$, and $\phi_s^0 \neq 0$, keeping $\delta\phi_i$ terms up to second order. Physically, the ϕ_q^0 and ϕ_s^0 magnetic flux can be supplied by a uniform external field. The $\delta\phi_a$ excitation can be supplied by a vertical line bisecting the qubit while the $\delta\phi_s$ excitation can be supplied by two symmetric horizontal control lines designed to null or minimize concomitant excitation of $\delta\phi_q$ and $\delta\phi_r$ as shown in Fig. 2 (the wanted $\delta\phi_q$ excitations will come from the bus). The rf excitations $\delta\phi_{a,s}$ are tuned to the transition frequency between $|e\rangle$ and $|0\rangle$, $|1\rangle$, or $|b\rangle$. Thus the full expression for $\delta\phi_a$ for the $b \leftrightarrow e$ transition is thus given by

$$\delta\phi_a^{(e,b)} = \delta\phi_a^{(b)}(t)e^{i(E_e - E_b)t/\hbar + i\varphi_b} \tag{3}$$

where $\delta\phi_a^{(b)}(t)$ is the adiabatically varying modulation of the rf pulse envelope. The time varying phase $\varphi_b(t)$ may be introduced as a frequency modulation of the carrier at the transition frequency $(E_e - E_b)/\hbar$ with the FM pulse frequency given by $\omega_{eb}(t) = (E_e - E_b)/\hbar + d\varphi_b(t)/dt$.

The Hamiltonian for the jth qubit in the rotating frame with all rf sources on, may thus be expressed as the DCZ Hamiltonian of Eq. (1) with the Rabi frequencies for the three needed transitions given by

$$\Omega_0 = \eta_H\langle 0|\sin(\chi)|e\rangle\cos(\phi_q^0/2)\delta\phi_a^{(0)} \tag{4a}$$

$$\Omega_1 = \rho\langle 1|\cos(2\chi)|e\rangle\sin(\phi_s^0 + \phi_q^0)\delta\phi_s^{(1)} \tag{4b}$$

and

$$\Omega_b = \eta_H\langle b|\sin(\chi)|e\rangle\cos(\phi_q^0/2)\delta\phi_a^{(b)} \tag{4c}$$

1.2 Coupling the resonant LC bus to the qubits

To enable two-qubit gates to be carried out, each of the qubits is coupled to a resonant LC bus by mutual inductance coupling between a loop in the bus and the two inner cells of the qubit as shown in Fig. 5. The bus is based on the trapped ion bus scheme of Refs. [3, 9, 10] and is similar to the resonant LC bus coupling of qubits in Refs. [11–13]. The

operators for flux and charge in an LC oscillator with resonant frequency $\omega = 1/\sqrt{LC}$, can be written in terms of creation and annihilation operators $\{\mathbf{a}^+, \mathbf{a}\}$ as

$$\mathbf{\Phi} = \sqrt{\frac{\hbar L\omega}{2}}(\mathbf{a} + \mathbf{a}^+), \quad \boldsymbol{Q} = i\sqrt{\frac{\hbar}{2L\omega}}(\mathbf{a} - \mathbf{a}^+) \tag{5}$$

If there are N qubits coupled to the bus, and a fraction $f_Q\mathbf{\Phi}$ is available for coupling to the qubits, the amount of flux coupled to each qubit will be $f_Q\mathbf{\Phi}/N$. The second-order terms in the Hamiltonian expansion will then yield interaction terms for even–even (or odd–odd) transitions $\hat{\Omega}_1^j\sigma_{j1}^0(\mathbf{a} + \mathbf{a}^+)$ and even–odd transitions $\hat{\Omega}_0^j\sigma_{j0}^0(\mathbf{a} + \mathbf{a}^+)$ and $\hat{\Omega}_b^j\sigma_{jb}^0(\mathbf{a} + \mathbf{a}^+)$, where

$$\sigma_{j\mu}^{\varphi_\mu} = e^{i\varphi_\mu}|e\rangle_j\langle\mu| + h.c. \text{ Hermitian conjugate} \tag{6}$$

and

$$\hat{\Omega}_0^j = -\left(\frac{\eta_H}{2}\right)\sin\left(\frac{\phi_q^0}{2}\right)\langle 0|\sin(\chi)|e\rangle 2\pi f_q\frac{\sqrt{\hbar L\omega/2}}{(N\Phi_0)\delta\phi_a^{(0)}} \tag{7a}$$

$$\hat{\Omega}_1^j = \rho\cos(\phi_s^0 + \phi_q^0)\langle 1|\cos(2\chi)|e\rangle 2\pi f_q\frac{\sqrt{\hbar L\omega/2}}{(N\Phi_0)\delta\phi_s^{(1)}} \tag{7b}$$

$$\hat{\Omega}_b^j = -\left(\frac{\eta_H}{2}\right)\sin\left(\frac{\phi_q^0}{2}\right)\langle a|\sin(\chi)|e\rangle 2\pi f_q\frac{\sqrt{\hbar L\omega/2}}{(N\Phi_0)\delta\phi_a^{(b)}} \tag{7c}$$

Adopting the Sørensen and Mølmer [5, 6] bichromatic bus scheme used by DCZ, which requires only virtual bus excitations, the effective Hamiltonian for a pair $\{j, k\}$ of qubits coupled by the resonant LC bus may be written as

$$\frac{H_{j,k}}{2E_J} = \left(\frac{1}{\delta}\right)\left[\left(\frac{\delta}{\delta_0}\right)|\hat{\Omega}_0^j||\hat{\Omega}_0^k|\sigma_{j0}^{\varphi_0}\sigma_{k0}^{\varphi_0} - |\hat{\Omega}_1^j||\hat{\Omega}_1^k|\sigma_{j1}^{\varphi_1}\sigma_{k1}^{\varphi_1} + |\hat{\Omega}_b^j||\hat{\Omega}_b^k|\sigma_{jb}^{\varphi_b}\sigma_{kb}^{\varphi_b}\right] \tag{8}$$

This expressions differs from those in DCZ and Refs. [5, 6] due to the fact that we have taken into account the slightly different parameters of each qubit, and have allowed for a third detuning frequency offset δ_0 in addition to the DCZ frequency offset δ.

The total capacitance C will consist of the capacitance between the wires forming the bus and any additional capacitance added. The bus frequency $\omega = 1/\sqrt{LC}$ is chosen to avoid direct excitation of transitions in the qubit and to optimize the number of qubits in the system. To remain within the quasi-static limit, the maximum extent of the bus is $\sim 0.1\lambda_s$, where λ_s is the substrate wavelength. Assuming a bus frequency of 3 GHz, and a *substrate refractive index* $n_s = 3.0$ yields $\lambda_s/10 = 0.33$ mm. Assuming $(2E_J)/h = 200$ GHz, with $r = 0.675$, $M_\chi = 100$ the expressions (4c) and (7c) with $\delta\phi_a = 0.001 \times 2\pi$ yield $\Omega_b/2\pi = 0.152$ GHz and $\hat{\Omega}_b^j/2\pi = 0.627/\sqrt{N}$ MHz. The Rabi frequencies for two-qubit gates given in Eq. (8) may be increased from this value by taking the offset frequencies δ and δ_0 to be small fractions of $\hat{\Omega}_b^j$, and by choosing n such that the rf frequency $\omega_{\text{rf}} = (E_2 - E_1)/\hbar + n \cdot \omega$ is distant from any allowed transition

frequency so that the value of $\delta\phi_a$ could be increased. An example would be to choose n such that $\omega_{\rm rf} \approx (E_7 - E_1)/\hbar$.

We note that by setting $\phi_q = 0$, the middle cells in Fig. 1 may be eliminated and their junctions combined. The bus for these two-cell versions should then be moved to the right (or left) cell. From Eqs (4) and (7) we see that for Fig. 1(b), all one-qubit terms would survive but only the even two-qubit term (7b) would survive for $\phi_q = 0$. This would still allow a universal set of gates to be formed but without the extra degree of control from the even–odd transition terms (7a) and (7c). The two-cell version of Fig. 1(a) would have similar losses. For Fig. 1(c), all even transition terms vanish [14]. For one-qubit gates, an even term could be fashioned for $|1\rangle \rightarrow |e\rangle$ by using second-order odd transitions since the energy denominator for the intermediate state transition $|1\rangle \rightarrow |0\rangle$ is small.

1.3 Non-Abelian holonomic gates

The basic set of DCZ single qubit gates $U_1^{(j)} = e^{i\phi_1|1_j\rangle\langle 1_j|}$, $U_Y^{(j)} = e^{i\phi_Y\sigma_Y^{(j)}}$, and the two-qubit gate $U_{11}^{(j,k)} = e^{i\phi_{11}|1_j,1_k\rangle\langle 1_j,1_k|}$ are sufficient for all of the operations needed to carry out holonomic quantum computations. The DCZ Berry phases ϕ_1, ϕ_Y, and ϕ_{11}, are given by their implicit dependence on θ and φ as:

$$\phi_1 = -\frac{1}{2}\oint \sin(\theta)\, d\theta\, d\varphi \tag{9}$$

with

$$\Omega_0 = 0, \quad \Omega_1 = -\Omega' \sin\left(\frac{\theta}{2}\right)e^{i\varphi}, \quad \Omega_b = \Omega'' \cos\left(\frac{\theta}{2}\right)$$

$$\phi_Y = \oint \sin(\theta)\, d\theta\, d\varphi \tag{10}$$

with

$$\Omega_0 = \Omega \sin(\theta)\cos(\varphi), \quad \Omega_1 = \Omega' \sin(\theta)\sin(\varphi), \quad \Omega_b = \Omega''\cos(\theta)$$

with $\Omega = \Omega' = \Omega''$ and

$$\phi_{11} = -\frac{1}{2}\oint \sin(\theta)\, d\theta\, d\varphi \tag{11}$$

with

$$\Omega_0 = 0, \quad \frac{|\hat{\Omega}_1^j \hat{\Omega}_1^k|}{|\hat{\Omega}_b^j \hat{\Omega}_b^k|} = \tan\left(\frac{\theta}{2}\right), \quad \varphi_1 - \varphi_b = \frac{\varphi}{2}$$

The minimal set of gates for quantum computation (two single-qubit gates and one two-qubit gate) must form a noncommuting set, which implies that their geometric phases must be generated by non-Abelian holonomies [1]. The computational basis during an adiabatic evolution cycle rotates into "dark" states that maintain zero eigenvalues. An example of dark states for the $U_Y^{(j,k)}$ gate Hamiltonian would be $|D_{Y1}\rangle = \cos(\theta)(\cos(\varphi)|0\rangle_j + \sin(\varphi)|1\rangle_j) - \sin(\varphi)|b\rangle_j$ and $|D_{Y2}\rangle = \cos(\varphi)|0\rangle_j - \sin(\varphi)|1\rangle_j$. Since the gate Hamiltonians

have zero eigenvalues for these states, there is no dynamical phase contribution from the gates to the computational basis states [1].

Using expressions for the geometric phase in [1], the DCZ set can be completed with the single-qubit X rotation and two-qubit $X_{\alpha\beta,\alpha'\beta'}$ and $Y_{\alpha\beta,\alpha'\beta'}$ rotations where σ_x and σ_y are replaced by $\{|\alpha\beta\rangle\langle\alpha'\beta'| + |\alpha\beta\rangle\langle\alpha'\beta'|\}$ and $\{-i|\alpha\beta\rangle\langle\alpha'\beta'| + i|\alpha'\beta'\rangle\langle\alpha\beta|\}$, respectively, and $|\alpha\beta\rangle$ (and $|\alpha'\beta'\rangle$) is one of the two-qubit states $\{|0_j0_k\rangle, |0_j1_k\rangle, |1_j0_k\rangle, |1_j1_k\rangle\}$. The expression for the X rotation is given by $U_X^{(j)} = e^{i\phi_x\sigma_x^{(j)}}$ where

$$\phi_X = \oint \sin(\theta)\, d\theta\, d\varphi \tag{12}$$

with

$$\Omega_0 = \Omega\sin(\theta)\cos(\varphi), \quad \Omega_1 = \Omega'\sin(\theta)\sin(\varphi)e^{i\pi/2}, \quad \Omega_b = \Omega''\cos(\theta)$$

For $Y_{\alpha\beta,\alpha'\beta'}$ rotation the two-qubit Hamiltonian can be written as

$$H_{j,k}^{Y_{\alpha\beta,\alpha'\beta'}} = \left(\frac{1}{\delta}\right)\left[\left(\frac{\delta}{\delta_0}\right)|\hat{\Omega}_{\alpha\beta}^{j}||\hat{\Omega}_{\alpha\beta}^{k}|\sigma_{j\alpha}^{\varphi_{\alpha\beta}}\sigma_{k\beta}^{\varphi_{\alpha\beta}} - |\hat{\Omega}_{\alpha'\beta'}^{j}||\hat{\Omega}_{\alpha'\beta'}^{k}|\sigma_{j\alpha'}^{\varphi_{\alpha'\beta'}}\sigma_{k\beta'}^{\varphi_{\alpha'\beta'}}\right.$$
$$\left. + |\hat{\Omega}_b^{j}||\hat{\Omega}_b^{k}|\sigma_{jb}^{\varphi_b}\sigma_{kb}^{\varphi_b}\right] \tag{13}$$

The $Y_{\alpha\beta,\alpha'\beta'}$ rotation is then given by

$$U_{Y_{\alpha\beta,\alpha'\beta'}}^{(j,k)} = e^{i\phi_{Y_{\alpha\beta,\alpha'\beta'}}(-i|\alpha_j,\beta_k\rangle\langle\alpha_j',\beta_k'| + i|\alpha_j',\beta_k'\rangle\langle\alpha_j,\beta_k|)}$$

with

$$\phi_{Y_{\alpha\beta,\alpha'\beta'}} = \oint \sin(\theta)\, d\theta\, d\varphi \quad \text{and} \quad \Omega_{\alpha\beta} = \Omega\sin(\theta)\cos(\varphi), \tag{14}$$

with

$$\Omega_{\alpha'\beta'} = \Omega'\sin(\theta)\sin(\varphi), \quad \Omega_b = \Omega''\cos(\theta)$$

The $X_{\alpha\beta,\alpha'\beta'}$ rotation can be similarly derived following the pattern of the single-qubit X and Y rotations.

1.4 Fault tolerance of U_1 and U_{11} and U_Y and $U_{Y_{\alpha\beta,\alpha'\beta'}}$ holonomic gates

Assuming that it will not be possible to adjust the three microwave sources at each qubit to obtain equal basic Rabi frequencies Ω for the three needed transitions, we have looked at the effect of unequal basic Rabi frequencies $\{\Omega, \Omega', \Omega''\}$ on the value of the resulting gate rotation angle. We define an "input" gate rotation angle ϕ_{in} as the Berry angle given in Eqs (9), (10), or (11) for a perfectly adjusted system with a three-step pulse sequence: $\{\theta = 0 \to \pi/2,\ \varphi = 0\}$, $\{\theta = \pi/2,\ \varphi = 0 \to \varphi_{\text{final}}\}$, $\{\theta = \pi/2 \to 0,\ \varphi = \varphi_{\text{final}}\}$. The pulse envelope used is $\theta(t) = \hat{\theta}(\tanh(\lambda(t + t_0)) - \tanh(\lambda(t - t_0)))/2$, $\varphi(t) = \hat{\varphi}(\tanh(\lambda t + 1)/2$, with $\lambda = 1/2$, $t_0 = 20$, $\hat{\theta} = \pi/2$, $\Omega = \Omega_\lambda = 2\pi$. The gate rotations presented below are calculated in the restricted Hilbert space $\mathcal{H}_0 = \{|0\rangle, |1\rangle, |e\rangle, |b\rangle\}$. In Fig. 4(a) we have plotted the resulting gate rotation angle ϕ_{out} for the U_1 gate for $\{\Omega, \Omega', \Omega''\} = \Omega_\lambda\{0, 1.0, 1.0\}$, $\Omega_\lambda\{0, 1.0, 1.2\}$, and $\Omega_\lambda\{0, 1.0, 1.4\}$. Since all of the gate rotation angles lie on a straight line for a given set of basic Rabi

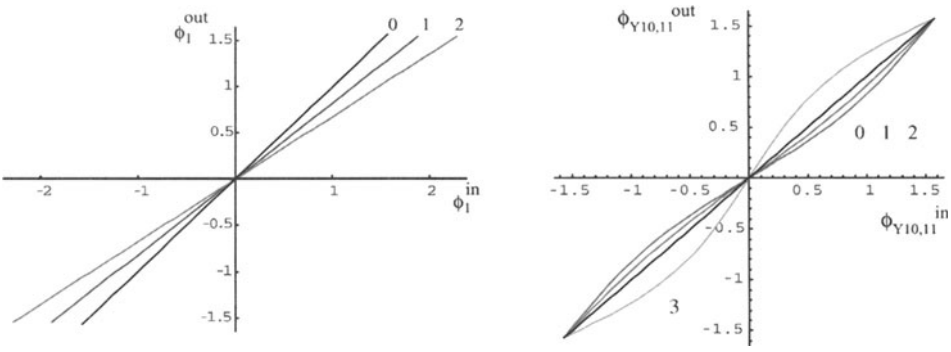

Figure 4. (a) Output vs. input rotation angle for basic Rabi frequency error sets 0, 1, 2; (b) Output vs. input rotation angle for basic Rabi frequency error sets 0, 1, 2, 3.

frequencies, measurement of a single pair of input and output rotation angles will then determine the needed input angle for any desired output rotation angle. The behavior of all gates like U_{11} that have $\Omega_0 = 0$ will be similar.

In Fig. 4(b) we have plotted the output rotation angle for the $U_{Y_{10,11}}$ gate for $\{\Omega, \Omega', \Omega''\} = \Omega_\lambda\{1.0, 1.0, 1.0\}$, $\Omega_\lambda\{1.0, 1.22, 0.83\}$, $\Omega_\lambda\{1.00, 1.44, 0.66\}$, and $\Omega_\lambda\{1.00, 0.66, 1.34\}$. For this gate all of the output rotation angles for a given set of basic Rabi frequencies lie on a 45° rotated sine curve. Measurement of a single pair of input and output rotation angles can then determine the needed input angle for any desired output rotation angle. The behavior of all gates like U_X, U_Y, and $U_{X_{\alpha\beta,\alpha'\beta'}}$ that have adiabatic envelopes similar to Eq. (10) will have behavior similar to that of $U_{Y_{\alpha\beta,\alpha'\beta'}}$. Unlike the U_{11} and U_1 gates, there are also two points at $\pm\pi/2$ where the output rotation angle perfectly matches the input rotation angle. Thus any of the gates U_X, U_Y, $U_{X_{\alpha\beta,\alpha'\beta'}}$, or $U_{Y_{\alpha\beta,\alpha'\beta'}}$ at rotation angle $\pm\pi/2$ will be fault tolerant with respect to microwave pulse amplitude errors. Investigation of the fault tolerance properties of gates when the Hilbert space is not restricted to $\mathcal{H}_0$ requires optimizing the potential, the resonant pulses, and bus parameters to minimize leakage out of $\mathcal{H}_0$, and will be addressed in a future paper.

1.5 Connecting buses into a network

It is also possible to connect groups of buses in an open branching network as first described in Ref. [4]. To transcribe this feature to the holonomic qubits and gates described above requires distinguishing a particular qubit (or qubits) that is to be assigned the sole task of transferring gate excitations from one bus to a second and vice versa. This is shown schematically in Fig. 5. Since the $U_{Y_{10,11}}$ is fault tolerant at rotation angle $\pm\pi/2$, we shall employ it to connect buses and define it as

$$U_{CY_{j,k}}(\pm) = \{|0_j0_k\rangle\langle 0_j0_k| + |0_j1_k\rangle\langle 0_j1_k| \mp |1_j1_k\rangle\langle 1_j0_k| \pm |1_j0_k\rangle\langle 1_j1_k|\} \tag{15}$$

To carry out a two-qubit $U_{CY_{j,k}}(\pm)$ gate between a control qubit j on bus 1 and a target qubit k on bus 2 via the common transfer qubit t (assumed to be in its ground state), it is necessary

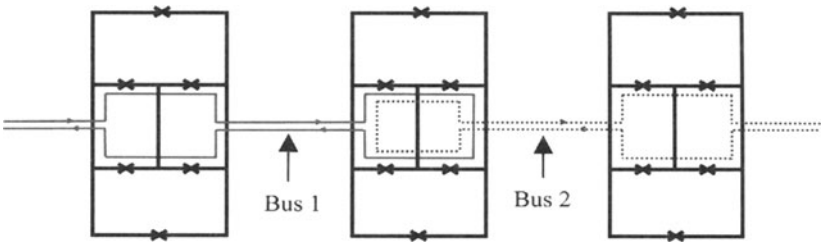

Figure 5. Schematic of two coupled buses and transfer (center) qubit.

to first carry out a $U_{CY_{j,t}}(-)$ gate with qubit j the control qubit and qubit t the target qubit. A second $U_{CY_{t,k}}(-)$ gate with qubit t the control and qubit k the target and a final $U_{CY_{j,t}}(-)$ gate with qubit j the control qubit and qubit t the target qubit achieve the desired result with control qubit t returned to its original ground state. While they are not perfectly fault tolerant, three control-not gates, between (j, t), (t, k), and (j, t) would also have the overall effect of a control-not between j and k with t reset to its original ground state.

To carry out a control-y over a number of buses, it is necessary to first carry out a sequence of $U_{CY_{i,j}}(-)$ starting from the control qubit, through all of the intervening transfer qubits to the target qubit, followed by a final sequence of $U_{CY_{i,j}}(-)$ from the original qubit to the last transfer qubit in order to reset the transfer qubits to their original ground states. The sequence involving two transfer qubits would thus be $U_{CY_{i,j}}(-)$ between (j, t_1), (t_1, t_2), (t_2, k) followed by resetting transfer qubits with $U_{CY_{i,j}}(-)$ applied to (t_1, t_2) and (j, t_1). The maneuvers described in the preceding paragraph may be chained across as many coupled buses as required (given an environment where perfect coherence is possible). This allows open branching networks of coupled buses to be formed, enlarging the possible number of interacting qubits in a single quantum computer.

2. CONCLUSIONS

We have shown that it is possible to design a system comprised of Josephson junction prism qubits coupled inductively to a resonant LC bus that is capable of carrying out holonomic quantum computations. The effective Hamiltonian is zero throughout an entire computation, so there is no dynamical evolution of the system. In the restricted Hilbert space $\mathcal{H}_0$, one- and two-qubit X and Y rotation gates are shown to be tolerant of pulse amplitude errors for rotation angles of $\pm\pi/2$. The behavior of one- and two-qubit gates at arbitrary rotation angles, when pulse amplitude errors are present, can be predicted if one measurement can be made to determine an appropriate input/output curve.

Acknowledgements

The author appreciates helpful conversations with Alexey Ustinov, Jeffrey Yepez, Farrukh Abdumalikov, and Jim Ernstmeyer. This work was carried out with support from Air Force Office of Scientific Research AFOSR.

REFERENCES

[1] J. Pachos, P. Zanardi, and M. Rasetti, *Phys. Rev.* **A61**, 010305(R) (2000), J. Pachos Preprint http://www.xxx.lanl.gov/abs/quant-ph/0007110.
[2] L.-M. Duan, J. I. Cirac, and P. Zoller, *Science*, **292**, 1695 (2001).
[3] J. I. Cirac and P. Zoller, *Phys. Rev. Lett.* **74**, 4091 (1995).
[4] S. P. Yukon, *Physica* **C 368**, 320, (2002).
[5] J. E. Mooij, T. P. Orlando, L. Levitov, L. Tian, C. H. van der Wal, and S. Lloyd, *Science* **285**, 1036 (1999).
[6] T. P. Orlando, J. E. Mooij, L. Tian, C. H. van der Wal, L. S. Levitov, S. T. P. Orlando, S. Lloyd, and J. E. Mooij, *Science* **290**, 773, (2000).
[7] D. S. Crankshaw and T. P. Orlando, *IEEE Trans. Appl. Sup.* **11**, 1006 (2001).
[8] K. M. Unwin and F. M. Arscott, *Proc. Roy Soc. Edinb.* **71**, 28 (1971).
[9] A. Sørensen and K. Mølmer, *Phys. Rev Lett.* **82**, 1971 (1999).
[10] A. Sørensen and K. Mølmer, *Phys. Rev Lett.* **82**, 1835 (1999).
[11] Y. Makhlin, G. Schön, and A. Shnirman, *J. Low Temp. Phys.* **118**, 751 (2000).
[12] Y. Makhlin, G. Schön, and A. Shnirman, *Rev. Mod. Phys.* **73**, 357 (2001).
[13] O. Buisson and F. W. Hekking, in *Macroscopic Quantum Coherence and Quantum Computing* (Dordrecht, Kluwer Academic), p. 137 (2001).
[14] Mooij, J. E., these proceedings MQC2 2002.

INCOHERENT AND COHERENT TUNNELING OF MACROSCOPIC PHASE IN FLUX QUBITS

S. Saito[1], H. Tanaka[1], H. Nakano[1], M. Ueda[1,2], and H. Takayanagi[1]
[1]*NTT Basic Research Laboratories, NTT Corporation, 3-1, Morinosato-Wakamiya, Atsugi, Kanagawa 243-0198, Japan*
[2]*Department of Physics, Tokyo Institute of Technology, Meguro-ku, Tokyo 152-8551, Japan*

Abstract: We successfully distinguished flux qubit states by means of single-shot measurement with a high-resolution dc-SQUID. We studied the readout results of the qubit states for two types of sample (classical and quantum) and found that the classical sample exhibited incoherent macroscopic tunneling between two flux states. With the quantum sample, we directly observed the superposition states of the qubit without microwave-spectroscopy experiments.

Keywords: Flux qubit, Single-shot measurement, Incoherent tunneling, Macroscopic quantum Tunneling, Superposition

1. INTRODUCTION

The quantum computer is a novel architecture that is capable of extremely fast computation. The basic element of a quantum computer is the qubit, for which there are many candidates. Solid-state qubits have advantages in terms of integration, but the many quantum degrees of freedom affect their coherence. Of the solid-state qubits, superconducting qubits have a longer coherence time because of their superconducting energy gap. These superconducting qubits, which have already been confirmed experimentally, are based on charge states [1, 2] and flux states [3, 4] and phase states in a single Josephson junction [5]. We are studying the three-Josephson-junction flux qubits first proposed by Mooij and his co-workers [6]. The readout for this flux qubit is undertaken using a dc-SQUID coupled to the qubit via mutual inductance. Until now, we have had to average many readout results to distinguish the qubit states because the switching current of the SQUID has a much wider distribution than the qubit signal. However, our dc-SQUIDs have good resolution and we can distinguish the qubit state by single-shot measurement [7, 8]. In this work, we studied the readout results of the qubit states obtained by single-shot measurements for two types of sample (classical and quantum).

Quantum Computing and Quantum Bits in Mesoscopic Systems
Edited by Leggett *et al.*, Kluwer Academic/Plenum Publishers, 2004

2. TWO-LEVEL SYSTEM IN THREE-JOSEPHSON JUNCTION QUBIT

The qubit we studied consists of a superconducting loop with three Josephson junctions in series (Fig. 1). Junctions 1 and 2 have a Josephson energy E_J and a charging energy $E_C = e^2/2C$, where C is the junction capacitance and e is the electron charge. Junction 3 has a Josephson energy βE_J and a capacitance βC. Here, β is a parameter between 0.5 and 1.0. Applied magnetic flux Φ_{qb} penetrates the qubit's loop. We consider that the loop inductance is negligible and we ignore the self-generated flux. The arrows define the phase direction.

By using flux quantization $\gamma_1 - \gamma_2 + \gamma_3 = -2\pi\Phi_{qb}/\Phi_0$, the total Josephson energy of the qubit is [9]

$$\frac{U}{E_J} = 2 + \beta - \cos\gamma_1 - \cos\gamma_2 - \beta\cos\left(2\pi\frac{\Phi_{qb}}{\Phi_0} + \gamma_1 - \gamma_2\right) \tag{1}$$

This energy is periodic in γ_1 and γ_2 with the period 2π. When the applied flux Φ_{qb} is close to $\Phi_0(n + 1/2)$, where n is an integer, each unit cell has two potential minima, namely a double well potential. Hereafter, we focus on the case of $n = 0$. We chose $\beta = 0.8$ in order to obtain the isolated double well potential, which has no inter-cell coupling. The classical states in each well $|\downarrow\rangle$ and $|\uparrow\rangle$ correspond to the persistent currents I_P with the opposite sign and their magnitude I_{P0} is close to the critical current of the weakest junction. Their energies are $E = \pm I_{P0}(\Phi_{qb} - \Phi_0/2) \equiv \pm\varepsilon/2$ (see Fig. 2(a)). For a qubit with appropriate parameters, these two classical states are coupled via a quantum tunneling matrix element $\Delta/2$ through the barrier between the wells and form the superposition states $|0\rangle = a|\downarrow\rangle + b|\uparrow\rangle$, $|1\rangle = b^*|\downarrow\rangle - a^*|\uparrow\rangle$, $|a|^2 + |b|^2 = 1$. The quantum tunneling leads to an "anti-crossing" with the symmetric and antisymmetric superposition of the macroscopic persistent currents for $\Phi_{qb} \approx \Phi_0/2$ (see Fig. 2(b)). Thus, the qubit's loop becomes a macroscopic two-level quantum system.

The qubit Hamiltonian in terms of Pauli spin matrices σ_x and σ_z is

$$H_{qb} = \frac{\varepsilon}{2}\sigma_z - \frac{\Delta}{2}\sigma_x \tag{2}$$

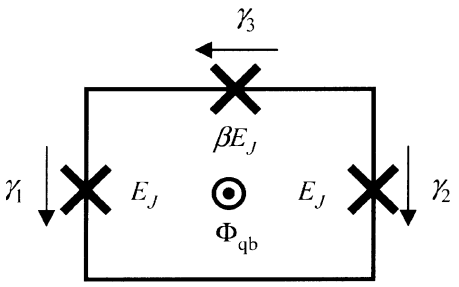

Figure 1. Schematic view of the flux qubit. The crosses represent Josephson junctions; γ_i is the gauge-invariant phase difference across the ith junction.

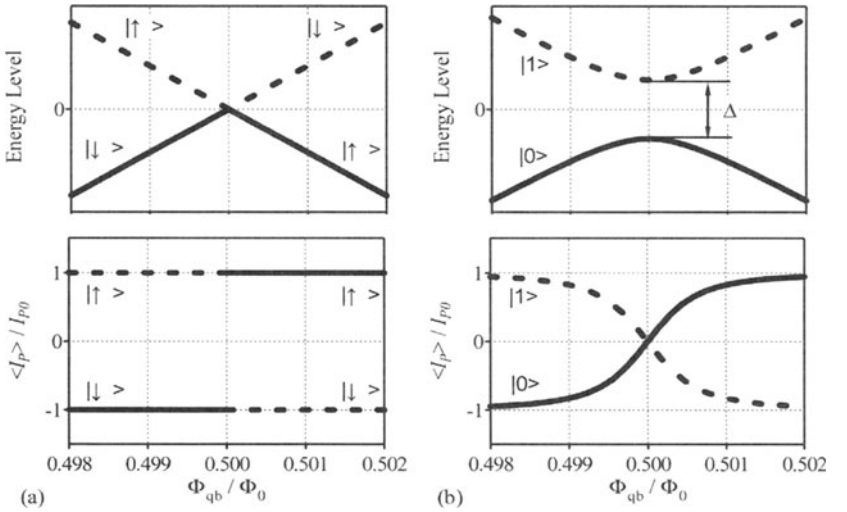

Figure 2. Energy levels (upper graphs) and persistent currents (lower graphs) of qubits as a function of applied magnetic flux Φ_{qb}/Φ_0. (a) In the classical case ($E_J \gg E_C$), tunneling energy Δ is almost zero. The ground state (solid curve) and the first excited state (dashed curve) correspond to the "down" state $|\downarrow\rangle$ and the "up" state $|\uparrow\rangle$ for $\Phi_{qb}/\Phi_0 < 0.5$ and this is reversed for $\Phi_{qb}/\Phi_0 > 0.5$. The normalized expected quantum value of the persistent current $\langle I_P\rangle/I_{P0}$ is completely separated into two branches. (b) In the quantum case ($E_J \approx 80E_C$), tunneling energy Δ is finite. The ground state (solid curve) and the first excited state (dashed curve) are superpositions of $|\downarrow\rangle$ and $|\uparrow\rangle$. $\langle I_P\rangle/I_{P0}$ have rounded step shapes. The step width is dependent on Δ.

For a qubit with an E_J value one or two orders of magnitude greater than E_C, the system should have two low-energy quantum levels, E_0 and E_1, according to

$$E_{0(1)} = -(+)\sqrt{\left(\frac{\varepsilon}{2}\right)^2 + \left(\frac{\Delta}{2}\right)^2} \tag{3}$$

When $\Phi_{qb} = \Phi_0/2$, the energy splitting $\Delta E \equiv E_1 - E_0 = \Delta$. Typically the Δ-value is between 1 and 10 GHz (0.05 to 0.5 K).

The expected quantum mechanical value of the loop persistent currents $\langle I_P\rangle$ is the opposite of the derivative of the energy $E_{0(1)}$. Then we obtain

$$\langle I_P\rangle_{0(1)} = +(-)I_{P0}\frac{\varepsilon}{\sqrt{\varepsilon^2 + \Delta^2}} \tag{4}$$

where $\langle I_P\rangle_0$ and $\langle I_P\rangle_1$ are the expected quantum mechanical values of the loop persistent current related to the qubit ground state $|0\rangle$ and the first excited state $|1\rangle$. Figure 2 shows the energy levels $E_{0(1)}$ and $\langle I_P\rangle_{0(1)}$ plotted in units of I_{P0} as a function of applied magnetic flux. The energy difference ε between $|\downarrow\rangle$ and $|\uparrow\rangle$ is almost proportional to $\Phi_{qb} - \Phi_0/2$ in

the vicinity of $\Phi_{qb} = \Phi_0/2$. Therefore, we can read the horizontal coordinate of Fig. 2 as ε, and $\varepsilon = 0$ at $\Phi_{qb} = \Phi_0/2$.

Thus far, we have only considered the situation at zero Kelvin. However, thermal effects modify $\langle I_P \rangle$. The qubit forms a quantum two-level system and the second excited state is too high in terms of energy to be thermally excited. Hence we can only take account of the two expected persistent currents $\langle I_P \rangle_{0(1)}$ corresponding to the two lowest levels. The thermal average of expected quantum value for the persistent current can be written as

$$\langle I_P \rangle_T = \frac{\sum_{n=0,1} \langle I_P \rangle_n \exp[-E_n/(k_B T)]}{\sum_{n=0,1} \exp[-E_n/(k_B T)]} = I_{P0} \frac{\varepsilon}{\sqrt{\varepsilon^2 + \Delta^2}} \tanh\left(\frac{\sqrt{\varepsilon^2 + \Delta^2}}{2k_B T}\right) \tag{5}$$

where k_B is Boltzman's constant. Equation (5) shows that the applied magnetic flux dependence of $\langle I_P \rangle_T$ has a rounded step shape.

We should mention that the thermal average of the expected values of the persistent current $\langle I_P \rangle_T$ depends on temperature. Therefore, experimentally averaged readout results of a qubit should have temperature dependence in accordance with Eq. (5). In contrast, if we can distinguish the ground state $|0\rangle$ and the first excited state $|1\rangle$ of the qubit by a single-shot measurement, the readout results corresponding to $|0\rangle$ and $|1\rangle$ should have no temperature dependence in accordance with Eq. (4).

3. EXPERIMENTAL PREPARATION

The flux qubit and the dc-SQUID for its readout consisted of an aluminum micrometer-sized loop with three and two unshunted Josephson junctions, respectively. We fabricated the samples with e-beam lithography and the standard shadow evaporation technique [10]. We controlled the qubit parameter E_J/E_C by changing the junction area size of the qubit while maintaining a β-value of 0.8. We estimated E_C from the designed junction area size of the qubit and a typical specific capacitance of 100 fF/μm^2. E_J was estimated from the switching current of the dc-SQUID I_{SW0} at zero magnetic field and the ratio of the junction area between the qubit and the SQUID. I_{SW0} was deduced from the gap voltage V_g and the normal resistance R_n of the SQUID using the Ambegaokar–Baratoff relation [11]. The value of $V_g = 420$ μV is extracted from the I–V curve of the SQUID and R_n was estimated from the high-bias part of the I–V curve.

We can calculate the energy levels and wavefunctions of the qubits from the E_J and E_C values described above. Table 1 shows the sample parameters. The plasma frequency

Table 1. A comparison of the parameters for qubits. All the energies are in units of GHz.

	E_J	E_C	$h\omega_m$	Δ
Sample A	510	0.97	38	0.0001
Sample B	310	3.7	60	0.5

ω_m was derived from the effective capacitance C_m and the curvature of the potential energy at the bottom of the well in the $\gamma_m = (\gamma_1 - \gamma_2)/2$ direction. In sample A, each well had about five energy levels and the ground state wavefunction was well localized in each well. In sample B, each well had only one level and the ground state wavefunction is somewhat extended between the two wells.

Measurements were carried out in a dilution refrigerator at temperatures of about 30 mK. We placed the refrigerator in a three-fold μ-metal shield. A magnetic field was applied perpendicularly to the substrate by a superconducting solenoid. We swept the bias current by applying a continuous-triangle wave. To detect the flux produced by the qubit, we measured the switching current of the SQUID.

4. RESULTS

Figure 3(a) and (b) show the magnetic field dependence of the switching current of dc-SQUIDs around $\Phi_{qb}/\Phi_0 = 0.5$ and 1.5. Here we subtracted the background signal from the raw data and normalized the subtracted data. Each point in the figures shows the readout result of the qubit state obtained by a single-shot measurement. We measured the switching current of the SQUID repeatedly while slowly sweeping the magnetic field. The measurement repetition rate was 140 Hz.

In sample A where $E_J/E_C = 520$ (Fig. 3(a)), we can clearly see two separated branches. The lower branch means that the qubit is in the "down" state $|\downarrow\rangle$. The upper branch means that the qubit is in the "up" state $|\uparrow\rangle$.

In sample B where $E_J/E_C = 83$ (Fig. 3(b)), we can still see two separated branches but there are also two continuous steplike structures in the vicinity of $\Phi_{qb}/\Phi_0 = 1.5$. One is clear but the other is obscure. These steps have the opposite sign to each other and they cross at $\Phi_{qb}/\Phi_0 = 1.5$. We measured sample B around $\Phi_{qb}/\Phi_0 = 1.5$ because the dc-SQUID has sufficient resolution to distinguish the qubit states in these magnetic fields

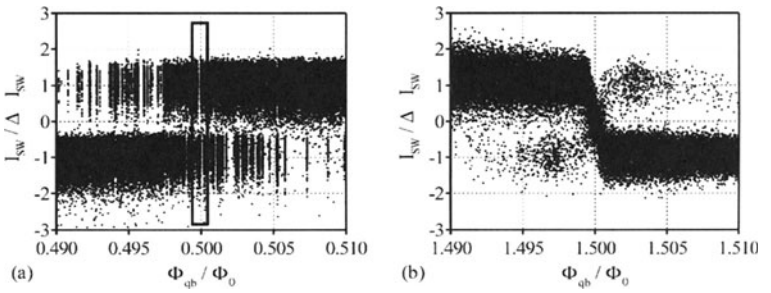

Figure 3. Readout results of the qubit. We extracted the step structures by subtracting the background signal from the raw data. After the subtraction, we normalized the switching currents of the dc-SQUIDs I_{SW} by half the step height ΔI_{SW}. (a) Readout results of the qubit with $E_J/E_C = 520$ (sample A); $M = 17\,\text{pH}$, $\Delta I_{SW} = 9\,\text{nA}$, $T = 34\,\text{mK}$. (b) Readout results of the qubit with $E_J/E_C = 83$ (sample B). The dominant step has the opposite sign to that in Fig. 3(a) because we performed the measurement for sample B around $\Phi_{qb}/\Phi_0 = 1.5$ and the magnetic field dependence of the switching current (before the subtraction) has a negative slope around that value; $M = 7\,\text{pH}$, $\Delta I_{SW} = 1.4\,\text{nA}$, $T = 20\,\text{mK}$.

and insufficient resolution around $\Phi_{qb}/\Phi_0 = 0.5$. There is little difference between the qubit states around $\Phi_{qb}/\Phi_0 = 0.5$ and 1.5.

5. DISCUSSION

First, we focus on the readout result of sample A. Figure 4(a) shows an enlargement of the box area in Fig. 3(a). We can clearly see a telegraphic signal. This signal means that the qubit jumped stochastically from one well to the other and stayed there for a certain dwell time τ. We define the transition rate as $\Gamma = 1/\langle\tau\rangle$. Here, $\langle\tau\rangle$ is the average dwell time.

Figure 4(b) shows the temperature dependence of Γ in sample A. Γ decreases with decreasing temperature below the crossover temperature [12]

$$T_{cr} = \frac{\hbar\omega_m}{2\pi k_B}\left[\sqrt{(1+\alpha^2)} - \alpha\right] \tag{6}$$

where α is the dimensionless dissipation coefficient in the two-level system. If we assume that the qubit is shunted by ohmic resistance R, the dissipation can be expressed in terms of R as $\alpha = (2\Phi_m)^2/2\pi\hbar R$, where $2\Phi_m$ is the distance between the minima of the double-well potential. The incoherent transition rate between the wells is given by [13, 14]

$$\Gamma = \frac{\sqrt{\pi}\Delta_r^2}{2\omega_C}\frac{\Gamma(\alpha)}{\Gamma(\alpha+1/2)}\left[\frac{\pi k_B T}{\hbar\omega_C}\right]^{2\alpha-1} \tag{7}$$

where $\Delta_r = \Delta\exp[-\alpha/2]$ is the reduced gap energy with dissipation α. This equation was confirmed experimentally in the two-level system of an rf-SQUID by Han *et al.* [15]. The cut-off frequency ω_C is of the order of the plasma frequency ω_m in the limit of $RC_m\omega_m \gg 1$ as is the case with our system. We fitted our data below T_{cr} to Eq. (7). Here, ω_C and α were

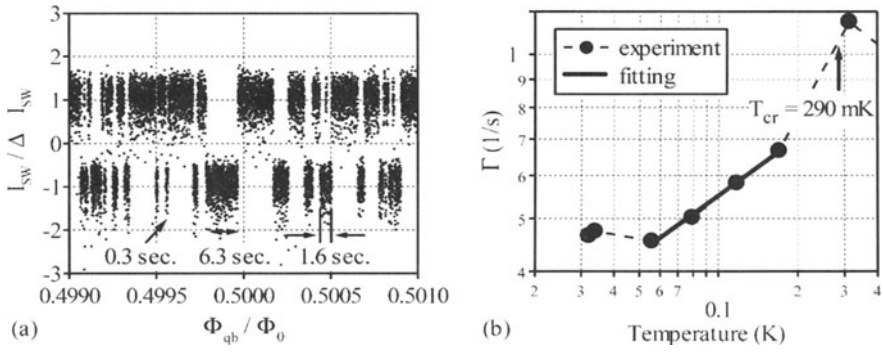

Figure 4. (a) An enlargement of the box area in Fig. 3(a). We can estimate the dwell time τ from the telegraphic signal and the repetition rate of the measurement (140 Hz). It is between 0.1 and 10 s. (b) Temperature dependence of the transition rate Γ in sample A. The crossover temperature T_{cr} between the quantum tunneling region and the thermal activation region is 290 mK.

fitting parameters and Δ was estimated by the numerical calculation (see Table 1). From the fitting line in Fig. 5, we obtained ω_C, which was of the order of ω_m. This is reasonable in our case. In addition, we obtained $\alpha = 0.625$, which corresponded to the shunt resistance of 3.1 kΩ. This value was comparable to the damping resistance for the rf-SQUID, which was between 3 and 6 kΩ, as reported by Rouse *et al.* [16].

From Eq. (7), Γ should approach zero as $T \to 0$. However, Γ becomes constant for temperatures below 50 mK. We believe that this is because the true temperature of the sample is saturated below 50 mK due to some external noise, and not because of macroscopic quantum tunneling (MQT) to the continuum in a washboard potential [17, 18]. Our reason for this is as follows. For MQT, Γ should approach a constant value at $T = 0$ with $\ln[\Gamma(T)]/\ln[\Gamma(0)] \propto T^2$ [12]. However our data did not reveal the T^2 dependence. This led us believe that a qubit where $E_J/E_C = 520$ exhibits incoherent tunneling in a two-level system.

Second, we focus on the readout result of sample B where $E_J/E_C = 83$. We can clearly see the readout results appearing between two separated branches in Fig. 3(b), although we did not average the results. What does this mean? If we perform a strong measurement on the qubit superposition state $|0\rangle = (|\downarrow\rangle + |\uparrow\rangle)/\sqrt{2}$, it should shrink to the classical state $|\downarrow\rangle$ or $|\uparrow\rangle$, then we should observe two separated branches. In contrast, weak measurement cannot separate the superposition state because it has insufficient energy to destroy the superposition of $|\downarrow\rangle$ and $|\uparrow\rangle$ via tunneling energy Δ [19]. Hence the dc-SQUID reads out the qubit state directly without invoking any shrinkage of the qubit wavefunction. In other words, we observe the expected quantum mechanical value of the flux induced by the qubit persistent current (see Eq. (4)). We believe that the readout results appearing between the two branches mean that the measurement is weak and we expect to observe the qubit superposition state in the sample B experiment. The following discussion substantiates this claim.

Figure 3(b) shows clear and dominant rounded step and also shows obscure rounded step with the opposite sign. The shapes of these two steps remained unchanged up to

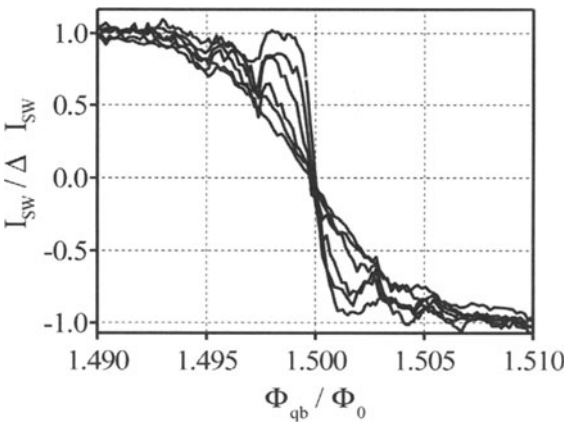

Figure 5. Temperature dependence of the average readout results for sample B. Each point was averaged over 1000 switching events. Each steplike curve was measured at $T = 20$, 50, 100, 200, 300, 400 mK from narrow step to wide step.

350 mK (not shown). This behavior was in good agreement with Eq. (4). Figure 5 shows the temperature dependence of the average readout results. The width of the step decreases with decreasing temperature even below 350 mK. This is clear evidence that the ratio of the populations for the steps in Fig. 3(b) changes with temperature, and these results qualitatively correspond to Eq. (5). Therefore, we believe that the two steps in Fig. 3(b) correspond to the ground state $|0\rangle$ and the first excited state $|1\rangle$ of the qubit. This allows us to conclude that a qubit with $E_J/E_C = 83$ exhibits quantum superposition states and a single-shot measurement can distinguish $|0\rangle$ and $|1\rangle$.

Above 350 mK, we observed only one rounded step and its width increased with temperature. We believe that the thermal activation rate is so high that we cannot distinguish the qubit states. Therefore, we obtain the thermally averaged readout results between $|0\rangle$ and $|1\rangle$ even in a single-shot measurement. This high temperature (>350 mK) behavior can be reproduced by Eq. (5).

In Fig. 5, two peaks and two dips appear at the magnetic fields that are symmetrical with respect to $\Phi_{qb}/\Phi_0 = 1.5$. These structures correspond to energy differences $\Delta E \equiv E_1 - E_0$ of 5 and 10 GHz. Since we did not apply any microwaves during the measurement, we consider these structures to be due to high-frequency noise transmitted through the SQUID's leads or the resonant mode of the sample holder box.

6. SUMMARY

We successfully distinguished qubit states by employing single-shot measurement with a high resolution dc-SQUID. By using the SQUID, we observed that the qubit with $E_J/E_C = 520$ exhibits incoherent macroscopic tunneling between two flux states. From the temperature dependence of the incoherent tunneling rate, we obtained the damping parameter $\alpha = 0.625$, which corresponds to the dissipation at a shunt resistance of 3.1 kΩ.

We observed two rounded steps in the readout results of the $E_J/E_C = 83$ qubit. The clear and dominant step corresponds to the superposition ground state of the qubit and obscure step to the first excited state. We confirmed that the shapes of these steps have no temperature dependence below 350 mK, however the ratio of the population for the two steps changes with temperature. These results are consistent with quantum mechanical theory. We are convinced, therefore, that our qubit is in the superposition state and was detected without the need for microwave-spectroscopy experiments.

Acknowledgement

We thank J. E. Mooij, C. J. P. M. Harmans, and S. Ishihara for motivating this research, and C. H. van der Wal and Y. Nakamura for useful discussions and suggestions.

REFERENCES

[1] Y. Nakamura, Yu. A. Pashkin, and J. S. Tsai, *Nature* **398**, 786–788 (1999).
[2] D. Vion, A. Aassime, A. Cottet, P. Joyez, H. Pothier, C. Urbina, D. Esteve, and M. H. Devoret, *Science* **296**, 886–889 (2002).
[3] C. H. van der Wal, A. C. J. ter Haar, F. K. Wilhelm, R. N. Schouten, C. J. P. M. Harmans, T. P. Orlando, S. Lloyd, and J. E. Mooij, *Science* **290**, 773–777 (2000).
[4] J. R. Friedman, V. Patel, W. Chen, S. K. Tolpygo, and J. E. Lukens, *Nature* **406**, 43–46 (2000).

[5] Y. Yu, S. Han, X. Chu, S.-I. Chu, and Z. Wang, *Science* **296**, 889–892 (2002).
[6] J. E. Mooij, T. P. Orlando, L. Levitov, L. Tian, C. H. van der Wal, and S. Lloyd, *Science* **285**, 1036–1039 (1999).
[7] H. Tanaka, Y. Sekine, S. Saito, and H. Takayanagi, *Supercond. Sci. Technol.* **14**, 1161–1165 (2001).
[8] H. Tanaka, Y. Sekine, S. Saito, and H. Takayanagi, *Phisica C* **368**, 300–304 (2002).
[9] T. P. Orlando, J. E. Mooij, L. Tian, C. H. van der Wal, L. S. Levitov, S. Lloyd, and J. J. Mazo, *Phys. Rev.* B **60**, 15398–15413 (1999).
[10] G. J. Dolan, *Appl. Phys. Lett.* **31**, 337–339 (1977).
[11] V. Ambegaokar and A. Baratoff, *Phys. Rev. Lett.* **10**, 486–489 (1963).
[12] S. Washburn, R. A. Webb, R. F. Voss, and S. M. Faris, *Phys. Rev. Lett.* **54**, 2712–2715 (1985).
[13] A. J. Leggett, S. Chakravarty, A. T. Dorsey, M. P. A. Fisher, A. Garg, and W. Zwerger, *Rev. Mod. Phys.* **59**, 1–85 (1987).
[14] S. Chakravarty and A. J. Leggett, *Phys. Rev. Lett.* **52**, 5–8 (1982).
[15] S. Han, J. Lapointe, and J. E. Lukens, *Phys. Rev. Lett.* **66**, 810–813 (1991).
[16] R. Rouse, S. Han, and J. E. Lukens, *Phys. Rev. Lett.* **75**, 1614–1617 (1995).
[17] R. F. Voss and R. A. Webb, *Phys. Rev. Lett.* **47**, 265–268 (1981).
[18] M. H. Devoret, J. M. Martinis, and J. Clarke, *Phys. Rev. Lett.* **55**, 1908–1911 (1985).
[19] H. Nakano *et al.*, in preparation.

DECOHERENCE IN FLUX QUBITS DUE TO 1/f NOISE IN JOSEPHSON JUNCTIONS

D. J. Van Harlingen[a], B. L. T. Plourde, T. L. Robertson, P. A. Reichardt, and John Clarke
Department of Physics, University of California, Berkeley and Materials Sciences Division, Lawrence Berkeley National Laboratory, Berkeley, CA 94720, USA

1. INTRODUCTION

There has recently been substantial progress in observing the superposition of charge and flux quantum states [1–5] in superconducting devices and of quantum states in a current-biased Josephson junctions [6, 7]. These experiments are of considerable interest not only from a fundamental point of view but also because such devices may ultimately be used as qubits in a quantum computer [8]. Probably the single largest issue in the eventual exploitation of these devices is decoherence, and it is of key importance to understand the various sources. In addition to extrinsic contributors to decoherence, there are also intrinsic sources, for example, the resistance of the tunnel junction at voltages below $2\Delta/e$ (Δ is the energy gap), the motion of trapped charge, the motion of trapped flux vortices, and the $1/f$ noise (f is frequency) in the critical current of Josephson junctions.

In this article we are concerned with the origin of $1/f$ noise in the critical current of Josephson tunnel junctions and with the decoherence induced in superconductor magnetic flux qubits by critical current fluctuations. We begin in Section 2 with a brief review of the Dutta–Horn [9] picture of $1/f$ noise, a simplified model that sets the scene for much of the ensuing discussion. Section 3 briefly describes $1/f$ noise in Josephson junctions and Superconducting QUantum Interference Devices (SQUIDs), establishes a "universal value" for its magnitude, discusses thermally activated and tunneling mechanisms, and reports an experiment on $1/f$ noise at temperatures below 1 K. In Section 4 we relate decoherence in flux qubits to critical current $1/f$ noise, and in Section 5 we present our conclusions.

In related work on this subject, Shnirman *et al.* [10] have studied decoherence due to $1/f$ noise in the environment, Paladino *et al.* [11] have investigated the effects of bistable charge fluctuators on decoherence, and Martinis *et al.* [12] have calculated the decoherence in current-biased Josephson junctions due to $1/f$ critical current noise.

---

[a]Permanent address: Department of Physics, University of Illinois at Urbana-Champaign, 1110 W. Green St., Urbana, IL 61801.

Quantum Computing and Quantum Bits in Mesoscopic Systems
Edited by Leggett *et al.*, Kluwer Academic/Plenum Publishers, 2004

2. DUTTA–HORN MODEL FOR $1/f$ NOISE

A Random Telegraph Signal (RTS) is produced by random transitions between the states of a double potential well. As a function of time, the measured variable shows abrupt transitions between two levels, which we label 1 and 2. We define $1/\tau_1$ as the rate of a transition from 1 to 2 and $1/\tau_2$ as the rate of the reverse transition. If, for simplicity, we set $1/\tau = 1/\tau_1 = 1/\tau_2$, the power spectrum is a Lorentzian of the form [13–16]

$$S(f) \propto \frac{\tau}{1 + (2\pi f \tau)^2} \tag{1}$$

We consider an ensemble of such fluctuators, each with a characteristic barrier height U_i, and assume that the transitions are thermally activated so that the characteristic times are given by $\tau_i = \tau_0 \exp(U_i/k_B T)$, where $1/\tau_0$ is an attempt frequency. For a barrier height distribution $D(U)$, the spectral density of the noise is [9]

$$S(f, T) \propto \int_0^\infty dU\, D(U) \left[\frac{\tau_0 \exp(U/k_B T)}{1 + (2\pi f \tau_0)^2 \exp(2U/k_B T)} \right] \tag{2}$$

The kernel in brackets has its maximum at $2\pi f \tau_0 \exp(U/k_B T) = 1$, defining a characteristic barrier energy $\tilde{U} = -k_B T \ln(2\pi f \tau_0)$. For $f = 1$ Hz and $\tau_0 = 10^{-10}$ s, $\tilde{U} \sim 20 k_B T$. Provided $D(U)$ varies slowly on the scale of $k_B T$, we can take $D(U)$ outside the integral to find

$$S(f, T) \propto \frac{D(\tilde{U}) k_B T}{f} \tag{3}$$

thus yielding $1/f$ noise. We note that although τ is exponential in T, $S(f, T)$ is linear in T. This is because the kernel, which peaks at $\tilde{U} \propto T$, moves through the distribution of RTSs as the temperature varies, selecting only those processes that have characteristic frequencies in the window of interest.

3. $1/f$ NOISE IN JOSEPHSON JUNCTIONS AND SQUIDS

3.1 $1/f$ Noise in dc-SQUIDs

Consider a dc-SQUID [17]—two resistively-shunted Josephson junctions with critical currents I_{01} and I_{02} connected in parallel in a superconducting loop — current-biased with a current I at a flux $\Phi = (2n + 1)\Phi_0/4$ to maximize its flux-to-voltage transfer function $(\partial V/\partial \Phi)$. Here, $\Phi_0 \equiv h/2e$ is the flux quantum, approximately 2.07×10^{-15} Wb, and V is the voltage across the SQUID. The spectral density of the voltage $1/f$ noise across the SQUID can be written in the form [18]

$$S_v(f) = \left(\frac{\partial V}{\partial \Phi}\right)^2 S_\Phi(f) + \left(\frac{\partial V}{\partial (I_{01} + I_{02})}\right)^2 S_{I_0}(f) + 2\left(\frac{\partial V}{\partial (I_{01} - I_{02})}\right)^2 S_{I_0}(f) \tag{4}$$

Here, $S_\Phi(f)$ is the spectral density of the $1/f$ "flux noise" due to the motion of flux vortices in the superconducting body of the SQUID, and $S_{I_0}(f)$ is the spectral density of the critical current fluctuations of each junction. The second term on the right-hand side of Eq. (4) arises from "in-phase fluctuations" of the two incoherent $1/f$ noises in the two junctions, and the third term from "out-of-phase fluctuations" of the two noise sources which induce a $1/f$ noise current around the SQUID loop. The second term is reduced by the widely-used flux modulation scheme [19], while the third term is reduced by a bias reversal scheme [18].

The origin of flux noise in superconducting films has been widely studied, particularly in the case of high transition temperature (T_c) superconductors [20]. The noise arises from thermally-activated hopping of vortices among pinning sites, each process constituting a RTS. Although flux noise was a major problem in the early development of high-T_c SQUIDs, it has been essentially eliminated by patterning the films into narrow lines [21]. For a line of width w, flux lines will not enter until the ambient field exceeds a threshold value [22] of approximately Φ_0/w^2, about 100 μT for $w = 4$ μm. High-T_c SQUIDs patterned into 4-μm-wide slots or holes exhibit low levels of $1/f$ noise when cooled in fields up to about 100 μT, and much greater levels of noise when cooled in higher fields. Recently, Stan *et al.* [23] used a Hall probe to determine the density of vortices in Nb films, and concluded that vortices did not enter below a threshold field given by a similar formula. Since flux qubits are typically patterned with linewidths of 1 μm or less and the threshold field for $w = 1$ μm is roughly 2 mT, 40 times larger than the Earth's field, it seems safe to conclude that intrinsic flux noise should not be a problem for these devices.

3.2. $1/f$ Critical current noise

In the generally accepted picture [24] of $1/f$ noise in tunnel junctions, an electron from one electrode enters a trap in the barrier for a period of time, and subsequently exits. While the electron is trapped, it locally modifies the height of the tunnel barrier, changing the resistance of the junction, and, in the case of a Josephson junction, also the critical current. For a junction of area A the change in critical current is $\Delta I_0 = (\Delta A/A)I_0$, where ΔA is the effective area of the junction eliminated by the temporary presence of the trapped electron. The spectral density for one trap is proportional to $(\Delta I_0)^2$, so that the spectral density $S_{I_0}(f)$ for N identical, independent traps thus scales as $N(\Delta I_0)^2$ or $(nA) \cdot (\Delta A/A)^2 I_0^2$, where n is the number of traps per unit area. Consequently, for a given junction technology we expect

$$\frac{S_{I_0}(f)}{I_0^2} \propto \frac{1}{A} \tag{5}$$

Measurements of low-frequency critical current noise show two broad classes of behavior. Submicron junctions [25] sometimes exhibit a small number of Lorentzian spectra, indicating that only one or two RTSs are active at the relevant temperature and frequencies. Figure 1 shows the voltage power spectrum $S_V(f)$ for a 0.08 μm^2 Al-AlO$_x$-Al tunnel junction at 0.3 K. Two Lorentzians with characteristic frequencies of 100 Hz and 2.5 kHz have been fitted. The lower frequency fit yields a voltage noise $S_V^{1/2}(f) = 1.4 \times 10^{-8}$ V/Hz$^{1/2}$ below the knee frequency and thus a critical current noise $S_{I_0}^{1/2}(f) \approx S_v^{1/2}(f)/R_D \approx 7 \times 10^{-11}$ A/Hz$^{1/2}$ where $R_D \approx 200\ \Omega$ is the dynamic resist-

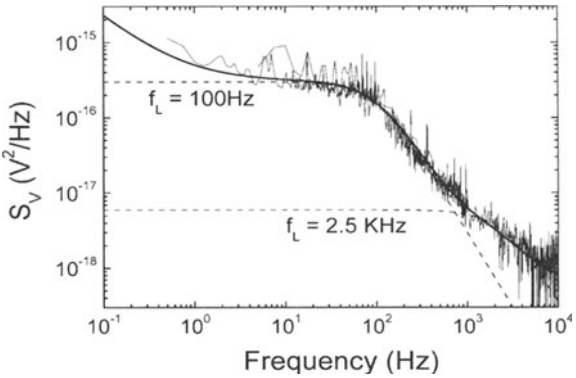

Figure 1. Voltage noise power spectrum of an Al-AlO_x-Al junction at temperature 0.3 K and voltage 2.5 mV. The junctions' parameters are: area 0.08 μm^2, critical current 8 μA, and shunt resistance 20 Ω.

ance. We have assumed $|(\partial V/\partial I_0)_I| \approx (\partial V/\partial I)_{I_0} = R_D$ for a bias current only slightly above the critical current. For a bandwidth of 100 Hz, the inferred value of ΔI_0 is 0.7 nA, leading to $\Delta I_0/I_0 = 9 \times 10^{-5}$ for the measured critical current $I_0 = 8$ μA. Finally, we deduce $\Delta A = A(\Delta I_0/I_0) = 7$ nm^2, corresponding to a trap radius of about 1.5 nm.

Relatively large Josephson junctions with areas of at least several square micrometers, on the other hand, tend to show low-frequency noise that scales approximately as $1/f$, indicating that a significant number of RTSs are active. Table 1 shows a compilation of

Table 1. Critical current $1/f$ noise at temperature 4.2 K and frequency 1 Hz.

Materials	Area (μm^2)	I_0 (μA)	$S_{I_0}^{1/2}$ (1 Hz) (pA/$Hz^{1/2}$)	$A^{1/2}S_{I_0}^{1/2}$ (1 Hz)/I_0 [μm(pA/$Hz^{1/2}$)/μA]
Nb-AlO_x-Nb[a]	9	9.6	36	11
	8	2.6	6	7
	115	48	35	8
	34	12	41	20
Nb-O_x-PbIn[b]	4	21	74	7
	4	4.6	46	20
	4	5.5	25	9
	4	5.7	34	12
	4	11.4	91	16
Nb-NbO_x-PbInAu[c]	1.8	30	184	8
PbIn-O_x-Pb[d]	6	510	6	15
Average				12

[a]Savo *et al.* [26].
[b]Wellstood [27].
[c]Foglietti *et al.* [28].
[d]Koch *et al.* [29].

$S_{I_0}^{1/2}(1\text{ Hz})$ at 4.2 K for 11 junctions made with four different technologies. The last column shows the quantity $A^{1/2}S_{I_0}^{1/2}(1\text{ Hz})/I_0$ to be remarkably consistent, given the different materials and the wide range of areas and critical currents. For future reference, we will adopt an average $1/f$ noise spectral density

$$S_{I_0}(1\text{ Hz}, 4.2\text{ K}) \approx \left[\frac{144(I_0/\mu\text{A})^2}{A/\mu m^2}\right](\text{pA})^2/\text{Hz} \tag{6}$$

3.3 Electron trapping mechanisms

We briefly discuss the electron trapping process for the case $|eV| > 2\Delta$, where Δ is the superconducting energy gap. For these voltages, one usually determines resistance fluctuations by measuring the voltage noise at constant bias current.

The total rate for a given RTS process can be written as

$$\tau^{-1} = \tau_{\text{act}}^{-1} + \tau_{\text{tun}}^{-1} \tag{7}$$

where the thermal activation rate is given by [30]

$$\tau_{\text{act}}^{-1} = \tau_0^{-1} \exp\left[\frac{-(E_B - \gamma_a eV)}{k_B T}\right] \tag{8}$$

and the tunneling rate for $eV > k_B T$ by [30]

$$\tau_{\text{tun}}^{-1} = \tau_0^{-1}\left[1 + C\left(\frac{k_B T}{eV}\right)^2\right]\exp\left[-2\left(\frac{2mE_B}{\eta^2}\right)^{1/2} d(1 - \gamma_t eV)\right] \tag{9}$$

Here, E_B and d are the barrier height and thickness, C is a parameter calculated for Poole–Frenkel tunneling, and γ_a and γ_t are coefficients empirically chosen to model the observed voltage dependence. Measurements by Rogers and Buhrman [30] show a clear crossover from activated to tunneling behavior at around 15 K. Interestingly, to obtain reasonable agreement with Eq. (9) they had to use an atomic mass for m, suggesting that ionic reconfiguration plays a dominant role in the tunneling process. Wakai and Van Harlingen [31] demonstrated the voltage dependence of the tunneling rates.

We note that, despite the T^2 variation of the prefactor in Eq. (9), the temperature dependence of the power spectrum arising from an ensemble of fluctuators in the tunneling regime is dominated by the exponent and hence has only a weak temperature dependence. For example, for the representative parameters $C = 540$, $\gamma_t = 12.8\text{ eV}^{-1}$, $m^{1/2}d = 3 \times 10^{-23}\text{ kg}^{1/2}\text{ m}$, $\tau_0^{-1} = 5 \times 10^{10}\text{ s}^{-1}$ and $V = 2\text{ mV}$, one finds $S(f, T) \propto T^{0.075}$.

3.4 Critical current noise at low temperatures

Since experiments on qubits are performed at millikelvin temperatures, one clearly requires measurements of the critical current $1/f$ noise on junctions made with the same technology in the same temperature range. Unfortunately, there are few such measurements. Wellstood [27] carried out experiments at these temperatures on Nb-

NbO_x-PbIn SQUIDs with a flux bias of $n\Phi_0$ so that $(\partial V/\partial\Phi)$ was precisely zero and only the in-phase contribution in Eq. (4) was nonzero. The devices were connected in series with a small resistor and the input coil of a readout SQUID. A current source was connected across the resistor to voltage-bias the junctions at about 1 μV, and the critical current fluctuations were measured directly with the readout SQUID.

The noise spectral density of five such devices was measured over the temperature range 0.08–4.2 K, and found to scale approximately as $1/f$ at low frequencies. The magnitude of $S_{I_0}(1\text{ Hz})$ was remarkably consistent over the five devices, and scaled as T^2, with a suggestion of a flattening at about 0.2 K. The values of the noise at 1 Hz and 4.2 K are listed in Table 1, and contribute to the average value given in Eq. (6). To our knowledge, this is the only set of data exhibiting a T^2 dependence, and the issue of whether or not this behavior extends to lower temperatures is of crucial importance to the development of qubits involving Josephson junctions.

The observed T^2 dependence is incompatible with the electron trapping mechanism in the tunneling regime, as described in Section 3.3. For thermal activation, a model yielding a T^2 dependence has been proposed by Kenyon *et al.* [32] in the context of charge $1/f$ noise, but is equally applicable to critical current noise. In this model, one assumes that the two-state systems are asymmetric, and that the depths of the two wells, U_1, and U_2, are independent random variables. Under this assumption, the spectral density of the noise is given by

$$S_{I_0}(f) \propto \int_0^\infty \int_0^\infty dU_1\, dU_2 \frac{D(U_1, U_2)}{\tau_1(U_1) + \tau_2(U_2)} \frac{1}{(2\pi f)^2 + [\tau_1^{-1}(U_1) + \tau_2^{-1}(U_2)]^2} \tag{10}$$

If we assume $D(U_1, U_2)$ to be independent of U_1 and U_2 and that the processes are thermally activated, we can carry through the integration to find

$$S_{I_0}(f) \propto \frac{D(U_1, U_2)(k_B T)^2}{f} \tag{11}$$

3.5 $1/f$ Noise in Al-AlO_x-Al junctions below 1 K

In an attempt to measure the $1/f$ noise in submicron Josephson junctions, we fabricated a SQUID with 0.11 μm^2 Al-AlO_x-Al junctions. The estimated loop inductance was 400 pH, the critical current per junction was about 2.5 μA and the CuAu shunt on each junction was about 20 Ω. Operated in a flux-locked loop with flux modulation (but not bias reversal), at 0.3 K, the SQUID yielded the flux noise shown in Fig. 2. The observed white noise level was attributed to the room temperature amplifier. This plot yields $S_\Phi^{1/2}(0.2\text{ Hz}) \leq 7 \times 10^{-6}\,\Phi_0/\text{Hz}^{1/2}$, corresponding to $S_\Phi^{1/2}(1\text{ Hz}) \leq 3 \times 10^{-6}\,\Phi_0/\text{Hz}^{1/2}$. Assuming that the $1/f$ noise is due solely to critical current fluctuations leads to $S_{I_0}^{1/2}(1\text{ Hz}) \approx S_\Phi^{1/2}(1\text{ Hz})/2^{1/2}L \leq 10\,\text{pA/Hz}^{1/2}$. By comparison, the average value in Eq. (6), scaled linearly with temperature to 0.3 K, yields 9 $\text{pA/Hz}^{1/2}$. Although it would have been more satisfying to observe the actual value of the $1/f$ noise, the fact that the measured noise in a submicron Al-AlO_x-Al junction at 0.3 K does not exceed the empirical prediction is somewhat reassuring.

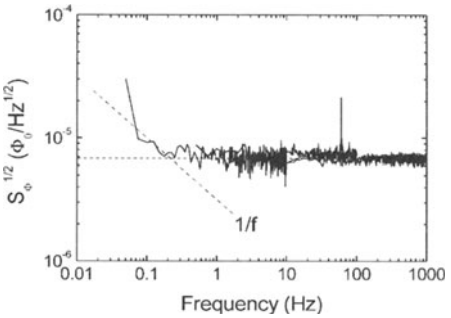

Figure 2. Flux noise spectrum of an Al-AlO_x-Al dc-SQUID in a flux-locked loop at 0.3 K. SQUID parameters are inductance 400 pH, critical current per junction 2.5 μA, and shunt resistance per junction 30 Ω.

3.6. Comment on temperature dependence of $1/f$ noise

The reported T^2 dependence of the $1/f$ noise at low temperatures disagrees with the usual model of critical current $1/f$ noise in superconducting tunnel junctions, which requires a *single* electron to be transferred from one electrode into a trap in the barrier and subsequently from the trap into an available state in the other electrode. In the first place, there is strong evidence that the charge trapping occurs via tunneling in the temperature range considered so that the noise should be relatively temperature independent. Further, for eV, $k_BT \ll 2\Delta$ both the available number of single electrons and the available number of final single-electron states scale as $\exp(-\Delta/k_BT)$ so that the charge trapping process is expected to freeze out at low temperatures. This leads one to seek alternative explanations.

One possibility [33] is that the $1/f$ noise is associated with leakage currents at voltages below $2\Delta/e$, which do not exhibit an exponential temperature dependence. Such leakage currents presumably occur between opposing normal regions of the electrodes, conceivably at the edges of the junctions or along the core of a flux vortex penetrating the junction. An investigation of the correlation between leakage currents and $1/f$ noise would be of great interest. Other possible sources of the $1/f$ noise include the motion of electrons between traps in the substrate, which produces charge noise in single electron transistors, and the motion of electrons between traps within the tunnel barrier. The motion of vortices in or near the junction could also create a thermally-activated contribution to the critical current fluctuations.

4. DECOHERENCE IN QUBITS DUE TO CRITICAL CURRENT $1/f$ NOISE

4.1 Frequency modulation from critical current fluctuations

We consider a qubit with quantum states $|0\rangle$ and $|1\rangle$ separated by an energy $\hbar\Omega$. A fluctuation δI_0 in the critical current produces a fluctuation $(\partial\Omega/\partial I_0)_\Phi \delta I_0$ in the qubit

frequency that in turn leads to phase noise and thus to decoherence. Our first task is to calculate the dimensionless quantity

$$\Lambda = \left| \left(\frac{I_0}{\Omega} \right) \left(\frac{\partial \Omega}{\partial I_0} \right)_\Phi \right| \tag{12}$$

which characterizes the sensitivity of the tunneling frequency to critical current changes, for the one-junction and three-junction qubits.

We begin with the one-junction qubit (rf-SQUID), which is characterized by the variable $\beta_L = 2\pi L I_0/\Phi_0$, where L is the loop inductance. We first consider the ground state behavior of this qubit before moving on to a treatment of entangled excited states which were exploited in the experiments by Friedman *et al.* [3] At the degeneracy point, the tunneling frequency (ground state splitting) is given in the WKB approximation as [34]

$$\Omega(\beta_L) = \omega_0 \exp\left(-\left[\frac{(\beta_L - 1)^{3/2} \lambda}{2^{1/2}} \right] \right) \tag{13}$$

provided $k_B T \ll \hbar\omega_0$. Here $\omega_0 = 2[(\beta_L - 1)/(LC)]^{1/2}$ is the small-oscillation frequency in either potential well, C is the junction capacitance, $\lambda = (8CI_0\Phi_0/\pi^3\hbar)^{1/2}$ is the "degree of classicality" and $V_0 = 3\Phi_0^2(\beta_L - 1)^2/8\pi^2 L$ is the barrier height. We choose the parameters [3] $L = 240$ pH and $C = 103$ fF (junction area $\sim 2\,\mu\text{m}^2$), and vary β_L.

In Fig. 3(a) we plot $\omega_0/2\pi$ and $\Omega/2\pi$ versus β_L for these parameters. We note an interesting point: at $\beta_L = 1.02$ we find $(\partial\Omega/\partial\beta_L) = 0$, that is, the frequency is insensitive to critical current fluctuations. This fact is reflected in Fig. 3(b), where we see that Λ rises smoothly from zero for $\beta_L = 1.02$. Finally, Fig. 3(c) shows how the fractional change in tunneling frequency, $\delta\Omega/\Omega$, varies with β_L for three values of the fractional change in critical current, $\delta I_0/I_0$. If we choose $I_0 = 1.46\,\mu$A ($\beta_L = 1.06$), which gives a reasonable tunneling rate ($\Omega/2\pi = 2.52$ GHz), we find $\Lambda = 40.6$, meaning that a 1 ppm change in the critical current causes a 40.6 ppm change in the tunneling frequency.

However, the qubit described above is unrealistic since it is not possible to confine the ground state energy $\eta\omega_0/2$ within the potential well while maintaining a sufficiently large

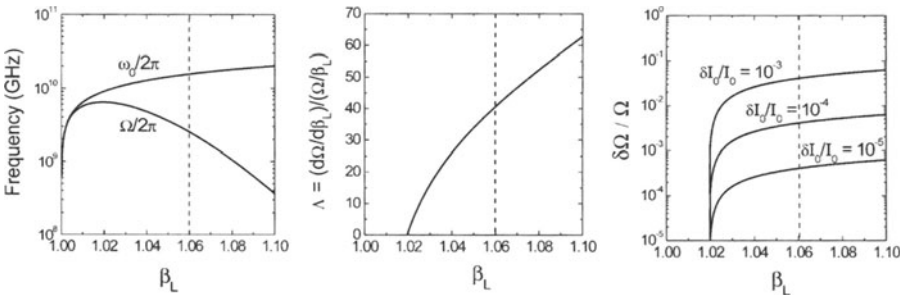

Figure 3. One-junction (rf-SQUID) qubit: (a) Plasma frequency $\omega_0/2\pi$ and tunneling frequency $\Omega/2\pi$ vs. β_L; (b) Frequency modulation factor Λ vs. β_L; (c) Fractional tunneling frequency shift for changes in the junction critical current. The dashed lines are drawn at $\beta_L = 1.06$.

tunneling frequency. The experiments of Friedman *et al.* [3] actually involved tunneling between excited states in an asymmetric potential. We have examined the sensitivity of this experiment to critical current fluctuations by looking at the energy dependence of the excited state solutions of the Schrödinger equation for the same device parameters $L = 240$ pH and $C = 103$ fF, but for a larger critical current $I_0 = 2.05\ \mu$A ($\beta_L = 1.50$) and flux bias $\Phi = 0.514\ \Phi_0$. This produces an asymmetric double well potential with tunneling barriers $U_1 = 4.640$ K and $U_2 = 13.226$ K. For tunneling between the third excited state of the shallow well and the ninth excited state of the deep well, we find a tunneling frequency $\Omega/2\pi = 0.732$ GHz and a critical current sensitivity factor $\Lambda = 43.2$. For tunneling between the confined levels with the highest energy, the fourth and tenth, we find $\Omega/2\pi = 4.83$ GHz and $\Lambda = 34.2$. We note that both this scenario and the ground state device considered above show similar sensitivity to critical current variations.

We turn next to the three-junction qubit [4, 35], and regard the Josephson coupling energy $E_J = I_0\Phi_0/2\pi$ as the control variable. Here, I_0 is the critical current of two of the three junctions; that of the third smaller junction is $I_{0s} = aI_0$ ($a < 1$). At the degeneracy point, the tunneling frequency for intra-cell tunneling is

$$\Omega(E_J) = \omega_m \exp -\left[\frac{4a(1+2a)E_J}{E_C}\right]^{1/2} \sin\phi_m^* - \phi_m^*/2a \tag{14}$$

where $E_C = e^2/2C$ is the charging energy, $\omega_m = [4(4a^2-1)(E_JE_C/a(1+2a)]^{1/2}/\eta$ is the relevant plasma frequency, and $\phi_m^* = \cos^{-1}(1/2a)$. Since the smaller junction primarily controls the barrier height whereas the larger junctions mostly contribute to the loop inductance, the variations of Ω with the two critical currents differ in magnitude and sign. Thus, it is necessary to consider the contribution from each junction separately; simply varying I_0 in Eq. (14) significantly underestimates the response. Figure 4(a) shows $\omega_m/2\pi$ and $\Omega/2\pi$ versus I_0, and Fig. 4(b) shows Λ_s versus I_0, where Λ_s characterizes the variation of the tunneling frequency for changes of the small junction alone (determined by varying

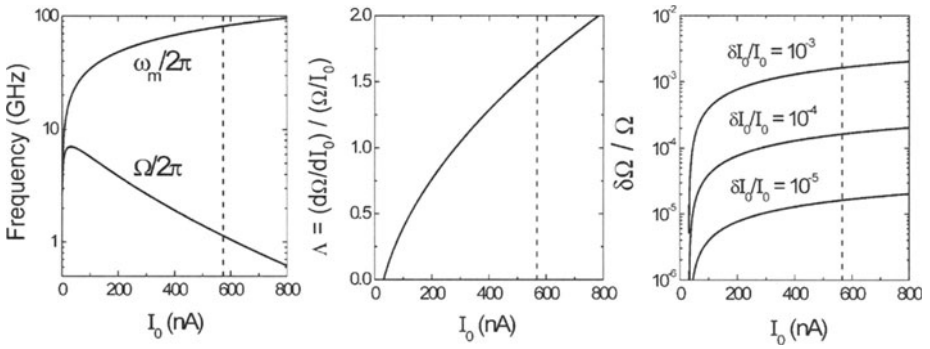

Figure 4. Three-junction qubit: (a) Plasma frequency $\omega_m/2\pi$ and tunneling frequency $\Omega/2\pi$ vs. critical current I_0; (b) Frequency modulation factor Λ_s vs. I_0; (c) Fractional tunneling frequency shifts for different changes in the small junction critical current. The dashed lines are drawn at $I_0 = 570$ nA.

of the ratio parameter a). The values of the parameters used are those in the experiment of van der Wal *et al.* [4], $L = 11$ pH, $C = 2.6$ fF (junction area $\sim 0.05\ \mu m^2$), and $a = 0.82$. Figure 4(c) shows the fractional change in tunneling frequency versus I_0 for three values of the small junction variation $\delta I_{0s}/I_{0s}$. For the critical current in the experiment of van der Wal *et al.* [4], $I_0 = 570$ nA for which $\Omega/2\pi = 1.14$ GHz, we find $\Lambda_S = 12.8$. Varying I_0 (and a so that the product aI_0 remains fixed) enables us to compute $\Lambda_L = 4.0$ for the large junctions. If we assume that the critical currents of the three junctions fluctuate independently, we find an effective $\Lambda = (\Lambda_S^2 + 2\Lambda_L^2)^{1/2} \sim 14.0$. This result is supported by simulations based on the WKB approximation [36].

The results for the one-junction and three-junction qubits are summarized in Fig. 5, where we plot $\delta\Omega/\Omega$ versus $\delta I_0/I_0$. The one-junction qubit is somewhat more sensitive to a given critical current fluctuation than the three-junction device, but it is necessary to consider the magnitude of the $1/f$ noise in each case to assess the resulting decoherence.

4.2. Decoherence due to critical current fluctuations

We now discuss how the $1/f$ fluctuations in the critical current lead to decoherence. This problem has been formulated by Martinis *et al.* [12] for the current-biased junction [7], and we adopt their treatment. The fluctuation $\delta I_0(t)$ is related to the spectral density of the critical current noise via the correlation function

$$\langle \delta I_0(0) \delta I_0(t) \rangle = \int_0^\infty df S_{I_0}(f) \cos 2\pi f t \tag{15}$$

At constant flux bias, after a time t has elapsed, the phase changes by

$$\phi(t) = \left(\frac{\partial \Omega}{\partial I_0}\right)_\Phi \int_0^t dt' \delta I_0(t') \tag{16}$$

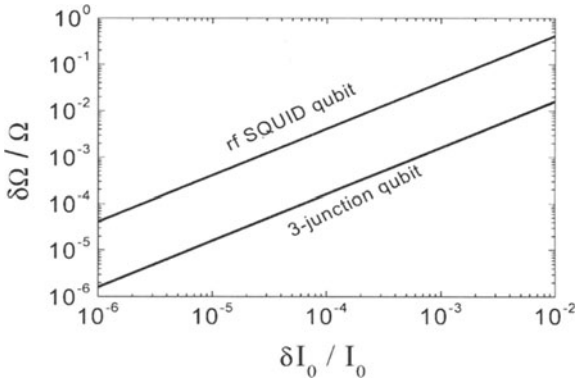

Figure 5. Comparison of the sensitivity of the tunneling frequency to critical current changes for the one-junction qubit in the ground state and for the three-junction qubit.

Since $\langle \delta I_0(t) \rangle = 0$, $\langle \phi(t) \rangle = 0$; however, $\langle \phi^2(t) \rangle \neq 0$. Thus, each time one makes a measurement of the qubit state, there will be a randomization of the phase. The mean square phase noise at time t is given by

$$\begin{aligned}\langle \phi_n^2(t) \rangle &= \left(\frac{\partial \Omega}{\partial I_0}\right)_\Phi^2 \left\langle \int_0^t dt' \delta I_0(t') \int_0^t dt'' \delta I_0(t'') \right\rangle \\ &= \left(\frac{\partial \Omega}{\partial I_0}\right)_\Phi^2 \int_0^\infty df S_{I_0}(f) \int_0^t dt' \Re e^{-i2\pi f t'} \int_0^t dt'' \Re e^{-i2\pi f t''} \\ &= \left(\frac{\partial \Omega}{\partial I_0}\right)_\Phi^2 \int_{f_m}^{f_s} df S_{I_0}(f) \frac{\sin^2(\pi f t)}{(\pi f)^2} \end{aligned} \tag{17}$$

Here, $\Re$ designates the real part. In writing Eq. (17), we assume that we measure N time points to map the probability oscillations, each point being an average over n flux state measurements of duration t_s. Thus, the highest frequency of interest is the sampling time $f_s = 1/t_s$ and the lowest relevant frequency is the time to make the entire measurement, $f_m = 1/Nnt_s$. Typically, one might expect $f_s/f_m \geq 10^5$.

Writing the critical current spectral density as $S_{I_0}(f) = s_{I_0}(1\,\text{Hz})/f$, where the coefficients $s_{I_0}(1\,\text{Hz})$ has units of (Ampere) [2], and carrying out the integral, one finds [12]

$$\langle \phi_n^2(t) \rangle \approx \left[\left(\frac{\partial \Omega}{\partial I_0}\right)_\Phi^2 s_{I_0}(1\,\text{Hz}) \ln(0.4/f_m t) \right] t^2 \approx \left(\frac{t}{\tau_\phi}\right)^2 \tag{18}$$

The latter expression neglects the time dependence in the logarithmic term and is a valid approximation for $f_m t = 0.15$ and $f_s \leq 20 f_m$, conditions that are likely to be satisfied for typical experiments. This defines an effective decoherence time τ_ϕ, but we note the unusual result that $\langle \Phi_n^2(t) \rangle$ scales as t^2, indicating that the decoherence is evidently not simply interpretable as a rate [12]. Rather, one should consider Eq. (18) as representing a change in the quantum oscillation frequency each time a measurement is repeated. To estimate the logarithmic term, we assume $f_m \sim 1$ Hz, corresponding to 100 time points, each point being the average of 1000 flux measurements, each of which takes 10 μs. Setting $t \sim t_s = 10$ μs, we find $\ln(0.4/f_m t) \sim 10$, so that

$$\tau_\phi \sim \left(\frac{I_0}{\Omega \Lambda}\right) \left(\frac{1}{10 s_{I_0}(1\,\text{Hz})}\right)^{1/2} \tag{19}$$

using Eq. (12) for Λ. Using Eq. (6) and assuming the $1/f$ noise scales as T^2, we find the following expression for the dephasing time

$$\tau_\phi \sim (0.11) \frac{(A/\mu\text{m}^2)^{1/2}}{(\Omega/\text{GHz})\Lambda(T/\text{K})}\,\mu\text{s} \tag{20}$$

We note that $\tau \propto 1/T$ provided that S_{I_0} (1 Hz) varies as T^2.

Table 2 lists L, I_0, β_L, A, C, $\Omega/2\pi$, Λ, τ_ϕ, and $\Omega\tau_\phi/2\pi$ for the two types of qubits. We see that our estimates of τ_ϕ indicate a decoherence time of 2.4 μs for the one-junction

Table 2. Parameters for the one-junction qubit in the ground state and three-junction qubit (van der Wal *et al.* [4]).

Parameters	One-junction	Three-junction
L (pH)	240	11
I_0 (μA)	1.46	0.570
β_L	1.06	0.019
A (μm^2)	2	0.05
C (fF)	103	2.6
$\Omega/2\pi$ (GHz)	2.52	1.14
Λ	40.6	14.0
τ_ϕ (μs)	2.4	2.5
$\Omega\tau_\phi/2\pi$	6000	2800

qubit, and 2.5 μs for the three-junction qubit, virtually the same. The corresponding values of $\Omega\tau_\phi/2\pi$, which give an estimate of the number of observable quantum oscillations, are $\sim$6000 and $\sim$2800, respectively. By comparison, for the current-biased junction at the same temperature, Martinis *et al.* [12] find $\tau_\phi \sim 12$ μs and $\Omega\tau_\phi/2\pi \sim 82\,000$. Thus, in all three cases, the number of coherent oscillations potentially observable is predicted to be greater than 1000.

5. CONCLUDING REMARKS

Despite ongoing studies over more than two decades, the origin of $1/f$ noise in the critical current of Josephson junctions is still not fully understood. Although there is strong evidence that the noise derives from a superposition of random telegraph signals produced by charge trapping and untrapping processes, the origin of the T^2 dependence observed by Wellstood [27] remains puzzling. This temperature dependence can be explained within the framework of a two-well potential in which the two barrier heights are independent random variables, provided one assumes thermally-activated processes, rather than the tunneling processes one might expect. Furthermore, the absence of a temperature dependence of the form $\exp(-\Delta/k_BT)$ is difficult to understand in a picture in which the trap exchanges single electrons with superconducting electrodes. Clearly more work is required to understand this low temperature behavior.

We have found that the spectral density of the $1/f$ noise from a number of different experiments with different junction technologies scales surprisingly well as $[144(I_0/\mu\text{A})^2/(\text{A}/\mu\text{m}^2)](\text{pA})^2/\text{Hz}$ at 4.2 K. Based solely on Wellstood's results, we have chosen to scale this number with $(T/4.2\,\text{K})^2$ to predict the $1/f$ noise at lower temperatures. We have made measurements on a single, submicron Al-AlO_x-Al device at 0.3 K which show that the noise did not exceed the value predicted by the scaling. How well this scaling holds up as more junctions are investigated and whether the T^2 dependence holds down to (say) 10 mK are questions that should be addressed with some urgency. These measurements must of necessity be made with a SQUID amplifier; the use of submicron junctions with relatively high critical currents should enhance the magnitude of the noise and make its observation easier.

We have calculated the parametric effect of small changes in the critical current I_0 of one-junction and three-junction flux qubits on the tunneling rates Ω at the degeneracy point. In each case, there is a value of I_0 at which $(\partial\Omega/\partial I_0)_\Phi$ vanishes, corresponding to the point at which the dependences of the prefactor and exponent of the tunneling rate precisely cancel. We introduce the normalized parameter $\Lambda = |(I_0\partial\Omega/\Omega\partial I_0)_\Phi|$ and use the extrapolated magnitude of the $1/f$ noise to investigate dephasing in the two kinds of qubits at 0.1 K, following the treatment by Martinis *et al.* [12]. This formulation predicts that the mean square phase noise $\langle\phi_n^2(t)\rangle$ scales as t^2, so that the decoherence is not interpretable as a rate. Rather, the tunneling frequency is different each time a measurement is made. For both kinds of qubit, this approach predicts that one can expect to observe more than 1000 coherent oscillations. Furthermore, if the T^2 dependence of the $1/f$ noise does continue at temperatures down to (say) 10 mK, the decoherence time, which scales as $1/T$, will become remarkably long at such low temperatures. We note also that even if $1/f$ noise is present, the use of spin echoes can significantly reduce its effects [5, 12, 37].

Finally, this formulation could readily be extended to qubits away from the degeneracy point or in excited states, simply by calculating the appropriate values of Λ. It could also be used to investigate the effects of $1/f$ noise in the flux bias point originating either from magnetic vortex motion or from current noise in the flux power supply by calculating the quantity $(\partial\Omega/\partial\Phi)_{I_0}$.

Acknowledgements

We are indebted to John Martinis for prepublication copies of his papers, and to him, Daniel Esteve, Fred Wellstood, and Frank Wilhelm for helpful discussions. We thank Jim Lukens for pointing out the importance of allowing the critical currents in the three-junction qubit to fluctuate independently. This research was supported by the Director, Office of Science, Office of Basic Energy Sciences, Division of Materials Sciences and Engineering of the U.S. Department of Energy under Contract DE-AC03-76SF00098, and by the National Science Foundation under grant NSF-EIA01-21568. DVH acknowledges the Miller Institute at the University of California at Berkeley for support.

REFERENCES

[1] V. Bouchiat, D. Vion, P. Joyez, D. Esteve, and M. H. Devoret, Quantum coherence with a single Cooper pair, *Phys. Scr.* **T76**, 165 (1998).

[2] Y. Nakamura, C. D. Chen, and J. S. Tsai, Spectroscopy of energy-level splitting between two macroscopic quantum states of charge coherently superposed by Josephson coupling, *Phys. Rev. Lett.* **79**, 2328–2331 (1997).

[3] J. R. Friedman, V. Patel, W. Chen, S. K. Tolpygo, and J. E. Lukens, Quantum superposition of distinct quantum states, *Nature* **406**, 43–46 (2000).

[4] C. H. van der Wal, A. C. J. ter Haar, F. K. Wilhelm, R. N. Schouten, C. J. P. M. Harmans, T. P. Orlando, S. Lloyd, and J. E. Mooij, Quantum superposition of macroscopic persistent-current states, *Science* **290**, 773–777 (2000).

[5] D. Vion, A. Aassime, A. Cottet, P. Joyez, H. Pothier, C. Urbina, D. Esteve, and M. H. Devoret, Manipulating the quantum state of an electrical circuit, *Science* **296**, 886–889 (2002).

[6] Y. Yu, S. Han, X. Chu, S. -I. Chu, Z. Wang, Coherent temporal oscillations of macroscopic quantum states in a Josephson junction, *Science* **296**, 889–892 (2002).

[7] J. M. Martinis, S. Nam, J. Aumentado, and C. Urbina, Rabi oscillations in a large Josephson-junction qubit (unpublished).

[8] M. Nielsen and I. Chuang, *Quantum computation and quantum information* (Cambridge, UK, Cambridge University Press, 2000).
[9] P. Dutta and P. M. Horn, Low-frequency fluctuations in solids: $1/f$ noise, *Rev. Mod. Phys.* **53**, 497–516 (1981).
[10] A. Shnirman, Y. Makhlin, and G. Schön, Noise and decoherence in two-level systems (cond-mat/0202518).
[11] E. Paladino, L. Faoro, G. Falci, and R. Fazio, Decoherence and $1/f$ noise in Josephson qubits, *Phys. Rev. Lett.* **88**, 228304-1-4 (2002).
[12] J. M. Martinis, S. Nam, J. Aumentado, K. M. Lang, and C. Urbina, Decoherence of a superconducting qubit from bias noise (unpublished).
[13] S. Machlup, *J. Appl. Phys.* **25**, 341 (1954).
[14] J. Bernamont, *Ann. Phys. (Leipzig)* **7**, 71 (1937).
[15] F. K. du Pré, *Phys. Rev.* **78**, 615 (1950).
[16] A Van der Ziel, *Physica* **16**, 359 (1950).
[17] R. C. Jaklevic, J. Lambe, A. H. Silver, and J. E. Mercereau, Quantum interference effects in Josephson tunneling, *Phys. Rev. Lett.* **12**, 159–160 (1964).
[18] R. H. Koch, J. Clarke, W. M. Goubau, J. M. Martinis, C. M. Pegrum, and D. J. Van Harlingen, Flicker ($1/f$) noise in tunnel junction dc-SQUIDs, *J. Low Temp. Phys.* **51**, 207–224 (1983).
[19] R. L. Forgacs and A. F. Warnick, Digital-analog magnetometer utilizing superconducting sensor, *Rev. Sci. Instrum.* **38**, 214–219 (1967).
[20] M. J. Ferrari, M. Johnson, F. C. Wellstood, J. J. Kingston, T. J. Shaw, and J. Clarke, Magnetic flux noise in copper oxide superconductors, *J. Low Temp. Phys.* **94**, 15–61 (1994).
[21] E. Dantsker, S. Tanaka, and J. Clarke, High-T_c SQUIDs with slots or holes: low $1/f$ noise in ambient magnetic field, *Appl. Phys. Lett.* **70**, 2037–2039 (1997).
[22] J. R. Clem (unpublished).
[23] G. Stan, S. Field, and J. M. Martinis (unpublished)
[24] C. T. Rogers and R. A. Buhrman, Composition of $1/f$ noise in metal-insulator-metal tunnel junctions, *Phys. Rev. Lett.* **53**, 1272–1275 (1984).
[25] R. T. Wakai and D. J. Van Harlingen, Low frequency noise and discrete charge trapping in small-area tunnel junctions dc SQUIDs, *Appl. Phys. Lett.* **49**, 593–595 (1986).
[26] B. Savo, F. C. Wellstood, and J. Clarke, Low-frequency excess noise in Nb-Al_2O_3-Nb Josephson tunnel junctions, *Appl. Phys. Lett.* **50**, 1757–1759 (1987).
[27] F. C. Wellstood, Excess noise in the dc-SQUID: 4.2 K to 20 mK, Ph.D. thesis, University of California, Berkeley (1988).
[28] V. Foglietti, W. J. Gallagher, M. B. Ketchen, A. W. Kleinsasser, R. H. Koch, S. I. Raider, and R. L. Sandstrom, Low-frequency noise in low $1/f$ noise dc SQUIDs, *Appl. Phys. Lett.* **49**, 1393–1395 (1986).
[29] R. H. Koch, D. J. Van Harlingen, and J. Clarke, Superconducting quantum interference device with very low magnetic flux noise energy, *Appl. Phys. Lett.* **41**, 197–199 (1982).
[30] C. T. Rogers and R. A. Buhrman, Nature of single-localized-electron states derived from tunneling measurements, *Phys. Rev. Lett.* **55**, 859–862 (1985).
[31] R. T. Wakai and D. J. Van Harlingen, Direct lifetime measurements and interactions of charged defect states in submicron Josephson junctions, *Phys. Rev. Lett.* **58**, 1687–1690 (1987).
[32] M. Kenyon, C. J. Lobb, and F. C. Wellstood, Temperature dependence of low-frequency noise in Al-Al_2O_3-Al single-electron transistors, *J. Appl. Phys.* **88**, 6536–6540 (2000).
[33] M. J. Feldman, private communication.
[34] A. J. Leggett, Quantum mechanics at the macroscopic level, Les Houches, Session XLVI—Chance and Matter, edited by J. Souletie, J. Vannimenus, and R. Stora (Amsterdam, Elsevier, 1987), pp. 395–506.
[35] T. P. Orlando, J. E. Mooij, L. Tian, C. H. van der Wal, L. S. Levitov, S. Lloyd, and J. J. Mazo, Superconducting persistent-current qubit, *Phys. Rev.* **B60**, 15398–15413 (1999).
[36] T. L. Robertson, D. J. Van Harlingen, B. L. T. Plourde, P. A. Reichardt, and John Clarke, unpublished.
[37] Y. Nakamura, Y. A. Pashkin, T. Yamamoto, and J. S. Tsai, Charge echo in a Cooper-pair box, *Phys. Rev. Lett.* **88**, 047901-1-047901-4 (2002).

ZEEMAN SPLITTING IN QUANTUM DOTS

S. Lindemann[1], T. Ihn[1], T. Heinzel[1], K. Ensslin[1,a], K. Maranowski[2], and A. C. Gossard[2]
[1]*Solid State Physics Laboratory, ETH Zürich, 8093 Zürich, Switzerland*
[2]*Materials Department, University of California, Santa Barbara, CA 93106, USA*

Abstract: Coulomb blockade resonances in quantum dots are investigated as a function of magnetic fields applied in the plane of the electron gas. For weak coupling of the dot to the leads, where the Coulomb resonances are basically dominated by individual quantum states, we observe strongly fluctuating Coulomb peak positions, which can be qualitatively explained by linear Zeeman shifts. For strong coupling the peak positions are quite well described by the linear Zeeman shift in spite of the fact that transport occurs through multiple levels. From the point of view of a single particle picture the spin degrees of freedom are remarkably stable.

Keywords: Quantum dots, Spin

1. INTRODUCTION

The energy spectra of quantum dots have been investigated by Coulomb blockade experiments [1, 2]. If the tunnel coupling of a small island to its leads is sufficiently small, the width of a Coulomb resonance is limited by temperature. For sufficiently small quantum dots, where the average level separation Δ is larger than kT and the level width Γ, that is, $\Delta \gg kT$, Γ, the amplitude and position of a Coulomb resonance is governed by the properties of an individual quantum state. While the charge domain of such experiments is well investigated and understood, the spin properties of quantum dots require further research. Here we set out to explore how the separation of neighboring Coulomb maxima depends on an in-plane magnetic field and is compatible with Zeeman splitting of energy levels. In particular, we study this behavior as the coupling of the quantum dot to its environment is tuned from the single to the multi-level transport regime. In the single-level regime the Coulomb peak spacing fluctuates strongly within the limits set by Zeeman splitting. For strong coupling, that is, multi-level transport, the peak separation is well explained by the expectations of Zeeman splitting for single-particle levels. This allows the identification of specific spin states as well as the sequential population of

[a]E-mail: ensslin@phys.ethz.ch

single-particle states with orbital and spin degrees of freedom. The results presented in this conference proceedings are based on Refs. [3] and [4].

2. EXPERIMENTAL RESULTS

Our quantum dots are fabricated by electron beam lithography on an electron gas embedded in a parabolic quantum well (PQW) [5] with a suitably designed back gate electrode [6]. The position of the electron gas in the growth direction can be tuned by front and back gate voltages [7]. Quantum dots on such PQWs have been investigated [8] in the regime where the second subband for the confinement in growth (z-) direction is occupied and switching behavior of the Coulomb blockade peaks has been observed that can be attributed to the occupation of the second subband [8]. Here we focus on the regime where only one subband is occupied and switching events are absent. The quantum dots are as stable as those fabricated on regular two-dimensional electron gases (2DEGs) in heterostructures. With the back gate we drive the system to rather low densities $n_s < 1.5 \times 10^{15}\ \mathrm{m}^{-2}$ such that the interaction parameter $r_s \propto 1/\sqrt{n_s}$ can be as large as 1.5 as in Ref. [9] but smaller than in experiments on Si [10].

Figure 1 shows Coulomb blockade resonances as a function of plunger gate voltage. In this gate voltage interval we clearly see a transition from weak, to intermediate, and to strong coupling of the quantum dot to source and drain, as indicated by comparison of the Coulomb blockade peak width with the single-particle level spacing. In this paper we focus on the weak and strong coupling regime. A more comprehensive discussion of the data for all coupling regimes and various magnetic field orientations is published elsewhere [3].

Figure 2(a) presents spacings of neighboring Coulomb peaks. As mentioned before, the lever arm relating plunger gate voltage to energy in the dot is extracted from the measured Coulomb diamonds [13] in Fig. 2. The change of lever arm with plunger gate voltage is explicitly taken into account. The curves are relatively flat up to magnetic fields of about 0.8 T. With the bare g-factor of GaAs, $g = -0.44$, the Zeeman splitting is about $E_Z = |g|\mu_B = 25\ \mu\mathrm{eV/T}$. The electron temperature as determined from the Coulomb blockade peak width of $3.5kT = 42\ \mu\mathrm{eV}$ results in $T \approx 140\,\mathrm{mK}$. As long as the Zeeman splitting is small compared to thermal smearing one does not expect a Zeeman shift. Only when the Zeeman splitting exceeds thermal smearing, a single spin level dominates the conductance peak which then shifts in accordance with this level. This explains why the Zeeman splitting can only clearly be observed at magnetic fields above 1 T, where the Zeeman splitting is larger than kT. All the peaks have been fitted to a thermally broadened line shape in order to obtain the peak positions most precisely. The effects of g-factor tuning as observed in Ref. [14] are not relevant for the present sample design.

We often observe an abrupt change in peak position at $B \approx 0.8\,T$ (see Fig. 1). Background charge rearrangements are a very unlikely cause for these effects since only some peaks are affected and not the entire spectrum. A possible reason could be exchange effects, which could suddenly set in once the Zeeman gap exceeds kT in a bootstrap effect. However, the magnitude of the jump as well as the extrapolation of the high-field behavior of peak separation down to $B = 0$ do not support this hypothesis.

It is important to note that in this weak coupling regime only peak spacing 2-1 and 3-2 follow roughly the expected slope for a Zeeman energy-shift, $-g\mu_B$ and $+g\mu_B$, respectively. Disregarding the strong peak spacing fluctuations, all the other peak spacings show a more or less flat behavior or slopes corresponding to a value less than expected for

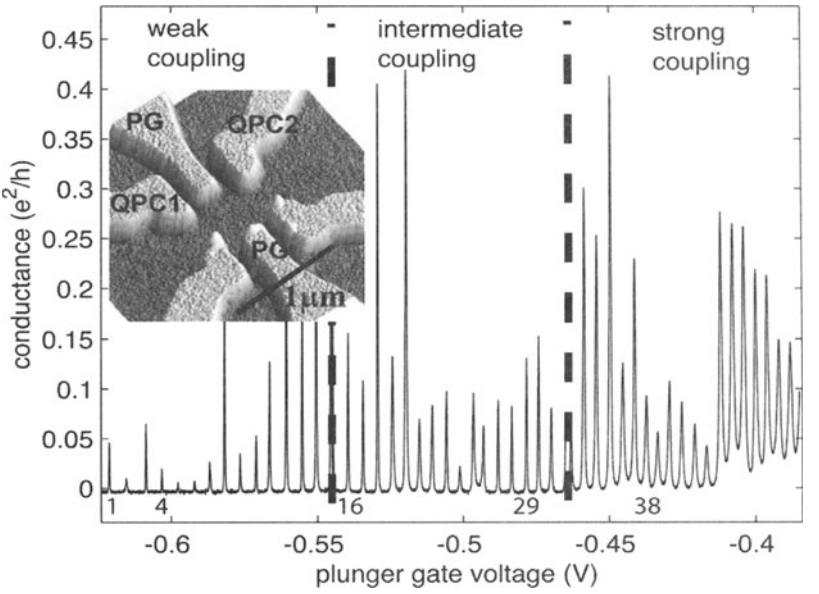

Figure 1. Coulomb blockade conductance peaks vs. plunger gate voltage taken at $B_{\text{total}} = 0$ and with a back gate voltage $V_{\text{bg}} = -4.5$ V. The numbers at the bottom of the figure are used to identify peaks. This numbering is used throughout the paper. The vertical dashed lines divide the data into three regimes, namely weak, intermediate, and strong coupling. The inset in the upper left shows a scanning force microscope image of the surface gates defining the quantum dot. Two pairs of gates (QPC1 and QPC2) form the entrance and exit quantum point contacts. A pair of plunger gates (PG) allows the electron number in the dot to be tuned.

Zeeman splitting. This behavior would agree with the notion that in a closed few-electron dot subsequent levels are preferentially filled with parallel spins in analogy to Hund's rules for atoms. Only very rarely, neighboring peaks correspond to opposite spins (see peaks 3-2 and 2-1). However, as mentioned above, we observe strong peak spacing fluctuations as a function of parallel magnetic field as also reported in Ref. [12]. We have no detailed understanding of these fluctuations but speculate that the ground state of the dot may be changed due to correlation effects as a function of parallel magnetic field causing the observed behavior.

For more positive plunger gate voltages ($V_g > -0.47$ V in Fig. 1) the conductance of the dot increases and the dot becomes strongly coupled to the leads. We present the Coulomb peak spacing versus parallel magnetic field in Fig. 3. The traces roughly fall into three categories, namely linear up or down movement in magnetic field and flat curves almost independent of magnetic field. On the right-hand side in Fig. 3(b) the theoretical expectation based on the bulk g-factor of GaAs is plotted in the same graph. There are clear deviations from these lines, namely peak spacing 41-40 actually displays a larger slope than expected. Especially for back gate sweeps (not shown) we find many peak spacing slopes strongly exceeding the expected Zeeman splitting.

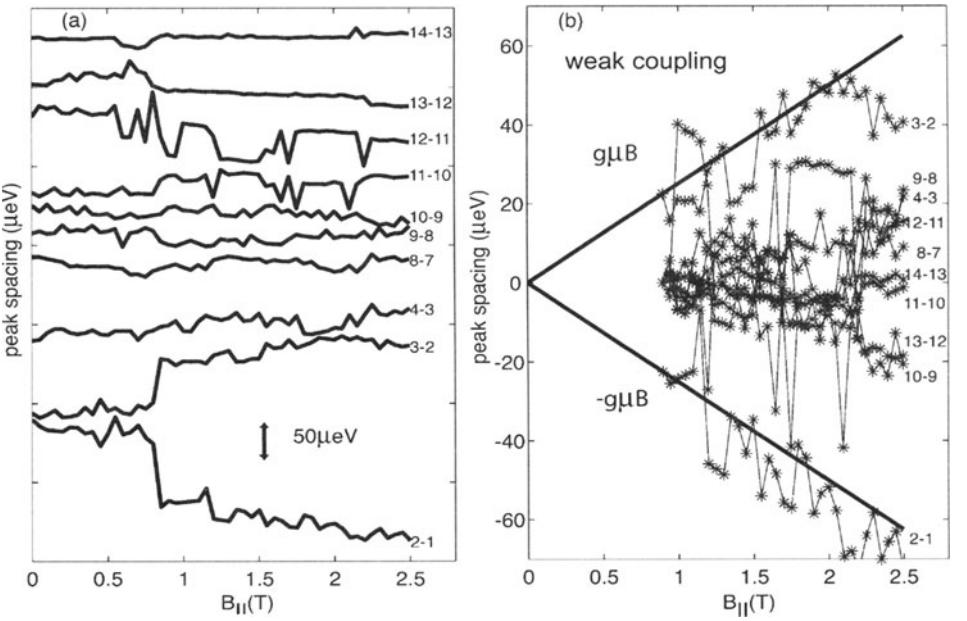

Figure 2. (a) Evolution of peak spacing of the weak coupling regime with in-plane magnetic field. The peak spacing is extracted from the measured peak motion, converted into energy using the lever arm α from the nonlinear conductance measurements and vertically offset for clarity. (b) Peak spacings offset to align spacings at $B_{\|} = 0\,\mathrm{T}$ and converted into an energy using the corresponding lever arm α extracted from the Coulomb diamonds. The slope vs. B corresponds to the change in ground state spin as each electron is added and hence indicates the change of the spin from one state to the other. The straight lines show the slope as expected for the bulk GaAs g factor $|g| = 0.44$.

Trying to extract possible sequences of ground state spins s_N we are successful for peaks 34 to 47 with the result that 85% of all ground states have spin $|s_N| = 0$ or $1/2$ and the rest is $|s_N| = 1$. Including peaks 32 to 33 in the analysis leads to unreasonably high spin states up to $7/2$. We also find it impossible to obtain a reasonable sequence for the intermediate and strong coupling regime combined. The occurrence of ground state spins $S > 1$ seems to be unreasonable for our dot with 50–100 electrons. Therefore, one could ask whether there are other mechanisms that can disturb the sequence of experimental peak shifts. One possible scenario could be that occasionally the ground state spin of the dot changes parametrically with the plunger gate voltage *within the Coulomb blockade*, that is, in the valley between two conductance peaks. Such a change could not be detected but would lead to unrealistic sequences of spin states. However, from the fact that our analysis works well for sequences of 10 to 15 conductance peaks, we are confident that such irregularities are the exception rather than the rule.

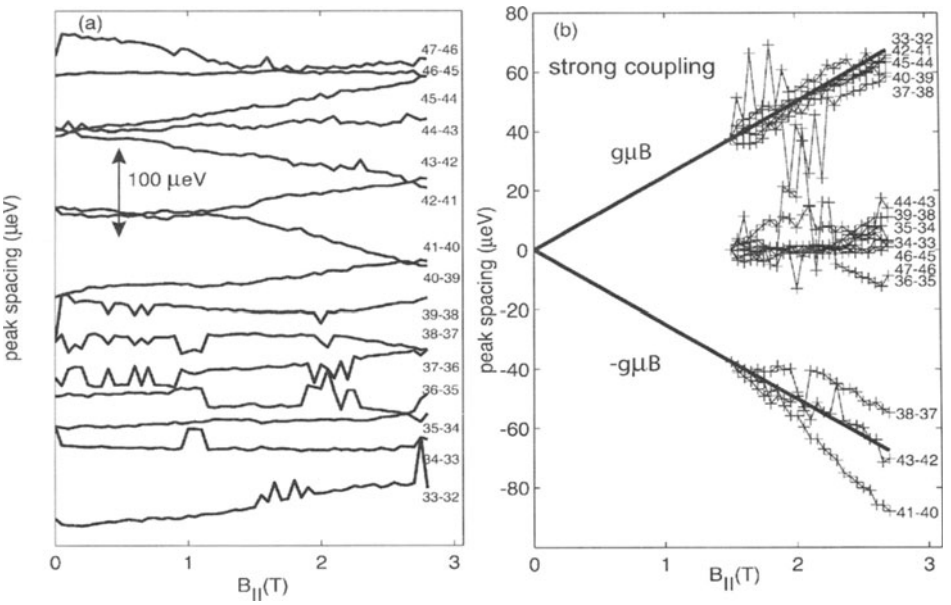

Figure 3. (a) Evolution of peak spacing (strong coupling regime) with in-plane magnetic field. (b) Peak spacings offset to align spacings at $B_{\|} = 0\,\mathrm{T}$ and converted into an energy using the corresponding lever arm α extracted from the Coulomb diamonds.

3. DISCUSSION

In a single particle picture, where the exchange interaction is neglected, one would expect that orbital states would be successively populated by spin-up and spin-down electrons. For our quantum dot we estimate interactions to be important, since the corresponding two-dimensional density is low. In this case exchange interactions are expected to have a significant influence in maximizing the ground state spin and values $s_N > 1/2$ can be expected [15–17]. In addition, it has been predicted [18] that only very few spin-pairs occur in such a case. To our knowledge, the question of how the dot–lead coupling influences the sequence of ground state spins in strongly interacting quantum dots has not been theoretically addressed.

Experimentally, the assumption that orbital effects play a minor role for the linear change in Coulomb peak separation as a function of parallel field is on relatively safe ground, since the diamagnetic shift influences all levels in a very similar way. Our data suggest that the linear behavior of the Coulomb peaks in $B_{\|}$ found in all coupling regimes is governed by linear Zeeman splitting. The extracted g-factor is found to be similar to that of the bare value in bulk GaAs. Our experimental observations in the intermediate and strong coupling regimes agree qualitatively with the existing predictions for closed dots with strong interactions. Not only the observation of states, which move linearly in energy

as a function of parallel field but also the sequence of spin-up and spin-down single-electron states not necessarily in sequential order, supports this view.

Occasionally, interactions in our system seem to be strong enough such that by the addition of an individual electron the corresponding many-particle state exhibits $s_N \geq 1$ behavior [19]. The number of electrons in our dot changes by a factor of two in the investigated range of plunger gate voltage. Since the interaction parameter r_s is proportional to the inverse of the square root of the electron density, and the dot also increases its geometric size with increasing electron number, we can assume that r_s does not change much (probably less than 20%) within the investigated parameter range. It is therefore expected that the occurrence of higher spin states (such as $s_N = 1$) would not change much and remain small but significant throughout the regimes. This agrees with the observations in the intermediate and strong coupling regimes. In the weak coupling the data indicate that several successive electrons occupy states with the same spin direction, which is an analogy of Hund's rules for atoms. The total spin of the dot may therefore take on values even larger than 1. However, the strong fluctuations in the peak positions make this analysis not as conclusive as in the other coupling regimes. It was previously observed [12] that the weak coupling regime, which is naively expected to give the best results for the analysis of spin states, since the peaks are narrowest, does not prove itself very definitive for such investigations.

In the intermediate and strong coupling regime, on the other hand, subsequent states of the dot seem to be less frequently occupied with parallel spins as compared to the weak coupling regime. In the intermediate coupling regime the occurrence of spin-pairs would therefore be more likely. However, also in this regime the $B_\parallel$ data indicate that the total ground state spin of the dot occasionally takes on values of at least $s_N = 1$. Although a precise determination of the spin of the dot cannot be uniquely reconstructed from the sequence of slopes, we find $s_N > 1/2$ only rarely. In the strong coupling regime the conductance peaks become wider and single-level transport cannot be achieved. This leads to a general enhancement of correlations in position and amplitude between neighboring peaks. Trying to reconstruct possible sequences of ground state spins from the measured data in $B_\parallel$ we come to realize that even in the strong coupling regime one cannot avoid involving at least $s_N = 1$ states, although they occur infrequently. The occurrence of three well-defined branches with slopes $\pm g\mu_B$ and 0 is not obvious in the strong coupling regime. If transport through several levels with possibly different spins contributes to the position and amplitude of a given Coulomb blockade peak, one would expect averaging of the corresponding Zeeman shifts. This would reduce the slope of peak separations as a function of in-plane field, similar to the effect of temperature.

Generally speaking we find that the spin behavior is more robust than expected from the involved energy scales. A similar statement was recently made by Glazman and co-workers in the context of the Kondo effect in strongly coupled dots in which charge quantization no longer occurs [20].

4. CONCLUSIONS

The behavior of Coulomb blockade peaks with magnetic fields applied in the plane of quantum dots in semiconductor heterostructures has been investigated for a range of coupling regimes between the dot and its leads. In the weak coupling regime the positions of the Coulomb blockade resonances show strong fluctuations, which inhibit assignments

of spin to a given state but are suggestive of large ground state spin in the dot. In the strong coupling regime the interpretation of the data still follows the single-level transport picture in parallel magnetic field. However, some states show a stronger parallel magnetic field dependence as one would expected for weakly interacting $s = 1/2$ particles with the bare g-factor of GaAs. In both, the intermediate and the strong coupling regime, total ground state spins larger than $1/2$ occur occasionally and spin-pairs are rare. These findings are in good agreement with theoretical predictions for strongly interacting quantum dots.

Acknowledgements

It is a pleasure to thank A. Sachrajda, S. Ulloa, and W. Zwerger for valuable discussions. Financial support by the Schweizerischer Nationalfonds and the NCCR Nanoscience is gratefully appreciated.

REFERENCES

[1] M. A. Kastner, *Rev. Mod. Phys.* **64**, 849 (1992).
[2] L. P. Kouwenhoven, C. M. Marcus, P. L. McEuen, S. Tarucha, R. M. Westervelt, and N. S. Wingreen, in *Mesoscopic electron transport*, eds. L. P. Kouwenhoven, G. Schön, and L. L. Sohn (Kluwer 1997).
[3] S. Lindemann, T. Ihn, T. Heinzel, W. Zwerger, K. Ensslin, K. Maranowski, and A. C. Gossard, *Phys. Rev. B.*, in press.
[4] S. Lindemann, T. Ihn, T. Heinzel, W. Zwerger, K. Ensslin, K. Maranowski, and A. C. Gossard, Proceedings of the 26th International Conference on the Physics of Semiconductors (ICPS), Edinburgh, 2002
[5] A. C. Gossard, *IEEE J. Quant. Electron.* **22**, 1649 (1986).
[6] K. D. Maranowski, J. P. Ibbetson, K. L. Campman, and A. C. Gossard, *Appl. Phys. Lett.* **66**, 3459 (1995).
[7] G. Salis, B. Graf, K. Ensslin, K. Campman, K. Maranowski, and A. C. Gossard, *Phys. Rev. Lett.* **79**, 5106 (1997).
[8] S. Lindemann, T. Ihn, T. Heinzel, K. Ensslin, K. Maranowski, and A. C. Gossard, *Physica E* **13**, 638 (2002).
[9] P. L. McEuen, E. B. Foxman, J. Kinaret, U. Meirav, M. A. Kastner, Ned S. Wingreen, and S. J. Wind, *Phys. Rev.* B **45**, 11419 (1992).
[10] F. Simmel, D. Abusch-Magder, D. A. Wharam, M. A. Kastner, and J. P. Kotthaus, *Phys. Rev.* B **59**, 10441 (1999).
[11] D. S. Duncan, D. Goldhaber-Gordon, R. M. Westervelt, K. D. Maranowski, and A. C. Gossard, *Appl. Phys. Lett.* **77**, 2183 (2000).
[12] J. A. Folk, C. M. Marcus, R. Berkovits, I. L. Kurland, I. L. Aleiner, and B. L. Altshuler, *Physica Scripta* **T90**, 26 (2001).
[13] E. B. Foxman, P. L. McEuen, U. Meirav, N. S. Wingreen, Y. Meir, P. A. Belk, N. R. Belk, M. A. Kastner, and S. J. Wind, *Phys. Rev.* B **47**, 10020 (1993).
[14] G. Salis, Y. Kato, K. Ensslin, D. C. Driscoll, A. C. Gossard, and D. D. Awschalom, *Nature* **414**, 619 (2001).
[15] R. Berkovits, *Phys. Rev. Lett.* **81**, 2128 (1998).
[16] A. V. Andreev and A. Kamenev, *Phys. Rev. Lett.* **81**, 3199 (1998).
[17] P. W. Brouwer, Y. Oreg, and B. I. Halperin, *Phys. Rev.* B **60**, R13977 (1999).
[18] H. U. Baranger, D. Ullmo, and L. I. Glazman, *Phys. Rev.* B **61**, R2425 (2000).
[19] L. P. Rokhinson, L. J. Guo, S. Y. Chou, and D. C. Tsui, *Phys. Rev.* B **63**, 035321 (2001).
[20] L. I. Glazman, F. W. J. Hekking, and A. I. Larkin, *Phys. Rev. Lett.* **83**, 1830 (1999).

GATE ERRORS IN SOLID-STATE QUANTUM COMPUTER ARCHITECTURES

X. Hu and S. Das Sarma
Condensed Matter Theory Center, Department of Physics, University of Maryland, College Park, MD 20742-4111, USA

Abstract: We review our work on the interplay between non-resonant gates and solid state environment in various solid state quantum computer architectures and the resulting gate errors. Particular, we show that adiabatic condition can be satisfied in small quantum dots, while higher energy excited states can play important role in the evolution of a Cooper-pair-box based quantum computer model. We also show that complicated bandstructure such as that of Si can pose a severe gate control problem.

1. INTRODUCTION

It has been pointed out for a long time that quantum mechanics may provide great advantages over classical physics in physical computation [1, 2]. The recent rapid growth of research on quantum computation [3] started after Shor's factorization algorithm [4] and quantum error correction codes [5, 6] were developed. For a quantum system to be used as a quantum computer (QC), it has to satisfy some stringent conditions [7]. In short, it should possess a scalable Hilbert space; the state of such a system should be easily initialized; the system should have a long decoherence time; there should be a set of universal unitary gates applicable to the system; and last but not least, every single quantum bit (qubit) of the system should be faithfully measured. Here we would like to review our work on the quantum gates and their operations in various solid-state quantum computer architectures.

Many two-level systems have been proposed as candidates for qubits in a solid-state QC. Typical examples include electron spins, nuclear spins, electron charge states, Cooper pair charge states, superconducting flux states, and many more [8–14]. One major motivation for these solid-state devices is their potential in scalability. However, solid-state structures also present complex environments and fast decoherence rates [15]. Furthermore, in most solid-state QC schemes, nonresonant gate operations [8, 11, 13, 16] are crucial or important components. It is thus necessary to understand how the environmental elements affect the QC coherent evolution, and clarify the effects of imperfections in nonresonant gate operations. In the following, we will review some of the results we have obtained for three different QC architectures: the spin-based quantum dot QC, the Cooper-pair-box-based QC, and the donor-nuclear-spin-based Si QC.

Quantum Computing and Quantum Bits in Mesoscopic Systems
Edited by Leggett *et al.*, Kluwer Academic/Plenum Publishers, 2004

2. NONADIABATIC OPERATIONS IN A DOUBLE QUANTUM DOT

Let us first discuss our work on the spin-based quantum dot quantum computer (QDQC) in GaAs [8, 9]. Here two-qubit operation is based on the nearest neighbor exchange coupling, which produce the exchange splitting between the ground singlet and triplet states. For small quantum dots, with large single particle excitation energy E_s and large on-site Coulomb repulsion energy E_C and at low temperatures ($k_BT \ll \min\{E_s, E_C\}$), the low-energy dynamics is dominated by the electron spins. In other words, one can focus on the spin part of the two-electron Hilbert space that involves only the ground singlet and triplet states and cut off the rest of the Hilbert space. For example, at $T \sim 100$ mK and with $\min\{E_s, E_C\} \sim 1$ meV, the thermal occupation of the higher energy orbital states is less than 10^{-50}, which can be safely neglected. Thus one can quite faithfully prepare a single electron in a single dot in its ground orbital state and/or two electrons in a double dot in the ground singlet/triplet state manifold. For a double dot, after the state is initialized, as long as the applied quantum gates satisfy adiabatic conditions, the system would remain in the ground state manifold, so that Heisenberg exchange Hamiltonian would describe the dynamics of the double quantum dot exactly. However, the size of a gated quantum dot is limited from below by gate and device dimensions, while the gate operating time is limited from above by the electron spin decoherence time. Thus it is necessary to quantitatively assess the adiabatic condition for two-qubit operations in a double dot of realistic dimensions, so as to determine whether exchange gates can be sufficiently fast to guarantee a large gate-time/decoherence-time ratio, while slow enough to produce correctably small nonadiabatic errors.

We have performed a quantitative evaluation of the adiabatic condition in a double quantum dot [17] using the results of our molecular orbital calculation of the double energy spectra [9]. Specifically, we prepare a two-electron state in the ground singlet state with a high barrier between the double dot. As the system evolves, the barrier height between the two dots is first lowered, then raised back to the original value. If Heisenberg exchange Hamiltonian is exact for this system, its state should remain in the ground singlet state. Any loss from this state would then constitute a leakage from the QC Hilbert space and a gate error.

Our calculation is essentially an integration of the time-dependent Schrödinger equation for the two-electron double quantum dot:

$$\frac{\partial c_k(t)}{\partial t} = \sum_{i \neq k}^{N} \frac{c_i(t)}{E_k(t) - E_i(t)} \langle k| \frac{\partial H(t)}{\partial t} |i\rangle \exp\left\{ \frac{1}{i\hbar} \int_{-\infty}^{t} (E_i(\tau) - E_k(\tau))\, d\tau \right\} \tag{1}$$

Here $c_k(t)$ are the coefficients as we expand the two-electron state on the instantaneous eigenstates $|k\rangle$: $\psi(t) = \sum_k c_k(t) u_k(t)$ and $H(t)u_k(t) = E_k(t)u_k(t)$, where $H(t)$ is the time-dependent system Hamiltonian. The explicit time-dependence of H is in the inter-dot barrier height. Since initially the system is entirely in the ground singlet state, $c_k(t = 0) = \delta_{k0}$ for all k. The energy spectra we use are for a double dot with Gaussian confinements of 30 nm radii and 40 nm inter-dot distance [9]. The energy barrier height V_b ranges between 14 meV and 35 meV, corresponding to exchange splitting of 280 μeV to 3.3 μeV. By varying the barrier variation time, we can quantitatively evaluate the change in the ground singlet state population, thus obtaining a lower limit to the gate operating time using the criterion of quantum error correction code threshold.

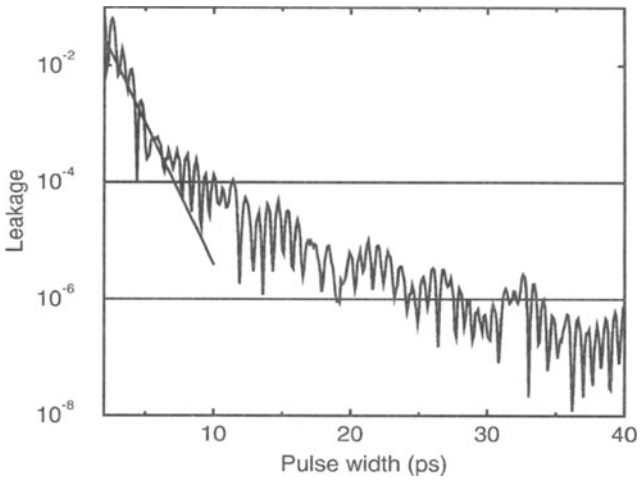

Figure 1. Leakage as a function of the pulse width 2τ of the exchange gate. The two-electron state is initially in the ground singlet state. The two horizontal lines represents the commonly used thresholds for quantum error correction. The fitted line at the small pulse width indicates the initial rapid decrease in the error rate (leakage) as the pulse becomes wider (or the gate operation becomes slower).

The result of our calculation is plotted in Fig. 1 [17]. The leakage (y-axis) is defined as $1 - |c_0|^2$ which is zero before the gate is applied, and should be zero if the gate is perfectly adiabatic. Aside from several interesting features [17], Fig. 1 demonstrates that for gating time longer than $30 \sim 40$ ps, leakage in our double dot system should be sufficiently small ($\lesssim 10^{-6}$) so that the currently available quantum error correction schemes would be effective. On the other hand, an exchange splitting of 0.1 meV corresponds to about 20 ps gating time for a swap gate [8] (with rectangular pulse) at the shortest. Therefore, the adiabatic condition does not place an extra burden on the operation of the two-qubit gates such as a swap—there is in general no need to significantly increase the gating time in order to accommodate the adiabatic requirement.

Note that the current calculation is done for a pair of quite small quantum dots. Larger dots would have meant smaller excitation energies and a threshold gating time that is longer in order to satisfy the adiabatic condition.

3. NONSUDDEN OPERATIONS IN A COOPER PAIR BOX

Another example we have considered is the Cooper pair box quantum computer (CPBQC) [17]. The Hamiltonian of a Cooper pair box (CPB) can be written on the basis of charge number states of the box:

$$\begin{aligned} H &= 4E_C(\hat{n} - n_g)^2 - E_J \cos\hat{\phi} \\ &= \sum_n \left[4E_C(n - n_g)^2 |n\rangle\langle n| - \frac{E_J}{2}(|n\rangle\langle n+1| + |n+1\rangle\langle n|) \right] \end{aligned} \tag{2}$$

where E_C is the charging energy of a CPB, E_J is the Josephson coupling between the CPB and an external superconducting lead, n_g represents the applied voltage on the CPB in terms of an effective charge number, and n refers to the number of extra Cooper pairs in the box. Due to the periodic nature of the Josephson coupling, the eigenstates of a CPB form energy bands. The two states $|\uparrow\rangle$ and $|\downarrow\rangle$ for a CPB qubit correspond to the two lowest energy levels at $n_g = 1/2$, where the eigenstates are approximately $|\downarrow\rangle = (|0\rangle + |1\rangle)/\sqrt{2}$ and $|\uparrow\rangle = (|0\rangle - |1\rangle)/\sqrt{2}$ with a splitting of about E_J.

Similar to the case of QDQC discussed above, higher excited states play an important role in the dynamics of a CPBQC when it is subjected to nonresonant operations [18]. The particular operation we considered is the sudden pulse gate to shift n_g, thus bringing a system from a pure ground state ($|0\rangle$ at, for example, $n_g = 1/4$) to a coherent superpositioned state ($(|\uparrow\rangle + |\downarrow\rangle)/\sqrt{2}$ at $n_g = 1/2$). Such a simple description of the pulse gate is only valid when $E_J/E_C \to 0$. Since E_J determines the gate speed of a CPBQC, such a condition is not practical for a realistic QC. Furthermore, in real experiments, the pulse gate always has finite rise/fall times (nonsudden). In Ref. [16], the pulse rise time is in the range of 30 to 40 ps. Such gradual rise and fall of the pulse gate inevitably lead to more errors, which have been considered in the context of two-level systems [16, 19, 20]. What we have done is to calculate the fidelity of the pulse gate taking into account the finite rise/fall time, the higher excited states, and the complete composition of all the eigenstates [17].

In Fig. 2 we plot the state fidelity as a function of rise time. Here the state fidelity is defined as the maximum probability for the CPB to be in the first excited state after the

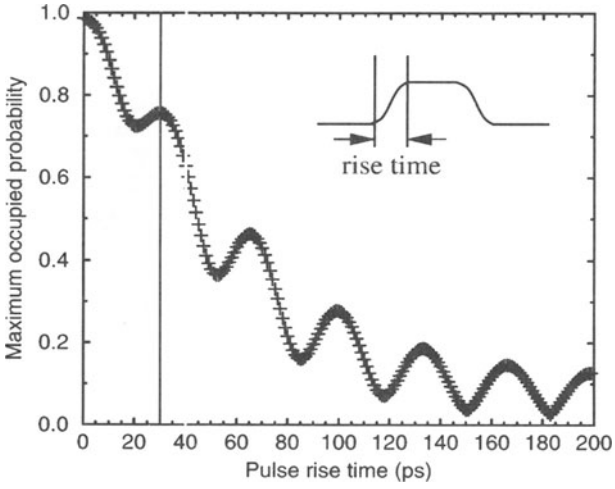

Figure 2. State fidelity as a function of the finite rise/fall time of a pulse gate in a single Cooper pair box. The fidelity here is defined as the maximum probability (which implies particular choices of pulse duration τ_p as this probability varies periodically with τ_p) of the CPB in the first excited state after the application of a pulse gate with the state starting from the ground state (represented by n_g goes from 0.255 to 0.5, then back to 0.255 after a period of time τ_p). The CPB is treated as a multi-level system (on the basis of $|-10\rangle, \ldots, |0\rangle, |1\rangle, \ldots, |10\rangle$). The lineshape of the rise/fall of the pulse is a sinusoidal function of time. The system parameters are chosen as the values used in Ref. [16]. The two vertical lines give the range of rise/fall time from the same source.

pulse gate when n_g returns to 0.255. Figure 2 shows that the fidelity of the pulse gate decreases oscillatorily instead of monotonically as the pulse rise time increases. The oscillations (with periods around 30 ps) in the curves represent the coherent evolution of the CPB during the rise/fall of the pulse voltage. For pulses used in Ref. [16] with rise/fall time in the range of 30 to 40 ps, the fidelity is only 60 to 70%, apparently not sufficient for manipulations required by quantum computation. Further calculations also demonstrate that including higher excited states is important in correctly evaluating the fidelity dependence on the rise time of the nonresonant sudden pulse gate [17].

4. IMPLICATIONS OF Si BAND STRUCTURE

The previous two examples demonstrate the interplay of nonresonant gate operations and states from the full Hilbert space, and the resulting leakage from the computational space. Solid-state environment can affect the operation of a QC in other subtle ways. For example, modern technology can produce extremely pure silicon crystals that have the intrinsic property of very small spin-orbit coupling. Thus electron and nuclear spins in Si have a very "quiet" environment—the spin relaxation times are extremely long in Si [21, 22]. It is therefore natural to use Si as a host material for spin-based QC architectures [11]. However, Si is an indirect gap semiconductor. There are actually six equivalent minima in its conduction band that are away from the center of the First Brillouin zone and

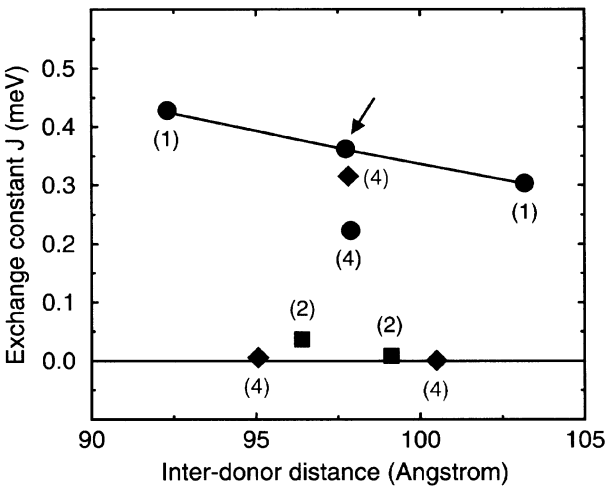

Figure 3. Variations in the exchange coupling between two phosphorus donors in Si. The arrow points at the circle that represents the value of electron exchange at the reference configuration with the two donors exactly along the [100] direction and separated by 18 lattice constants. The circles connected by a line refer to pairs along the [100] direction, displaced by one lattice constant with respect to the reference position. The rest of the symbols represent displacements of one member of the donor pair into one of its first (squares), second (diamonds), or third (circles) nearest neighbor positions. The numbers in parentheses next to the symbols are their degeneracies, respectively.

close to the zone boundary. The implication of this complexity is that confined electron states (whether the confinement is provided by a donor or a gate-produced electrostatic potential in the form of a quantum dot) in general have contributing components from all the valleys, which can then lead to atomic scale spatial oscillations of electronic properties such as electron density and two-electron exchange coupling.

We have performed a Heitler–London calculation for the two-electron exchange splitting for two phosphorus donors in Si [23]. The Si:P system is being studied as a candidate of nuclear spin-based quantum computers [11, 24]. Donor electron exchange is a crucial intermediary in the effective nuclear spin exchange interaction that is the basis of the two-qubit operations in such a QC architecture. Our calculation indeed shows a fast-varying exchange, as is demonstrated in Fig. 3, which shows that a movement of one member of the donor pair into its nearest or second nearest neighbor sites can completely suppress the exchange coupling between the two donor electrons.

In the original proposal of Si QC [11], electron exchange is tuned by applied gate voltages, which would shift the electron wavefunctions. Thus the two-qubit gates here are exposed to atomic-scale oscillations. The direct implication of the oscillatory exchange is that the gate voltages corresponding to the peak exchange coupling have to be well controlled, optimally close to a local maximum where the exchange is least sensitive to the gate voltage. Since the oscillatory exchange period is close to lattice spacing, the positioning of the donor electrons by the surface gates must be controlled at least to that precision.

Acknowledgements

We thank financial support from ARDA and LPS and collaborations (on the donor exchange in Si) and helpful discussions with Belita Koiller.

REFERENCES

[1] D. Deutsch, *Proc. R. Soc.* A **400**, 97 (1985); D. Deutsch and R. Josza, *Proc. R. Soc.* A **439**, 553 (1992).
[2] R. P. Feynman, *Int. J. Theor. Phys.* **21**, 467 (1982); *Found. Phys.* **16**, 507 (1986).
[3] A. Steane, *Rep. Frog. Phys.* **61**, 117 (1998); C. H. Bennett and D. P. DiVincenzo, *Nature* **404**, 247 (2000).
[4] P. W. Shor, in *Proceedings of the 35th Annual Symposium on the Foundations of Computer Science*, ed. by S. Goldwasser (Los Alamitos, IEEE Computer Society, 1994), p. 124.
[5] P. W. Shor, *Phys. Rev.* A **52**, 2493 (1995).
[6] A. M. Steane, *Phys. Rev. Lett.* **77**, 793 (1996).
[7] D. P. DiVincenzo, *Fortschr. Phys.* **48**, 771–783 (2000).
[8] D. Loss and D. P. DiVincenzo, *Phys. Rev. A* **57**, 120 (1998).
[9] X. Hu and S. Das Sarma, *Phys. Rev. A* **61**, 2301 (2000); **64**, 042312 (2001).
[10] R. Vrijen *et al.*, *Phys. Rev. A* **62**, 012306 (2000).
[11] B. E. Kane, *Nature* **393**, 133 (1998); *Fortschr. Phys.* **48**, 1023 (2000).
[12] V. Privman, I. D. Vagner, and G. Kventsel, *Phys. Lett. A* **239**, 141 (1998); D. Mozyrshy, V. Privman, and M. L. Glasser, *Phys. Rev. Lett.* **28**, 5112 (2001).
[13] A. Shnirman, G. Schön, and Z. Hermon, *Phys. Rev. Lett.* **79**, 2371 (1997); Y. Makhlin, G. Schon, and A. Shnirman, *Rev. Mod. Phys.* **73**, 357 (2001).
[14] D. V. Averin, *Solid State Comm.* **105**, 659 (1998).
[15] X. Hu, R. de Sousa, and S. Das Sarma, LANL preprint cond-mat/0108339.
[16] Y. Nakamura, Y. A. Pashkin, and J. S. Tsai, *Nature* **398**, 786 (1999).
[17] X. Hu and S. Das Sarma, *Phys. Rev. A*, in press (2002). Cond-mat/0202152.
[18] R. Fazio, G. Massimo Palma, and J. Siewert, *Phys. Rev. Lett.* **83**, 5385 (1999).

[19] M.-S. Choi, R. Fazio, J. Siewert, and C. Bruder, *Europhys. Lett.* **53**, 251 (2001).
[20] S. Oh, quant-ph/0201068.
[21] G. Feher, *Phys. Rev.* **114**, 1219 (1959).
[22] A. Abragam, *The Principles of Nuclear Magnetism* (Oxford, London, 1961).
[23] B. Koiller, X. Hu, and S. Das Sarma, *Phys. Rev. Lett.* **88**, 027903 (2002).
[24] J. L. O'Brien *et al.*, *Phys. Rev.* B **64**, 161401(R) (2001).

QUANTUM COMPUTING WITH ELECTRON SPINS IN QUANTUM DOTS

L. M. K. Vandersypen, R. Hanson, L. H. Willems van Beveren, J. M. Elzerman, J. S. Greidanus, S. De Franceschi and L. P. Kouwenhoven
Department of Applied Physics, DIMES, and ERATO Mesoscopic Correlation Project, Delft University of Technology, PO Box 5046, 2600 GA Delft, The Netherlands

Abstract: We present a set of concrete and realistic ideas for the implementation of a small-scale quantum computer using electron spins in lateral GaAs/AlGaAs quantum dots. Initialization is based on leads in the quantum Hall regime with tunable spin-polarization. Readout hinges on spin-to-charge conversion via spin-selective tunneling to or from the leads, followed by measurement of the number of electron charges on the dot via a charge detector. Single-qubit manipulation relies on a microfabricated wire located close to the quantum dot, and two-qubit interactions are controlled via the tunnel barrier connecting the respective quantum dots. Based on these ideas, we have begun a series of experiments in order to demonstrate unitary control and to measure the coherence time of individual electron spins in quantum dots.

Keywords: Quantum computing, Quantum dots, Electron spin resonance

1. INTRODUCTION

The spin of a single electron placed in a static magnetic field $\vec{B}_0$ provides a natural two-level system suitable as a qubit in a quantum computer [1]. Loss and DiVincenzo proposed isolating individual electrons in a quantum dot array and showed that the electron spins can in principle be initialized, coherently manipulated, and read out [2]. While there has been continued theoretical work in this area [3, 4], the Loss–DiVincenzo proposal has not yet been realized experimentally. We have recently begun such experiments and present here the concrete and realistic path we are taking towards the experimental demonstration of single- and two-qubit gates and the creation of entanglement of spins in quantum dot systems.

[a]E-mail: lieven@qt.tn.tudelft.nl

2. QUBIT

The qubit is represented by the spin of a single electron in a quantum dot defined by electrostatic gates on top of a $GaAs/Al_xGa_{1-x}As$ heterostructure. The spin ground state $|\uparrow\rangle$ and excited state $|\downarrow\rangle$ are separated in energy by the Zeeman splitting $\Delta E_z = g_d \mu_B B_0$, with g_d the dimensionless g-factor in the dot, μ_B the Bohr magneton, and B_0 the static magnetic field strength. Taking $g_d = 0.44$, the bulk value in GaAs (we neglect the sign), we have $\Delta E_z \approx 25\ \mu$eV per Tesla in B_0.

For comparison, the charging energy of a dot, e^2/C, with C the total capacitance of the dot, is typically a few meV, much larger than the Zeeman energy. The discrete energy level spacing is about a meV in small dots, also larger than ΔE_z [5, 6]. In what follows, we will assume that the electron always remains in the orbital ground state.

Although it may not be strictly necessary to work with few-electron dots, operation with one electron in each dot makes the experiment much more transparent. Following other groups [7, 8], we have recently realized lateral, split-gate quantum dots with a controllable number of electrons down to ...2, 1, 0 electrons [9].

3. INITIALIZATION

The primary goal of initialization is to place the qubit in a pure (i.e. well-known) state, say $|\uparrow\rangle$, as this is the desired initial state for most quantum algorithms [1]. The additional ability to initialize the qubit to $|\downarrow\rangle$, or alternatively to a mixed state where the spin is probabilistically in $|\uparrow\rangle$ or $|\downarrow\rangle$, would be very useful for testing whether the readout schemes of Section 4 can distinguish $|\uparrow\rangle$ from $|\downarrow\rangle$. We first present two methods for initialization to the pure state $|\uparrow\rangle$, and then discuss a variant for initialization to a mixed state.

Initialization to the ground state occurs naturally when we allow the electron spin to reach thermal equilibrium at high B_0 and low temperature T. $\Pr[|\uparrow\rangle]$, given by the Boltzman factor, is over 99% when

$$g_d \mu_B B_0 > 5 k_B T \tag{1}$$

with k_B Boltzman's constant. This condition is easily satisfied at, for example, 5 T and 300 mK ($g_d = 0.44$). Thermal equilibration on the dot is a very simple and robust initialization approach, which can be used for any B_0 orientation and does not require

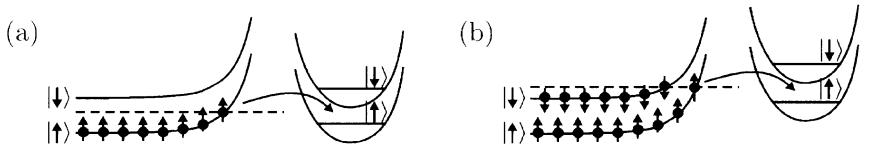

Figure 1. The chemical potential for a single ↑ or ↓ electron in a quantum dot, coupled to leads in the quantum Hall regime with (a) filling factor $\nu = 1$ and (b) $\nu = 2$. The dashed line indicates the Fermi level E_F and the solid lines in the leads represent the lowest spin-split Landau level. Note that a self-consistent (in)compressible edge state picture does not affect the arguments in this paper.

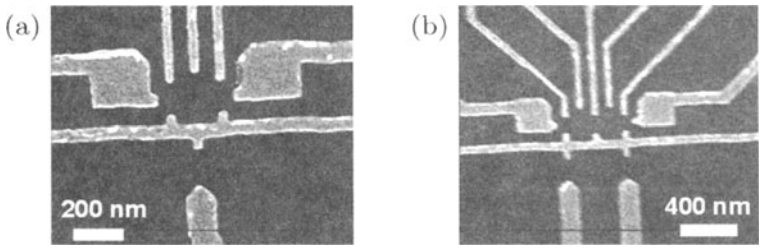

Figure 2. SEM images of (a) a single quantum dot and (b) two coupled quantum dots. A quantum point contact placed opposite the quantum dots permits detection of the number of electrons on the dots. The large square gates serve to locally control the electron density in the leads right next to the tunnel barriers to the dots.

spin-polarized leads. It takes about $5T_1$ to reach equilibrium, which may be on the order of 1 ms (T_1 is the spin relaxation time).

Alternatively, we can let an electron tunnel to an empty dot from $\uparrow$-polarized leads. This gives a qubit initialized to $|\uparrow\rangle$, as long as the spin is conserved during tunneling, which is plausible based on transport measurements in two-dimensional electron gases (2DEGs) [10]. Highly polarized leads can be obtained in the quantum Hall regime with filling factor $\nu = 1$ (Fig. 1(a)). Only the lowest spin-split Landau level is then occupied, provided $g_l\mu_B B_0 > 5k_B T$, analogous to Eq. (1) (g_l is the g-factor in the leads). In fact, magnetotransport measurements in 2DEGs with odd ν have shown that for an electron in the leads to go from $|\uparrow\rangle$ to $|\downarrow\rangle$, it must overcome not only the single-particle Zeeman energy but also the many-body exchange energy between the electrons in the leads [11]. We can describe this situation via an effective g-factor $g_{l,\mathrm{eff}}$, which can be as large as ten times g_l. The leads are thus spin-polarized as long as $g_{l,\mathrm{eff}}\mu_B B_0 > 5k_B T$. Tunneling from spin-polarized leads also offers a way to robust pure-state initialization, and the tunnel time can easily be tuned under 1 μs.

Initialization to a mixed state can be obtained by letting an electron tunnel to an empty dot from unpolarized or partially polarized leads. The probabilities for $\uparrow$ and $\downarrow$ electrons to tunnel to the dot depend on the spin-polarization in the leads, on the Fermi level in the leads E_F relative to the $|\uparrow\rangle$ and $|\downarrow\rangle$ levels in the dot and on the distance between the dot and the $|\uparrow\rangle$ and $|\downarrow\rangle$ edge states in the leads [7, 12, 13] (Fig. 1(b)). These parameters can be tuned via electrostatic gates which control the electron density in the leads and the potential of the dot (Fig. 2(a)).

4. READOUT

The ideal readout scheme offers high-fidelity, single-shot, strong quantum measurements [1]. This implies that the measurement must be switched off completely during the computation stage in order to avoid rapid decoherence. Furthermore, the measurement time must be shorter than T_1. Finally, the distinction between the $|\uparrow\rangle$ and $|\downarrow\rangle$ states must be very sharp.

The magnetic moment of a single electron spin is so weak that it has never been detected directly. Previous measurements of single electron spins were based on optical

techniques [14–16]. Also, various proposals exist for conversion of spin information to electrical charge [17] or current [4], both of which can be measured with high sensitivity. Here, we propose to use spin-to-charge conversion: the electron on the dot quickly leaves the dot if it is, say, in $|\uparrow\rangle$, whereas it stays on the dot if it is in $|\downarrow\rangle$. Next, the number of charges on the dot is measured. If there still is one electron charge on the dot, we know the qubit was in $|\downarrow\rangle$, and if there is no charge left, the qubit was in $|\uparrow\rangle$.

Spin-selective tunneling could in principle be realized using tunnel barriers made from magnetic materials [18]. However, such materials cannot yet be integrated with $GaAs/Al_xGa_{1-x}As$ heterostructures. Therefore, we propose instead to operate with spin-polarized leads (quantum Hall regime with $\nu = 1$), which provide a reference spin orientation against which the qubit spin orientation can be compared.

In order to motivate our proposed scheme, let us start with some approaches which will *not* work. First, if both the $|\uparrow\rangle$ and $|\downarrow\rangle$ levels in the dot lie below E_F, the electron can never escape from the dot. Second, if E_F lies above the $|\uparrow\rangle$ but below the $|\downarrow\rangle$ dot level, the qubit electron can only tunnel out if it is in $|\downarrow\rangle$; however, as soon as the qubit electron leaves the dot, another electron will enter the dot and occupy $|\uparrow\rangle$, so we always end up with one electron charge on the dot and no information about the spin state. Third, if E_F lies below the $|\uparrow\rangle$ and $|\downarrow\rangle$ levels of the dot and $g_{l,\text{eff}} = g_d$, the tunnel process out of the dot is not spin-selective.

However, if $g_{l,\text{eff}} \neq g_d$, the tunnel process *is* spin-selective (Fig. 3). We recall from Section 3 that in $\nu = 1$ leads, the exchange interaction increases the total energy of $\downarrow$ electrons with respect to $\uparrow$ electrons and thus suppresses the $\downarrow$ probability. Similarly, we expect that the increased energy of the $|\downarrow\rangle$ level in the leads reduces the probability that a $\downarrow$ electron will tunnel to the leads from the quantum dot, while $\uparrow$ electrons can tunnel to the leads easily.

An alternative spin-selective tunneling process, inspired by Ref. [4], consists of allowing a second electron to tunnel onto the dot from $\nu = 1$ leads. This $\uparrow$ electron will form a singlet state with the qubit electron if the qubit spin was in $|\downarrow\rangle$, whereas they will form a triplet if the qubit was in $|\uparrow\rangle$. Since the singlet and triplet energies can be made very different [19], the second electron will or will not enter the dot depending on the qubit state. As before, subsequent single-shot measurement of the charge on the dot will reveal the qubit state.

We expect both readout schemes to be very robust: $g_{l,\text{eff}}\mu_B B_0$ is as much as 1 meV (11 Kelvin) for $B_0 = 5$ T and $g_{l,\text{eff}} = 5$ [11]. The singlet–triplet energy difference can also be of the order of a meV [3, 19]. Readout schemes based on the Zeeman splitting (≈ 0.1 meV) are likely less reliable.

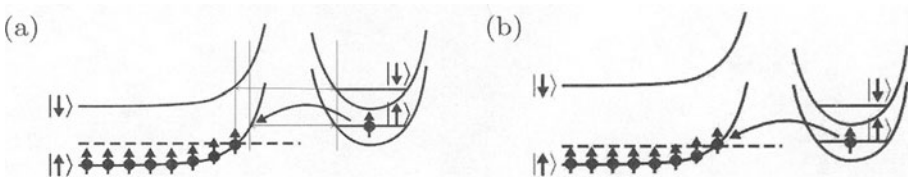

Figure 3. (a) When $g_{l,\text{eff}} > g_d$, the dot-lead tunnel rate can be significantly lower for $|\downarrow\rangle$ electrons than for $|\uparrow\rangle$ electrons, because of the difference in tunnel distances. (b) When $g_{l,\text{eff}} \gg g_d$, the $|\downarrow\rangle$ states in the leads are unreachable energetically for an electron in the dot.

Measurement of the number of electron charges on the dot must be completed in a time T_m short compared to T_1. Furthermore, if the electron is supposed to tunnel, it should do so in a time T_t short compared to T_m. If the electron is not supposed to tunnel, it should not do so for a time T_{nt} long compared to T_m. In summary, we need $T_t < T_m < T_1, T_{nt}$. Taking $T_1 \geq 100$ μs [20] and $T_t \approx 0.1$ μs, we must measure the charge in a time T_m of 1–10 μs.

A variety of highly sensitive charge meters exist, such as single-electron transistors (SETs), RF-SETs and quantum point contacts (QPCs) [8, 21]. We have opted to use a QPC (Fig. 2), since it is easy to fabricate and integrate with lateral quantum dots, and because we expect its charge sensitivity to be sufficient to determine the number of electron charges on the dot within 1–10 μs (using a low-temperature follower stage with output impedance of a few kΩ).

Finally, we point out that the qubit measurement can be switched off by going to the Coulomb blockade regime with the number of electrons on the dot fixed to one. At this point, charge readout contains no information about the spin state, and does not cause back-action on the qubit. The qubit measurement is switched on by setting the dot potential so that spin-selective tunneling becomes possible, and spin information is converted into charge information.

5. ELECTRON SPIN RESONANCE

A microwave magnetic field $\vec{B}_1$ oscillating in the plane $\perp$ to $\vec{B}_0$ at a frequency $f_0 = g_d \mu_B B_0/h$, in resonance with the spin precession about $\vec{B}_0$, will cause the spin to make transitions between $|\uparrow\rangle$ and $|\downarrow\rangle$. Evidently, if $g_l = g_d$, the spins in the leads would also be on resonance, and the spin polarization in the leads would disappear. Fortunately, g varies with B_0, n and the geometry of the structure [22], thus we expect $g_l \neq g_d$. The choice of B_0 strength is a trade-off between reliable initialization and readout (strong B_0 is better) and experimental convenience (low f_0 is easier). A field of 5 T seems reasonable: with $g_d = 0.44$, high-fidelity initialization and readout should be within reach (Sections 3 and 4), and $f_0 \approx 30$ GHz.

Properly timed bursts of microwave power tip the spin state over a controlled angle, for example, 90° or 180°. In order to observe Rabi oscillations, the Rabi period must be at most of the order of the phase randomization time constant T_2. The T_2 of a single electron spin in a quantum dot has never been measured, but based on experiments with electrons in 2DEGs, we expect that T_2 may be >100 ns [10]. For a Rabi period of 150 ns ($f_1 = 6.66$ MHz), we need a microwave field strength B_1 of ≈1 mT. For single-qubit rotations much faster than T_2, a much stronger B_1 is needed.

In order to just observe electron spin resonance (ESR), however, B_1 can be much smaller. Steady-state solution of the Bloch equations with a continuous wave (CW) microwave field B_1 applied on-resonance with the spin transition, gives $\Pr[|\uparrow\rangle] = [1 + 1/(1 + (2\pi f_1)^2 T_1 T_2)]/2$ [23]. Thus, in order to disturb $\Pr[|\uparrow\rangle]$ an observable amount away from 1, we need $f_1 \geq 1/(2\pi\sqrt{T_1 T_2})$. Taking $T_1 = 100$ μs and $T_2 = 100$ ns, we need $f_1 \geq 50$ kHz, and thus $B_1 = 0.01$ mT, one hundred times less than needed to observe Rabi oscillations.

Excitation of ESR microwave magnetic fields commonly relies on microwave cavities, but unfortunately, a lot of power is dissipated in metallic cavities: over 1 W for

$B_1 = 1$ mT at $f_0 = 30$ GHz and still about 100 μW for $B_1 = 0.01$ mT [24]. Superconducting cavities are not an option since B_0 is too large.

The alternative we pursue is to send an alternating current through a wire running close by the dot. The wire can be seen as a lumped element if it is much shorter than the wavelength, which is a few mm at 30 GHz near the surface of a GaAs substrate. If the wire terminates a 50 Ω transmission line and has an impedance $\ll 50\ \Omega$, it represents a shorted termination and the current is maximum at the wire (Fig. 4(a)).

If the wire is placed well within one wavelength λ from the quantum dot, the dot is in the near-field region and the electric and magnetic field distribution produced by the AC current is the same as for a DC current [24]. At a distance $r \ll \lambda$ from the center of the wire, a current I through a wire with circular cross-section thus produces a magnetic field $B_1 = \mu I/2\pi r$, and no electric field. If the wire is located off-chip, say, 200 μm away from the dot, and μ equals the magnetic susceptibility in vacuum μ_0, we need a current of about 1 A to produce a 1 mT microwave field, and 10 mA to get 0.01 mT. A wire integrated on-chip could be placed much closer to the dot, say 200 nm away, so the current needed is only $\approx$1 mA or 10 μA, respectively.

Energy dissipation by high-frequency currents in transmission lines takes place through ohmic, dielectric, and radiation losses [24]. For the on-chip section of the transmission line (a coplanar waveguide or coplanar striplines) and for the wire termination, radiation losses can be kept low by placing the sample inside a cavity with lowest resonance frequency above the operating frequency (longest dimension below 5 mm). At 30 GHz, dielectric losses are typically of the same order as ohmic losses, but in the on-chip section, the wire cross-section is so small that ohmic losses dominate. The off-chip section of the transmission line is a semi-rigid coaxial connection, which has relatively low loss and is thermally anchored to the higher temperature stages of the cryostat.

The ohmic losses in the on-chip lines thus dominate; we estimate them to be of order 10 μW for $I = 1$ mA. Even considering additional power dissipation due to dielectric and other losses, the total dissipated power should be well below the thermal budget at the mixing chamber of a dilution refrigerator (a few 100 μW at 100 mK), especially if the duty cycle is kept low. Nevertheless, local and instantaneous heating of the device is still a concern so we will keep losses down by maximizing the cross-section of the metal lines, by minimizing r, and by constructing a good heat-link from the chip to the mixing chamber.

For $\vec{B}_0 \perp$ to the surface (needed for operation in the quantum Hall regime), $\vec{B}_1$ must run through the dot in a direction parallel to the surface, so we must place the wire above the dot, and not to its side. It can be located on top of an insulating dielectric layer (Fig. 4(b)).

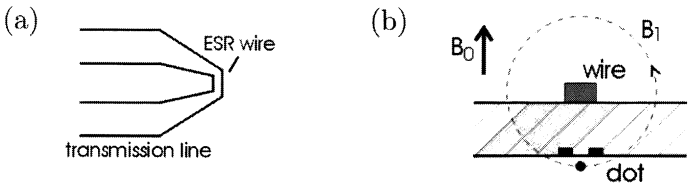

Figure 4. Schematic drawing of a microfabricated wire deposited on an insulating layer on top of the substrate. (a) Top view and (b) cross-section view.

Finally, individual addressing of one among several qubits could be achieved, in principle, via local gate electrodes, which push the individual electron wavefunctions towards a semiconductor layer with a different composition and hence a different g-factor (in $Al_xGa_{1-x}As$, g changes from -0.44 to 0.4 when x varies from 0 to 1). In this way, the electrons can be shifted into or away from resonance with the applied microwave field as desired [25, 26].

6. THE $\sqrt{\text{SWAP}}$ GATE

Two electron spins S_1 and S_2 in neighboring quantum dots are coupled to each other by the exchange interaction, which takes the form $J(t)S_1 \cdot S_2$. The result of this interaction is that the states of the two spins are swapped after a certain time. An interaction active for half this time performs the $\sqrt{\text{SWAP}}$ gate, which has been shown to be universal for quantum computation when combined with single qubit rotations [3]. In fact, the exchange interaction is even universal by itself when the state of each qubit is encoded in the state of three electron spins [27].

The strength $J(t)$ of the exchange interaction depends on the overlap of the respective electron wavefunctions, which varies exponentially with the voltage applied to the gate controlling the tunnel barrier between the two dots. For very small dots with interdot distance of a few tens of nm, J may be as large as 100 GHz [3]. For current sizes of dots and an interdot distance of $\approx$200 nm, J may still correspond to a frequency of a few tens of GHz, so two-qubit gates could be performed in $<$100 ps.

We can explore the operation of the SWAP gate as soon as initialization and readout are reliable, without requiring ESR [2]. Imagine qubit 1 is prepared in a pure state $|\uparrow\rangle$ and qubit 2 is prepared in a statistical mixture of $|\uparrow\rangle$ and $|\downarrow\rangle$. Measurement of qubit 1 should then always give $|\uparrow\rangle$ while measurement of qubit 2 should give probabilistically $|\uparrow\rangle$ or $|\downarrow\rangle$. After application of the SWAP gate, in contrast, measurement of qubit 2 should always give $|\uparrow\rangle$, while measurement of qubit 1 should give a probabilistic outcome.

7. OUTLOOK

In summary, we have presented a procedure for initialization with tunable spin-polarization, for reliable single-shot spin-to-charge conversion and charge measurement, for electron spin resonance with a microfabricated wire, and for two-qubit gates using the exchange interaction. All these schemes can be realized with current technology and we have begun experiments using the devices shown in Fig. 2.

The estimated quantum gate duration achievable at present is a few tens of ns. This requires $T_2 > 100$ μs in order to reach error probabilities per operation below 10^{-4}, needed for fault-tolerant quantum computation [1]. Speeding up single-spin rotations requires much stronger microwave fields, which probably means that alternative ways for excitation must be found that dissipate less power than cavities or wires.

The long-term promise of electron spin qubits in GaAs/AlGaAs quantum dots clearly depends crucially on the coherence times T_2 and T_1. Theoretical studies of decoherence of electron spins in quantum dots have focussed mostly on energy exchange with the bath, that is, T_1 [28]. The decay time for an electron in an excited orbital state to the ground orbital state has been measured to exceed 200 μs when a spin flip was involved in the

transition [20], so this gives hope that the T_1 (spin relaxation time for an electron in the Zeeman split orbital ground state) may also be >100 μs. The T_2 for isolated electron spins has never been measured—it is one of the primary objectives of our work.

Acknowledgements

We thank C. J. P. M. Harmans, W. G. van der Wiel, M. Blaauboer, S. Tarucha, and D. Loss for useful discussions. We acknowledge financial support from the DARPA grant DAAD19-01-1-0659 of the QuIST program, the Dutch Organization for Fundamental Research on Matter (FOM), and the European Union through a TMR Program Network.

REFERENCES

[1] M. A. Nielsen and I. L. Chuang, *Quantum Computation and Quantum Information* (Cambridge, England, Cambridge University Press, 2000).
[2] D. Loss and D. P. DiVincenzo, Quantum computation with quantum dots, *Phys. Rev.* A **57**, 120–126 (1998).
[3] G. Burkard, D. Loss, and D. P. DiVincenzo, Coupled quantum dots as quantum gates, *Phys. Rev.* B **59**, 2070–2078 (1999).
[4] V. N. Golovach and D. Loss, Electron spins in artificial atoms and molecules for quantum computing, *Semicond. Sci. Tech.* **17**, 355–366 (2002).
[5] L. P. Kouwenhoven *et al.*, Electron transport in quantum dots. In L. P. Kouwenhoven, L. L. Sohn, and G. Schön, eds., *Proc. of the NATO Advanced Study Institute on Mesoscopic Electron Transport*, pp. 105–214. Kluwer Series (1997).
[6] L. P. Kouwenhoven, D. G. Austing, and S. Tarucha, Few-electron quantum dots, *Reports on Progress in Physics* **64**, 701–736 (2001).
[7] M. Ciorga *et al.*, Addition spectrum of a lateral dot from Coulomb and spin-blockade spectroscopy, *Phys. Rev.* B **61**, R16315–8 (2000).
[8] D. Sprinzak, Y. Ji, M. Heiblum, D. Mahalu, and H. Shtrikman, Charge distribution in a Kondo correlated quantum dot, *Phys. Rev. Lett.* **88**, 176805 (2002).
[9] J. M. Elzerman *et al.*, *in preparation* (2002).
[10] J. M. Kikkawa and D. D. Awschalom, Lateral drag of spin coherence in gallium arsenide, *Nature* **397**, 139–141 (1999).
[11] T. Englert, D. C. Tsui, A. C. Gossard, and C. Uihlein, *g*-Factor enhancement in the 2D electron gas in GaAs/AlGaAs heterojunctions, *Surface Science*, **113**, 295–300 (1982).
[12] P. L. McEuen *et al.*, Self-consistent addition spectrum of a Coulomb island in the quantum hall regime, *Phys. Rev.* B **45**, 11419–11422 (1992).
[13] N. C. van der Vaart *et al.*, Time-resolved tunneling of single electrons between Landau levels in a quantum dot, *Phys. Rev. Lett.* **73**, 320–323 (1994).
[14] J. Wrachtrup, C. Vonborczyskowski, J. Bernard, M. Orrit, and R. Brown. Optical detection of magnetic resonance in a single molecule, *Nature* **363**, 244–245 (1993).
[15] J. Kohler *et al.*, Magnetic resonance of a single molecular spin, *Nature* **363**, 242–244 (1993).
[16] D. Gammon *et al.* Electron and nuclear spin interactions in the optical spectra of single GaAs quantum dots, *Phys. Rev. Lett.* **86**, 5176–5179 (2001).
[17] B. E. Kane, A silicon-based nuclear spin quantum computer, *Nature* **393**, 133–137 (1998).
[18] G. A. Prinz, Magnetoelectronics, *Science* **282**, 1660–1663 (1998).
[19] S. Tarucha *et al.*, Direct coulomb and exchange interaction in artificial atoms, *Phys. Rev. Lett.* **84**, 2485–2489 (2000).
[20] T. Fujisawa, D. G. Austing, Y. Tokura, Y. Hirayama, and S. Tarucha, Allowed and forbidden transitions in artificial atoms, *Nature* (2002).
[21] M. Field *et al.*, Measurements of Coulomb blockade with a non-invasive voltage probe, *Phys. Rev. Lett.* **70**, 1311–1314 (1993).

[22] M. Dobers, K.v. Klitzing, and G. Weiman, Electron-spin resonance in the 2D electron gas of GaAs-Al_xGa_{1-x} heterostructures. *Phys. Rev.* B **38**, 5453 (1988).
[23] A. Abragam, *Principles of Nuclear Magnetism* (Oxford, Clarendon Press, 1961).
[24] J. D. Jackson, *Classical Electrodynamics* (New York, Wiley, 1998).
[25] G. Salis *et al.*, Electrical control of spin coherence in semiconductor nanostructures, *Nature* **414**, 619–622 (2001).
[26] H. W. Jiang and E. Yablonovitch, Gate-controlled electron spin resonance in GaAs/Al_xGa_{1-x}As heterostructures, *Phys. Rev.* B **64**, 041307 (2001).
[27] D. P. DiVincenzo, D. P. Bacon, D. A. Lidar, and K. B. Whaley, Universal quantum computation with the exchange interaction, *Nature* **408**, 339 (2000).
[28] A. V. Khaetskii and Y. V. Nazarov, Spin relaxation in semiconductor quantum dots, *Phys. Rev.* B **61**, 12639–12642 (2000).

RELATION BETWEEN DEPHASING AND RENORMALIZATION PHENOMENA IN QUANTUM TWO-LEVEL SYSTEMS

A. Shnirman[1] and G. Schön[1,2]
[1]*Institut für Theoretische Festkörperphysik, Universität Karlsruhe, 76128 Karlsruhe, Germany*
[2]*Forschungszentrum Karlsruhe, Institut für Nanotechnologie, 76021 Karlsruhe, Germany*

Abstract: We observe that experimental conditions, for example, details of the initial state preparation, determine to what extent the environment leads to dephasing or to renormalization effects. We analyze an exactly solvable limit of the spin-boson model where the relation between both can be demonstrated explicitly.

1. INTRODUCTION

The dynamics of quantum two-level systems has always been a focus of interest, but recently attracted increased attention because of the prospects of quantum state engineering and related low-temperature experiments. A crucial requirement for many of these concepts is the preservation of phase coherence in the presence of a noisy environment. Frequently it is sufficient to model the environment by a bath of harmonic oscillators, with frequency spectrum adjusted to reproduce the observed power spectrum. The resulting "spin-boson" models have been studied in the literature, in particular the one with bilinear coupling and "Ohmic" spectrum, but spin-boson models with different power spectra appear equally interesting in view of several experiments. In this article we, therefore, analyze spin-boson model with general power spectra with respect to relaxation, dephasing, and renormalization processes at low temperatures. We study the dephasing of nonequilibrium initial states. We show how the state preparation affects the effective high-frequency cut-off and separates renormalization from dephasing effects.

2. SPIN-BOSON MODEL

In this section we review the properties of spin-boson models, which have been studied extensively before [1, 2]. A quantum two-level system is modeled by a spin degree

Quantum Computing and Quantum Bits in Mesoscopic Systems
Edited by Leggett *et al.*, Kluwer Academic/Plenum Publishers, 2004

of freedom in a magnetic field. It is coupled linearly to an oscillator bath. The total Hamiltonian is

$$\mathcal{H} = \mathcal{H}_{\rm ctrl} + \sigma_z \sum_j c_j (a_j + a_j^\dagger) + \mathcal{H}_{\rm b} \tag{1}$$

where the controlled part is $\mathcal{H}_{\rm ctrl} = -(1/2)B_z\sigma_z - (1/2)B_x\sigma_x = -(1/2)\Delta E(\cos\theta\,\sigma_z + \sin\theta\,\sigma_x)$, the oscillator bath is described by $\mathcal{H}_{\rm b} = \sum_j \hbar\omega_j a_j^\dagger a_j$, and the bath 'force' operator $X = \sum_j c_j(a_j + a_j^\dagger)$ is assumed to couple linearly to σ_z. For later convenience $\mathcal{H}_{\rm ctrl}$ has also been written in terms of a mixing angle $\theta = \tan^{-1}(B_x/B_z)$, depending on the direction of the magnetic field, and the energy splitting of the eigenstates, $\Delta E = \sqrt{B_x^2 + B_z^2}$.

In thermal equilibrium the Fourier transform of the symmetrized correlation function of the force operator is given by

$$S_X(\omega) \equiv \langle [X(t), X(t')]_+ \rangle_\omega = 2\hbar J(\omega) \coth \frac{\hbar\omega}{2k_{\rm B}T} \tag{2}$$

Here the bath spectral density has been introduced, defined by $J(\omega) \equiv (\pi/\hbar)\sum_j c_j^2 \times \delta(\omega - \omega_j)$. At low frequencies it typically has a power-law form up to a high-frequency cut-off ω_c,

$$J(\omega) = \frac{\pi}{2}\hbar\alpha\omega_0^{1-s}\omega^s\Theta(\omega_c - \omega) \tag{3}$$

Generally one distinguishes Ohmic ($s = 1$), sub-Ohmic ($s < 1$), and super-Ohmic ($s > 1$) spectra. In Eq. (3) an additional frequency scale ω_0 has been introduced. Since it appears only in the combination $\alpha\omega_0^{1-s}$ it is arbitrary and in Ref. [1] has been chosen equal to the high-frequency cut-off. Here we prefer to distinguish both frequencies, since the cut-off ω_c will play an important role in what follows.

We first consider the Ohmic case in the weak damping regime, $\alpha \ll 1$. If ΔE is not too small (the exact condition reads $\Delta E > \alpha T$) it is natural to describe the evolution of the system in the eigenbasis of $\mathcal{H}_{\rm ctrl}$, which are

$$|0\rangle = \cos\frac{\theta}{2}|\uparrow\rangle + \sin\frac{\theta}{2}|\downarrow\rangle \quad \text{and} \quad |1\rangle = -\sin\frac{\theta}{2}|\uparrow\rangle + \cos\frac{\theta}{2}|\downarrow\rangle \tag{4}$$

Denoting by τ_x and τ_z the Pauli matrices in the eigenbasis, we have

$$\mathcal{H} = -\frac{1}{2}\Delta E\tau_z + (\sin\theta\tau_x + \cos\theta\tau_z)X + \mathcal{H}_{\rm b} \tag{5}$$

Two dissipative rates describe the dynamics of the system. The relaxation rate describes the relaxation of the diagonal elements of the density matrix to their equilibrium value. The dephasing rate describes vanishing of the off-diagonal elements. In Refs [1] and [2] the dephasing and relaxation times were evaluated in a path-integral technique. In the regime $\alpha \ll 1$ it is easier to employ the perturbative (diagrammatic) technique developed in Ref. [3] and the standard Bloch–Redfield approximation. The rates are

$$\Gamma_{\rm relax} \equiv \tau_{\rm relax}^{-1} = \frac{1}{\hbar^2}\sin^2\theta S_X\left(\omega = \frac{\Delta E}{\hbar}\right) \tag{6}$$

$$\Gamma_\varphi \equiv \tau_\varphi^{-1} = \frac{1}{2}\Gamma_{\rm relax} + \frac{1}{\hbar^2}\cos^2\theta S_X(\omega = 0) \tag{7}$$

where $S_X(\omega) = \pi\alpha\hbar^2\omega\coth(\hbar\omega/2k_BT)$. We observe that only the "transverse" part of the fluctuating field X, coupling to τ_x and proportional to $\sin\theta$, induces transitions between the eigenstates (4) of the unperturbed system. Thus the relaxation rate (6) is proportional to $\sin^2\theta$. The "longitudinal" part of the coupling of X to τ_z, which is proportional to $\cos\theta$, does not induce relaxation processes. It does, however, contribute to dephasing since it leads to fluctuations of the eigenenergies and, thus, to a random relative phase between the two eigenstates. This is the origin of the "pure" dephasing contribution to Eq. (7), which is proportional to $\cos^2\theta$. We rewrite Eq. (7) as $\Gamma_\varphi = (1/2)\Gamma_{\rm relax} + \cos^2\theta\Gamma_\varphi^*$, where $\Gamma_\varphi^* = S_X(\omega = 0)/\hbar^2 = 2\pi\alpha k_BT/h$ is the pure dephasing rate.

3. LONGITUDINAL COUPLING, EXACT SOLUTION FOR FACTORIZED INITIAL CONDITIONS

The last forms of Eqs (6) and (7) express the two rates in terms of the noise power spectrum at the relevant frequencies. These are the level spacing of the two-state system and zero frequency, respectively. The expressions apply in the weak-coupling limit for spectra which are regular at these frequencies. For the relaxation rate (6) the generalization to sub- and super-Ohmic cases merely requires substituting the relevant $S_X(\omega = \Delta E/\hbar)$. However, this does not work for the pure dephasing contribution. Indeed $S_X(\omega = 0)$ is infinite in the sub-Ohmic regime, while it vanishes for the super-Ohmic case and the Ohmic case at $T = 0$. As we will see this does not imply infinitely fast or slow dephasing in these cases. To analyze these cases we study the exactly soluble model of longitudinal coupling, $\theta = 0$.

Dephasing processes are contained in the time evolution of the quantity $\langle\tau_+(t)\rangle$ obtained after tracing out the bath. This quantity can be evaluated analytically for $\theta = 0$ (when $\tau_+ = \sigma_+$) for an initial state which is described by a factorized density matrix $\hat\rho(t = 0) = \hat\rho_{\rm spin}\otimes\hat\rho_{\rm bath}$ (which implies that the two-level system and bath are initially disentangled). In this case the Hamiltonian $\mathcal{H} = -(1/2)\Delta E\sigma_z + \sigma_z X + \mathcal{H}_b$ is diagonalized by a unitary transformation by $U \equiv \exp(-i\sigma_z\Phi/2)$ where the bath operator Φ is defined as

$$\Phi \equiv i\sum_j \frac{2c_j}{\hbar\omega_j}(a_j^\dagger - a_j) \tag{8}$$

After some algebra, using the fact that the initial density matrix is factorized, we obtain $\langle\sigma_+(t)\rangle \equiv \mathcal{P}(t)e^{-i\Delta Et}\langle\sigma_+(0)\rangle$ where

$$\mathcal{P}(t) = {\rm Tr}[e^{i\Phi(0)/2}e^{-i\Phi(t)}e^{i\Phi(0)/2}\hat\rho_{\rm bath}] \tag{9}$$

The expression (9) applies for any initial state of the bath as long as it is factorized from the spin. In particular, we can assume that the spin was initially (for $t \le 0$) kept in the state $|\uparrow\rangle$ and the bath had relaxed to the thermal equilibrium distribution for this spin value: $\hat\rho_{\rm bath} = \hat\rho_\uparrow \equiv Z_\uparrow^{-1}e^{-\beta\mathcal{H}_\uparrow}$, where $\mathcal{H}_\uparrow = \mathcal{H}_b + \sum_j c_j(a_j + a_j^\dagger)$. In this case we can rewrite the density matrix as $\hat\rho_{\rm bath} = e^{i\Phi/2}\hat\rho_b e^{-i\Phi/2}$, where the density matrix of the decoupled bath is given by $\hat\rho_b \equiv Z_b^{-1}e^{-\beta\mathcal{H}_b}$, and the function $\mathcal{P}(t)$ reduces to

$$\mathcal{P}(t) \to P(t) \equiv {\rm Tr}(e^{-i\Phi(t)}e^{i\Phi}\hat\rho_b) \tag{10}$$

This expression (with Fourier transform $P(E)$) has been studied extensively in the literature [1, 4–7]. It can be expressed as $P(t) = \exp K(t)$, where

$$K(t) = \frac{4}{\pi\hbar}\int_0^\infty d\omega \frac{J(\omega)}{\omega^2}\left[\coth\left(\frac{\hbar\omega}{2k_BT}\right)(\cos\omega t - 1) - i\sin\omega t\right] \tag{11}$$

For an Ohmic bath at nonzero temperature and not too short times, $t > \hbar/k_BT$, it reduces to $\mathrm{Re}\,K(t) \approx -S_X(\omega = 0)t/\hbar^2 = -2\pi\alpha k_BTt/\hbar$, consistent with Eq. (7) in the limit $\theta = 0$.

Table 1. Decay of $|\langle\sigma_+(t)\rangle|$ in time for different bath spectra.

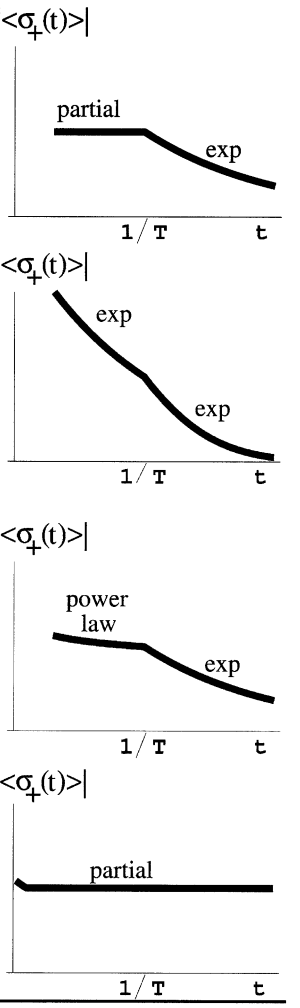

- Ohmic: $J(\omega) = (\pi/2)\alpha\omega\Theta(\omega_c - \omega)$:

  for $\omega_c^{-1} \ll t \ll T^{-1}$ $\quad |\langle\sigma_+(t)\rangle| \approx (\omega_c t)^{-2\alpha}$
  for $t \gg T^{-1}$ $\quad |\langle\sigma_+(t)\rangle| \approx e^{-2\pi\alpha Tt}$

- Sub-Ohmic: $J(\omega) = (\pi/2)\alpha\omega_0^{1-s}\omega^s\Theta(\omega_c - \omega)$ and $0 < s < 1$:

  for $\omega_c^{-1} \ll t \ll T^{-1}$ $\quad |\langle\sigma_+(t)\rangle| \approx e^{-\alpha(\omega_0 t)^{1-s}}$
  for $t \gg T^{-1}$ $\quad |\langle\sigma_+(t)\rangle| \approx e^{-\alpha Tt(\omega_0 t)^{1-s}}$

- Super-Ohmic: $J(\omega) = (\pi/2)\alpha\omega_0^{1-s}\omega^s\Theta(\omega_c - \omega)$ and $1 < s < 2$:

  for $\omega_c^{-1} \ll t \ll T^{-1}$ $\quad |\langle\sigma_+(t)\rangle| \approx e^{-\alpha(\omega_c/\omega_0)^{s-1}}$
  for $t \gg T^{-1}$ $\quad |\langle\sigma_+(t)\rangle| \approx e^{-\alpha Tt(\omega_0 t)^{1-s}}$

- Soft gap: $J(\omega) = (\pi/2)\alpha\omega_0^{1-s}\omega^s\Theta(\omega_c - \omega)$ and $s > 2$:

  for $\omega_c^{-1} \ll t$ $\quad |\langle\sigma_+(t)\rangle| \approx e^{-\alpha(\omega_c/\omega_0)^{s-1}}$

For $1/\omega_c < t < \hbar/k_B T$, and thus for all times at $T = 0$, one still finds a decay of $\langle \sigma_+(t) \rangle$ governed by Re $K(t) \approx -2\alpha \ln(\omega_c t)$, which implies a power-law decay

$$\langle \sigma_+(t) \rangle = (\omega_c t)^{-2\alpha} e^{-i\Delta E t/\hbar} \langle \sigma_+(0) \rangle \tag{12}$$

Thus even at $T = 0$, when $S_X(\omega = 0) = 0$, the off-diagonal elements of the density matrix decay in time. All oscillators up to the high-frequency cut-off ω_c contribute to this decay. The physical meaning of this result will be discussed later. We can also define a cross-over temperature T^* below which the power-law decay dominates over the subsequent exponential one. A criterion is that at $t = \hbar/k_B T^*$ the short-time power-law decay has reduced the off-diagonal components already substantially, that is, $\langle \sigma_+(\hbar/k_B T^*) \rangle = 1/e$. This happens at the temperature $kT^* = \hbar\omega_c \exp(-1/2\alpha)$. Thus the dephasing rate is $\Gamma_\varphi^* = k_B T^*/\hbar$ for $T < T^*$ and $\Gamma_\varphi^* = 2\pi\alpha k_B T/\hbar$ for $\alpha T > T^*$.

For a sub-Ohmic bath with $0 < s < 1$ due to the high density of low-frequency oscillators exponential dephasing is observed even for short times, $|\langle \sigma_+(t) \rangle| \propto \exp[-\alpha(\omega_0 t)^{1-s}]$ for $t < \hbar/k_B T$, as well as for longer times, $|\langle \sigma_+(t) \rangle| \propto \exp[-\alpha T t(\omega_0 t)^{1-s}]$ for $t > \hbar/k_B T$. In the exponents of the short- and long-time decay laws we have omitted factors which are of order one, except if s is close to either 1 or 0, in which case a more careful treatment is required. The dephasing rates resulting from the decay laws are $\Gamma_\varphi^* \propto T^* = \alpha^{1/(1-s)}\omega_0$ (cf. Ref. [8]) for $T < T^*$ and $\Gamma_\varphi^* \propto (\alpha T/\omega_0)^{1/(2-s)}\omega_0$ for $T > T^*$. Again the cross-over temperature T^* marks the boundary between the regimes where either the initial, temperature-independent decay or the subsequent decay at $t > \hbar/k_B T$ is more important.

Finally we discuss the super-Ohmic regime, $s > 1$. In this case, within a short time of order ω_c^{-1}, the exponent Re $K(t)$ increases to a finite value Re $K(\infty) = -\alpha(\omega_c/\omega_0)^{s-1}$ and then remains constant for $\omega_c^{-1} < t < \hbar/k_B T$ (we again omit factors of order one and note that the limit $s \to 1$ requires more care). This implies an initial reduction of the off-diagonal element $|\langle \sigma_+(t) \rangle|$ followed by a saturation at $|\langle \sigma_+(t) \rangle| \propto \exp[-\alpha(\omega_c/\omega_0)^{s-1}]$. For $t > \hbar/k_B T$ an exponential decay develops, $|\langle \sigma_+(t) \rangle| \propto \exp[-\alpha T t(\omega_0 t)^{1-s}]$, but only if $s < 2$. This decay is always dominant and, thus, there is no cross-over in this case, that is, $T^* = 0$. For $s \geq 2$ there is almost no additional decay.

The results obtained for different bath spectra are summarized in Table 1.

4. PREPARATION EFFECTS

In the previous section we considered specific initial conditions with a factorized density matrix. The bath was prepared in an equilibrium state characterized by temperature T, while the spin state was arbitrary. The state of the total system is, thus, a nonequilibrium one and dephasing is to be expected even at zero bath temperature. In this section we investigate what initial conditions may arise in real experiments.

The fully factorized initial state just described can in principle be prepared by the following Gedanken experiment: The spin is forced, for example, by a strong external field, to be in a fixed state, say $|\uparrow\rangle$. The bath, which is kept coupled to the spin, relaxes to the equilibrium state of the Hamiltonian $\mathcal{H}_\uparrow$, for example, at $T = 0$ to the ground state $|g_\uparrow\rangle$ of $\mathcal{H}_\uparrow$. Then, at $t = 0$, a *sudden* pulse of the external field is applied to change the spin state, for example, to a superposition $(1/\sqrt{2})(|\uparrow\rangle + |\downarrow\rangle)$. Since the bath has no time to respond, the resulting state is $|i\rangle = (1/\sqrt{2})(|\uparrow\rangle + |\downarrow\rangle) \otimes |g_\uparrow\rangle$. Both components of this initial wavefunction now evolve in time according to the Hamiltonian (1). The first,

$|\uparrow\rangle \otimes |g_\uparrow\rangle$, which is an eigenstate of (1), acquires only a trivial phase factor. The time evolution of the second component is more involved. Up to a phase factor it is given by $|\downarrow\rangle \otimes \exp(-i\mathcal{H}_\downarrow t/\hbar)|g_\uparrow\rangle$ where $\mathcal{H}_\downarrow \equiv \mathcal{H}_b - \sum_j c_j(a_j + a_j^\dagger)$. As the state $|g_\uparrow\rangle$ is not an eigenstate of $\mathcal{H}_\downarrow$, entanglement between the spin and the bath develops, and the coherence between the components of the spin's state is reduced by the factor $|\langle g_\uparrow| \exp(-i\mathcal{H}_\downarrow t/\hbar)|g_\uparrow\rangle| = |\langle g_0| \exp(-i\Phi(t))\exp(i\Phi)|g_0\rangle| = |P_{\omega_c}(t, T = 0)| < 1$. The function $P(t)$ was defined in Eq. (10). The subscript ω_c is added to indicate the value of the high-frequency cut-off of the bath which will play an important role in what follows.

In a real experiment of the type discussed the preparation pulse takes a finite time, τ_p. For instance, the $(\pi/2)_x$-pulse which transforms the state $|\uparrow\rangle \to (1/\sqrt{2})(|\uparrow\rangle + |\downarrow\rangle)$, can be accomplished by putting $B_z = 0$ and $B_x = \hbar\omega_p$ for a time span $\tau_p = \pi/2\omega_p$. During this time the bath oscillators partially adjust to the changing spin state. The oscillators with (high) frequencies, $\omega_j \gg \omega_p$, follow the spin adiabatically. In contrast, the oscillators with low frequency, $\omega_j \ll \omega_p$, do not change their state. Assuming that the oscillators can be split into these two groups, we see that just after the $(\pi/2)_x$-pulse the state of the system is $(1/\sqrt{2})(|\uparrow\rangle \otimes |g_\uparrow^h\rangle + |\downarrow\rangle \otimes |g_\downarrow^h\rangle) \otimes |g_\uparrow^l\rangle$ where the superscripts "h" and "l" refer to high- and low-frequency oscillators, respectively. Thus, we arrive at an initial state with only the low-frequency oscillators factorized from the spin. For the off-diagonal element of the density matrix we obtain

$$|\langle\sigma_+(t)\rangle| = Z(\omega_c, \omega_p)|P_{\omega_p}(t)| \tag{13}$$

where $Z(\omega_c, \omega_p) \equiv |\langle g_\uparrow^h | g_\downarrow^h\rangle|$ and $P_{\omega_p}(t)$ is given by the same expressions as before, except that the high-frequency cut-off is reduced to ω_p.

The high-frequency oscillators still contribute to the reduction of $|\langle\sigma_+(t)\rangle|$—via the factor $Z(\omega_c, \omega_p)$—however, this effect is reversible. To illustrate this we consider the following continuation of the experiment. After the $(\pi/2)$ pulse we allow for a free evolution of the system during time t with magnetic field $B_z = \Delta E$ along the z axis. Then we apply a $(-\pi/2)$ pulse and measure σ_z. Without dissipation the result would be $\langle\sigma_z\rangle = \cos(\Delta E t)$. With dissipation the state of the system after time t is

$$\frac{1}{\sqrt{2}}(e^{i\Delta E t/2}|\uparrow\rangle \otimes |g_\uparrow^h\rangle \otimes |g_\uparrow^l\rangle + e^{-i\Delta E t/2}|\downarrow\rangle \otimes |g_\downarrow^h\rangle \otimes e^{-i\mathcal{H}_\downarrow t/\hbar}|g_\uparrow^l\rangle) \tag{14}$$

After the $(-\pi/2)$ pulse (also of width $\pi/2\omega_p$) we obtain the following state:

$$\begin{aligned}&\frac{1}{2}|\uparrow\rangle \otimes |g_\uparrow^h\rangle \otimes (e^{i\Delta E t/2}|g_\uparrow^l\rangle + e^{-i\Delta E t/2}e^{-i\mathcal{H}_\downarrow t/\hbar}|g_\uparrow^l\rangle)\\ &\quad + \frac{1}{2}|\downarrow\rangle \otimes |g_\downarrow^h\rangle \otimes (-e^{i\Delta E t/2}|g_\uparrow^l\rangle + e^{-i\Delta E t/2}e^{-i\mathcal{H}_\downarrow t/\hbar}|g_\uparrow^l\rangle)\end{aligned} \tag{15}$$

From this we finally get $\langle\sigma_z\rangle = \mathrm{Re}[P_{\omega_p}(t)e^{-i\Delta E t}]$. Thus the amplitude of the coherent oscillations of σ_z is reduced only by the factor $|P_{\omega_p}(t)|$ associated with slow oscillators. The high-frequency factor $Z(\omega_c, \omega_p)$ does not appear. To interpret this result we note that we could have discussed the experiment in terms of renormalized spins $|\tilde{\uparrow}\rangle \equiv |\uparrow\rangle|g_\uparrow^h\rangle$ and $|\tilde{\downarrow}\rangle \equiv |\downarrow\rangle|g_\downarrow^h\rangle$, and assuming that the high-frequency cut-off of the bath is ω_p.

It is interesting to compare further the two scenarios with instantaneous and finite-time preparation further. The time evolution after the instantaneous preparation is governed by $P_{\omega_c}(t)$. For $T \ll \omega_p$ and $t \gg 1/\omega_p$ and arbitrary spectral density $J(\omega)$ it satisfies the following relation: $P_{\omega_c}(t) = Z^2(\omega_c, \omega_p)P_{\omega_p}(t)$, which follows from $\langle g^h_\uparrow | \exp(-i\mathcal{H}_\downarrow t/\hbar)|g^h_\uparrow\rangle \to |\langle g^h_\uparrow | g^h_\downarrow\rangle|^2$ for $t \gg 1/\omega_p$. Thus for the instantaneous preparation the reduction due to the high-frequency oscillators is equal to $Z^2(\omega_c, \omega_p)$, while a look at the finite-time preparation result (13) shows that in this case the reduction is weaker, given by a single power of $Z(\omega_c, \omega_p)$ only. Moreover, in the slow preparation experiment the factor $Z(\omega_c, \omega_p)$ originates from the overlap of two "simple" wavefunctions, $|g^h_\uparrow\rangle$ and $|g^h_\downarrow\rangle$, which can be further adiabatically manipulated, as described above, and this reduction can be recovered. This effect is to be interpreted as a renormalization. On the other hand, for the instantaneous preparation the high-frequency contribution to the dephasing originates from the overlap of the states $|g^h_\uparrow\rangle$ and $e^{-i\mathcal{H}_\downarrow t/\hbar}|g^h_\uparrow\rangle$. The latter is a complicated excited state of the bath with many nonzero amplitudes evolving with different frequencies. There is no simple (macroscopic) way to reverse the dephasing associated with this state. Thus we observe that the time scale of the manipulating pulses determines the border between the oscillators responsible for dephasing and the oscillators responsible for renormalization.

5. SUMMARY

The examples presented above show that experimental conditions, for example, details of the system's initial state preparation, that determine which part of the environment contributes to dephasing and which part leads to renormalization. For a quantum two-state system with a nonequilibrium initial state, described by a factorized initial density matrix, dephasing persists down to zero bath temperature. An Ohmic environment leads to a power-law dephasing at $T = 0$, while a sub-Ohmic bath yields exponential dephasing. The reason is that the factorized initial state, even with the bath in the ground state of the bath Hamiltonian, is actually a superposition of many excited states of the total coupled system. In a real experiment only a part of the environment, the oscillators with low frequencies, can be prepared factorized from the two-level system. These oscillators still lead to dephasing, whereas the high-frequency oscillators lead to renormalization effects. The finite preparation time $\sim 1/\omega_p$ also introduces a natural high-frequency cut-off in the description of dephasing effects.

Acknowledgements

We thank Y. Makhlin for valuable contributions to the present work and M. Büttiker, M. H. Devoret, D. Esteve, Y. Gefen, D. Golubev, Y. Imry, D. Loss, A. D. Mirlin, A. Rosch, U. Weiss, R. Whitney, and A. D. Zaikin for stimulating discussions. The work is part of the EU IST Project SQUBIT and of the CFN (Center for Functional Nanostructures) which is supported by the DFG (German Science Foundation).

REFERENCES

[1] A. Leggett, S. Chakravarty, A. Dorsey, M. Fisher, A. Garg, and W. Zwerger, Dynamics of the dissipative two-state system, *Rev. Mod. Phys.* **59**, 1 (1987).

[2] U. Weiss, *Quantum Dissipative Systems* (Singapore: World Scientific, 2nd edition).

[3] H. Schoeller and G. Schön, Mesoscopic quantum transport: resonant tunneling in the presence of strong Coulomb interaction, *Phys. Rev.* B **50**, 18436 (1994).
[4] S. V. Panyukov and A. D. Zaikin, Quantum fluctuations and quantum dynamics of small Josephson junctions, *J. Low Temp. Phys.* **73**, 1 (1988).
[5] A. A. Odintsov, Effect of dissipation on the characteristics of small-area tunnel junctions: application of the polaron model, *Sov. Phys. JETP* **67**, 1265 (1988).
[6] Yu. V. Nazarov, Anomalous current–voltage characteristics of tunnel junctions, *Sov. Phys. JETP* **68**, 561 (1989).
[7] M. H. Devoret, D. Esteve, H. Grabert, G. L. Ingold, and H. Pothier, Effect of the electromagnetic environment on the Coulomb blockade in ultrasmall tunnel junctions, *Phys. Rev. Lett.* **64**, 1824 (1990).
[8] W. G. Unruh, Maintaining coherence in quantum computers, *Phys. Rev.* A **51**, 992 (1995).

SUPERCONDUCTING QUANTUM COMPUTING WITHOUT SWITCHES

M. J. Feldman[a] and X. Zhou[b]
Department of Electrical and Computer Engineering, University of Rochester, Rochester, NY 14627, USA

Abstract: This Chapter presents a very simple architecture for a large-scale superconducting quantum computer. All of the SQUID qubits are fixed-coupled to a single large superconducting loop.

1. INTRODUCTION

What physical system is most appropriate for building a quantum computer? The proponents of one implementation or another usually discuss this question by reference to DiVincenzo's criteria [1]. These five criteria very nicely summarize the requirements for the physical realization of a quantum information processing system.

For our purposes, four of these criteria can be combined into a single one: good qubits. That has many implications, but we will say no more about it here. For this paper, let us assume ideal qubits. The other criterion, number four, is "A 'universal' set of quantum gates". This addresses the interactions between qubits rather than the nature of the qubits themselves. A quantum computer is, at least, a set of interacting qubits.

In this paper we will first discuss the "no switch" problem regarding superconducting implementations of quantum computing. In brief, it has been difficult to come up with a satisfactory scheme to switch the coupling between two superconducting qubits on and off. Then we will mention several possibilities for quantum computing using fixed, rather than switchable, couplings between qubits, and indicate why these are unsatisfactory for superconducting qubits as well.

Our solution to this situation is based on recent work [2] in which a virtual switch, rather than a substantial physical switch, is realized by carrying out the steps of the quantum computation in and out of designed "interaction free subspaces", which are analogous to decoherence free subspaces. We will give examples of how these virtual switches can be employed in a variety of different architectures for a superconducting quantum computer.

E-mail: [a]feldman@ece.rochester.edu
E-mail: [b]xizhou@ece.rochester.edu

Quantum Computing and Quantum Bits in Mesoscopic Systems
Edited by Leggett *et al.*, Kluwer Academic/Plenum Publishers, 2004

Finally we explore one particular architecture at much greater length. Many SQUID qubits are fixed-coupled to a single large superconducting loop. We show that this is adequate for large-scale quantum computing, and specify the requisite parameters. The parameters are chosen for rf-SQUID qubits [3,4] but this architecture is equally appropriate for persistent current SQUID qubits [5] as well.

2. THE "NO-SWITCH" PROBLEM

Quantum algorithms are generally formulated in terms of a collection of qubits subject to a sequence of single-qubit operations and two-qubit gates. A two-qubit gate such as the CNOT can be represented by a unitary 4×4 matrix over the bases of the two qubits. Taken literally, such an algorithm implies that there are three distinct modes of operation of a quantum computer. Two qubits have: (1) the idle mode in which information is stored in qubits which do not evolve, (2) the single-qubit operation mode in which local fields applied to qubit 1 have no effect on qubit 2, and (3) the two-qubit operation mode in which qubit 1 and qubit 2 are coupled together and a quantum gate is realized through the coupling Hamiltonian. The two-qubit Hamiltonian that expresses this is

$$H = -\vec{B}_1(t) \cdot \vec{\sigma}_1 - \vec{B}_2(t) \cdot \vec{\sigma}_2 + \sum_{\alpha,\beta} J_{12}^{\alpha\beta}(t)\sigma_1^{\alpha}\sigma_2^{\beta} \tag{1}$$

where σ values are the Pauli matrices, $\vec{B}_i$ is the local field at qubit i, and J_{12} is the coupling strength. $\vec{B}_i$ and J_{12} are time dependent under external control. To alternate between the three operational modes it is necessary that $\vec{B}_i$ be turned on and off as required and J_{12} be turned on and off as required. In other words, there must be a switch between qubit 1 and qubit 2.

In both flux and charge [6,7] superconducting qubits, the control of the time dependence of B_x and B_z is relatively "easy". As illustrated in Fig. 1, time-dependent B_x and B_z fields on superconducting qubits are achieved by simply varying the biases. The fixed coupling between qubits is "easy" for the superconducting qubits as well, as shown in Fig. 2. The flux qubits can be coupled by a simple inductive connection, and the charge qubits can be coupled by a simple capacitive connection between them. This is certainly "easy" too. In fact a fixed inductive coupling between rf-SQUID qubits was illustrated in the first paper written on superconducting quantum computing [3].

Variable coupling between superconducting qubits is much harder. There are many proposed schemes, but it is generally agreed that none of these proposed switches is

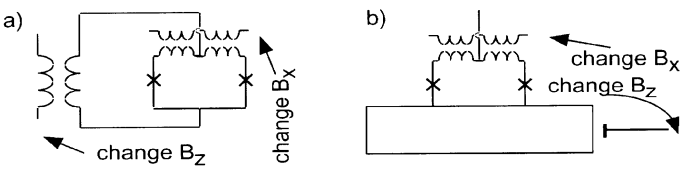

Figure 1. (a) A flux qubit biased near $\Phi_0/2$, for which the remove from one-half flux quantum acts as the B_z field, and the suppression of the effective critical current acts as the B_x field. (b) A charge qubit, for which the remove from a single-charge voltage bias acts as the B_z field, and the suppression of the effective critical current acts as the B_x field.

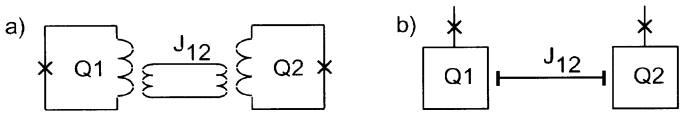

Figure 2. (a) Inductively coupled flux qubits; (b) Capacitively coupled charge qubits.

completely satisfactory [8]. Some early examples are Averin's proposal [9] to couple charge qubits by moving the charge among the charge islands, and Schön *et al.*'s LC resonator "bus" [8, 10]. Perhaps the simplest variable superconducting switch was first described by Mooij *et al.* [11]. It is essentially a solid superconducting loop broken by a Josephson junction which can be open circuited—it is an rf-SQUID in which the critical current can be reduced to zero. More recent schemes are a differential version of the rf-SQUID switch [12], the "Bloch transistor" [13], and the INSQUID [14].

These are only a few of the proposals for switches linking the qubits in a superconducting quantum computer. Some of these schemes are not practical, but for the most part they could possibly be used but they just seem awkward. Many of them require external controls, which are likely to be important sources of decoherence. Many require an unrealistic level of parameter control to operate successfully. Others appear to be difficult to scale to a many qubit system. In any case, none of these proposals has garnered outside support, and new and more elaborate proposals keep appearing in the literature.

3. FIXED-COUPLED QUANTUM COMPUTER

One may consider making a quantum computer without switches. Any interaction between qubits, fixed or variable, is sufficient for a universal quantum gate. Such a computer however may be more difficult to realize in practice.

An early example is the spin-lattice quantum computer [15], in which the "spins" (qubits) are hard-wired into a lattice. There are no switches; rather, the entire lattice is addressed by global fields. This paradigm for quantum computing requires more complex manipulations to perform simple operations, and it can be tedious to render quantum algorithms into lattice interactions. Although widely referenced, this scheme has not been much adopted by others. For superconducting systems, the spin lattice architecture seems a particular waste of resources, in that single-bit operations that are "easy" for superconducting qubits are not at all utilized.

A prominent quantum computer architecture today is the NMR molecular system. In NMR, coupling between the qubits is indeed fixed. There is no reason in principle not to build a hard-wired superconducting quantum computer following the NMR model. In the NMR model, complex synthesized "refocusing pulses" are required to reverse the evolution of unwanted phase shifts incurred by the always-on couplings. The complexity of such refocusing pulses grows with the size of the system. More discouraging, the refocusing pulses for a superconducting system would need to be at many orders of magnitude higher frequency than for NMR, and this may be impossible to achieve with the precision required, with today's technology.

So it is seen that switches between qubits are not absolutely essential for quantum computing, but they are likely to be a practical necessity for large-qubit systems.

4. INTERACTION FREE SUBSPACES

Recent work [2] has shown that logical qubits consisting of two or more physical qubits can be constructed to code quantum information in an "interaction free subspace" (IFS) such that there is no interaction between these qubits even though they are physically coupled. This is analogous to the more familiar "decoherence free subspace" (DFS), which can be employed to isolate quantum information from interacting with environmental modes that would lead to decoherence [16]. The DFS concept is widely utilized; it assumes that there are symmetries in the coupling of the qubits to their environment, and employs those symmetries to avoid decoherence. The IFS is different in that it relies on symmetries in the coupling between qubits, which can be created by the experimenter. Information is coded in such a way that when a logical qubit is in its IFS it is not affected by other qubits to which it is physically coupled (i.e., switch is open). Single-bit operations can be performed when the neighboring qubits are in their IFS. When two coupled logical qubits are removed from their IFS, two bit gates can be performed (i.e., switch is closed). Other logical qubits in their IFS are not affected by these operations.

IFS operations are discussed at length in Ref. [2]. Here we will merely present an example. We assume diagonal interactions between physical qubits of the form $J_{12}\sigma_1^z\sigma_2^z$. Our quantum computer is a one-dimensional Ising lattice of logical IFS qubits as illustrated in Fig. 3. For the Ising interaction it is sufficient to use two physical qubits, the dots labelled "a" and "b" in the figure, to compose the logical qubit, "qubit 1". The coupling between the physical qubits are either J_Q or J' as labelled. Then it is easy to see that the following basis states

$$|0\rangle = |\uparrow_a, \downarrow_b\rangle, |1\rangle = |\downarrow_a, \uparrow_b\rangle \tag{2}$$

are annihilated by the interaction Hamiltonian $H_{\text{int}} = J'(\sigma_{1a}^z + \sigma_{1b}^z)(\sigma_{2a}^z + \sigma_{2b}^z)$. Therefore, if these states are used to code quantum information, the logical qubits do not affect each other.

Arbitrary single-bit operations can be performed on logical qubit 1 using $\vec{B}_a(t)$ and $\vec{B}_b(t)$ with the fixed a–b coupling J_Q. Neighboring logical qubits must remain each in its IFS during the operations on qubit 1. Reference [2] details how a CNOT gate can be performed on qubit 1 and qubit 2. The CPHASE gate (equivalent to CNOT up to single-bit gates) is achieved by: first flip the state of both qubit $1b$ and qubit $2b$ to remove the logical qubits from IFS; then follow a set of prescribed rotations of the physical qubits and allow the logical qubits to interact for a certain amount of time; then again flip the state of both qubit $1b$ and qubit $2b$ to return the logical qubits back into IFS. The time required for this is $\pi/16J'$.

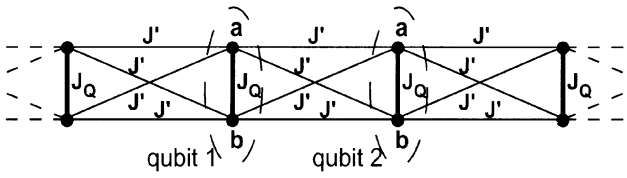
J'
a
J'
a
J'
J'
J'

The linear architecture shown in Fig. 3 is one of many possibilities, chosen for clarity of explanation alone. It is equally as possible to make a two-dimensional array. In the next section we will consider in detail a very different architecture in which all of the physical qubits are inductively fixed-coupled to a single large superconducting loop. Note that this prevents the use of parallel operations because only a few qubits can be out of their IFS at once. The linear array would allow great parallelism if two-thirds of all qubits are concurrently undergoing two-qubit gate operations. Between these two extremes is an architecture with qubit clusters coupled together by link qubits. It is seen that the IFS virtual switch encourages great versatility in quantum computer architecture. Eventually, one may hope that the computer architecture be designed for greatest suitability for classes of quantum algorithms to be addressed.

5. THE INDUCTOR BUS QUANTUM COMPUTER

Figure 3 seems to imply that close-coupled physical qubits should compose a logical qubit, and this logical qubit is coupled to only several other logical qubits. In fact, neither of these constraints is necessary. An architecture in which every physical qubit is coupled to every other physical qubit, with all equal coupling strength, satisfies the conditions for IFS as well. There are very natural implementations for this kind of quantum computer architecture using superconducting qubits. For instance, many superconductor charge qubits could be capacitively coupled to a single floating conductor island. We will examine the situation where many SQUID qubits are coupled each by a fixed mutual inductance to a single large solid superconducting loop—the "inductor bus".

The inductor bus quantum computer is illustrated in Fig. 4. N (an even number) identical rf-SQUIDS are inductively coupled to a superconducting inductor loop with self inductance L_b (b stands for "bus"). All couplings have the same mutual inductance M.

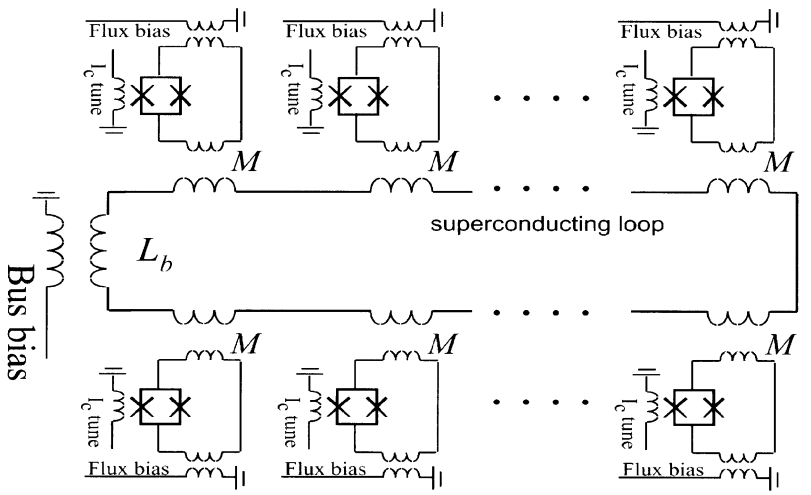

Figure 4. The "inductor bus" quantum computer.

The flux linking the bus inductor loop is Φ_b. Its external flux bias is Φ_{bx}. The current in the bus is I_b. All rf-SQUIDS have the same inductance L, the same capacitance C and the same Josephson energy E_J ($=I_c\Phi_0/2\pi$). The total flux, the flux bias, and the current of the ith ($i = 1, 2, \ldots, N$) rf-SQUID are Φ_i, Φ_{ix}, and I_i. Note that Φ_b, the total magnetic flux in the loop cannot change because it is a solid superconducting loop. So when the current in one of the rf-SQUIDS changes, the current in the loop must change slightly to maintain Φ_b. This couples to all of the other rf-SQUIDS.

5.1 The system Hamiltonian

We mentioned that the flux in the inductor loop must be quantized in units of the flux quantum $h/2e$: $\Phi_b = n\Phi_0$, n being any integer. For simplicity let us take $n = 0$ and $\Phi_{bx} = 0$. We can write down the flux equations for the rf-SQUIDS and the bus, taking into account all biases on the inductive loops:

$$\Phi_i = \Phi_{ix} + MI_b + LI_i, \quad i = 1, 2, \ldots, N \tag{3}$$

$$L_bI_b + \sum_{i=1}^{N} MI_i = 0 \tag{4}$$

These equations allow us to solve for the currents in terms of the fluxes, which can be used to calculate the inductive energy $E_{\text{ind}} = \frac{1}{2}\sum_{i=1}^{N} LI_i^2 + \frac{1}{2}L_bI_b^2 + \sum_{i=1}^{N} MI_bI_i$ of the system. We are interested in the limit of weak coupling

$$NM^2/LL_b \ll 1 \tag{5}$$

Keeping terms to the lowest order in M^2/LL_b, and adding the charging and Josephson energies of the rf-SQUIDS, we obtain the system Hamiltonian

$$H = \sum_{i=1}^{N} H_i + H_{\text{int}} \tag{6}$$

where H_i values are the self-Hamiltonians of the rf-SQUIDS (with the normalized self inductance),

$$H_i = -\frac{\hbar^2}{2C}\frac{\partial^2}{\partial\Phi_i^2} + \frac{(\Phi_i - \Phi_{ix})^2}{2L/(1 + (M^2/LL_b))} - E_J\cos\left(2\pi\frac{\Phi_i}{\Phi_0}\right) \tag{7}$$

and H_{int} is the interaction Hamiltonian between pairs of rf-SQUIDS,

$$H_{\text{int}} = \frac{M^2}{L_b}\sum_{i>j}^{N}\frac{(\Phi_i - \Phi_{ix})}{L}\frac{(\Phi_j - \Phi_{jx})}{L} \tag{8}$$

The summation in Eq. (8) is between each pair of rf-SQUIDS. Equation (8) describes the coupling between each pair of isolated rf-SQUIDS through an effective mutual inductance

$M_{\text{eff}} = M^2/L_b$. The other effect seen here is that the self inductance of the rf-SQUIDS is renormalized slightly:

$$L \to \frac{L}{(1 + (M^2/LL_b))} \tag{9}$$

Under low temperatures, if we bias the rf-SQUIDS appropriately they are effectively two-state systems. Then we can rewrite Eq. (6) using the Pauli matrices,

$$H = \sum_{i=1}^{N} \{-\hbar \Delta_i(I_i^C)\sigma_i^x + \varepsilon_i(\Phi_{ix})\sigma_i^z\} + \sum_{i>j}^{N} J\sigma_i^z\sigma_j^z \tag{10}$$

where Δ_i and ε_i are the tunneling matrix element and energy offset between the two potential wells of the ith rf-SQUID, controllable via its critical current I_i^C and flux bias Φ_{ix}. The eigenstates of σ^z correspond to the left and right well localized states. J is the always on and fixed coupling strength between the rf-SQUIDS proportional to the effective mutual inductance M^2/L_b.

5.2 Initialization and computation

This has been discussed in Ref. [2]. The first step is to flux bias all the rf-SQUIDS near to the symmetrical point $\Phi_0/2$, but far enough away to assure that they end up in the lower of their two flux localized states. Then raise the barrier height of the rf-SQUID potential such that there is no tunneling between the two flux states ($\Delta = 0$), and turn their flux bias to the symmetry point $\Phi_0/2$. The rf-SQUIDS are left in the left (or right) well. At the symmetry point $\varepsilon = 0$ as well, therefore the Hamiltonian of the qubits is 0, and the qubit state is frozen.

Two of the physical qubits are chosen to constitute a logical qubit. (The choice is arbitrary!) The next step is to flip the state of one of these physical qubits. This can be done by lowering its potential barrier to obtain a finite tunneling rate Δ and letting it evolve for $t = \pi/\hbar\Delta$ (a π pulse). The qubit will shift from the left well to the right well. The potential barrier is restored to freeze the state of the qubit. Now the two physical qubits are in the IFS ($|\uparrow\downarrow\rangle$ and $|\downarrow\uparrow\rangle$) and the logical qubit is decoupled from the bus. In their IFS, the two physical qubits apply a 0 net flux on the bus. The other qubits are still in their left wells and they do apply a flux to the bus. Then, all of the other qubits are treated the same way until all logical qubits are driven into the IFS.

The large superconducting loop may start with flux in it, $n \neq 0$. Even if $n = 0$, during the initialization there is a large current in the loop and some current $I_b \neq 0$ will remain because of inevitable variations in SQUID parameters. These currents have no effect on the IFS code states. Still, one is uncomfortable that, for large N, small unforseen errors might compound. If this is a concern, it is possible to keep $I_b = 0$ by changing the bus flux bias Φ_{bx} a little. Another possibility is to break the solid superconducting loop by a very small series resistor, sub-$\mu\Omega$, such that L_b/R is comparable to the initialization time but much longer than the run time of the quantum computer.

The computation proceeds through a series of single physical qubit operations that induce rotations around the x and z directions of each physical qubit. These operations are realized by changing the tunneling rate Δ and the energy offset ε of the rf-SQUIDS

(cf. Eq. (10) and Fig. 1(a)). Then a computation of any complexity can be performed using the logical qubits in and out of the IFS, accessing only these single physical qubit operations, as prescribed in Ref. [2].

5.3 Parameters

Finally let us specify the parameters required for the inductor bus quantum computer in Fig. 4. We will see that the computer may include a large number of qubits, at least $N \sim 1000$, for realistic parameters allowed by the current technology, assuming as always ideal qubits.

The relevant parameters for a single rf-SQUID are L, I_c, and C. We choose $L = 150\,\text{pH}$, $C = 80\,\text{fF}$, and $I_c = 3\,\mu\text{A}$. These are familiar numbers, very similar to the values considered in Ref. [17]. Solving the Schrödinger equation numerically, we find when the critical current is unsuppressed, the tunneling matrix element Δ is about 30 Hz, therefore the tunneling can be considered completely off in this case. Suppressing I_c down to 2.375 μA gives a tunneling matrix element $\Delta \approx 2.6\,\text{GHz}$, which allows to flip the state of the rf-SQUID (a π pulse in the x direction) in about 0.4 ns. Flux biasing the rf-SQUID off the symmetrical point $\Phi_0/2$ by $0.15\,\text{m}\Phi_0$ gives an ε of about 2.7 GHz. This allows rotations around the z direction with a speed of a few GHz.

The two-bit operation speed is determined by the strength of qubit coupling, J. The single physical bit operations should be much faster than the two-bit operations. Referring to Eq. (10), this means that Δ and ε (when they are on) should be much larger than J (which is always on). We choose the two-bit operation time to be tens of ns. Evaluating the interaction Hamiltonian Eq. (8) in the qubit bases, we find that an effective mutual inductance (M^2/L_b) of about 2 fH results in a coupling strength J of about 25 MHz. This is comfortably satisfied with $L_b = 2\,\text{nH}$ and $M = 2\,\text{pH}$. This is satisfactory because $M \ll L$ and $M \ll L_b$, so $M^2/LL_b \ll 1$.

How many qubits N can be attached to the bus? First of all, the weak coupling limit (Eq. (5)) requires

$$N \ll \frac{LL_b}{M^2} \tag{11}$$

The other practical consideration is $N < L_b/M$, just by a simple geometrical argument. We assume a planar circuit geometry where all inductors are realized by single-turn thin-film conductors lithographed over a ground plane [17]. Then the inductance per unit length of conductor will be roughly the same for all inductors, and $M \sim kL_{bi}$, where L_{bi} is the section of L_b coupled to the ith rf-SQUID, and k is the coupling constant, necessarily less than 1. Clearly, the maximum $N = L_b/L_{bi} \sim kL_b/M$, as stated above. For $L_b = 2\,\text{nH}$ and $M = 2\,\text{pH}$, $N_{\max} = 1000$, which satisfies the weak coupling limit of Eq. (11). N in the inductor bus quantum computer can be made larger than 1000 only by the undesirable recourse of decreasing the coupling strength and the speed of two-bit operations.

6. CONCLUSIONS

We give a prescription for a large-scale $N \sim 1000$ superconducting quantum computer. It is based on the idea of "interaction free subspace" presented in Ref. [2].

Solving the "no switch" problem without the need to use a physical switch, it will help in the effort to construct a practical superconducting quantum computer.

REFERENCES

[1] D. P. DiVincenzo, The physical implementation of quantum computation, *Fortschritte der Physik* **48**, 771 (2000).

[2] X. Zhou, Z.-W. Zhou, G.-C. Guo, and M. J. Feldman, Quantum computation with untunable couplings, accepted for publication in *Phys. Rev. Lett.* (2002).

[3] M. F. Bocko, A. M. Herr, and M. J. Feldman, Prospects for quantum coherent computation using superconducting electronics, *IEEE Trans. Appl. Supercond.* **7**, 3638 (1997).

[4] J. R. Friedman, V. Patel, W. Chen, S. K. Tolpygo, and J. E. Lukens, Quantum superposition of distinct macroscopic states, *Nature* **406**, 43 (2000).

[5] C. H. van der Wal, A. C. J. ter Haar, F. K. Wilhelm, R. N. Schouten, C. J. P. M. Harmans, T. P. Orlando, S. Lloyd, and J. E. Mooij, Quantum superposition of macroscopic persistent-current states, *Science* **290**, 773 (2000).

[6] Y. Nakamura, Y. A. Pashkin, and J. S. Tsai, Coherent control of macroscopic quantum states in a single-Cooper-pair box, *Nature* **398**, 786 (1999).

[7] D. Vion, A. Aassime, A. Cottet, P. Joyez, H. Pothier, C. Urbina, D. Esteve, and M. H. Devoret, Manipulating the quantum state of an electrical circuit, *Science* **296**, 886 (2002).

[8] Y. Makhlin, G. Schön, and A. Shnirman, Quantum-state engineering with Josephson junction devices, *Rev. Mod. Phys.* **73**, 357 (2001).

[9] D. V. Averin, Adiabatic quantum computation with Cooper pairs, *Solid State Commun.* **105**, 659 (1998).

[10] Y. Makhlin, A. Shnirman, and G. Schön, Josephson junction qubits with controlled couplings, *Nature* **386**, 305 (1999).

[11] J. E. Mooij, T. P. Orlando, L. S. Levitov, L. Tian, Caspar, H. van der Wal, and S. Lloyd, Josephson persistent-current qubit, *Science* **285**, 1036 (1999).

[12] T. V. Filippov, J. Mannik, S. K. Tolpygo, and J. E. Lukens, Tunable transformer for qubits based on flux states, manuscript submitted to *IEEE Trans. Appl. Supercond.* (2002).

[13] K. K. Likharev, unpublished presentation.

[14] T. L. Robertson, B. L. T. Plourde, A. García-Martínez, P. A. Reichardt, B. Chesca, R. Kleiner, Y. Makhlin, G. Schön, A. Shnirman, F. K. Wilhelm, D. J. Van Harlingen, and J. Clarke, Superconducting device to isolate, enlarge, and read out quantum flux states, preprint.

[15] S. Lloyd, A potentially realizable quantum computer, *Science* **261**, 1569 (1993).

[16] L.-M. Duan and G.-C. Guo, Preserving coherence in quantum computation by pairing quantum bits, *Phys. Rev. Lett.* **79**, 1953 (1997). P. Zanardi and M. Rasetti, Noiseless quantum codes, *Phys. Rev. Lett.* **79**, 3306 (1997). D. A. Lidar, I. L. Chuang, and K. B. Whaley, Decoherence-free subspaces for quantum computation, *Phys. Rev. Lett.* **81**, 2594 (1998).

[17] M. J. Feldman and M. F. Bocko, A realistic experiment to demonstrate macroscopic quantum coherence, *Physica C* **350**, 171 (2001).

SCALABLE ARCHITECTURE FOR ADIABATIC QUANTUM COMPUTING OF NP-HARD PROBLEMS

W. M. Kaminsky[a] and S. Lloyd
Massachusetts Institute of Technology, Cambridge, MA 02139, USA

Abstract: We present a comprehensive review of past research into adiabatic quantum computation and then propose a scalable architecture for an adiabatic quantum computer that can treat NP-hard problems without requiring local coherent operations. Instead, computation can be performed entirely by adiabatically varying a magnetic field applied to all the qubits simultaneously. Local (incoherent) operations are needed only for: (1) switching on or off certain pairwise, nearest-neighbor inductive couplings in order to set the problem to be solved; and (2) measuring some subset of the qubits in order to obtain the answer to the problem.

Keywords: Quantum computing, Combinatorial optimization, Adiabatic, Scalable implementation, NP

1. INTRODUCTION

Adiabatic quantum computation [1] is a recently proposed, general approach to solving NP-hard combinatorial minimization problems [2]. It consists of constructing a set of qubits with a time-dependent Hamiltonian $\hat{H}(t)$ whose starting point $\hat{H}_s$ has a ground state that is quickly reachable simply by cooling and whose final point $\hat{H}_p$ has couplings that encode the cost scheme of a desired minimization problem. The name "adiabatic" comes from the fact that if the qubits are initialized in the ground state of $\hat{H}_s$ and if $\hat{H}(t)$ is varied slowly enough, then the qubits will overwhelmingly be in the ground state of $\hat{H}(t)$ at all times t, thus in principle completely bypassing the usual concern about local minima in $\hat{H}_p$ confounding the search for the problem's solution.

Sections 2 and 3 review the literature to date on adiabatic quantum computation. Section 4 presents the main result of this paper: a scalable architecture for an adiabatic quantum computer. Section 5 concludes.

[a]E-mail: wmk@mit.edu

2. LITERATURE REVIEW: THE TIME COMPLEXITY OF ADIABATIC QUANTUM COMPUTATION

The general time complexity of adiabatic quantum computation is still an open problem. Intuitively, the key to fast, successful adiabatic computation is to ensure that $\hat{H}(t)$ always possesses a sizable spectral gap between its instantaneous ground and excited states, thus allowing one to vary $\hat{H}(t)$ quickly while still not ever providing enough energy to excite the system significantly out of its instantaneous ground state. Determining the asymptotic time complexity of adiabatic quantum computation remains an open problem because for n qubits, $\hat{H}(t)$ is a $2^n \times 2^n$ matrix, and hence analytically obtaining lower bounds on the spectral gap is extremely difficult unless $\hat{H}(t)$ possesses significant symmetry.

Presently, there are three major results on the time complexity of adiabatic quantum computation. Together, they yield the general picture that for essentially unstructured NP-hard minimization problems like finding the ground state of a random-field magnet, adiabatic quantum computing should offer polynomial speedups—probably in the range of cube-root to sixth-root—over a Metropolis algorithm (simple cooling) approach to the same problems. Furthermore, for structured NP-hard minimization problems such as 3-SAT and MAX CLIQUE, adiabatic quantum computation can quite possibly offer exponential speedups over any classical algorithm (assuming $P \neq NP$)—at least on average.

More specifically, the first major time-complexity result is that adiabatic quantum computation can search an unsorted list of N items for a single identifiable item in $O(\sqrt{N})$ time [3], thus matching the speedup of Grover's algorithm [4]. This, however, is a naïve way of characterizing the performance of adiabatic quantum computation on unstructured searches because an nth-root speedup still means that the minimum spectral gap in $\hat{H}(t)$ is exponentially shrinking, and practically one always needs to operate above some finite temperature limit.

It is therefore much more realistic when analyzing unstructured problems to abandon the idea that the system can always remain overwhelmingly in the instantaneous ground state of $\hat{H}(t)$ and instead view adiabatic quantum computing as an enhanced form of annealing. The potential for enhancement intuitively derives from two facts. First, quantum systems can tunnel through energy barriers instead of waiting for thermal excitation over them. Second, with a time-dependent Hamiltonian $\hat{H}(t)$, one need not face the same barriers as those in energy landscape $\hat{H}_p$ of one's problem.

For example, consider an Ising model of the form

$$\hat{H}_p = \sum_{i,j} J_{ij} \hat{\sigma}_z^{(i)} \hat{\sigma}_z^{(j)} \tag{1}$$

where the couplings $\{J_{ij}\}$ are randomly drawn with a zero-mean Gaussian distribution from the interval $[-1, 1]$. If the Ising model cannot be drawn as a planar graph (with spins as vertices and nonzero couplings as edges), then finding the ground state of $\hat{H}_p$ is an NP-hard problem [5]. Quite general considerations of the distribution of low-lying excitations of any frustrated system such as that of Eq. (1) imply that simply cooling the system from $T = \infty$ to $T = 0$ in a time τ (physically, "∞" means "sufficiently high to make all possible states essentially equiprobable") leaves an average residual energy

$$\langle E(\tau) \rangle - E_{\text{ground}} \sim \ln(\tau)^{-\xi} \quad (\xi \leq 2) \tag{2}$$

in the limit of large τ [6]. Monte Carlo simulations imply that ξ can be as low as 1 for cooling to the ground states of some NP-hard random-field Ising models [7]. In contrast, if instead one applies a transverse magnetic field to the system that decreases from $H = \infty$ to $H = 0$ in time τ (all done at $T = 0$), then according to a model [8] that calculates the residual energy as the cumulative result of Landau–Zener type transitions [9] at the avoided level crossings between the instantaneous ground state and first excited states of the resulting time-dependent Hamiltonian

$$\hat{H}(t) = \hat{H}_p + \Gamma(t) \sum_i \hat{\sigma}_x^{(i)} \quad (\Gamma(0) = \infty, \Gamma(\tau) = 0) \tag{3}$$

one finds much improved performance

$$\langle E(\tau) \rangle - E_{\text{ground}} \sim \ln(\tau)^{\xi_{\text{QU}}} \quad (\xi_{\text{QU}} \approx 6) \tag{4}$$

The greater size of the exponent ξ_{QU} in Eq. (4) over the exponent ξ in Eq. (2) is the basis of the second major time-complexity result—adiabatic quantum computation on a given unstructured NP problem should at least provide cube-root and perhaps as much as sixth-root speedups over a Metropolis algorithm (simple cooling) approach to the same problem.

The third, and perhaps most interesting, time-complexity result—the possibility of exponential speedup on almost all difficult instances of NP-hard problems—comes from explicit numerical integrations of Schrödinger's equation to simulate adiabatic computation on sets of small instances of these problems ($\leq$26 bits is roughly the limit of current supercomputers). Since the class NP is a worst-case complexity measure, it is important to consider problem instances that are most likely to be truly difficult. For example, Hogg [10] studied random 3-SAT, which is the problem of finding a string of n bits that completely satisfies m Boolean clauses, each of the form a OR b OR c where

1. The literals a, b, and c refer to three distinct bits chosen uniformly at random;
2. Each literal, with 50% probability, contains a negation.

In the limit of large n, random 3-SAT instances exhibit a first-order phase transition from being highly likely to have a satisfying assignment when $m/n < 4.25$ to being highly unlikely to have a satisfying assignment when $m/n > 4.25$, and it has been observed that the most difficult instances to solve appear to fall on the phase boundary [11]. Hogg studied instances generated as near as possible to this phase boundary $m/n = 4.25$ and found that for $n \leq 26$ bits (the largest number that could be numerically analyzed) the median run time scaled only as $O(n^3)$.

Random 3-SAT instances at the phase boundary still tend to have exponentially many satisfying solutions which, although they constitute an exponentially small fraction of the 2^n possible bit strings, one might worry constitute enough degeneracy to distort study of such small instances of $\leq$26 bits. Hence, the earlier studies of Farhi *et al.* [1] and Childs *et al.* [12] focused on randomly generating NP-complete problem instances with unique satisfying assignments ("USA instances") rather than some ratio of constraints to bits. Median run times scaling only as $O(n^2)$ were observed for both USA instances of random EXACT COVER up to 20 bits [1] and random MAX CLIQUE up to 18 bits [12]. (Random EXACT COVER is the problem of finding a string of n bits that satisfies m clauses of the form $a + b + c = 1$ where the literals a, b, c are distinct bits chosen uniformly at random. Random MAX CLIQUE is the problem of finding the largest subgraph for which every

pair of points is connected by an edge within an n-vertex graph constructed such that each pair of vertices is connected by an edge with 50% probability.)

The above MAX CLIQUE result may be seen to carry extra significance because it is widely conjectured there does not exist any classical polynomial-time algorithm that can identify cliques in such n-vertex random graphs of size $>(1+\varepsilon)\log_2(n)$ for any $\varepsilon > 0$. In contrast, the maximum clique of an n-vertex random graph is almost always $>\log_2(n)$ and on average is $2\log_2(n)$. This discrepancy is in fact used as the basis for a cryptographic scheme [13].

3. LITERATURE REVIEW: ROBUSTNESS OF ADIABATIC QUANTUM COMPUTATION VERSUS DECOHERENCE

Beyond the potential for significant speedups over classical computing, which is an attraction that adiabatic quantum computing shares with other proposed methods of quantum computing, adiabatic quantum computing is especially attractive for being intrinsically robust against environmental noise [14]. First, since an adiabatic algorithm aims to keep its qubits in the instantaneous ground state of the computational Hamiltonian $\hat{H}(t)$, dissipation is not intrinsically harmful, but potentially helpful. (Of course, one cannot depend wholly on dissipation because then classical thermal annealing could have solved the problem with equal efficiency.) Secondly, if indeed the spectral gap of $\hat{H}(t)$ is large enough so that the system can be kept overwhelmingly in just one energy eigenstate (namely, the ground state), then the dephasing problem can be essentially circumvented. This is because so long as $\hat{H}(t)$ dominates over the environmental couplings to the qubits, the energy eigenstates of $\hat{H}(t)$ will be the preferred basis for dephasing, meaning that an adiabatic quantum computer based on $\hat{H}(t)$ would never present the environment with a superposition of states that it could dephase.

Such dominance is easy to achieve in the canonical spin-boson model with an Ohmic environment having an exponential cut-off after a frequency ω_c [15]. That is, if Δ_o denotes the bare energy splitting in the qubits due to coherent tunnelling between their limiting, classical states in the absence of coupling to the environment and α represents the (dimensionless) slope of the environmental spectral density at $\omega = 0$, then one can conclude nonperturbatively that the environmentally corrected tunnel splitting Δ is

$$\begin{aligned}\Delta &= \Delta_o\left(\frac{\Delta_o}{\omega_c}\right)^{\alpha/(1-\alpha)} \\ &= \Delta_o\left[1 - \alpha\ln\left(\frac{\omega_c}{\Delta_o}\right) + O(\alpha^2)\right]\end{aligned} \tag{5}$$

Hence, if $\alpha \ll 1$ and ω_c is only a few orders of magnitude above Δ_o, then $\Delta \approx \Delta_o$ meaning that the qubits' Hamiltonian does indeed dominate over the environmental couplings and its energy eigenbasis is the preferred basis for dephasing.

This desirable situation should not be changed by the addition of $1/f$ or other low-frequency-dominated noise to the Ohmic environment. Components in the environmental spectral density that are of much lower frequency than the bare tunnel splitting Δ_o denote environmental dynamics that are much slower than that of the qubits. Therefore,

essentially regardless of the qubit-environment coupling, these components can only become entangled to time-averaged properties of the qubits such as their energy [16]. While low-frequency components could thus significantly change dephasing rates, they should not change the fact that the environment respects the energy eigenbasis of the qubits' Hamiltonian as the preferred basis for dephasing, meaning that adiabatic algorithms would still essentially circumvent the dephasing problem.

4. MAIN RESULT: A SCALABLE ARCHITECTURE FOR ADIABATIC QUANTUM COMPUTING

Another special advantage of adiabatic quantum computing is the main point of this paper: there exists a simple, scalable architecture for adiabatic quantum computation that can handle NP-hard problems without requiring local coherent manipulations of the qubits. The starting point for the architecture is the fact that it is NP-hard to calculate the ground state of a two-dimensional antiferromagnetically coupled Ising model placed in a magnetic field even if each Ising spin is coupled to no more than three others [5]. In other words, if $G = (V, E)$ is a planar graph with vertices V and edges E and even if every vertex in V belongs to ≤ 3 edges in E, then it is NP-hard to find the ground state of

$$\hat{H} = \sum_{i \in V} \hat{\sigma}_z^{(i)} + \sum_{(i,j) \in E} \hat{\sigma}_z^{(i)} \hat{\sigma}_z^{(j)} \tag{6}$$

which is an Ising model with spins at the vertices V, equal strength antiferromagnetic couplings along the edges E, and a homogeneously applied field giving each spin a Zeeman splitting equal to the antiferromagnetic coupling strength. (The direction of this applied field sets the "z-axis.")

This proof of NP-hardness isomorphically maps the above Ising model onto the MAX INDEPENDENT SET problem, which is the problem of finding for a graph $G = (V, E)$ the largest subset S of the vertices V such that no two members of S are joined by an edge from E. Solving MAX INDEPENDENT SET for a given graph $G = (V, E)$ is completely equivalent to solving MAX CLIQUE for the graph's complement $G^c \equiv (V, (V \times V)/E)$. (In other words, G^c connects with edges all the pairs of vertices that were unconnected in G and disconnects all the pairs that were connected.) Therefore, the MAX CLIQUE results [12, 13] referenced above imply that MAX INDEPENDENT SET is an equally interesting problem for treatment by adiabatic quantum computation, likely admitting not even a rough approximation in polynomial time classically, yet apparently admitting efficient solution by quantum adiabatic evolution—at least in small instances (and thus, hopefully, for almost all, if not all, larger instances).

There exists a simple, regular architecture that can be programmed to pose the above NP-hard Ising model ground state problem for any instance with $\leq n$ spins. One way to see this is to recall that any planar graph G with ≤ 3 edges per vertex admits a topologically equivalent embedding Q in a square grid of $\leq 9n^2$ vertices [17]. In other words, there exists a map Q that (1) maps each vertex v of G onto a distinct point $Q(v)$ of the grid and (2) inserts "dummy vertices" so as to map an edge $\mathbf{e}$ connecting vertices u and v of G into a path $Q(\mathbf{e})$ on the square grid such that $Q(u)$ and $Q(v)$ are its endpoints and such that if $\mathbf{e}$ and $\mathbf{f}$ are two distinct edges of G, then $Q(\mathbf{e})$ and $Q(\mathbf{f})$ do not intersect

(except, obviously, if **e** and **f** share an endpoint, in which case $Q(\mathbf{e})$ and $Q(\mathbf{f})$ will also share an endpoint).

Thus, one simple, regular architecture would be of the type depicted below in Fig. 1: two stacked square grids of ferromagnetic and antiferromagnetic couplings, respectively, having at the center of each square a qubit with a ferromagnetic coupling to, say, the inductive couplings meeting at the lower right corner of the square. Since a useful adiabatic scheme would be one like Eq. (3), which merely adds a homogeneous, steadily decreasing transverse magnetic field to the problem Hamiltonian, the coherent evolution of the qubits could be affected simply with a globally applied magnetic field. This avoids the need both for any local coherent manipulations as well as for *tunable* rather than merely *switchable* couplings. Furthermore, as the the switching of the couplings is necessary only for programming the desired instance to be solved, it can be done "offline," *before* any coherent manipulation of the qubits begins, thus obviating the need for "quiet" switches.

A final consideration for scalability is to calculate how much imprecision can exist in the parameters of the qubits, the couplings, and the applied field before one loses the ability to encode reliably in the above architecture any desired n-bit instance of MAX INDEPENDENT SET. To answer this, first recall that Ref. [5] proved that the maximum independent sets of a graph $G = (V, E)$ are in one-to-one correspondence with the ground state(s) of the Hamiltonian in Eq. (6), that is, an Ising model with spins at the vertices V, antiferromagnetic couplings all of equal strength along the edges E, and a homogeneous applied magnetic field giving every spin a Zeeman splitting equal to the antiferromagnetic coupling strength. However, so long as one is satisfied with obtaining any one of the maximum independent sets of G (which is reasonable since obtaining any one is

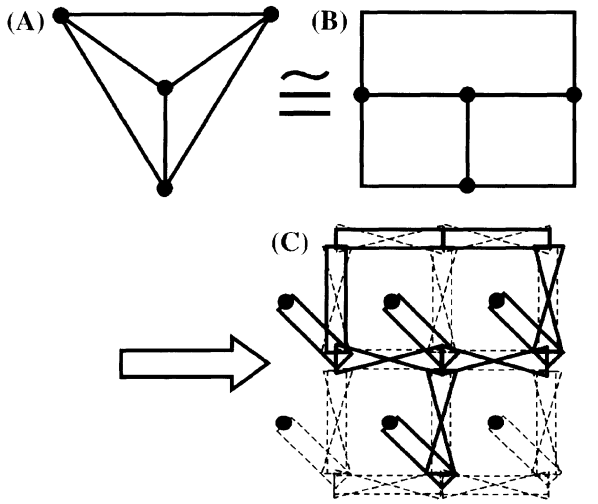

Figure 1. (A) A regular four-vertex graph for an Ising model. Vertices denote location of qubits, and edges denote antiferromagnetic couplings. (B) Topologically equivalent square grid embedding. (C) Possible implementation. Boldface lines denote couplings switched on, dashed lines denote couplings switched off.

NP-hard), one does not need to calibrate so precisely the couplings among themselves and to the applied field because the ground state(s) of any Ising model from the family

$$\hat{H} = \sum_{i \in V} J_i \hat{\sigma}_z^{(i)} + \sum_{(i,j) \in E} J_i J_j \hat{\sigma}_z^{(i)} \hat{\sigma}_z^{(j)} \tag{7}$$

where $\{J_i\}$ are *arbitrary* positive scalars that will also be ground state(s) of the Eq. (6) Ising model and hence maximum independent set(s) of G. Hence, in regard to programming the computer so that its final ground state has a large overlap with at least one solution of a desired instance of MAX INDEPENDENT SET, the proposed architecture is robust against *arbitrary* variance in the magnetic moments of the qubits. (Note, however, that while variance in $\{J_i\}$ poses no problem in programming the computer, it might still cause a problem in ensuring that the computer produces accurate solutions quickly. Specifically, as the variance becomes larger, the problem Hamiltonian (7) looks more and more like random field magnet than a "structured" NP problem, likely lessening the chances that the adiabatic scheme $\hat{H}(t)$ will keep a large spectral gap and thus permit a running time exponentially faster than any classical algorithm.)

More general errors can come from inhomogeneities in both the magnitude and the direction of the applied magnetic field and from inductive couplings beyond the desired ones between nearest neighbors. Thus, to Eq. (7) one can add the general perturbation

$$\hat{H}' = \sum_{k \in \{x,y,z\}} \sum_{i \in V} \varepsilon_k^{(i)} \hat{\sigma}_k^{(i)} + \sum_{k,l \in \{x,y,z\}} \sum_{i>j} \delta_{kl}^{(ij)} \hat{\sigma}_k^{(i)} \hat{\sigma}_l^{(j)} \tag{8}$$

Note that Pauli operator terms such as $\hat{\sigma}_k^{(i)}$ or $\hat{\sigma}_k^{(i)} \hat{\sigma}_i^{(j)}$ merely prescribe bit and/or phase flips in the eigenbasis of the Eq. (7) problem Hamiltonian, meaning that each of the perturbing terms in $\hat{H}'$ couples an unperturbed ground state to only one other unperturbed eigenstate. Therefore, if n denotes the number of qubits, λ denotes the largest of the scalars $\{\varepsilon_k^{(i)}, \delta_{kl}^{(ij)}\}$ in Eq. (8), and Δ denotes the minimum increase in energy caused by flipping 1 or 2 qubits of the ground state (thus, $\Delta \approx \min_i[2J_i]$), then $\lambda n^2/\Delta$ serves as a simple upper bound on the magnitude of the first-order correction to the ground state wavefunction. Higher order corrections should be well behaved since performing one or two bit flips on any excited state also typically entails an energy change of at least Δ, implying that the entire perturbation series correction should essentially converge like the geometric series $\sum_k (\lambda n^2/\Delta)^k$. Hence, the architecture's tolerance for general imprecision in the qubit couplings and inhomogeneity in the applied field decreases quadratically in the number of qubits. (If unwanted inductive couplings can be limited to a constant number of "next-nearest" neighbors, then the tolerance shall decrease only linearly.)

5. CONCLUSION

We have reviewed the theory of adiabatic quantum computation regarding its potential speedup over classical computation and its greater robustness toward noise over other forms of quantum computation. We then proposed a scalable architecture for adiabatic quantum computation based on the NP-hardness of calculating the ground state of a planar antiferromagnetically coupled Ising model placed in a magnetic field. Clearly,

such an architecture could be used with any qubit whose states have opposite magnetic dipole moments. Future work will present a detailed proposal for its implementation using superconducting persistent-current qubits [18], which constitute a current, promising approach to lithographable solid-state qubits.

Acknowledgements

This work is supported in part by ARDA and DoD under the AFOSR DURINT Program. WMK gratefully acknowledges fellowship support from the Fannie and John Hertz Foundation.

REFERENCES

[1] E. Farhi *et al.*, A quantum adiabatic algorithm applied to random instances of an NP-complete problem, *Science* **292**, 472–476 (2001).
[2] M. G. Garey and D. S. Johnson, *Computers and Intractability* (W.H. Freeman and Company, New York, 1979).
[3] J. Roland and N. J. Cerf, Quantum search by local adiabatic evolution, http://xxx.lanl.gov/abs/quant-ph/0107015 (2001).
[4] L. K. Grover, Quantum mechanics helps in searching for a needle in a haystack, *Phys. Rev. Lett.* **79**(2), 325–328 (1997).
[5] F. Barahona, On the computational complexity of Ising spin glass models, *J. Phys.* A **15**, 3241 (1982).
[6] D. A. Huse and D. S. Fisher, Residual energies after slow cooling of disordered systems, *Phys. Rev. Lett.* **57**(17), 2203–2206 (1986).
[7] G. S. Grest, C. M. Soukoulis, and K. Levin, Cooling-rate dependence for the spin-glass ground-state energy: implications for optimization by simulated annealing, *Phys. Rev. Lett.* **56**(11), 1148 (1986).
[8] G. E. Santoro, R. Martoňák, E. Tosatti, and R. Car, Theory of quantum annealing of an Ising spin glass, *Science* **295**, 2427–2430 (2002).
[9] L. D. Landau and E. M. Lifschitz, *Quantum Mechanics*, 3rd rev. ed. (Oxford, Butterworth-Heineman, 1977), Sec. 53.
[10] T. Hogg, Adiabatic quantum computing for random satisfiability problems, http://xxx.lanl.gov/abs/quant-ph/0206059 (2002).
[11] R. Monasson *et al.*, Determining computational complexity from characteristic 'phase transitions', *Nature* **400**, 133–137 (1999).
[12] A. M. Childs, E. Farhi, J. Goldstone, and S. Gutmann, Finding cliques by quantum adiabatic evolution, *Quant. Info. Comp.* **2**(3), 181–191 (2002).
[13] A. Juels and M. Peinado, Hiding cliques for cryptographic security, *Proc. 9th Annual ACM-SIAM SODA*, 678–684 (1998).
[14] A. M. Childs, E. Farhi, and J. Preskill, Robustness of adiabatic quantum computation, *Phys. Rev.* A **65**, 012322 (2002).
[15] A. J. Leggett *et al.*, Dynamics of the dissipative two-state system, *Rev. Mod. Phys.* **59**, 1–85 (1987).
[16] J. P. Paz and W. H. Zurek, Quantum limit of decoherence: Environment induced superselection of energy eigenstates, *Phys. Rev. Lett.* **82**(26), 5181–5185 (1999).
[17] L. G. Valiant, Universality considerations in VLSI circuits, *IEEE Trans. Comput.* **C30**(2), 135–140 (1981).
[18] J. E. Mooij *et al.*, Josephson persistent-current qubit, *Science* **285**, 1036–1039 (1999).

SEMICLASSICAL ANALYSIS OF $1/f$ NOISE IN JOSEPHSON QUBITS

E. Paladino[1], L. Faoro[2], A. D'Arrigo[3], and G. Falci[4]
[1]*NEST-INFM & Dipartimento di Metodologie Fisiche e Chimiche (DMFCI), Università di Catania, Viale A. Doria 6, 95125 Catania, Italy*
[2]*Institute for Scientific Interchange (ISI), Viale Settimo Severo 65, 10133 Torino, Italy & Istituto Nazionale di Fisica della Materia (INFM), Unità del Politecnico di Torino, Italy*
[3]*DMFCI, Università di Catania, Italy*
[4]*DMFCI, Università di Catania & INFM, Unità di Catania, Italy*

1. INTRODUCTION

Recent progress in the development of nanoscale electronic devices has enhanced the interest in the problem of $1/f$ noise. Numerous experiments have shown that the performance of single electron tunneling (SET) devices strongly suffer from offset charge fluctuations responsible for the observed $1/f$ charge noise [1]. Moreover it has been realized that such a noise plays a significant role in determining decoherence of solid-state implementations of qubits [1–7].

A high degree of quantum coherence represents one of the most crucial requirements for the implementation of quantum logic devices. Solid-state nanodevices are studied as possible implementations of a quantum computer [4] because of advantages that may come from their tunability and integrability. Recently, quantum coherent behavior has been detected in superconducting nanocircuits [3, 8]. On the other hand decoherence represents a serious limitation [9] due to the presence of low-energy excitations in the solid-state environment. Sources of decoherence in Josephson nanocircuits are electromagnetic fluctuations of the surrounding circuit, quasiparticle tunneling, fluctuating background charges (BC), and flux noise [4, 10].

In this contribution we perform a semiclassical analysis of decoherence in Josephson qubits originated from a discrete environment which we model as an ensemble of random telegraph fluctuators. Such a description applies to fluctuating charged impurities, which are responsible for the $1/f$ noise in SET devices, and are believed to represent the most serious limitation for Josephson charge qubits. Along the same lines, an analysis for the flux qubit interacting with trapped vortices can be performed. Other similar mechanisms of decoherence, such as the parametric effect of $1/f$ noise on the coupling energy of a Josephson junction [11], can be treated within our model (or at most would require a slight

Quantum Computing and Quantum Bits in Mesoscopic Systems
Edited by Leggett *et al.*, Kluwer Academic/Plenum Publishers, 2004

generalization), which specifically accounts for the discreteness of the random processes originated by the above noise sources.

The approach we present is corroborated by a more general fully quantum treatment of a discrete environment originating $1/f$ noise [6]. In Ref. [6] decoherence *during* the time evolution of the qubit has been investigated. The discrete nature of the environment leads to a number of peculiar features, like saturation effects and dependence on initial conditions. Within the semiclassical approach, we present here a detailed analysis of the loss of coherence in the qubit dynamics both during the time evolution (relevant for single-shot measurements) and in repeated measurements. We find that decoherence in operations of different kinds is determined by different physics aspects displayed by the discrete environment.

2. JOSEPHSON QUBIT AND PHASE ERRORS

A charge Josephson qubit in the presence of classical electrostatic noise sources is generally described by the following Hamiltonian

$$H = \frac{\delta E_C}{2}\sigma_z - \frac{E_J}{2}\sigma_x + E(t)\sigma_z \tag{1}$$

where the first two terms represent a Cooper-pair box [4, 12] operating in the regime $E_C \gg E_J \gg K_B T$. The charge basis $|0\rangle$, $|1\rangle$ is represented by the eigenstates of σ_z, with tunable splitting $\delta E_C(V_x) = E_C(1 - C_x V_x/e)$. The electrostatic coupling $E(t)\sigma_z$ generally describes fluctuations of the polarization of the superconducting island due to an environment. Thus $E(t)$ is a stochastic process, whose characteristics depend on its physical origin. For instance fluctuations of the electromagnetic environment (the circuit) determine a Gaussian noise, whereas a single coupled bistable fluctuator generates a random telegraph (RT) process. In a fully quantum description, decoherence stems from the entanglement between the qubit and the environment. The semiclassical approach is unable to capture this physics; rather "decoherence" is identified with the decay of the signal blurred by the external random source. This induces two kinds of errors, namely flips (unwanted transitions between the two states of the qubit) and "phase errors", that is, loss of coherence in the superposition of states.

The latter mechanism represents the most serious limitation to the observation of coherent dynamics of the qubit. In order to focus on this effect we study the qubit dynamics in the regime $E_J = 0$. In this case $[H, \sigma_z] = 0$; thus the charge on the qubit island is conserved, whereas superpositions of charge states dephase. Correspondingly the off-diagonal elements of the density matrix of the qubit in the charge basis, averaged over the possible realizations of the stochastic process $E(t)$ decay in time:

$$\frac{\langle \rho_{10}(t)\rangle}{\rho_{10}(0)} \equiv \left\langle \exp\left[-i\int_0^t dt' E(t')\right]\right\rangle = e^{-i\delta E_C t} e^{-\Gamma(t)+i\varepsilon(t)} \tag{2}$$

Equation (2) defines the decay function $\Gamma(t)$ to which we are mainly interested. For a generic random process the evaluation of the average in Eq. (2) requires the knowledge of all the cumulants of the stochastic process $E(t)$. A remarkable case is that of Gaussian processes, which are completely defined by the second cumulant $\langle E(t)E(t')\rangle_c$. In this work

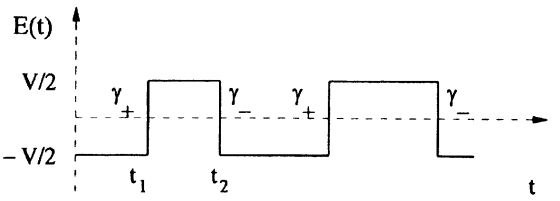

Figure 1. RT fluctuator switching between $\pm v/2$ with rates $\gamma_{\pm}$.

we will focus on processes $E(t) = \sum_i E^i(t)$, where $E^i(t)$ are random telegraph processes. In this latter case information beyond the second cumulant is needed.

3. RANDOM TELEGRAPH NOISE DUE TO BACKGROUND CHARGES

One of the most serious limitations for charge Josephson qubits is decoherence originating from fluctuating charged impurities [3–7]. It is generally agreed that the sources are switching traps for single electrons in dielectric materials surrounding the island. Here we model the effect of switching events in BCs as random telegraph (RT) processes. Many of them determine the total fluctuations, $E(t) = \sum_i E^i(t)$. Each $E^i(t)$ switches between two values $E^i_a = v_i/2$ and $E^i_b = -v_i/2$ with rates γ^i_+ and γ^i_- (Fig. 1). The average is related to the average population difference between the two states a and b of the BC, $\langle E(t)\rangle = -v/2\langle \delta p(t)\rangle$ and relaxes according to $\langle \delta p(t)\rangle = (\delta p_0 - \overline{\delta p})e^{-\gamma t} + \overline{\delta p}$ ($\gamma = \gamma_+ + \gamma_-$ is the total switching rate, δp_0, and $\overline{\delta p} = (\gamma_- - \gamma_+)/\gamma$ are the initial and the equilibrium population differences of the BC). For a stationary process $\delta p_0 = \overline{\delta p}$, and the Fourier transform of the second cumulant $\langle E(t)E(t+\tau)\rangle_c$, gives the power spectrum of the polarization fluctuations due to a single BC

$$s(\omega) = \int_0^\infty d\tau \langle E(\tau)E(0)\rangle_c e^{i\omega\tau} = \left(\frac{v}{2}\right)^2 \left(1 - \overline{\delta p}^2\right) \frac{\gamma}{\gamma^2 + \omega^2} \tag{3}$$

If BCs are statistically independent $\langle \rho_{01}(t)\rangle$ factorizes

$$\langle \rho_{10}(t)\rangle = \rho_{10}(0) e^{-i\delta E_C t} \prod_i e^{-\Gamma_i(t) + i\varepsilon_i(t)} \tag{4}$$

each contribution being due to an individual BC. Here we consider a set of random telegraph fluctuators giving $1/f$ noise. To this end we take a distribution of switching rates proportional to $1/\gamma$, for $\gamma \in [\gamma_m, \gamma_M]$ [13].

4. DECOHERENCE DUE TO A RANDOM TELEGRAPH FLUCTUATOR

The statistics of the effect of noise from a single BC are contained in the generating functional $Z(t|\eta) \equiv \langle \exp\{-i\int_0^t dt' \eta(t')E(t')\}\rangle$ which we will calculate for some selected choices of $\eta(t)$. We first consider decoherence *during* time evolution of the qubit, relevant for

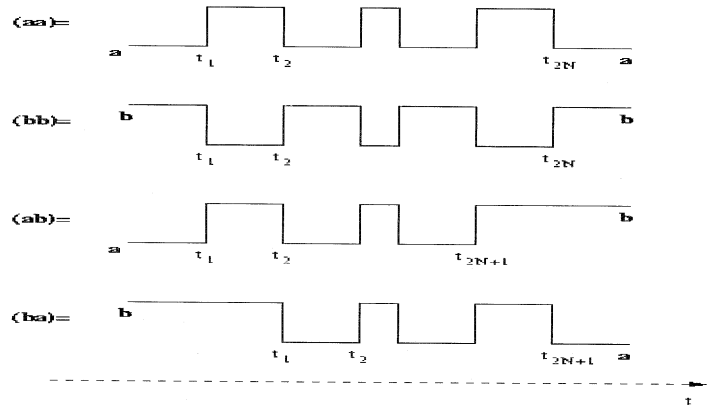

Figure 2. Possible RT fluctuator paths. If initial and final states are equal, the path has an even number of transitions, an odd number of flips occur if initial and final states are different.

single-shot measurements. In this case the qubit Hamiltonian is static, which amounts to taking $\eta(t) = 1$. In order to calculate $Z(t|1) \equiv Z(t)$ we have to take into account all the possible realizations of the stochastic processes $E(t)$ with fixed initial conditions for the fluctuator, δp_0. The fluctuator can follow one of the four kinds of paths illustrated in Fig. 2. Then we have to perform (i) a sum over all possible numbers of switches and (ii) an integration over the corresponding transition times. For each process in Fig. 2 we can define a probability density $\pi_{\alpha\beta}(t; t_m - t_1|0)$, ($\alpha$, β can be either a or b) of finding the fluctuator in the state β at time t once it has been prepared in the state α at time $t = 0$ after m transitions at times t_i, $i = 1, \ldots, m$. The probability densities of the elementary processes of having at most a single transition in a fixed time interval are found from the statistics of the populations of the two states a and b, $\langle p_\alpha(t)\rangle$, $\alpha = a, b$. The probability densities to stay in the states a and b are $\nu^0_{aa}(t_2|t_1) = \exp[-\gamma_+(t_2 - t_1)]$, and $\nu^0_{bb}(t_2|t_1) = \exp[-\gamma_-(t_2 - t_1)]$. The probability density of a single flip at time t_1 in the interval $t - t_0$ for instance from a to b reads $\pi_{ba}(t; t_1|t_0) = \exp[-\gamma_-(t - t_1)]\gamma_+ \exp[-\gamma_+(t_1 - t_0)]$. With this, the probability density of the complex processes $\pi_{\alpha\beta}(t; t_m - t_1|0)$ are given by

$$\begin{aligned}
\pi_{aa}(t; t_{2N} - t_1|0) &= (\gamma_+\gamma_-)^N e^{-\gamma_+ T_a - \gamma_- T_b} = (\gamma_+\gamma_-)^N e^{-\gamma_+ t - \gamma\delta\bar{p}T_{2N}} \\
\pi_{ab}(t; t_{2N+1} - t_1|0) &= (\gamma_+\gamma_-)^N \gamma_+ e^{-\gamma_- T_a - \gamma_+ T_b} = (\gamma_+\gamma_-)^N \gamma_+ e^{-\gamma_- t - \gamma\delta\bar{p}T_{2N+1}}
\end{aligned} \tag{5}$$

The probability densities $\pi_{bb}(t; t_m - t_1|0)$, $\pi_{ba}(t; t_m - t_1|0)$ are found from $\pi_{aa}(t; t_m - t_1|0)$, and $\pi_{ab}(t; t_m - t_1|0)$ with the replacements $\gamma_+ \to \gamma_-$, $\overline{\delta p} \to -\overline{\delta p}$. Each $\pi_{\alpha\beta}(t; t_m - t_1|0)$ only depends on the number $m = 2N$, $(2N + 1)$ of switches and on the total times T_α during which the random fluctuator has assumed value E_α. Thus we have

$$Z(t) = \langle e^{-i\int_0^t dt' E(t')}\rangle = \sum_{\alpha,\beta} p^0_\alpha z_{\alpha\beta}(t) \tag{6}$$

$$z_{\alpha\beta}(t) = \sum_{m=0}^{\infty} \int_0^t dt_m \ldots\ldots \int_0^{t_2} dt_1\, \pi_{\alpha\beta}(t; t_m - t_1|0) e^{-i(E_a T_a + E_b T_b)} \tag{7}$$

where p^0_α is the probability to find the fluctuator in the state α at time $t = 0$, and $m = 2N$ if $\alpha = \beta$ (the term $m = 0$ being 1), $m = 2N + 1$ if $\alpha \neq \beta$. The total times spent by the fluctuators in the state a or b, T_a and T_b, are given respectively by

$$T_b = \sum_{n=1}^{2N} (-1)^n t_n \equiv T_{2N}, \quad T_a = t - T_{2N}, \quad \alpha = \beta \tag{8}$$

$$T_b = \sum_{n=1}^{2N} (-1)^n t_n + t - t_{2N+1} \equiv t + T_{2N+1}, \quad T_a = -T_{2N+1}, \quad \alpha \neq \beta \tag{9}$$

From Eqs (5)–(9) we obtain the following expression for Z(t)

$$Z(t) = Ae^{-(\gamma/2)(1-\alpha)t} + (1 - A)e^{-(\gamma/2)(1+\alpha)t} \tag{10}$$

where we have defined $g = v/\gamma$, and

$$\alpha = \sqrt{1 - g^2 + 2ig\delta\bar{p}} \qquad A = \frac{(1 + \alpha + ig\delta p^0)}{2\alpha} \tag{11}$$

An interesting approximation of Eq. (10) is given by the second cumulant, which is obtained by expanding $\ln |Z(t)|$ in series of g at second order and taking $\delta p_0 = \overline{\delta p}$

$$\Gamma^{(2)}(t) = \frac{1}{\pi} \int_0^\infty d\omega \, s(\omega) \frac{1 - \cos(\omega t)}{\omega^2} \tag{12}$$

This approximation gives the effect of a Gaussian process $E(t)$ having the same power spectrum $s(\omega)$ given in Eq. (3).

5. DECOHERENCE DURING THE TIME EVOLUTION

The exact result of the semiclassical analysis gives a useful limiting case of decoherence due to a *quantum* discrete environment [6]. In fact Eqs (10) and (11) reproduce the results of Ref. [6] for "pure" dephasing due to an environment of quantum bistable fluctuators, in the regime in which each fluctuator performs a relaxation dynamics.

We find that "slow", $g \gg 1$, and "fast", $g \ll 1$, BCs influence the qubit dynamics in two qualitatively different ways. If $g \ll 1$, only the first exponential in Eq. (10) is important and the corresponding rate is $\sim s(0)$, the power spectrum of Eq. (3) at zero frequency (this is the result of the second-order perturbation theory in the qubit-fluctuator coupling). A very "fast", $g \ll 1$, bistable fluctuator behaves as a Gaussian fluctuating field for thermal equilibrium initial conditions. Instead if $g \gg 1$ both terms in Eq. (10) are of the same order, and decay with rate $\approx \gamma$. That is, for a slow fluctuator ($g \gg 1$) the contribution to the dephasing rate saturates to $\Gamma(t) \approx \gamma$ and the main effect of the coupling reduces to a static energy shift. At short times $t \ll 1/\gamma$, the initial condition, which may take the values $\delta p_0 = \pm 1$, determines the transient behavior. For typical initial conditions $\delta p_0 = \pm 1$, being generally $\delta p_0 \neq \overline{\delta p}$, corrections to the Gaussian approximation linear in g arise.

In the presence of many independent fluctuators $\langle \rho_{01}(t) \rangle$ is factorized and reads

$$\frac{\langle \rho_{10}(t) \rangle}{\rho_{10}(0)} = e^{-i\delta E_C t} \prod_i \{ A_i e^{-(\gamma_i/2)(1-\alpha_i)t} + (1 - A_i) e^{-(\gamma_i/2)(1+\alpha_i)t} \} \tag{13}$$

A detailed analysis of the dephasing due to a distribution of defects giving $1/f$ noise has been performed in Ref. [6]. A spectral analysis of the effect of a $1/\gamma$ distribution has shown that most effective fluctuators are those with $\gamma \geq \langle \nu \rangle$ (here $\langle \nu \rangle$ denotes the average over the distribution of (ν_i). All the slow fluctuators $\gamma \ll \langle \nu \rangle$ saturate and their overall effect is minimal despite their large number. In summary the discrete nature of the noise leads to the appearance of a new energy scale $\langle \nu \rangle$, which separates the set of BCs in two subsets whose physics turn out to be qualitatively different.

6. REPEATED MEASUREMENTS

We now study the effect of measurements repeated in the total time t_{meas}. This is the situation in the experiments of Refs. [3, 14], where the measured signal is the sum of repeated individual quantum evolutions. Each of these "samples" consists of a preparation pulse, followed by the free evolution and by a measuring pulse (Fig. 1). Fluctuating BCs on the one hand induce decoherence during the time evolution, as calculated in Section 5. On the other hand the polarization induced by the environment has sample-to-sample fluctuations. This situation is similar to inhomogeneous broadening in free induction decay type experiments [15]. A possible difference arises from the fact that the dynamics of the environment is strongly correlated in time. Our results allow us to discuss easily these effects since the initial conditions of each "sample", as given by Eq. (13), enter linearly only in the factors A_i. The decay of the output signal is thus obtained by substituting in Eq. (13) δp_0^j with proper averages $\langle\langle \delta p_0^j \rangle\rangle$. Here $\langle\langle \cdots \rangle\rangle$ indicates the average, for each independent fluctuator, over a distribution of δp_0^j obtained by sampling at N times during the whole measurement time t_{meas} a set of RT processes.

Fast enough fluctuators are averaged during t_{meas} so a rough approach is to use the thermal averages for fluctuators with $\gamma \geq \tilde{\gamma} = \min(\langle \nu \rangle, 1/t_{\text{meas}})$. Results in Fig. 4 (dotted lines) show that in this case dephasing, at short times, is approximately given by the oscillator environment approximation with a lower cut-off taken at $\omega \approx \tilde{\gamma}$. This clarifies the validity of the estimate in Ref. [5]. We also checked more accurate averaging procedures (solid lines in Fig. 4), which account for time correlations of the fluctuators' dynamics, and found that they are important only if $t_{\text{meas}} \approx \langle \nu_i \rangle$.

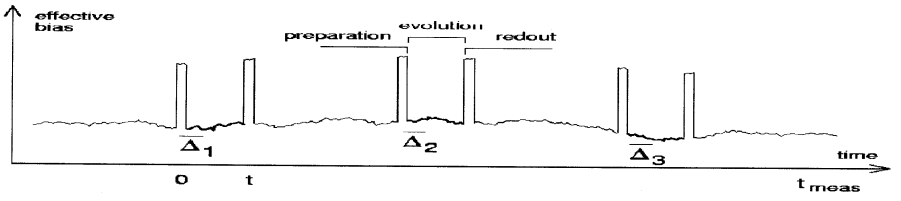

Figure 3. Repeated measurement processes, and sample fluctuations of the qubit polarization, $\bar{\Delta}_j$ during t_{meas}.

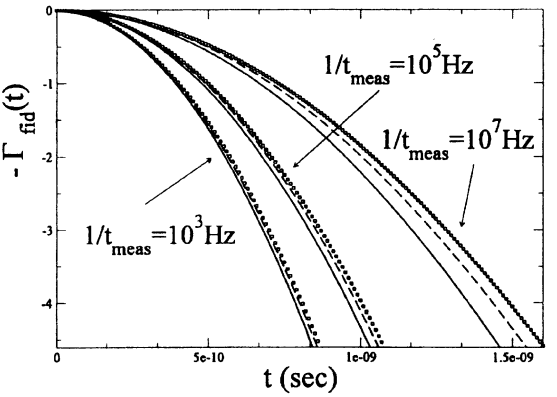

Figure 4. $\Gamma_{\rm fid}(t) \equiv \ln|\langle\langle Z(t)\rangle\rangle|$. Effect of different averages over initial conditions of the fluctuators. Relevant parameters of the $1/f$ spectrum give the measured noise level of Ref. [15]: $\langle\nu\rangle = 9.2 \times 10^6$ Hz, number of charges per decade $n_d = 10^5$, $\gamma_m = 1$ Hz, $\gamma_M = 10^9$ Hz. Dashed lines correspond to the oscillator environment approximation with a lower cut-off taken at $\omega \approx \tilde{\gamma}$.

7. "CHARGE ECHO" PROCESS

Echo-type techniques have been suggested as possible tools to reduce the decoherence effects originated from the low-frequency fluctuators of the $1/f$ spectrum [3, 5]. A "charge echo" experiment on a Josephson qubit has been recently performed [14]. Evaluation of dephasing due to random telegraph fluctuators in a spin-echo technique amounts to evaluating a modified generating functional $Z(2t|\eta)$, where $\eta(t') = 1$ for $t' \in [0, t]$, $\eta(t') = -1$ for $t' \in [t, 2t]$. Let us calculate this average, by following the same kind of analysis as Section 4. We shall initially consider that only one telegraph fluctuator is present in the environment. In this case, eight different complex processes must be taken into account during the time interval $[0, 2t]$. Each process is a combination of two complex processes like the ones described in Section 4 occurring in the intervals $[0, t]$, $[t, 2t]$. Switches of the random telegraph fluctuator during the time interval $[0, t]$ are characterized by the initial and final value of the fluctuator $E(0) = E_\alpha$ and $E(t) = E_\beta$ and by the total times $T_\alpha \alpha = a, b$. Switches during the interval $[t, 2t]$ are characterized by the initial state $E(t) = E_\beta$ and the final state $E(2t) = E_\chi$, $\chi = a, b$ and by the total time T'_α in which the fluctuators are in one of the two states α. Using the same notation as Eqs (6) and (7) we have

$$Z(2t|\eta) = \sum_{\alpha,\beta,\chi} p^0_\alpha z_{\alpha\beta}(t) z^*_{\beta\chi}(t) = \exp\{-\Gamma_{\rm echo}(t) + i\varepsilon_{\rm echo}(t)\} \tag{14}$$

which can be written as

$$Z(2t|\eta) = A_1 e^{-(1-{\rm Re}\alpha)\gamma t} + A_2 e^{-(1+{\rm Re}\alpha)\gamma t} + A_3 e^{-(1-i{\rm Im}\alpha)\gamma t} + A_4 e^{-(1+i{\rm Im}\alpha)\gamma t} \tag{15}$$

$$A_{1/2} = \frac{1}{4|\alpha|^2}\left[|1 \pm \alpha^2| + g^2 + 2ig(\delta p^0 - \delta\bar{p}) \pm 2\delta p^0 g {\rm Im}\,\alpha\right] \tag{16}$$

$$A_{3/4} = \frac{1}{4|\alpha|^2}\left[(\alpha \pm 1)(\alpha^* \mp 1) - g^2 - 2ig(\delta p^0 - \delta\bar{p}) \pm 2\delta p^0 g {\rm Re}\,\alpha\right]$$

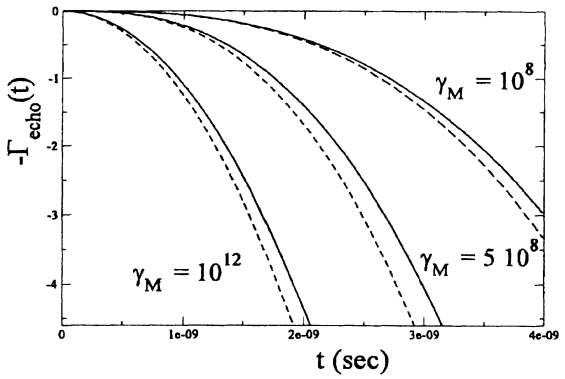

Figure 5. Decay of the echo amplitude for a $1/f$ spectrum, with noise level as in Fig. 4, with $\gamma_m = 1$ Hz and different γ_M. The dashed lines correspond to the oscillator environment approximation.

and α is defined in Eq. (11). The second cumulant expansion of Eq. (14) gives the reduction of the echo signal due to a Gaussian bath

$$\Gamma^{(2)}_{\text{echo}}(t) = \frac{2}{\pi}\int_0^\infty d\omega S(\omega)\frac{(1-\cos(\omega t))^2}{\omega^2} \tag{17}$$

In Fig. 5 we show the decay of the amplitude of the echo signal for a $1/f$ spectrum with fixed $\gamma_m = 1$ Hz, and changing γ_M. As expected, only fluctuators with $\gamma \geq 1/t$ play a role. If these fluctuators are weakly coupled (i.e. $t \ll 1/\langle v_i \rangle$, as probably occurs in the experiment in Ref. [14]) then they behave as an oscillator environment.

8. CONCLUSIONS

We have performed a semiclassical analysis of decoherence in Josephson qubits originated from an environment of RT fluctuators giving $1/f$ noise. The semiclassical analysis reproduced a useful limiting case of decoherence due to a quantum discrete environment. The main conclusion is the appearance of a new energy scale, the amplitude of the fluctuations v. This additional information, equivalent to the knowledge of the number of BCs per noise decade, allows, together with the knowledge of the power spectrum, predictions to be made in various physical situations. We obtained analytic formulae that allow detailed investigation of various processes, with no need of unjustified assumptions about the low-energy cut-off of the $1/f$ noise. In particular we give the justification of the estimates proposed in of Ref. [5]. Useful ways to estimate noise, performed by mimicking the random process $E(t)$ by an equivalent Gaussian process correspond to the second cumulant approximation of our formulae and their validity can be checked against a more realistic model of the statistics of the noise sources.

Acknowledgements

We thank R. Fazio, G. Schön, and A. Shnirman for useful discussions. Support from the EU (IST-FET SQUBIT) and INFM-PRA-SSQJ is acknowledged.

REFERENCES

[1] A. B. Zorin, F. J. Ahlers, J. Niemeyer, T. Weimann, H. Wolf, V. A. Krupenin, and S. V. Lotkhov, *Phys. Rev.* B **53**, 13682 (1996) and references therein.
[2] D. Loss and D. P. DiVincenzo, *Phys. Rev* A **57**, 120 (1998).
[3] Y. Nakamura, Yu. A. Pashkin, and J. S. Tsai, *Nature* **398**, 786 (1999).
[4] Y. Makhlin, G. Schön, and A. Shnirman, *Rev. Mod. Phys.*, **73**, 357 (2001) and references therein.
[5] A. Cottet, A. Steinbach, P. Joyez, D. Vion, H. Poitier, D. Esteve, and M. E. Huber, in *Macroscopic Quantum Coherence and Quantum Computing*, edited by D. V. Averin, B. Ruggiero, and P. Silvestrini (Kluwer, 2001), p. 111.
[6] E. Paladino, L. Faoro, G. Falci, and R. Fazio, *Phys. Rev. Lett.*, **88**, 228304 (2002); E. Paladino, L. Faoro, G. Falci, and R. Fazio, in *Macroscopic Quantum Coherence and Quantum Computing*, edited by D. V. Averin, B. Ruggiero, and P. Silvestrini (Kluwer, 2001), p. 359.
[7] A. Shnirman, Y. Makhlin, and G. Schön, cond-mat/0202518.
[8] D. Vion, A. Aassime, A. Cottet, P. Joyez, H. Pothier, C. Urbina, D. Esteve, and M. H. Devoret, *Science*, **296**, 886 (2002).
[9] W. Zurek, *Physics Today*, **44**, 36 (1991); M. Nielsen and I. Chuang, *Quantum Computation and Quantum Communication* (Cambridge Univ. Press, 2000).
[10] L. Tian, L. S. Levitov, C. H. van der Wal, J. E. Mooij, T. P. Orlando, S. Lloyd, C. J. P. M. Harmans, and J. J. Mazo, Prodeedings of the NATO-ASI on *Quantum Mesoscopic Phenomena and Mesoscopic Devices in Microelectronics*, edited by I. O. Kulik and R. Elliatioglu (Kluwer Academic, 2000), p. 429.
[11] D. J. Van Harlingen, B. L. T. Plourde, P. A. Reichardt, L. T. Robertson, and J. Clarke, in this volume.
[12] Y. Makhlin, G. Schön, and A. Shnirman, *Nature* **398**, 305 (1999); A. Shnirman, G. Schnö, and Z. Hermon, *Phys. Rev. Lett.* **79**, 2371 (1997).
[13] M. B. Weissman, *Rev. Mod. Phys.* **60**, 537 (1988).
[14] Y. Nakamura, Yu. A. Pashkin, T. Yamamoto, and J. S. Tsai, *Phys. Rev. Lett.*, **88**, 047901 (2002).
[15] C. P. Slichter, *Principles of Magnetic Resonance and Quantum Information*, 3rd ed. (Springer Verlag, 2000).

SOLID-STATE ANALOG OF AN OPTICAL INTERFEROMETER

K. Yu. Arutyunov, T. T. Hongisto, and J. P. Pekola
University of Jyväskylä, Department of Physics, P.B. 35, 40014, Jyväskylä, Finland

1. INTRODUCTION

To some extend one may treat a metal ring with two probes as a solid-state analog of an optical interferometer. One node can be considered as a beam splitter (bi-prism, for example), and the electric current at the other node as an equivalent to a light intensity of an interference pattern formed at a screen. In optics, to obtain a stationary pattern one should use a monochromatic source of radiation, as afterwards in a conventional passive media (i.e. air) the phase of the radiation is preserved. On the contrary, in solids the phase of a conducting electron wavefunction is randomly altered due to inelastic collisions (mainly phonons at high temperatures). Hence, to satisfy the condition of phase coherence, one should use loops with the circumference smaller than the characteristic phase breaking length. At temperatures $T < 1\,\mathrm{K}$ micron-size metal loops may fall into this limit. Experimentally the quantum interference manifests itself as periodic oscillations of the magnetoresistance [1]. In typical nanostructures with the diameter $d \sim 1\ \mu\mathrm{m}$, the magnitude of the effect is rather small $\Delta R/R < 10^{-3}$. The amplitude of the oscillations rapidly decreases with the increase of the loop circumference due to higher probability of the inelastic scattering events in a longer path. The unwanted phase breaking is eliminated in a superconducting state. As the resistance of a pure superconductor is zero, one should study magnetic field dependencies of the other superconducting parameters: critical temperature [2] or current [3], for example. The magnitude of the Little–Parks effect [2] in a loop with circumference L is proportional to $\sim \xi^2/L^2$, where ξ is the superconducting coherence length, and may reach $\Delta T_c \sim 10\,\mathrm{mK}$ for a micrometer-size "dirty limit" aluminum loop [3, 4]. In both cases the period of oscillations in units of magnetic flux through the area of the loop $\Delta\Phi$ is equal to the flux quantum New York: $\phi_0 = h/q$, where q is the effective particle charge is the electron charge e for normal metals and $2e$ for superconductors.

2. EXPERIMENT

We have fabricated hybrid Al-AlO_x-Cu microstructures, which may be considered as analogs to an optical interferometer: an aluminum loop overlapped at one point by a

Quantum Computing and Quantum Bits in Mesoscopic Systems
Edited by Leggett *et al.*, Kluwer Academic/Plenum Publishers, 2004

copper electrode through a tunnel barrier (Fig. 1, inset). The tunnel junction is an equivalent to an optical beam splitter. Typical thickness of the wires was about 30 nm, line width ~100 nm, the loop side varied from 0.4 to 25 μm. The overlapping area between the copper electrode and the aluminum loop was about 100 × 100 nm, resulting in a tunnel resistance R_T from 2 to 30 kΩ depending on the aluminum oxidation procedure. The superconducting critical temperature T_c of the co-evaporated aluminum films was about 1.35–1.40 K.

The current voltage characteristics $I(V)$ show the typical behavior for an NIS structure: negligible current at bias voltages below the superconducting energy gap $V_g = \Delta/2e$, abrupt increase of the current at $V = V_g$ and the quasi-Ohmic linear region at higher biases (Fig. 1). Experimentally we define the gap voltage V_g corresponding to the maximum of the first derivative $\max[dI/dV(V)] = dI/dV(V_g)$. The last assumption is particularly valid at low temperatures $T \ll T_c$, where the $dI/dV(V)$ dependencies are very "sharp".

At fixed bias voltages the dependencies of the tunnel current on external perpendicular magnetic field $I(V = \text{const}, H)$ show pronounced oscillating behavior (Fig. 2). The amplitude and the period of oscillations is constant at magnetic fields H much smaller than the critical value H_c, which is typically about 30–40 mT for our aluminum nanostructures. Close to the critical value the amplitude of the oscillations drops due to suppression of the superconducting gap by the magnetic field. The period of the oscillations at high magnetic fields can be different from that at low fields.

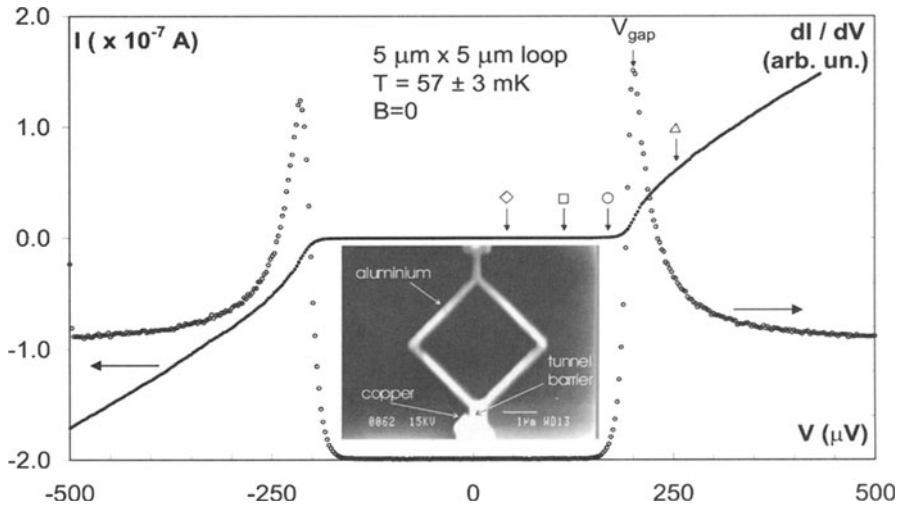

Figure 1. Typical $I(V)$ and $dI/dV(V)$ characteristics at zero magnetic field. Arrows indicate the bias voltages at which magnetic field sweeps in Fig. 2 are shown. Inset: SEM image of a typical nanostructure.

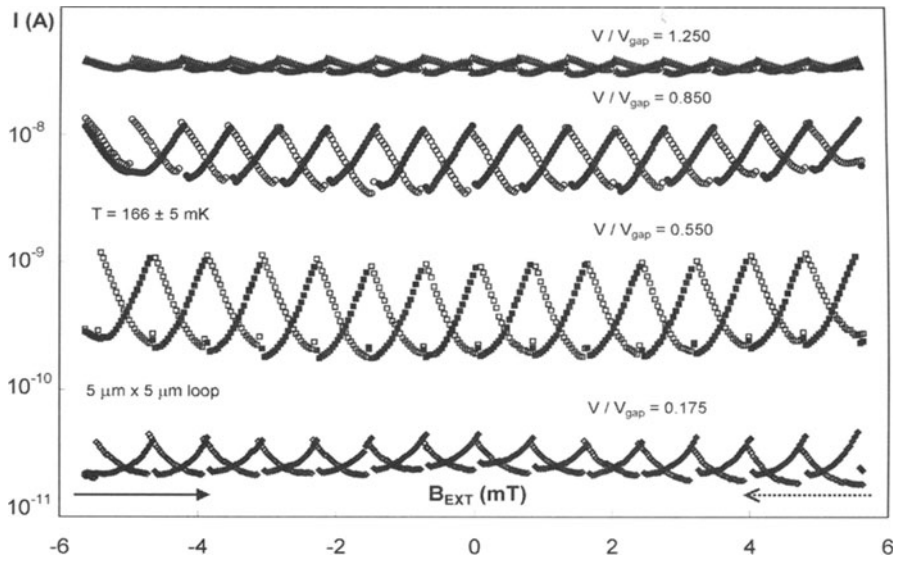

Figure 2. Example of $I(V = \text{const}, H)$ dependencies taken at $T = 166 \pm 6$ mK at various voltage biases, normalized by the gap voltage V/V_{gap}. Arrows show the direction of the field sweep.

As the last effect is not well understood, hereafter we will consider only the oscillations at small fields, corresponding to few periods of oscillations and numerically not exceeding ~20 mT for the smallest loops ($L^2 \leq 1$ μm^2). For larger areas the period of the oscillations is much smaller than the critical magnetic field. The dependencies $I(V = \text{const}, H)$ are hysteretic, being different if the absolute value of the magnetic field is increased or decreased (Fig. 2). Formally, one may conclude that they form a set of "parabolas" jumping to particular branches of the curves depending on the sign of dH/dt. If the variation of the magnetic field is small and does not cause jumps to a new "quantum state" ("parabola"), the dependencies $I(V = \text{const}, H)$ are not hysteretic. The above oscillating behavior is nicely reproducible for a given sample, and is qualitatively similar for all studied structures.

The normalized amplitude of the current oscillations $\Delta I/I_{\max}(V = \text{const}, H)$ depends on the bias V, reaching its maximum at voltages slightly below the gap value V_g (Figs 2 and 3). What is surprising is the large magnitude of the effect: at low temperatures ($T \sim 50$ mK) $\Delta I/I_{\max} \sim 1$ at biases close to the gap value. Note that the corresponding effect in a normal metal [1] has magnitude <0.1%, and in superconducting loops the oscillations of the critical temperature (Little–Parks effect) are also rather small $\Delta T_c/T_c \sim 1\%$ [2–4]. The oscillations with the high magnitude of the effect $\Delta I/I_{\max}(V \sim V_g, H) \sim 1$ are observed for loops with the smallest size of the loop ($L \leq 5$ μm), while the effect is still quite pronounced up to the loop side $L = 25$ μm.

Probably the most unusual result is the absolute value of the oscillations period. As has been mentioned, the period of current oscillations $\Delta\Phi_I$ was expected to be equal to h/e

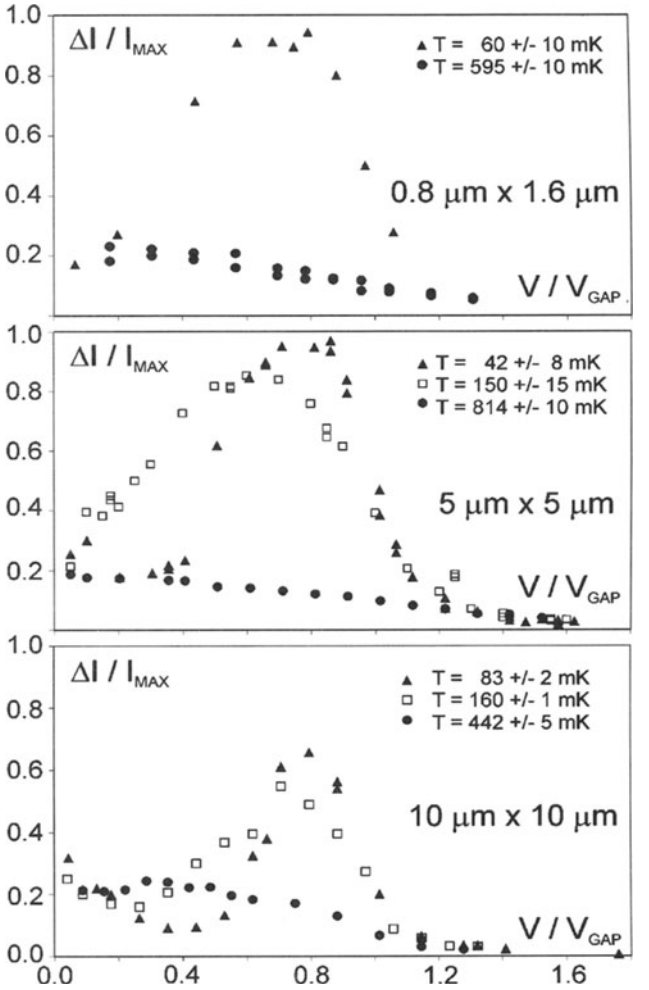

Figure 3. The normalized magnitudes of the current oscillations $\Delta I/I_{\max}$ vs. normalized bias voltage V/V_{gap} at various temperatures for three samples, which differ by the size of the loop.

or $h/2e$, depending, probably (?) on the bias voltage. The experimentally observed period is constant for the particular loop size (and the bias), but equals h/e for the smallest loops and significantly exceeds h/e for larger structures (Fig. 4). Within the accuracy of the experiment this effect is not sample dependent and is reasonably quantitatively reproducible for the structures with the same area of loop.

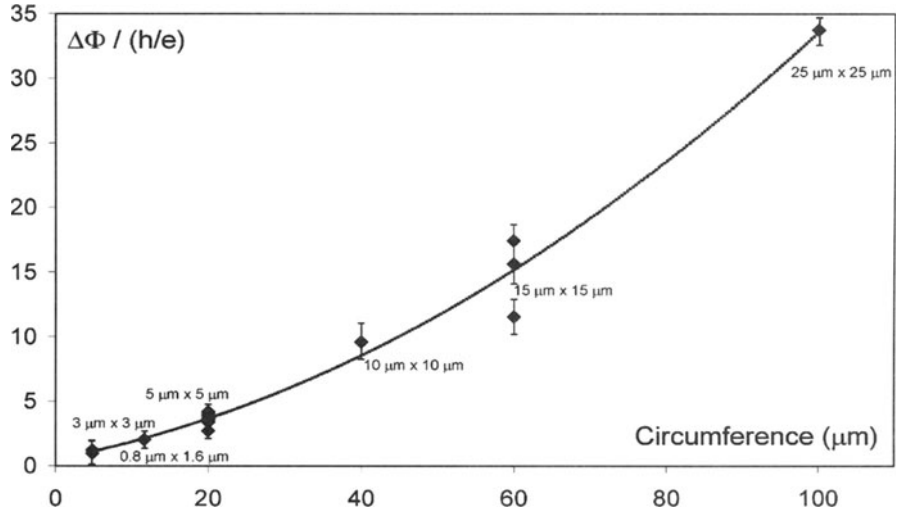

Figure 4. Experimental period of current oscillations $\Delta\Phi_I$ normalized by the normal metal flux quantum $\phi_0 = h/e$ vs. loop circumference. Line is a guide for eyes.

3. DISCUSSION

It is pointless to say that after obtaining the striking discrepancy between the expected and the observed periods of the oscillations, we have re-calibrated the three different coils used in our experiments, as well as re-measured the dimensions of the samples using two scanning electron microscopes. The early results were found to be quantitatively valid. As an additional check, the magnetoresistance of 95 × 5 μm complete aluminum loop with four probes (no normal metal and no tunnel barriers) has been measured. Though the magnitude of the oscillations $\Delta R/R$ in the resistive state is significantly damped due to the factor $\sim\xi^2/L^2$, the period accurately equals the expected value of $h/2e$ consistent with the Little–Parks effect [2].

Note that the naïve model assuming that the oscillations originate from the periodic modulation of the superconducting energy gap by the magnetic field (the Little–Parks effect) fails both qualitatively and quantitatively. First, the magnitude of the gap modulation is too small to give almost 100% variation of the tunnel current of an NIS structure. Second, this contribution should result in strictly $h/2e$ periodicity. Probably the related effects have been reported in structures containing double tunnel barriers [5]. However, contrary to those observations, in our experiments the period of the oscillations varies in strong magnetic fields (not always!), and is nonsignificant (<15%). Measurements in the current bias mode $V(I = \text{const}, H)$ did show qualitatively similar oscillating behavior with unusually large period $\Delta\Phi_V$, but which differs from the period $\Delta\Phi_I$ of the voltage bias mode $I(V = \text{const}, H)$ by a factor of 15–40% (Fig. 5).

For the moment we do not have a reasonable explanation for the observed phenomena. Formally one may conclude that the periodicity is governed either by the

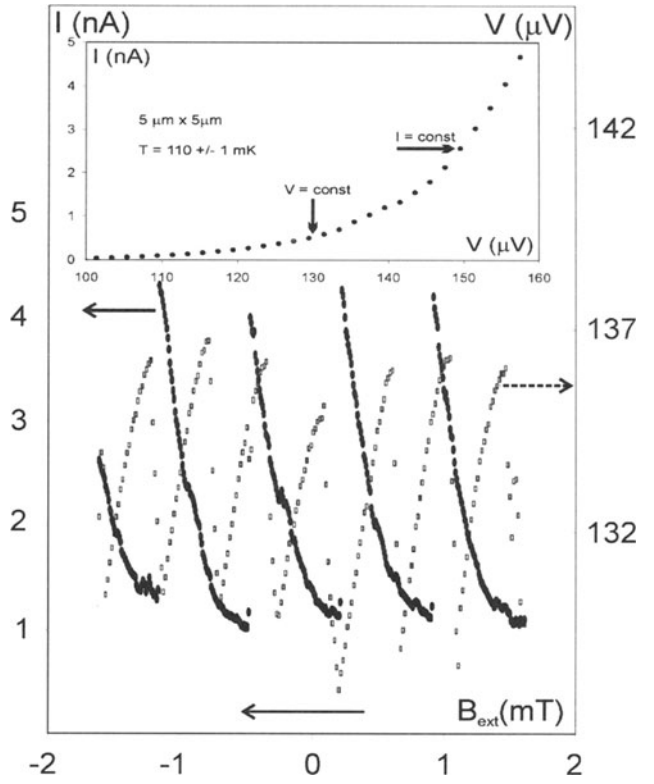

Figure 5. Current oscillations $I(V = 13\ \mu\text{V}, H, T = 148 \pm 2\ \text{mK})$ at a fixed bias voltage (left axis, solid symbols) and voltage oscillations $V(I = 2.7\ \text{nA}, H, T = 153 \pm 1\ \text{mK})$ at a fixed bias current (right axis, open symbols). Arrow at the bottom shows the direction of the magnetic field sweep. Inset: the enlarged part of the $I(V, H = 0, T = 110 \pm 1\ \text{mK})$ characteristics. Arrows indicate the points where the dependencies in the main plot were measured.

multiple flux penetration $n \times \phi_0 = n \times (h/q)$, with q being equal to e or $2e$ (?), or by a renormalized flux quantum $\phi_0^* = h/q$, with a fractional charge $q < e$.

The first possibility is improbable to give a stable periodicity, rather than a random, strongly hysteretic pattern depending on the energy barrier for vortices to penetrate (exit) the loop area specific for a particular sample. Note that in our dirty limit structures with the mean free path $l \sim 30$ nm the coherence length ξ is smaller than the bulk value for pure aluminum ξ_0: $\xi \sim 0.85(l\xi_0)^{1/2} \sim 200$ nm, but is still larger than the studied nanostructure line width $w \sim 100$ nm. It means that there is no room for vortex cores to be located within the wire area. A control 5×5 μm sample containing no loop (solid square aluminum electrode) overlapped with a usual copper probe through a tunnel junction did not show up any reproducible periodic structure at $I(V = \text{const}, H)$ dependencies. One may conclude that the non-single-connected geometry of the superconducting electrode is essential.

The second possibility ($q < e$) is very intriguing taking into consideration the fact that nonequilibrium quasi-particles in a superconductor do have fractional charges [6]. One might assume that the observed oscillations originate from the interference of the nonequilibrium quasi-particles, injected from the normal electrode. This hypothesis might nicely explain the large oscillation period at biases above the energy gap ($V > V_g$), but fails to fit the data at smaller biases. Additionally, although the relaxation length of nonequilibrium quasi-particles in aluminum is known to be anomalously large [7], it still looks quite improbable for quasi-particles to preserve their phase on distances as large as $4L = 100$ μm. Further experimental and theoretical work is necessary to find the explanation of the observed phenomena.

Acknowledgements

The authors would like to acknowledge D. Esteve for helpful discussion. The work was supported by the Russian Foundation for Basic Research (Grant 01-02-17427) and the Academy of Finland under the Finnish Centre of Excellence Program 2000-2005 No. 44875, Nuclear and Condensed Matter Program at JYFL.

REFERENCES

[1] C. P. Umbach, S. Washburn, R. B. Laibowitz, and R. A. Webb, Magnetoresistance of small, quasi-one-dimensional, normal-metal rings and lines, *Phys. Rev.* B **30**, 4048–4051 (1984).

[2] W. A. Little and R. D. Parks, Observation of quantum periodicity in the transition temperature of a superconducting cylinder, *Phys. Rev. Lett.* **9**, 9 (1962).

[3] K. Yu. Arutyunov, J. P. Pekola, A. B. Pavolotski, and D. A. Presnov, Nonlocality in superconducting nanostructures, *Phys. Rev.* B **64**, 064519-1–064519-6 (2001).

[4] C. Strunk, V. Bruyndoncx, V. V. Moshchalkov, C. Van Haesendonck, and I. Bruynseraede, Nonlocal effects in mesoscopic superconducting aluminum structures, *Phys. Rev.* B **54**, R12701–R12704 (1996).

[5] A. Kanda, K. Ishibashi, Y. Aoyagi, and T. Sugano, Magnetoresistance of single-electron tunneling transistor with a superconducting loop, *Czech. J. Phys.* **46**, 2297–2298 (1996); A. Kanda, K. Ishibashi, Y. Aoyagi, and T. Sugano, in *Physics and Applications of Mesoscopic Josephson Junctions* (The Physical Society of Japan, 1999), pp. 305–323.

[6] M. Tinkham, *Introduction to Superconductivity* (McGraw-Hill Inc., 1996).

[7] J. Clarke, in *Nonequilibrium Superconductivity, Phonons, and Kapitza Boundaries*, edited by K. E. Gray (New York, Plenum Press, 1981), pp. 353–422.

SINGLE ELECTRON TRANSISTORS WITH $Al/AlO_x/Nb$ AND $Nb/AlO_x/Nb$ JUNCTIONS

R. Dolata, H. Scherer, A. B. Zorin, and J. Niemeyer
Physikalisch-Technische Bundesanstalt, Bundesallee 100, 38116 Braunschweig, Germany

1. INTRODUCTION

Superconducting quantum-coherent devices with small tunnel junctions offer the possibility to manipulate single Cooper pairs and control macroscopic quantum states. They may be used to construct current standards [1] and qubits [2]. For optimum performance, most devices require the Josephson coupling energy $E_J \equiv (h/4\pi e)I_c = (R_K/R)\Delta/8$ to be of the same order as the charging energy $E_C = e^2/2C_\Sigma$, where $R_K = h/e^2 \approx 25\ \mathrm{k}\Omega$, R is the junction tunnel resistance, Δ is the superconducting energy gap, and C_Σ is the total capacitance of the island.

Modern nanotechniques allow C_Σ to be reduced and hence E_C to increase in Al-based junctions ($\Delta_{\mathrm{Al}} \approx 0.2$ meV), but it is hard to keep E_J equal to E_C, because this condition requires very transparent barriers. With the use of Nb-based junctions ($\Delta_{\mathrm{Nb(bulk)}} \approx 1.5$ meV) it should be possible to increase the Josephson coupling energy by almost one order of magnitude for the same tunnel resistance: $E_J^{\mathrm{Nb-Nb}} \approx 7.3\,E_J^{\mathrm{Al-Al}}$. Further, an increased Δ is important since it should suppress disturbing quasi-particle tunneling onto or from the island [3]. Composite $Al/AlO_x/Nb$ junctions are a first step towards the highly desirable $Nb/AlO_x/Nb$ junctions because the Josephson coupling energy is still larger than that of Al junctions, that is, $E_J^{\mathrm{Al-Nb}} \approx 2.2E_J^{\mathrm{Al-Al}}$.

2. SAMPLE FABRICATION

Traditionally, most devices based on single electron tunneling (SET) effects are fabricated by shadow evaporation techniques using suspended masks [4]. Usually, these masks are made of polymethylmethacrylate (PMMA) or related copolymers (PMMA-PMAA) and patterned by high-resolution electron beam lithography [5]. These techniques provide easy lift-off and work successfully for soft materials like aluminum, which is the most widely used metal for the preparation of SET devices. Due to its low evaporation temperature aluminum can easily be deposited by evaporation without producing high

Quantum Computing and Quantum Bits in Mesoscopic Systems
Edited by Leggett *et al.*, Kluwer Academic/Plenum Publishers, 2004

thermal loads to the suspended masks. Another important advantage of Al is the possibility of creating high-quality tunnel barriers by thermal oxidation, forming a thin layer of AlO_x. Unfortunately, high-quality NbO_x tunnel barriers cannot be made by thermal oxidation of the Nb surface [6]. That is why an intermediate thin layer of Al is usually deposited onto the Nb film and oxidized to create a barrier of AlO_x [7].

PMMA-based masks have been repeatedly used for the fabrication of submicron Nb structures [8–11]. The use of PMMA generally entails strong deterioration of the superconducting properties of the Nb; the transition temperature T_c and hence the effective gap energy $\Delta_{Nb,eff}$ are reduced far below the Nb bulk values. A decrease in the transition temperature is observed with decreasing layer thickness and linewidth [11, 12]. The most probable reason for this is the outgassing of the PMMA polymer during the evaporation of the high-melting Nb due to radiation heating from the electron beam gun (*e*-gun) evaporation source [12, 13].

Dubos *et al.* [13] developed a novel lift-off process for the preparation of high-quality submicron Nb structures, based on the use of the thermostable polymer polyethersulfone (PES). PES remains mechanically tough up to temperatures of about 200°C and shows very low outgassing compared to PMMA.

Preliminary attempts to fabricate submicron Nb lines by *e*-gun evaporation using PMMA masks resulted in a strong reduction of the critical temperature T_c. To improve the T_c of the Nb structures, PMMA was replaced by PES, following roughly the procedure described in Ref. [13]. Details of our fabrication process for stencil masks, composed of a PES bottom layer and a Ge top layer forming the suspended bridges, have already been published [14]. Small Nb lines were fabricated by *e*-gun evaporation of Nb onto the PES-Ge masks and subsequent lift-off. Figure 1 shows the dependence of T_c on the width of the Nb lines when using PES- and PMMA-based masks. The resulting critical temperatures of

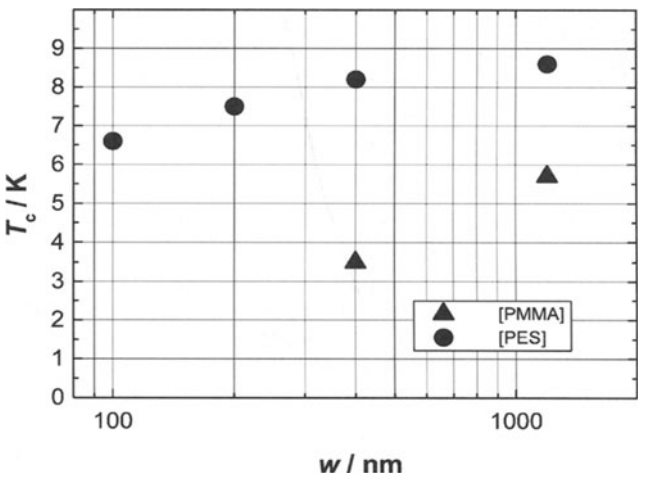

Figure 1. T_c vs. linewidth w of evaporated Nb wires approximately 50 nm in thickness, fabricated by lift-off with PMMA and PES masks.

our submicron Nb structures were found to be significantly higher for the PES masks compared with the PMMA masks and are similar to the published data [12, 13].

3. TRANSISTORS WITH Al/AlO$_x$/Nb JUNCTIONS

Using the shadow evaporation technique together with a PES-Ge mask, single electron transistors with Al/AlO$_x$/Nb junctions and high-quality superconducting niobium islands with an effective gap energy of up to $\Delta_{Nb,eff} \approx 1.25$ meV have recently been demonstrated [14]. The devices were prepared according to the standard angle evaporation procedure used for Al-based circuits. The sample was tilted to a first angle and an Al layer 35 nm in thickness was evaporated. Next, the AlO$_x$ tunnel barrier was formed by oxidation of the film in pure O_2. Process time and pressure were varied for different wafers. After pumping down of the O_2, an Nb layer 40 nm thick was evaporated using a second tilt angle. Finally, the stencil mask was lifted off.

The single electron transistors had resistances from 10 to 250 kΩ and total island capacitances between 0.3 and 0.6 fF. Thus the C_Σ value achieved in the Al/Nb transistors was of the order of the island capacitance for typical Al devices. Figure 2 shows a typical current–voltage characteristic of a single electron transistor with Al/AlO$_x$/Nb junctions. The transistors with low resistance ($R_n \approx 10$ kΩ) show critical currents of the order of some nA. The transistors with higher resistance ($R_n \approx 100$ kΩ) showed pronounced "Josephson-quasi-particle" (JQP) cycles, that is, resonant tunneling processes involving combined single Cooper pair and quasi-particle tunneling [15]. These current peaks could be modulated by the gate voltage with a period corresponding to e. Also, the switching current I_s of transistors with measurable critical currents was modulated e-periodically [14]. The ratio of characteristic energies E_J/E_C in these samples varies from 0.03 to 1.2, clearing the way for devices operating on single pairs. The results on the transistors with Al/AlO$_x$/Nb junctions and Nb islands can be considered as a first step towards the desirable Nb/AlO$_x$/Nb junctions.

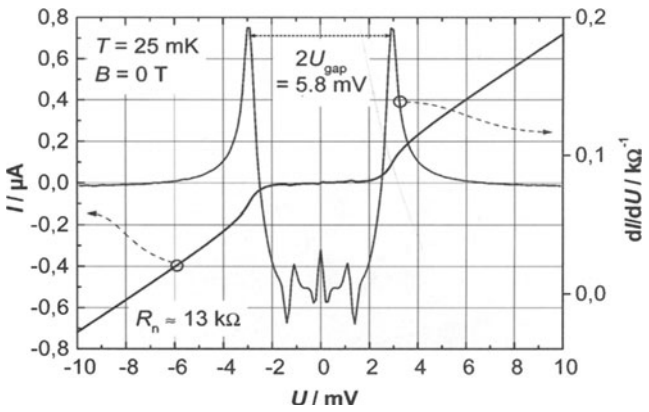

Figure 2. Current–voltage and differential conductance characteristics for an Al/AlO$_x$/Nb transistor with $R_n \approx 13$ kΩ. According to the maxima of dI/dU, the gap voltage $U_{gap} = 2(\Delta_{Nb,eff} + \Delta_{Al})/e$ was found to be about 2.9 mV, corresponding to $(\Delta_{Nb,eff} + \Delta_{Al}) \approx 1.45$ meV.

4. TRANSISTORS WITH Nb/AlO$_x$/Nb JUNCTIONS

Owing to the impossibility of creating high-quality tunnel barriers by thermal oxidation of Nb, the fabrication of devices with Nb/AlO$_x$/Nb junctions requires at least one additional Al layer for the generation of an oxide barrier. Starting the fabrication process with another additional Al layer was found to be helpful as it stabilized the Ge bridges of the PES-Ge masks against excessive bending due to intrinsic stress in the Nb films.

The sample with a PES-Ge mask was tilted to a first angle and an Al layer (12 nm in thickness) was evaporated. Then the first Nb layer 30 nm in thickness was deposited. After slightly changing the tilt angle, another Al layer 13 nm in thickness was evaporated. Next, the AlO$_x$ tunnel barrier was formed by oxidation in O_2 for 10 minutes at a pressure of 100 Pa. After pumping down the O_2, an Nb layer 50 nm thick was evaporated at a third tilt angle. This Nb layer formed the counterelectrode of the Nb/AlO$_x$/Nb junctions and the transistor islands. Finally, the stencil mask was lifted off.

A first run with the standard transistor layout successfully used for the fabrication of Al/AlO$_x$/Nb transistors [14] resulted in shorted junctions. This was probably due to incomplete coverage of the curved edges of the first Nb layer by the Al layer used for the creation of the tunnel barrier. In this case, the junctions may be shorted by noninsulating Nb oxides [6]. To overcome this drawback of the standard layout, a new design for the single junctions and the transistor islands was developed. It does not locate the junctions at the end of the Nb lines but at some distance from the end where the edge of the first Nb layer follows a straight line. This straight edge can more easily be covered completely with Al by correct adjustment of the evaporation angles. Figure 3 shows a micrograph of a transistor with Nb/AlO$_x$/Nb junctions fabricated using the new island layout.

Several wafers with identical sample layouts were prepared, carrying single junction and single electron transistor samples with four-terminal contact schemes. Among the samples on each chip, the junction sizes were varied in a defined way (the maximum nominal junction size was about 100 × 100 nm).

Figure 4 shows typical examples of the current–voltage and the corresponding differential conductance characteristics measured on transistors (R_n = 24 and 69 kΩ) of a chip cooled down to millikelvin temperatures. These samples exhibited gap voltages $U_{gap} = 4\Delta_{Nb,eff}/e$ of 3.3 and 4 mV, corresponding to $\Delta_{Nb,eff} \approx 0.8$ and 1.0 meV,

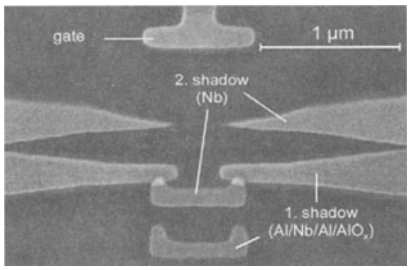

Figure 3. SEM micrograph of a transistor with U-shaped island and junction areas of about 0.007 µm^2. The second shadow of the electrodes was partly deposited against the side of the PES polymer wall and therefore removed during lift-off.

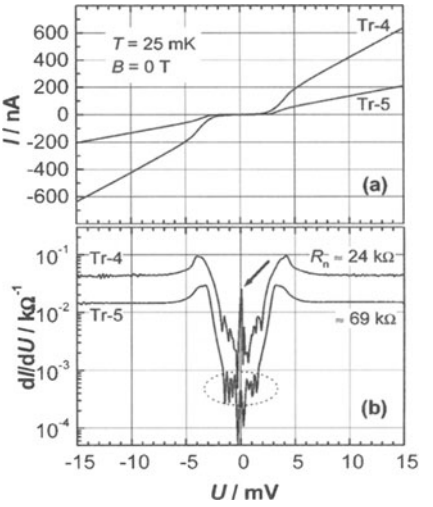

Figure 4. (a) Current–voltage and (b) differential conductance characteristics (logarithmic ordinate) measured on two transistor samples in the superconducting state ($T = 25$ mK). Gap voltages $U_{gap} = 4\Delta_{Nb,eff}/e$ of 3.3 and 4 mV were observed. Conductance peaks around zero bias, visible for the sample with lower resistance (arrow), indicate a supercurrent. On the sample with higher resistance, the pronounced subgap structure (circled) is caused by JQP cycles.

respectively. Also, we found $\Delta_{Nb,eff} \approx 1$ meV for the single junctions on the same chip (not shown). To our knowledge this is the highest value for the gap energy achieved so far in submicron Nb/AlO$_x$/Nb tunnel junctions prepared by shadow evaporation techniques. Still, the observed gap energy $\Delta_{Nb,eff}$ of the junctions is significantly smaller than the bulk value for Nb ($\Delta_{Nb(bulk)} \approx 1.5$ meV). This is probably due to a reduction of T_c in the 150 nm wide electrodes and island to about 7 K (compare Fig. 1) and a further decrease due to the proximity effect [16] as the junction base electrode consists of 30 nm Nb and 25 nm Al layers.

As Fig. 4(b) shows, pronounced structures were present in the differential conductance characteristic in the subgap voltage regime of the superconducting transistors, that could be modulated by the gate voltage with a period corresponding to e. These structures are similar to those found in the recently investigated Al/AlO$_x$/Nb transistors [14], and following the same reasoning, we attributed them to JQP cycles [15]. In the superconducting state, the transistor current could be modulated by the gate voltage V_g with a rather large maximum amplitude $\Delta I \approx 240$ pA (at $U = 1.5$ mV, not shown). All superconducting transistors examined showed a gate modulation characteristic with a periodicity corresponding to e. Also, the transistors show a leakage current in the subgap region that typically appeared in all structures investigated. We attribute this to the presence of quasi-particles that might enter the Nb island via parasitic conductance channels, or to the presence of intra-gap energy states caused by impurities and leading to quasi-particle tunneling events even at small bias.

The samples were also checked for the properties they show in magnetic fields. It turned out that $B \approx 6$ T was necessary to completely suppress the superconductivity in the samples. Figure 5(a) shows a set of $I(U)$ characteristics recorded at different gate voltages

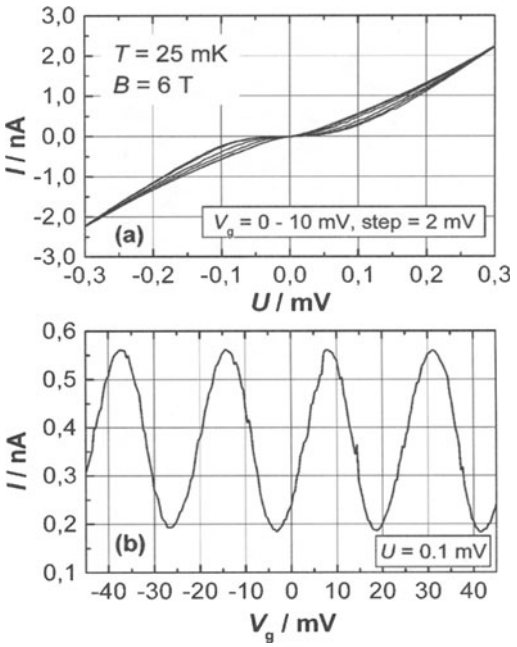

Figure 5. (a) Gate-modulated $I(U)$ characteristics measured on an transistor in the completely normal state at $B = 6$ T and $T = 25$ mK. (b) The maximum current modulation of about 350 pA, measured at $U = 100$ μV, with a modulation period $\Delta V_g = 23$ mV equivalent to e.

in the completely normal state, where we observed a maximum current modulation $\Delta I \approx 350$ pA in the transistor biased at $U = 100$ μV (Fig. 5(b)).

In contrast to traditional SET transistors made of $Al/AlO_x/Al$, the $I(U)$ curves of our $Nb/AlO_x/Nb$ samples appeared markedly nonlinear in the whole bias range investigated. Therefore, an estimation of the total island capacitance C_Σ by analysis of the offset voltage plot (i.e. $U_{off} = (U - I)dU/dI$ versus U in the normal state) was not feasible here. Instead, C_Σ was derived by analysis of the gate modulated $I(U)$ characteristics at low temperature in the normal state. The maximum blockade voltage of about 110 μV ± 20 μeV enabled us to estimate $E_C \approx 55$ μeV ± 10 μeV, corresponding to $C_\Sigma \approx 1.45$ fF ± 0.3 fF. This figure was also confirmed by model calculations for the gate modulation characteristics at different bias voltages, based on the orthodox theory of single electron tunneling, that resulted in reasonably good agreement with the measured curves (not shown).

Analyzing the Josephson coupling energy E_J of this sample, we arrived at $E_J \approx 75$ μeV (with $R = R_n/2 \approx 35$ kΩ and $\Delta = \Delta_{eff} \approx 0.85$ meV) in comparison with $E_C \approx 55$ μeV, which is close to the desired relation $E_C \approx E_J$.

5. CONCLUSION AND OUTLOOK

The shadow evaporation technique with PES-based masks allows the fabrication of mesoscopic $Al/AlO_x/Nb$ and $Nb/AlO_x/Nb$ devices with small capacitance. Significant

progress was achieved with respect to the effective gap energy approaching $\Delta_{Nb,eff} \approx 1.25$ meV and 1.0 meV, respectively, although it obviously is still smaller than $\Delta_{Nb(bulk)} \approx 1.5$ meV. Also, we observed remarkable gate modulation characteristics of the transistor samples in the superconducting and in the normal state.

The reduced gap energy, in combination with the observed subgap leakage currents, indicate problems with the quality of the Nb-based junctions. Since it is well known that Nb is a strong getter material, it can be concluded that its gap energy is reduced from the bulk value and probably intragap energy states are created by the incorporation of impurities. The main source for the contamination presumably is still the outgassing from the mask polymer due to radiation heating. A further reduction of $\Delta_{Nb,eff}$ is caused by the introduction of an Al underlayer and coating of the base electrode in the $Nb/AlO_x/Nb$ junctions. The evaporation of Nb results in highly stressed films, causing at least some bending of the stencil mask during the deposition process. The mentioned difficulties with Nb constitute considerable technical problems, but no physical limitations are known that in future might prevent the fabrication of mesoscopic Nb devices of higher quality. A possible significant improvement of the shadow evaporation technique may be the use of inorganic masks [12] for junction fabrication. Such masks should avoid the contamination of Nb and fulfil the requirement of mechanical robustness.

REFERENCES

[1] K. K. Likharev and A. B. Zorin, Theory of the Bloch-wave oscillations in small Josephson junctions, *J. Low Temp. Phys.* **59**, 347–382 (1985).

[2] Yu. Makhlin, G. Schön, and A. Shnirman, Quantum state engineering with Josephson-junction devices, *Rev. Mod. Phys.* **73**, 357–400 (2001).

[3] M. T. Tuominen, J. M. Hergenrother, T. S. Tighe, and M. Tinkham, Experimental evidence for parity-based 2e-periodicity in a superconducting single-electron tunneling transistor, *Phys. Rev. Lett.* **69**, 1997–2000 (1992); D. V. Averin and Yu. V. Nazarov, Single-electron charging of a superconducting island, *Phys. Rev. Lett.* **69**, 1993–1996 (1992).

[4] J. Niemeyer, Eine einfache Methode zur Herstellung kleiner Josephson-Elemente, *PTB-Mitt.* **84**, 251–253 (1974); G. J. Dolan, Offset masks for lift-off photoprocessing, *Appl. Phys. Lett.* **31**, 337–339 (1977).

[5] G. J. Dolan and J. H. Dunsmuir, Very small ($\geq$20 nm) lithographic wires, dots, rings, and tunnel junctions, *Physica* B **152**, 7–13 (1988).

[6] J. Halbritter, On the oxidation and on the superconductivity of niobium, *Appl. Phys.* A **43**, 1–28 (1987).

[7] J. M. Rowell, M. Gurvitch, and J. Geerk, Modification of tunneling barriers on Nb by a few monolayers of Al, *Phys. Rev.* B **24**, 2278–2281 (1981).

[8] Y. Harada, D. B. Haviland, P. Delsing, C. D. Chen, and T.Claeson, Fabrication and measurement of a Nb based superconducting single electron transistor, *Appl. Phys. Lett.* **65**, 636–638 (1994).

[9] K. Blüthner, M. Götz, A. Hädicke, W. Krech, T. Wagner, H. Mühlig, H.-J. Fuchs, U. Hübner, D. Schelle, and E. B. Kley, Single-electron transistors based on $Al/AlO_x/Al$ and $Nb/AlO_x/Nb$ tunnel junctions, *IEEE Trans. Appl. Supercond.* **7**, 3099–3102 (1997).

[10] D. Born, T. Wagner, W. Krech, U. Hübner, and L. Fritzsch, Fabrication of ultrasmall tunnel junctions by electron beam direct-writing, *IEEE Trans. Appl. Supercond.* **11**, 373–376 (2001).

[11] N. Kim, K. Hansen, J. Toppari, T. Suppula, and J. Pekola, Fabrication of mesoscopic superconducting Nb wires using conventional electron-beam lithographic techniques, *J. Vac. Sci. Technol.* B **20**, 386–388 (2002).

[12] T. Hoss, C. Strunk, and C. Schönenberger, Nonorganic evaporation mask for superconducting nanodevices, *Microelectron. Eng.* **46**, 149–152 (1999).

[13] P. Dubos, P. Charlat, Th. Crozes, P. Paniez, and P. Pannetier, Thermostable trilayer resist for niobium lift-off, *J. Vac. Sci. Technol.* B **18**, 122–126 (2000).

[14] R. Dolata, H. Scherer, A. B. Zorin, and J. Niemeyer, Single electron transistors with high-quality superconducting niobium islands, *Appl. Phys. Lett.* **80**, 2776–2778 (2002).

[15] T. A. Fulton, P. L. Gammel, D. J. Bishop, L. N. Dunkleberger, and G. J. Dolan, Observation of combined Josephson and charging effects in small tunnel junction circuits, *Phys. Rev. Lett.* **63**, 1307–1310 (1989); A. M. van den Brink, G. Schön, and L. J. Geerligs, Combined single-electron and coherent-Cooper-pair tunneling in voltage-biased Josephson junctions, *Phys. Rev. Lett.* **67**, 3030–3033 (1991); Y. Nakamura, T. Sakamoto, and J.-S. Tsai, Study of Josephson-quasiparticle cycles in superconducting single-electron transistors, *Jpn. J. Appl. Phys.* **34**, 4562–4565 (1995).

[16] N. R. Werthamer, Theory of the superconducting transition temperature and energy gap function of superposed metal films, *Phys. Rev.* **132**, 2440–2445 (1963).

TIME-LOCAL MASTER EQUATIONS: INFLUENCE FUNCTIONAL AND CUMULANT EXPANSION

H.-P. Breuer[1,2,a], A. Ma[2,3,b], and F. Petruccione[2,4,c]
[1]*Fachbereich Physik, Carl von Ossietzky Universität, D-26111 Oldenburg, Germany*
[2]*Fakultät für Physik, Universität Freiburg, D-79104 Freiburg, Germany*
[3]*Blackett Laboratory, Imperial College, Prince Consort Road, London, UK*
[4]*Istituto Italiano per gli Studi Filosofici, Via Monte di Dio 14, I-80132 Napoli, Italy*

Abstract: The non-Markovian behavior of open quantum systems interacting with a reservoir can often be described in terms of a time-local master equation involving a time-dependent generator which is not in Lindblad form. A systematic perturbation expansion of the generator is obtained either by means of van Kampen's method of ordered cumulants or else by use of the Feynman–Vernon influence functional technique. Both expansions are demonstrated to yield equivalent expressions for the generator in all orders of the system–reservoir coupling. Explicit formulae are derived for the second- and the fourth-order generator in terms of the influence functional.

Keywords: Open quantum system, Non-Markovian quantum processes, Influence functional, Time-convolutionless projection operator technique, Cumulant expansion, Stochastic wavefunction method

1. INTRODUCTION

The theory of open quantum systems [1] is concerned with the elimination of the degrees of freedom of the environment in order to get an equation of motion for the density matrix of the reduced system. For an appropriate description of an open system's dynamics that exhibits non-Markovian features a primary goal is to derive exact representations for the reduced density matrix. A closed expression for the density matrix can be obtained for a few analytically solvable models, such as for the damped harmonic oscillator and for free Brownian motion [2–4]. In many interesting cases, however, exact representations for the reduced density matrix serve as starting points of a perturbation expansion in the system–environment coupling and of the development of numerical integration schemes.

[a]E-mail: breuer@marvin.physik.uni-oldenburg.de
[b]E-mail: andrea@www.physik.uni-freiburg.de
[c]E-mail: petruccione@physik.uni-freiburg.de

Quantum Computing and Quantum Bits in Mesoscopic Systems
Edited by Leggett *et al.*, Kluwer Academic/Plenum Publishers, 2004

One possibility of carrying out this program is to derive a time-local master equation for the open system's density matrix $\rho_S(t)$ which takes the form

$$\frac{d}{dt}\rho_S(t) = \mathcal{K}(t)\rho_S(t) \tag{1}$$

where $\mathcal{K}(t)$ is a time-dependent generator, a superoperator in the reduced system's Hilbert space $\mathcal{H}_S$. As can be shown with the help of the time-convolutionless (TCL) projection operator technique [5, 6], a master equation of the form (1) indeed exists for small and intermediate couplings in the case of factorizing initial conditions. Note that Eq. (1) is local in time, that is, it does not involve an integration over the past history of the reduced system. Owing to the explicit time-dependence of the TCL generator $\mathcal{K}(t)$, however, it does not lead to a quantum dynamical semigroup and, therefore, the generator need not be in Lindblad form.

A perturbation expansion of the TCL generator $\mathcal{K}(t)$ may be found in two different ways. One way is to start from the formal solution of the von Neumann equation of the total system and to use van Kampen's technique of ordered cumulant expansion [7, 8]. Another way is to invoke the Feynman–Vernon influence functional representation of the reduced density matrix [2] and to obtain an expansion of the generator directly in terms of the influence phase. Both strategies will be compared in this paper and shown explicitly to yield identical expansions of the TCL generator.

To be specific we consider a system–reservoir model in which the reservoir consists of a collection of harmonic oscillators with frequencies ω_n and masses m_n. The corresponding coordinates and momenta are denoted by x_n and p_n, respectively. The reservoir Hamiltonian is therefore given by

$$H_B = \sum_n \left(\frac{1}{2m_n} p_n^2 + \frac{1}{2} m_n \omega_n x_n^2 \right) \tag{2}$$

The system–reservoir coupling is described by the interaction picture Hamiltonian

$$H_I(t) = -\alpha X(t) B(t) \tag{3}$$

where α represents an overall coupling constant, $X(t)$ is an interaction picture system operator (not necessarily the position coordinate), and $B(t)$ the interaction picture reservoir variable given by

$$B(t) = \sum_n \kappa_n \left(x_n \cos \omega_n t + \frac{p_n}{m_n \omega_n} \sin \omega_n t \right) \tag{4}$$

The constants κ_n describe the strength of the coupling of the reservoir mode n to the reduced system. The dynamics of the total system in the interaction picture is then determined by the von Neumann equation

$$\frac{d}{dt}\rho(t) = \alpha \mathcal{L}(t)\rho(t) \tag{5}$$

where we have introduced the Liouville superoperator $\mathcal{L}(t)$. It is defined by the relation

$$\mathcal{L}(t)\rho = i[X(t)B(t), \rho] \tag{6}$$

where ρ is any operator of the combined system.

The aim is to eliminate the variables of the reservoir to obtain an exact representation for the reduced density matrix $\rho_S(t)$ of the open system. The starting point is the following formal equation which relates the reduced density matrix $\rho_S(t)$ at time t to the density matrix $\rho(0)$ of the total system at the initial time 0,

$$\rho_S(t) = \mathrm{Tr}_B\left\{T_{\leftarrow} \exp\left[\alpha \int_0^t dt' \mathcal{L}(t')\right]\rho(0)\right\} \tag{7}$$

where Tr_B stands for the trace over the degrees of freedom of the environment and $T_{\leftarrow}$ denotes the chronological time-ordering operator.

Let us restrict ourselves here to an initial low-entropy state, which is given by a product state of the form

$$\rho(0) = \rho_S(0) \otimes \rho_B \tag{8}$$

Here, $\rho_S(0)$ is the density matrix at the initial time and ρ_B is the density matrix of the reservoir describing a thermal equilibrium state of temperature T which is given by the Gibbs state

$$\rho_B = \frac{1}{Z_B}\exp(-\beta H_B) \tag{9}$$

where $\beta = 1/k_B T$ denotes the temperature and k_B is the Boltzman constant. The normalization factor Z_B represents the reservoir partition function.

2. TIME-LOCAL MASTER EQUATIONS AND ORDERED CUMULANTS

We are looking for an appropriate expansion of the TCL generator of the master equation (1) with respect to the coupling constant α,

$$\mathcal{K}(t) = \sum_{n=1}^{\infty} \alpha^n \mathcal{K}_n(t) \tag{10}$$

A general formula for the nth-order contribution $\mathcal{K}_n(t)$ to the generator of the TCL master equation can be derived by employing a technique that was developed by van Kampen for the perturbation expansion of stochastic differential equations. To explain briefly this method we define for any superoperator $\mathcal{R}$ of the combined system a corresponding superoperator $\langle\mathcal{R}\rangle$ of the reduced system through the relation

$$\langle\mathcal{R}\rangle\rho_S \equiv \mathrm{Tr}_B\{\mathcal{R}(\rho_S \otimes \rho_B)\} \tag{11}$$

The formal representation (7) may thus be written in the equivalent form

$$\rho_S(t) = \left\langle T_{\leftarrow} \exp\left[\alpha \int_0^t dt' \mathcal{L}(t')\right]\right\rangle \rho_S(0) = \sum_{n=0}^{\infty} \frac{\alpha^n}{n!} \left\langle T_{\leftarrow} \left[\int_0^t dt' \mathcal{L}(t')\right]^n \right\rangle \rho_S(0) \quad (12)$$

where we have expanded the time-ordered exponential in powers of α. Explicitly, the first few terms of this expansion take the form

$$\rho_S(t) = \left[1 + \alpha \int_0^t dt_1 \langle \mathcal{L}(t_1)\rangle + \alpha^2 \int_0^t dt_1 \int_0^{t_1} dt_2 \langle \mathcal{L}(t_1)\mathcal{L}(t_2)\rangle \right.$$
$$\left. + \alpha^3 \int_0^t dt_1 \int_0^{t_1} dt_2 \int_0^{t_2} dt_3 \langle \mathcal{L}(t_1)\mathcal{L}(t_2)\mathcal{L}(t_3)\rangle + \cdots \right] \rho_S(0) \quad (13)$$

Differentiating this equation with respect to time we get

$$\frac{d}{dt}\rho_S(t) = \left[\alpha \langle \mathcal{L}(t)\rangle + \alpha^2 \int_0^t dt_1 \langle \mathcal{L}(t)\mathcal{L}(t_1)\rangle + \alpha^3 \int_0^t dt_1 \int_0^{t_1} dt_2 \langle \mathcal{L}(t)\mathcal{L}(t_1)\mathcal{L}(t_2)\rangle + \cdots \right] \rho(0)_S \quad (14)$$

The strategy is now to invert the expansion on the right-hand side of Eq. (13) with the aim to express $\rho_S(0)$ in terms of $\rho_S(t)$, and to substitute the result into Eq. (14). As was shown by van Kampen this procedure can be carried out in a systematic fashion to yield an expansion for the equation of motion in powers of the coupling. The result is a time-local master equation of the form (1), where the nth-order contribution to the TCL generator (10) is given by

$$\mathcal{K}_n(t) = \int_0^t dt_1 \int_0^{t_1} dt_2 \cdots \int_0^{t_{n-2}} dt_{n-1} \langle \mathcal{L}(t)\mathcal{L}(t_1)\mathcal{L}(t_2)\cdots\mathcal{L}(t_{n-1})\rangle_{\text{oc}} \quad (15)$$

The quantities

$$\langle \mathcal{L}(t)\mathcal{L}(t_1)\mathcal{L}(t_2)\cdots\mathcal{L}(t_{n-1})\rangle_{\text{oc}}$$
$$\equiv \sum (-1)^{(q-1)} \langle \mathcal{L}(t)\cdots\mathcal{L}(t_i)\rangle\langle \mathcal{L}(t_j)\cdots\mathcal{L}(t_k)\rangle\langle \mathcal{L}(t_l)\cdots\mathcal{L}(t_m)\rangle\langle\cdots\rangle \quad (16)$$

are called ordered cumulants. They are defined by the following rules. First, one writes down a string of the form $\langle \mathcal{L}\cdots\mathcal{L}\rangle$ with n factors of $\mathcal{L}$ in between the brackets. Next one partitions the string into an arbitrary number of q substrings ($1 \le q \le n$) of the form $\langle \mathcal{L}\cdots\mathcal{L}\rangle$ by inserting angular brackets between the $\mathcal{L}$s, whereby each substring contains at least one factor of $\mathcal{L}$. The resulting expression is multiplied by a factor $(-1)^{(q-1)}$ and all $\mathcal{L}$s are furnished with a time argument in the following way. The first factor is always $\mathcal{L}(t)$. The remaining $\mathcal{L}$s carry any permutation of the time arguments $t_1, t_2, \ldots, t_{n-1}$ with the only restriction that the time arguments in each substring must be ordered chronologically.

In Eq. (16) we thus have

$$t \geq \cdots \geq t_i, \quad t_j \geq \cdots \geq t_k, \quad t_l \geq \cdots \geq t_m, \ldots \tag{17}$$

Finally, the ordered cumulant is obtained by a summation over all possible partitions into substrings and over all allowed distributions of the time arguments.

For the thermal state (9) and an interaction which is linear in the reservoir coordinates and momenta, as in Eq. (3), we have

$$\langle \mathcal{L}(t_1)\mathcal{L}(t_2)\cdots\mathcal{L}(t_{2n+1})\rangle = 0 \tag{18}$$

Thus, only even-order contributions survive. The above rules then lead to the following explicit expressions for the second- and the fourth-order contributions to the TCL generator

$$\mathcal{K}_2(t) = \int_0^t dt_1 \langle \mathcal{L}(t)\mathcal{L}(t_1)\rangle \tag{19}$$

$$\begin{aligned}\mathcal{K}_4(t) = \int_0^t dt_1 \int_0^{t_1} dt_2 \int_0^{t_2} dt_3 (&\langle \mathcal{L}(t)\mathcal{L}(t_1)\mathcal{L}(t_2)\mathcal{L}(t_3)\rangle - \langle \mathcal{L}(t)\mathcal{L}(t_1)\rangle\langle \mathcal{L}(t_2)\mathcal{L}(t_3)\rangle \\ &- \langle \mathcal{L}(t)\mathcal{L}(t_2)\rangle\langle \mathcal{L}(t_1)\mathcal{L}(t_3)\rangle - \langle \mathcal{L}(t)\mathcal{L}(t_3)\rangle\langle \mathcal{L}(t_1)\mathcal{L}(t_2)\rangle)\end{aligned} \tag{20}$$

In general, one expects that a time-local master equation whose generator consists of only the first few terms of the expansion provides a good description of the reduced dynamics for weak and moderate couplings. However, it should be emphasized that an expansion of the form (10) need not exist for strong couplings. What happens in these cases is that Eq. (12) cannot be solved uniquely for $\rho_S(0)$. In other words, the initial state $\rho_S(0)$ is not uniquely determined by the state $\rho_S(t)$ at time t. Specific examples of the application of this technique to physical models and of the breakdown of the TCL expansion in the strong coupling regime are discussed in Ref. [1].

3. INFLUENCE FUNCTIONAL APPROACH

In each order of the cumulant expansion the TCL generator involves certain combinations of n-point correlation functions of the reservoir variables which enter the expressions (16) for the ordered cumulants. Another strategy of obtaining an expansion of the TCL generator is to eliminate first the reservoir variables completely from the expression (7). This is indeed possible for the present model since the initial state (8) is Gaussian with respect to the reservoir variables and because the system-reservoir interaction is linear in these variables. Following the procedure used in Ref. [9] one finds the following exact superoperator representation of the reduced density matrix

$$\rho_S(t) = T_{\leftarrow}^{X} \exp(i\alpha^2 \Phi_t[X_c, X_a])\rho_S(0) \tag{21}$$

where

$$i\Phi_t[X_c, X_a] = \int_0^t dt' \int_0^{t'} dt'' \left\{ \frac{i}{2} D(t' - t'') X_c(t') X_a(t'') - \frac{1}{2} D_1(t' - t'') X_c(t') X_c(t'') \right\} \tag{22}$$

Equation (21) provides a complete description of the influence of the reservoir on the reduced system. The motion of the system is determined by a time-ordered exponential whose complex phase $i\Phi_t[X_c, X_a]$ is a bilinear functional of the superoperators $X_c(t)$ and $X_a(t)$. The action of these superoperators on any matrix ρ is defined through the commutator and the anticommutator as

$$X_c(t)\rho = [X(t), \rho] \tag{23}$$

$$X_a(t)\rho = \{X(t), \rho\} \tag{24}$$

$T_{\leftarrow}^{X}$ denotes the time-ordering of these superoperators $X_c(t)$ and $X_a(t)$.

The time-ordered exponential function in Eq. (21) represents the superoperator analog of the Feynman–Vernon influence functional, which is usually derived utilizing path-integral techniques [2, 3]. Note that the double time-integral in Eq. (22) is already time-ordered for the integration is extended over the region $t \geq t' \geq t'' \geq 0$. Two fundamental two-point correlation functions enter the above expression for the influence phase, namely the commutator function

$$D(t - t') \equiv i[B(t), B(t')] \tag{25}$$

and the anticommutator function

$$D_1(t - t') \equiv \mathrm{Tr}_B(\{B(t), B(t')\}\rho_B) \tag{26}$$

which are known as dissipation and noise kernel, respectively.

In order to construct a perturbation expansion for a time-local equation of motion for the reduced density matrix we can proceed in a similar way as was done for the cumulant expansion. We first expand the exponential function in Eq. (21)

$$\begin{aligned} \rho_S(t) &= \sum_{m=0}^{\infty} \frac{i^m \alpha^{2m}}{m!} T_{\leftarrow}(\Phi_t[X_c, X_a])^m \rho_S(0) \\ &= \left[1 + i\alpha^2 \Phi_t[X_c, X_a] - \frac{\alpha^4}{2} T_{\leftarrow}(\Phi_t[X_c, X_a])^2 + \cdots \right] \rho_S(0) \end{aligned} \tag{27}$$

and take the time derivative which leads to the expression

$$\begin{aligned} \frac{d}{dt}\rho_S(t) &= \sum_{m=1}^{\infty} \frac{i^m \alpha^{2m}}{m!} \frac{d}{dt} T_{\leftarrow}(i\Phi_t[X_c, X_a])^m \rho_S(0) \\ &= \left[i\alpha^2 \frac{d}{dt} \Phi_t[X_c, X_a] - \frac{\alpha^4}{2} \frac{d}{dt} T_{\leftarrow}(\Phi_t[X_c, X_a])^2 + \cdots \right] \rho_S(0) \end{aligned} \tag{28}$$

A time-local master equation may again be found by solving Eq. (27) for $\rho_S(0)$ within the desired order and by substituting the result into the right-hand side of Eq. (28). It is obvious that this procedure yields an expansion for a time-local generator of the master equation which is identical to the one obtained from the cumulant expansion: The expansions (12) and (27) are indeed identical to all orders in the coupling and, therefore, lead to one and the same expansion of the TCL generator. The comparison of the respective expansions shows that the relations

$$T_{\leftarrow}^{X}(\Phi_t[X_c, X_a])^m = \frac{m!}{i^m(2m)!}\left\langle T_{\leftarrow}\left[\int_0^t dt' \mathcal{L}(t')\right]^{2m}\right\rangle \tag{29}$$

hold for all $m = 1, 2, 3, \ldots$

Let us illustrate this point by an explicit determination of the second- and the fourth-order generator. To lowest order Eq. (27) yields $\rho_S(t) = \rho_S(0)$. To obtain a second-order equation of motion we thus have to substitute this lowest-order expression into the right-hand side of Eq. (28), keeping only the first term. This leads to the second-order master equation

$$\frac{d}{dt}\rho_S(t) = \mathcal{K}_2(t)\rho_S(t) \tag{30}$$

with the generator

$$\mathcal{K}_2(t) = i\frac{d}{dt}\Phi_t[X_c, X_a] = \int_0^t dt_1 \langle \mathcal{L}(t)\mathcal{L}(t_1)\rangle \tag{31}$$

where we made use of Eq. (29) for $m = 1$. Obviously, this expression coincides with Eq. (19).

The fourth-order contribution of the TCL generator is found by first inverting Eq. (27) in second order which gives

$$\rho_S(0) = (1 - i\Phi_t[X_c, X_a])\rho_S(t) \tag{32}$$

and by inserting this expression into the right-hand side of Eq. (28), keeping only fourth-order terms. The resulting fourth-order master equation is, obviously,

$$\frac{d}{dt}\rho_S(t) = [\mathcal{K}_2(t) + \mathcal{K}_4(t)]\rho_S(t) \tag{33}$$

where the fourth-order contribution to the generator reads

$$\mathcal{K}_4(t) = -\frac{1}{2}\frac{d}{dt}T_{\leftarrow}(\Phi_t[X_c, X_a])^2 + \Phi_t[X_c, X_a]\frac{d}{dt}\Phi_t[X_c, X_a] \tag{34}$$

Invoking Eq. (29) for $m = 1$ and $m = 2$ this can be transformed into

$$\mathcal{K}_4(t) = \int_0^t dt_1 \int_0^{t_1} dt_2 \int_0^{t_2} dt_3 \langle \mathcal{L}(t)\mathcal{L}(t_1)\mathcal{L}(t_2)\mathcal{L}(t_3)\rangle - \int_0^t dt_1 \int_0^t dt_2 \int_0^{t_2} dt_3 \langle \mathcal{L}(t)\mathcal{L}(t_1)\rangle\langle \mathcal{L}(t_2)\mathcal{L}(t_3)\rangle. \tag{35}$$

Note that the t_2-integral in the second term on the right-hand side of this equation extends from 0 to t. The triple time-integral of this term may be brought into time-ordered form by appropriate substitutions of the time variables. More precisely, we may write this integral as a sum of three integrals each of which extends over the region $t \geq t_1 \geq t_2 \geq t_3 \geq 0$. In this way, one easily recognizes that Eq. (35) for the fourth-order generator becomes identical to Eq. (20).

By use of Eqs (31) and (34) one easily finds explicit expressions for the second- and for the fourth-order contribution to the TCL generator in terms of the dissipation and the noise kernel and of the commutator and the anticommutator superoperators, namely

$$\mathcal{K}_2(t) = \int_0^t dt_1 \left\{ \frac{i}{2} D(t - t_1) X_c(t) X_a(t_1) - \frac{1}{2} D_1(t - t_1) X_c(t) X_c(t_1) \right\}$$

and

$$\begin{aligned}
\mathcal{K}_4(t) = \frac{1}{4} \int_0^t dt_1 \int_0^{t_1} dt_2 \int_0^{t_2} dt_3 \{ & [D_1(t - t_2) D_1(t_1 - t_3) \\
& + D_1(t - t_3) D_1(t_1 - t_2)] X_c(t) X_c(t_1) X_c(t_2) X_c(t_3) \\
& - [D(t - t_2) D(t_1 - t_3) + D(t - t_3) D(t_1 - t_2)] X_c(t) X_c(t_1) X_a(t_2) X_a(t_3) \\
& - i[D_1(t - t_2) D(t_1 - t_3) + D(t - t_3) D_1(t_1 - t_2)] X_c(t) X_c(t_1) X_c(t_2) X_a(t_3) \\
& - i[D(t - t_2) D_1(t_1 - t_3) + D_1(t - t_3) D(t_1 - t_2)] X_c(t) X_c(t_1) X_a(t_2) X_c(t_3) \\
& + D(t - t_2) D(t_1 - t_3) X_c(t) X_a(t_2) X_c(t_1) X_a(t_3) \\
& - D_1(t - t_2) D_1(t_1 - t_3) X_c(t) X_c(t_2) X_c(t_1) X_c(t_3) \\
& + iD(t - t_2) D_1(t_1 - t_3) X_c(t) X_a(t_2) X_c(t_1) X_c(t_3) \\
& + iD_1(t - t_2) D(t_1 - t_3) X_c(t) X_c(t_2) X_c(t_1) X_a(t_3) \\
& + D(t - t_3) D(t_1 - t_2) X_c(t) X_a(t_3) X_c(t_1) X_a(t_2) \\
& - D_1(t - t_3) D_1(t_1 - t_2) X_c(t) X_c(t_3) X_c(t_1) X_c(t_2) \\
& + iD(t - t_3) D_1(t_1 - t_2) X_c(t) X_a(t_3) X_c(t_1) X_c(t_2) \\
& + iD_1(t - t_3) D(t_1 - t_2) X_c(t) X_c(t_3) X_c(t_1) X_a(t_2) \}.
\end{aligned}$$

4. CONCLUSIONS

The perturbation expansion of the generator of a non-Markovian, time-local master equation may be constructed through the technique of ordered cumulants or, equivalently,

by use of the exact influence functional expression for the reduced density matrix. We have made explicit the relation between both approaches, invoking the connection between time-ordered products of the influence phase and of the interaction Liouville operator.

It should be clear, however, that an expansion directly though the influence functional is only useful, of course, provided an explicit expression for the influence functional is available. This was the case in the present study for the reservoir was assumed to be describable by a Gaussian (thermal) state. In this respect, the ordered cumulant expansion is more general since it does not rely on the Gaussian property of the environment.

An important generalization of the present investigation could be to include non-factorizing initial conditions for the density matrix of the combined system–reservoir state. The corresponding correlations in the initial state lead to an inhomogeneity in the master equation. The expansion of this inhomogeneity in powers of the system–reservoir coupling is known from the time-convolutionless projection operator technique [5, 6], while the treatment of nonfactorizing initial conditions is also possible within the framework of the influence functional technique for Gaussian reservoirs [4].

Finally we emphasize that the derivation of a time-local generator may be important from the numerical point of view. Not only is a time-local master equation certainly easier to solve than a generalized master equation involving a retarded memory kernel, but it also offers the possibility of a stochastic unraveling of the master equation. To all orders in the coupling, the form of the TCL generator allows the design of an appropriate stochastic process $(\phi(t), \psi(t))$ for the state vector in a doubled Hilbert space $\mathcal{H}_S \oplus \mathcal{H}_S$ such that the average over the quantity $|\phi\rangle\langle\psi|$ yields the open system's density matrix [10]. The TCL form of the master equation thus gives rise to stochastic wavefunction algorithms for non-Markovian quantum processes.

REFERENCES

[1] H. P. Breuer and F. Petruccione, *The Theory of Open Quantum Systems* (Oxford, Oxford University Press, 2002).
[2] R. P. Feynman and F. L. Vernon, *Ann. Phys. (N.Y.)* **24**, 118–173 (1963).
[3] A. O. Caldeira and A. J. Leggett, *Physica* **121A**, 587–616 (1983).
[4] H. Grabert, P. Schramm, and G.-L. Ingold, *Phys. Rep.* **168**, 115–207 (1988).
[5] F. Shibata, Y. Takahashi, and N. Hashitume, *J. Stat. Phys.* **17**, 171–187 (1977).
[6] S. Chaturvedi and F. Shibata, *Z. Phys. B* **35**, 297–308 (1979).
[7] N. G. van Kampen, *Physica* **74**, 215–238 (1974).
[8] N. C. van Kampen, *Physica* **74**, 239–247 (1974).
[9] H. P. Breuer and F. Petruccione, *Phys. Rev.* A **63**, 032102-1(18) (2001).
[10] H. P. Breuer, B. Kappler, and F. Petruccione, *Phys. Rev.* A **59**, 1633–1643 (1999).

INDEX

1/f noise in Josephson Qubits, 171, 237
Adiabatic quantum computing of NP-Hard problems, 229
Adiabatic quantum gates, 34
Aharonov-Casher Effect, 23
Bose-Einstein condensates, 101
Decoherence, 13, 33, 111, 171, 241
Dephasing in quantum two-level systems, 211
Dissipation, 24, 34, 41, 51, 264
Gate errors in Solid-state quantum computer, 195
Holonomic gates and quantum computer, 149, 156
Influence of the measurement process, 139
Interaction of ultrafast laser pulse with JJ, 133
Isolated Quantum-mechanical system, 1
Josephson arrays, 69, 106
Macroscopic Quantum Coherence, 31, 41, 101, 161
Manipulation and readout in Josephson qubit, 13
Josephson qubit coupled to a resonant LC bus, 149
Nanostructures, 87, 95
Persistent current qubit, 59
Quantronium circuit, 15
Quantum cloning and NOT gates, 77
Quantum Dots, 185, 194, 201
Quantum Entanglement and Information, 47, 72
rf-SQUID system, 24, 31, 41
Shor's alogorithm, 123
Single Electron Transistor, 255
Solid-state analog of an optical interferometer, 247
Spin Boson Model, 211
Superconducting Quantum Computing without switches, 219
Time-dependent Schoedinger equation, 60
Time-local master equations, 263